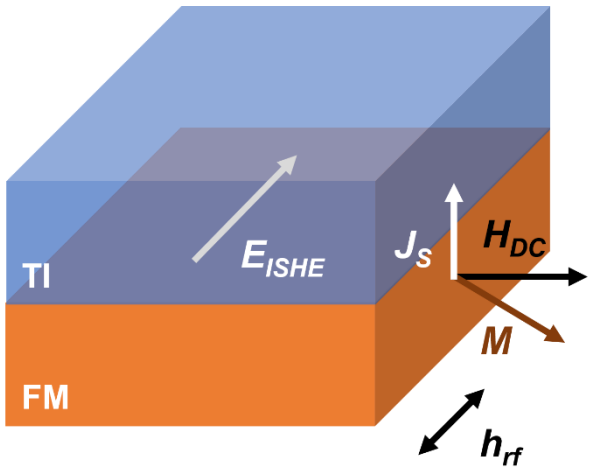


Insights into topological insulators Sb_2Te_3 nanostructures: towards spinorbitronics devices

Sofia Ferreira Teixeira
MAP-Fis Doctoral Program in Physics
Department of Physics and Astronomy
Faculty of Sciences, University of Porto
2022

Supervisor
Pro. André Miguel Trindade Pereira, FCUP

Co-supervisor
Prof. João Pedro Esteves de Araújo, FCUP

Sofia Luísa Soares Ferreira Nunes Teixeira

Insights into topological insulators Sb_2Te_3 nanostructures: towards spinorbitronics devices



Supervisor: *Prof. André Miguel Trindade Pereira*
Co-Supervisor: *Prof. João Pedro Esteves de Araújo*

Thesis submitted to the Faculty of Sciences of the University of Porto in partial fulfilment of the requirements for the degree of Doctor in Physics

Department of Physics and Astronomy
Faculty of Sciences of the University of Porto
2022

Primary institutions involved in this thesis







Other institutions







Doctoral Program











Funding





To my mother and family

”...and the world was not a boundless mystery, but a finite thing that could be comprehended.”

***Ken Follet**,*
The Pillars of the Earth

Acknowledgements

Over the last four years (and nine years if you count all of them here at DFA), I worked along side great people that made this thesis possible and helped me grow. So, already *thank you* to everyone.

The first and foremost person I will forever be grateful to is my supervisor, professor André Pereira. I have been working with you since my 2nd year of undergrad, making it eight years by the end of this PhD. And, throughout these years, not only did you always believe in me, you actually pushed me even further which culminated in this beautiful work we have achieved and in my growth from a physics nerd to a, hopefully, good scientist. Thank you for believing in me, for your patience, for your constant optimism (even if it sometimes annoyed me) and thank you for working with me to reach mine and our goals. This would have not been possible without your constant support and incentive.

To my co-supervisor, professor João Pedro Araújo, thank you also for your support throughout these years which allowed me to develop my ideas and work. To my other ”co-supervisor”, professor Lesley Cohen, who received me with open arms in her lab, which allowed me to go even further with our project, thank you for your great insights and ideas which took our work one step even further.

Secondly, I want to thank IFIMUP/LapMET for giving me access to their facilities, which allowed for the results performed in this thesis to be obtained. I am also thankful for the clean room and microscopy imaging access granted by CEMUP and to Rui Rocha for the microscopy measurements. I would also like to thank, Dr. David Burn and Prof. Thorsten Hesjedal for your interest in collaborating in this project and for the XFMR measurements carried out at Diamond Light Source, and Dr. Alec Grow and INL for the HRTEM access and measurements.

Thank you also to the funding that made this thesis possible, namely FCT for the PhD grant PD/BD/141803/2018.

This thesis would not be possible without the community of IFIMUP. First, Dr. Ana Pires, I want to say again ”the most of warmest thank you’s”. Thank you for always being available to help and for your input with all the lab related stuff (and more). Thank you also for being someone I could always look up to for inspiration to carry on going. Thank you also to the members of our team for sharing the day to day lab and problems, and for the occasional venting which was always helpful, namely Ana Rita Sousa, Cátia Rodrigues, Joana Silva, Margarida Maia and Rui Costa. Another special word also goes to Cátia and Rui for being my ”partners in crime” for the MAP-Fis courses, which we got through together! To Dr. João Horta and Dr. Gonçalo Dias for their management of

the transport properties lab, availability to help with fixing anything wrong, and patience while helping to fix it, thank you. Your help was key at times for me to be able to finish this thesis. I would also like to thank Dr. Sergey Bunyaev, for the FMR measurements and analysis, and Dr. Gleb Kakazei, for his inputs on the FMR results, Dr. Catarina Dias, for all the support with the ion beam sputtering system, and Dr. Rui Vilarinho, for being available to assist us with the Raman measurements. Other ”IFIMUPianos”, with whom I did not work directly, must nevertheless be thanked, namely Ana Sofia Silva, Paula Quitério, Pedro Rodrigues (thank you for travelling with my samples!), Suellen Moraes and Vivian Andrade. You made having lunch always a nice and fun time, and, to my office mates, you turned our office into an enjoyable place to work.

I would also like to thank several people at the Department of Physics and Astronomy of the University of Porto, who have helped me during this PhD and throughout my years here, always with great sympathy and availability. To Eng. Franscico Carpinteiro, thank you for all your patience and help in fixing what kept being broken and for everything I have learned from you. To D. Isabel Alves and Dra. Armanda, thank you for the help when dealing with bureaucratic situations regarding my work at IFIMUP. To D. Armanda and D. Filomena, thank you for your always warm welcomes, willingness to help and goodwill, and to Dra. Florbela for all the help with the intricate bureaucratic details, especially considering my PhD. Thank you also to Ana Queirós for the clean room support and to Pedro Cruz for all the technical support and patience to put up with me.

I was also very well welcomed by another community, at Imperial College London. The group of professor Lesley Cohen made me feel at home during my time in London and, as such, a big thank you to everyone, namely Dr. Will Branford, Dr. Andy Moskalenko, Alex Chan, Alex Vanstone, Avinash Kumar, Freya Johnson, Dr. Jack Cartside and Kilian Stenning. In special, to Freya Johnson, thank you for you help and input, with the transport measurements, and Alex Chan, for teaching me the first steps in the FMR measurements and for welcoming me so well, not only to our lab but also our office and London in general (thank you for the games and movies nights!). Last but not least, I want to thank Alex Vanstone, for all the assistance with the never ending measurements, for being my partner for some of the greatest developments of this thesis and for the friendship. You not only made part of this thesis possible, but also all the lab times enjoyable, even when things were going wrong. I cannot also forget my office mates, which made my time in London truly enjoyable, namely Alex Chan, Emma Pearce, Mónica Mota, Paul Ditchl, Romain Tirole and Tahiyat Huq. You made lunch times fun, late nights in the office an actually nice time and the pints at the end of the day always made up for hbar food at lunch.

This cannot be complete without thanking all the people I have become friends with from the several groups, committees, association and societies I was involved in. First, I still need to mention PhysikUP. I handed over my presidency a couple of months before the start of my PhD, but it still had an impact on my work in the last four years, because

I saw the marvellous machine it had become. Thank you to Simão Sá and Margarida Maia that made this possible at the start, and then to my successors Carolina Silva and Rita Bugalhão (girl power, uh uh!) who just took it to a whole other level. Thank you also again to Carolina and Rita, and also to Mafalda Matos, Alexandra Oliveira, Pedro Vianez, Fernando Maia and Duartes ”DJs” (both Graça and Silva!) for joining me on the wild adventure of organising the international online competition PLANCKS and becoming the team anyone dreams of (my dream team!). I still do not change the joke I made regarding my PhD when we first announced our bid back in 2019.

To the International Association of Physics Students (IAPS) and everyone who created it and runs it for the great opportunities it has offered me. Thank you to my brothers and sisters in arms of the two executive committees I was in from 2017 to early 2019, namely Sabrina Gronow, Mattia Ivaldi, James Kneller, Pedro Vianez and Duarte Graça. We made some great things and ended up becoming greater friends. IAPS has given me the chance to also meet other amazing people who I am proud to call friends: Lucio Maria Milanese, Cyrus Walther, Alejandro Fernández Muñoz and Tobi Messer. As Lucio put it ”We are not the kind of people to settle at a low energy state” and thus, thank you for allowing me to always be at an excited state and for joining me in these adventures, even when I am about to decay back down to the ground state.

Friends that cannot also be forgotten are Pedro Vianez, Rúben Azinheira Alves and Adriana Ferreira. Pedro, thank you for being my friend for all these years, even when you went to the island. You were my companion in this PhD journey, and not only that because I dragged you with me to everything I could. You also had the patience to hear me vent about everything and anything work related and also life. Our amazing trip to Denver for the ”not cancelled” APS 2020 March meeting will never be forgotten (!), and I look forward to see what life has in store for us in this academic world. To Ruben a big thank you for not only joining me in the crazy project PhysikUP was, at a very unexpected time, but also for continuing being a friend I could rely on, especially if it was to share PhD woos, even though you also run away to the island. Thank you also to Adriana for always being there for a coffee or a fino to talk about our lives and PhDs that we ended up doing. Who would say the only two girls in the high school physics class would get here? But we did it, and we *are* doing it. Thank you!

The last gratitudes of this extensive acknowledgements go, however, to my family, who made me who I am. To my dad for all his attentiveness, to my godmum for always being there when I needed and to my goddad for always showing interest in my work and life. Also thank you to my cats, because you are family to me, and kept me company in the long writing hours and entertained me whenever a rest was needed throughout the four years (and my life). Lastly, to my mum, without whom all this would not have been possible. Thank you for always being there and supporting me, even when I am in a really bad mood, and for managing to calm me down and push me to carry on forward. Thank you.

Abstract

Spinorbitronics has emerged as a sub-field of spintronics, holding significant potential for generating efficient logic and data storage devices. It is based on the spin-orbit effects, exploiting the spin to charge interconversion (SCI) to control magnetic materials via spin-orbit torques (SOT). The development of such devices thus passes through optimisation of both the magnetic and SOC (Spin-Orbit Coupling) materials (such as Py, Pt, and Ta). Topological insulators (TIs) are a set of SOC materials that emerged in recent years, such as the 3D TI Bi_2Se_3 family of semiconductors. Such materials display a topological surface state (TSS), but owing to their strong SOC, a high SCI has been attained via the spin hall effect. In the light of this tendency, the present thesis is oriented towards advancing the implementation of spinorbitronics devices using TIs, namely Sb_2Te_3.

Sputtering was employed to fabricate nanostructures of Sb_2Te_3. The SCI effects were studied through spin pumping measurements implemented as a function of temperature for cryogenic temperatures. The electrical and thermal transport properties of the Sb_2Te_3 thin films were also analysed. Thin films with thicknesses between 35 and 300 nm have a high room temperature resistivity ranging from around 0.07 and 2 Ωcm, exhibiting a growing resistivity with cooling. The Seebeck coefficient demonstrates the coexistence of n-type and p-type conduction, the latter being more prominent at high temperatures and in thicker films. A surface n-type semiconductor channel can describe the electronic conduction of the films in parallel with a bulk p-type semiconductor, each associated with an activation energy-dependent conductivity. Weak antilocalisation (WAL) cusps are observed in the magnetoconductance below 10 K and at low magnetic fields. Analysis of the WAL effect indicates that only one two dimensional (2D) conduction channel is open at low temperatures for the thinner films. In contrast, for the thicker film, this 2D channel is masked by the other conduction channels. However, a magnetic localisation length L_ϕ between 62 nm and 90 nm at 2 K is observed for all thin films. This behaviour implies that as the bulk and surface activation energy conduction freeze out at low temperatures, the TSS carries the electrical conduction.

Bilayers of ferromagnet (FM) Py and Sb_2Te_3 thin films with thicknesses between 10 and 100 nm were also sputtered on glass substrates to further understand the electronic conduction and magnetisation dynamics in bilayer systems. Each layer is uniform and maintains the structure of the single independent thin films. Via the electrical resistance and Seebeck coefficient temperature dependences, a model for shunting effects in the conduction is proposed, which shows that the Py layer dominates the conduction and how its flow through the Sb_2Te_3 layer is reduced with cooling. Notwithstanding the con-

duction dominance of the Py layer, at low temperatures, the WAL effect is present in the magnetoreistance due to the TI states of Sb_2Te_3. L_ϕ was calculated from the bilayer magnetoconductance and it is the same value as the one obtained for the single Sb_2Te_3 thin films, further proving the shunting model proposed and showcasing that the TI states remain unaltered when Sb_2Te_3 is sputtered on top of Py. Ferromagnetic resonance (FMR) was also employed to study the magnetisation dynamics of the bilayers. By comparing with reference capped Py samples, the Gilbert damping shows an increase of 27% due to the presence of Sb_2Te_3, which, considering the morphological analysis, indicates that spin pumping occurs from the FM layer into the TI layer.

The Spin to Charge Conversion (SCC) of Sb_2Te_3 was characterised via Spin pumping experiments on the FM/TI sputtered bilayers. FMR characterisation was performed as a function of temperature, showing that the Gilbert damping is always higher for the the FM/TI bilayers than the capped reference Py samples. There is also an increase of 20% of the damping below 10 K, coinciding with the temperature range where the TSS is dominating the conduction. The spin diffusion length λ_{SD} was calculated from the magnetoconductance measurements to be approximately 27 nm at 2 K, with a reduction with cooling being noted. At room temperature, the spin Hall angle θ_{SH} value is -0.0033 $\pm$ 0.0004, having been calculated from two independent bilayers with the same thickness of Sb_2Te_3. Considering logic applications, Sb_2Te_3 has the needed resistivity and the SCI efficiency, namely the product of θ_{SH} and λ_{SD}, has a value of 0.016 nm.

Bearing in mind the current advances in technological applications, thin films of Sb_2Te_3 were also fabricated on flexible substrates. The effects of the plasma beam sputtering voltage on the structural and electronic transport properties were studied, unveiling small nanocrystallites of 3 to 20 nm in size. The resistivity shows a semiconductor behaviour, increasing with cooling and having high values, between 8.34 $\times 10^{-2}$ and 1.2 Ωcm, at room temperature. The Seebeck coefficient shows the coexistence of n-type and p-type conduction, the latter being more prominent at high temperatures. A surface n-type semiconductor channel conducting in parallel with a bulk p-type semiconductor describe the electronic conduction of the films. These conduction channels are characterised by an activation energy, which is also controlled by the sputtering conditions. Finally, flexible FM/TI/FM trialyers were also sputtered and had their structural and electronic properties characterised. From the magnetisation dynamics measurements, namely FMR and x-ray detected FMR (XFMR), it was discovered that Sb_2Te_3 can act as an effective spin sink in this stack trilayer.

Keywords Topological Insulators, Spinorbitronics, thin films, nanostructures, Spin to charge conversion, transport properties

Resumo

Spinorbitrónica apareceu como uma sub-área da eletrónica de spin, oferecendo a possibilidade de criação de dispositivos de lógica e armazenamento de dados eficientes. É baseada nos efeitos de spin-orbita, aproveitando-se da interconversão de carga e spin (SCI) para o controlo de materiais magnéticos via torque de spin orbita (SOT). O desenvolvimento de tais dispositivos passa pela a otimização de ambos materiais, magnéticos e de acoplamento spin orbita (SOC) (como Py, Pt e Ta). Isoladores topológicos (TIs) são um conjunto de materiais SOC que apareceram nos últimos anos, principalmente os TIs 3D, como a família de semicondutores do Bi_2Se_3. Estes materiais não só mostraram a existência do estado topológico de superfície (TSS), mas devido ao seu SOC, grandes SCIs através do efeito de spin Hall foram obtidas. Com esta tendência, esta tese foca-se no avanço da realização de dispositivos de spinorbitronica usando TIs, nomeadamente Sb_2Te_3.

Nanoestruturas de Sb_2Te_3 foram fabricadas por *sputtering*. Os efeitos de SCI foram estudados através de medidas de *spin pumping* que foram implementadas em função da temperatura e as propriedades de transporte elétricas e térmicas dos filmes finos de Sb_2Te_3 foram também analisadas. Filmes com espessuras entre 35 e 300 nm têm uma resistividade à temperatura ambiente entre 0.07 e 2 Ωcm, crescendo com o arrefecimento. O coeficiente de Seebeck mostra a coexistência de condução tipo n e p, sendo que a última é mais proeminente a temperaturas altas nos filmes mais espessos. A condução eletrónica pode ser descrita por um canal de superfície semicondutor do tipo n em paralelo com um *bulk* semiconductor tipo p, cada um com uma condutividade dependente de uma energia de ativação. As cúspides da anti-localização fraca (WAL) são observadas na magnetocondutância a baixo dos 10 K e a baixos campos magnéticos. A análise da WAL indica que só um canal de condução 2D está aberto às baixas temperaturas para os filmes mais finos, enquanto que para o filme mais espesso, este canal é mascarado pelos outros canais. No entanto, valores do comprimento de localização magnética entre 62 e 90 nm a 2 K são observados para todos os filmes. Este comportamento mostra que quando a condução do *bulk* e superfícies descrita pela energia de ativação é congelada a baixas temperaturas, a condução elétrica é feita pelo TSS.

Bicamadas do ferromagnético (FM) Py e Sb_2Te_3 com espessuras entre 10 e 100 nm foram fabricadas por *sputtering* em vidro para compreender melhor a condução elétrica e a dinâmica da magnetização nos sistemas de bicamadas. Cada filme é uniforme e mantem a estrutura dos filmes independentes. Através das dependências na temperatura da resistência e do coeficiente de Seebeck, um modelo para os efeitos

de *shunting* é proposto, mostrando como a condução é dominada pelo Py e como a que passa pelo Sb_2Te_3 é reduzida com arrefecimento. Apesar da condução dominante da camada de Py, a baixas temperaturas, a correção na magnetorresistência do efeito WAL devido aos estados TI do Sb_2Te_3 está presente. O L_ϕ foi calculado através da magnetocondutância da bicamada e é igual ao valor obtido pelo filme independente de Sb_2Te_3, provando o modelo de *shunting* proposto e mostrando que os estados do TI ficam inalterados quando o Sb_2Te_3 é fabricado no topo do Py. Ressonância ferromagnética (FMR) foi usada para estudar a dinâmica da magnetização das bicamadas. Fazendo uma comparação com amostras de Py *capped*, o amortecimento de Gilbert mostra um aumento de 27% devido à presença do Sb_2Te_3, que, considerando a análise morfológica, indica que o *spin pumping* ocorre do material FM para o TI.

A conversão de spin para carga (SCC) do Sb_2Te_3 foi estudada via experiências de *spin pumping* nas bicamadas FM/TI. A FMR foi medida em função da temperatura, mostrando que o amortecimento de Gilbert é sempre maior para as bicamadas de FM/TI do que para as amostras de referência capped do Py, com um aumento de 20% do amortecimento abaixo dos 10 K, que coincide com o intervalo de temperaturas no qual o TSS domina a condução. O comprimento de difusão de spin foi calculado pelas medidas de magnetocondutância, sendo aproximadamente 27 nm a 2 K, vendo-se uma redução com aquecimento. À temperatura ambiente, o ângulo de spin Hall tem o valor de -0.0033 $\pm$ 0.0004, tendo sido calculado para duas bicamadas diferentes, com a mesma espessura do Sb_2Te_3. Considerando aplicações lógicas, a eficiência pode ser considerada como o produto do ângulo de spin Hall pelo comprimento de difusão de spin, tendo sido obtido um valor de 0.016 nm, sendo que Sb_2Te_3 já tem o valor de resistividade necessário, para tais aplicações.

Considerando os avanços atuais das aplicações tecnológicas, filmes de Sb_2Te_3 foram também fabricados em substratos flexíveis. Os efeitos da tensão de *sputtering* nas propriedades estruturais e eletrónicas foram estudados, mostrando nanocristalites de 3 a 20 nm de tamanho. A resistividade mostra um comportamento semicondutor, aumentando com o arrefecimento, e tendo valores altos, entre 8.34 $\times$10–2 e 1.2 Ωcm, à temperatura ambiente. O coeficiente de Seebeck mostra a coexistência de condução tipo n e p, com a última sendo mais proeminente à temperatura alta. A condução eletrónica é descrita por um canal de superfícies semicondutor do tipo n em paralelo com um *bulk* semicondutor do tipo p. Estes canais de condução são descritos por energias de ativação, que são controladas pelas condições de *sputtering*. Finalmente, FM/TI/FM tricamadas flexíveis foram também fabricadas por *sputtering*, e as suas propriedades estruturais e eletrónicas analisadas. Através de medidas de FMR e FMR detetado por raios-X (XFMR), foi descoberto que o Sb_2Te_3 pode estar a atuar como um absorvente de spin eficiente nesta estrutura em tricamada.

Palavras-chave Isoladores topológicos, spinorbitrónica, filmes finos, nanoestruturas, conversão de spin para carga, propriedades de transporte

Contents

Acknowledgements **xi**

Abstract **xv**

Resumo **xvii**

Contents **xxii**

List of Figures **xxv**

List of Tables **xxvii**

List of Abbreviations and Symbols **xxix**

Thesis outline **1**

1 Introduction **11**

1.1 Spintronics 11

1.2 Spinorbitronics 12

1.2.1 Spin to charge interconversion 12

1.2.1.1 Spin Hall Effect 13

1.2.1.2 Edelstein Effect 14

1.2.2 Data storage and logic devices 14

1.2.3 Materials for spin-orbit torque applications 16

1.3 Topological Insulators 18

1.3.1 Electronic properties of 3D Topological insulators 18

1.3.2 Spin to charge interconversion in topological insulators 19

2 Methods **21**

2.1 Nanostructures fabrication 21

2.1.1 Ion Beam Sputtering 21

2.1.2 DC Magnetron Sputtering 23

2.2 Morphological and Structural Characterisation 25

2.2.1 Scanning Electron Microscopy (SEM) 25

2.2.2 Energy Dispersive X-ray Spectroscopy (EDS) 26

2.2.3 High resolution Transmission Electron Microscopy (HRTEM) . . . 27
2.2.4 Atomic Force Microscopy (AFM) . . . 28
2.2.5 X-Ray diffraction (XRD) . . . 29
2.2.6 X-Ray reflectivity (XRR) . . . 30
2.2.7 Raman Spectroscopy . . . 31
2.3 Transport Properties . . . 32
2.3.1 Electrical Resistance . . . 32
2.3.2 Magnetotransport . . . 34
2.3.2.1 Magnetoresistance . . . 34
2.3.2.2 Hall effect . . . 35
2.4 Ferromagnetic Resonance Spectroscopy (FMR) . . . 35
2.4.1 Vector Network Analyser Ferromagnetic Resonance (VNA-FMR) . 36
2.4.2 Lock-in amplifier Modulated Ferromagnetic Resonance (LIA-FMR) 37
2.4.3 X-Ray Detected Ferromagnetic Resonance (XFMR) . . . 39
2.5 Implementation of Spin Pumping measurements . . . 41
2.5.1 Injection of the spin current . . . 41
2.5.2 Evaluation of the spin to charge conversion . . . 43
2.5.3 Measurements of spin pumping voltage . . . 44
2.5.3.1 Observation of the Inverse Spin Hall Effect . . . 44
2.5.3.2 External Lock-in detection . . . 45
2.5.3.3 Open voltage nanovoltmeter measurements . . . 46

3 Design of a versatile Seebeck and Electrical Resistivity measurement setup for thin films 49
3.1 Introduction . . . 49
3.2 Principle and Setup . . . 50
3.2.1 Measurement apparatus . . . 50
3.2.2 Measurement setup . . . 51
3.3 Measurement Procedure . . . 52
3.3.1 Seebeck coefficient measurement . . . 52
3.3.1.1 Dynamic measurement . . . 52
3.3.1.2 Quasi-steady differential measurements . . . 53
3.3.2 Resistivity measurement . . . 53
3.4 Validation of the measurement setup and method . . . 55
3.4.1 Commercial Niobium foil . . . 55
3.4.2 Specular Spin Valve . . . 56
3.5 Conclusion . . . 57

4 Electronic conduction channels of topological insulator sputtered Sb_2Te_3 thin films 59
4.1 Introduction . . . 59

4.2 Morphology and structure of the sputtered films . . . 60
4.2.1 Structural characterisation . . . 60
4.2.2 Morphological characterisation . . . 64
4.3 Electronic transport properties . . . 65
4.4 Magnetotransport . . . 68
4.4.1 Hall effect . . . 69
4.4.2 Magnetoconductance . . . 69
4.5 Conclusion . . . 73

5 Thermo-magneto-electric properties of sputtered ferromagnetic/topological insulator bilayers 75
5.1 Introduction . . . 75
5.2 Morphological and Structural Properties of the FM/TI bilayers . . . 77
5.3 Electronic Properties of the FM/TI bilayers . . . 80
5.3.1 Resistivity and Seebeck Coefficient . . . 80
5.3.2 Magnetoresistance . . . 85
5.3.2.1 Temperature dependence of the Magnetoresistance . . . 85
5.3.2.2 Magnetoresistance at low temperatures . . . 87
5.4 Magnetisation dynamics at room temperature . . . 88
5.4.1 FM/TI bilayers . . . 88
5.4.2 Reference FM capped thin films . . . 90
5.4.3 Generated spin currents . . . 92
5.5 Conclusions . . . 92

6 Spin to charge current conversion for energy-efficient logic devices 95
6.1 Introduction . . . 95
6.2 Temperature dependence of the magnetisation dynamics . . . 97
6.2.1 Ferromagnetic resonance as a function of temperature . . . 97
6.2.2 Characterisation of the generated spin currents . . . 100
6.3 Spin pumping in the FM/TI bilayers . . . 101
6.4 Spin to charge conversion efficiency of Sb_2Te_3 . . . 103
6.5 Conclusions . . . 106

7 Sputtered topological insulator nanostructures towards flexible spintronics devices 109
7.1 Introduction . . . 110
7.2 Flexible Sb_2Te_3 topological insulator thin films . . . 111
7.2.1 Structural and Morphological characterisation . . . 111
7.2.2 Electronic properties . . . 113
7.3 Flexible FM/TI/FM trilayers . . . 119
7.3.1 Structural and Morphological Characterisation . . . 119
7.3.2 Electronic properties . . . 121

7.3.3 Magnetisation dynamics 123
7.4 Conclusion 127

8 Conclusions and Perspectives **129**
8.1 Conclusions 129
8.2 Perspectives 130

Bibliography **133**

List of Figures

1.1 Moore's Law and the Era of the Internet of Things (IoT). 11
1.2 Spin Hall effect. 13
1.3 MRAM technology. 15
1.4 Magnetoelectric spin-orbit logic (MESO) device. 16
1.5 Magnetisation switching via SHE of platinum. 17
1.6 The electronic properties of the Bi_2Se_3 topological insulators family. . . . 19
1.7 Spin to charge conversion by sputtered Bi_2Se_3 thin film. 20

2.1 Ion Beam Sputtering. 22
2.2 DC Magnetron Sputtering 25
2.3 Schematic diagram of the scanning electron microscope (SEM). 26
2.4 Overview of the basic components of a TEM system. 27
2.5 The AFM working modes. 28
2.6 XRD Bragg's relation 29
2.7 X-ray reflectivity curves. 31
2.8 Semi-classical representation of Raman scattering. 32
2.9 Experimental assembly for electrical resistivity measurements. 33
2.10 Magnetotransport contact geometries. 34
2.11 A schematic of the VNA-FMR system. 37
2.12 Lock-in amplifier modulated FMR system. 38
2.13 Schematic of the XFMR setup in transverse geometry. 40
2.14 Schematic representation of spin pumping. 43
2.15 NanOsc CryoFMR spin pumping measurements. 45
2.16 Spin pumping measurement comparison between the CryoFMR system and an external Lock-in. 46
2.17 Spin pumping measurement comparison between the CryoFMR system and the nanovoltmeter. 47

3.1 Setup and Sample Holder 51
3.2 The applied temperature difference. 53
3.3 Seebeck coefficient measurements by the quasi-steady differential method. 54
3.4 I-V curve resistance measurements. 54
3.5 Measurements of the commercial niobium foil and contact resistance of the setup. 55

3.6 Measurements of the Specular Spin Valve. 56

4.1 SEM and EDS of the Sb_2Te_3 100 nm thin film. 60
4.2 XRD pattern of the Sb_2Te_3 thin films. 61
4.3 Raman spectra of the Sb_2Te_3 thin films. 62
4.4 HRTEM analysis of the nanostructure of the Sb_2Te_3 thin films. 63
4.5 Quantity of Sb, Te and Si obtained through an EDS line scan of the 35 nm thin film. 63
4.6 AFM and SEM cross section images of the Sb_2Te_3 100 nm thin film. . . . 64
4.7 XRR patterns of the Sb_2Te_3 sputtered thin films. 65
4.8 Resistivity as a function of temperature of the Sb_2Te_3 thin films. 66
4.9 Seebeck coefficient as a function of temperature of the Sb_2Te_3 thin films. 67
4.10 The electronic conduction of the Sb_2Te_3 thin films. 68
4.11 Hall resistivity of Sb_2Te_3 100 nm thin film as a function of temperature. . . 69
4.12 Magnetoconductance of the Sb_2Te_3 thin films. 70
4.13 Magnetoconductance WAL parameters of the Sb_2Te_3 thin films. 72
4.14 Magnetoconductance parameters of the Sb_2Te_3 thin films. 73

5.1 SEM cross sectional images of the bilayers. 78
5.2 XRR of the bilayers with different layer thicknesses. 78
5.3 XRR of the bilayers with layers of the same thickness. 79
5.4 XRD patterns of the bilayers. 80
5.5 Resistance of the bilayers. 81
5.6 Permalloy resistance parameters. 82
5.7 Seebeck coefficient of the bilayers. 83
5.8 Cross-sectional area of the bilayer shunting conduction model. 85
5.9 Magnetoresistance of the bilayers at room temperature. 86
5.10 Temperature dependence of the magnetoresistance of the bilayers. . . . 87
5.11 Magnetoresistance of the bilayers at 2 K. 88
5.12 Shunting effect on the magnetoresistance. 89
5.13 Magnetisation dynamics of the bilayers. 89
5.14 Capped FM Py thin films magnetisation dynamics. 90
5.15 The spin mixing conduction and generated spin current of the Py/ST bilayers. 93

6.1 Ferromagnetic resonance absorption as a function of temperature. 97
6.2 Resonance field H_{res}frequency dependence. 98
6.3 Magnetisation and Anisotropy field dependence on temperature. 98
6.4 Ferromagnetic resonance linewidth ΔH frequency dependence. 99
6.5 Temperature dependence of the Gilbert Damping. 100
6.6 Spin mixing conduction and generated generated spin current as a function of temperature. 101

6.7 Spin pumping as a function of temperature in the Py(10)/ST(100) bilayer. 102
6.8 Spin pumping at room temperature. 103
6.9 Spin to charge conversion properties of Sb_2Te_3. 105
6.10 State of the art of SOC materials. 106

7.1 Structural characterisation of the flexible thin films. 111
7.2 Fits to the XRD diffractograms of the flexible Sb_2Te_3 thin films. 112
7.3 Grain sizes of the flexible Sb_2Te_3 thin films. 113
7.4 Electrical resistivity of the flexible Sb_2Te_3 thin films. 114
7.5 Seebeck Coefficient of the flexible Sb_2Te_3 thin films. 115
7.6 Analysis of the transport properties of the flexible Sb_2Te_3 thin films. 117
7.7 Structural and transport parameters of the Sb_2Te_3 thin films. 118
7.8 XRD diffractogram of the CoFe thin films. 119
7.9 XRD diffractogram of the trilayer samples. 120
7.10 XRR of the trilayer sample deposited on glass. 121
7.11 XRR of the trilayer samples deposited on the flexible PET substrate. . . . 122
7.12 Resistance of the trilayer samples and FM thin films. 122
7.13 Seebeck coefficient of the trilayer samples. 123
7.14 Ferromagnetic resonance of the trilayer system. 124
7.15 Preliminary measurement of the x-ray detected ferromagnetic (XFMR) resonance of the K:Py/ST(30)/CoFe trilayer. 126

List of Tables

2.1 Fabricated nanostructures. 24

5.1 Magnetisation dynamics parameters of the FM/TI bilayers at room temperature. 91

7.1 Magnetisation dynamics parameters of the flexible FM/TI/FM trilayers at room temperature. 124

List of Abbreviations and Symbols

- **AFM**, Atomic Force Microscopy
- **CEMUP**, Centro de Materiais da Universidade do Porto
- **CPW**, Coplanar waveguide
- **EDS**, Energy Dispersive X-ray Spectroscopy
- **FMR**, Ferromagnetic Resonance
- **IBS**, Ion Beam Sputtering
- **IEE**, Inverse Edelstein Effect
- **ISHE**, Inverse Spin Hall Effect
- **MR**, Magnetoresistance
- **Py**, Permalloy
- **SCC**, Spin to charge conversion
- **SCI**, Spin to charge interconversion
- **SEM**, Scanning Electron Microscopy
- **SOT**, Spin orbit torque
- **ST**, Sb_2Te_3
- **TC**, Thermocouple
- **TEM**, Transmission Electron Microscopy
- **VNA**, Vector Network Analyser
- **XFMR**, X-ray detected Ferromagnetic Resonance
- **XRD**, X-ray Diffraction
- **XRR**, X-ray Reflectivity
- $g^{\uparrow\downarrow}$, Spin mixing conduction
- h_{rf}, RF field
- H_k, Anisotropy field
- J_S, Spin current
- λ_{SD}, Spin Diffusion length
- L_{SO}, Spin-orbit relaxation length
- L_e, Electron mean free path
- L_ϕ, Phase coherence length
- $\triangle G$, Magnetoconductance
- M_S, Saturation Magnetisation
- ρ, Resistivity
- S, Seebeck Coefficient/Thermopower
- t, Thickness
- V_{Beam}, Sputtering Beam Voltage

Thesis outline

We are currently being ushered in the Era of the Internet of Things (IoT), mainly due to the increase of the available processing power in the last 50 years. This was achievable due to the extreme scaling down of the electronic components/devices, namely transistors, to the order of a few nanometers[1]. This increase was predicted by the Moore's law[2] and it was accompanied by the decreases of the power consumption and the manufacturing costs. However, these rapid improvements are quickly coming to a halt[3], at precisely the same time when our lives are more interconnected and digital than ever and the demand for electronic devices is growing. Moreover, the need of limiting the power consumption of these technologies, which is already more than 4% of the worldwide power consumption[4], must also be attained. As such, innovative solutions and new scientific avenues must be sought after.

Spintronics, which uses the spin degree of freedom of the electrons, has already been employed in several applications, and it could be part of the solution for the end of Moore's law. It has its birthday in the 1980's[5,6], with the control and generation of spin currents at its basis. Nowadays, several routes of controlling these spins are being investigated, with spinorbitronics emerging as one of the promising areas. It exploits the interplay of the spin and orbit phenomena in materials, and several applications in both magnetic data storage[7] and information processing[8], with low power consumption and high reliability, are being investigated.

Main Goal

The main goal of this thesis is to investigate tuned topological insulator (TI) nanostructures based on Sb_2Te_3, which could advance the implementation of TIs and creation of innovative spinorbitronics devices for data storage and logic applications. For this purpose, a scalable fabrication technique was employed, and the electric, thermal and magnetic properties of the nanostructures were widely explored to gain insights into their behaviour and efficiency. Towards this goal, this thesis leads to a significant number of scientific achievements, which constitute a step forward in the topological insulator spinorbitronics research area.

Scientific Achievements

The research conducted over the last four years in the framework of this thesis led to a number of novel scientific contributions, summarised as follows:

Sputtering of Topological Insulators Ion beam sputtering was employed to fabricate the topological insulator nanostructures investigated throughout this thesis. This technique was used to fabricate nanostructures on three different types of amorphous substrates (rigid fused silica glass, and flexible Kapton® and PET), where it was possible to observe the TI state conduction and the Inverse Spin Hall effect (ISHE), with the efficiency of the Spin to Charge conversion (SCC) of sputtered Sb_2Te_3 being calculated. This is a technique already present in both the semiconductor and spintronics industry. As such, optimisation of TI materials using it is a great step forward into the realisation of devices based on TIs for wide usages.

Measurements of electronic properties of nanostructures A custom setup was developed for the measurement of the electrical resistance and Seebeck coefficient. This setup was specially built to allow for the easy, fast and reliable measurement of thin film nanostructures. Using this custom setup, the temperature dependence of the electronic properties of several types of nanostructures was achieved. From these measurements, the type of conduction mechanisms were studied, with several important characterisation parameters having been obtained, such as activation energies and effective Fermi levels. Moreover, magnetotransport measurements were also implemented at cryogenic temperatures, which further allowed for the characterisation of the spintronic transport, with the TSS conduction being observed.

Development of SOT nanostructures Basic elements of SOT devices were investigated. The fabrication of several FM/TI bilayers was achieved, with their transport properties being scrutinised, which led to a shunting model being proposed. Stack FM/TI/FM trilayer nanostructures were also created, with the end goal of verifying how the spin flows through the TI. The magnetisation dynamics of these SOT elements was probed, which allowed the analysis of created and converted spin currents, with the bilayer SCC efficiency being obtained.

Implementation of spin to charge conversion measurements Spin pumping from FMR was implemented for the characterisation of the SCC in the bilayer systems. These measurements were implemented using a cryoFMR system (NanoOsc) and a special ISHE coplanar waveguide for the first time at Imperial College London, with the ISHE being observed. The FMR and ISHE were then examined, with their temperature dependence being attained. From the development of these measurements, the spin Hall

angle of the sputtered TI was calculated, with the SCC efficiency being fully characterised.

Progress towards novel spinorbitronics devices Further understanding of the basic bilayer element of SOT devices was achieved, with insights that can assist the production of future devices. Moreover, flexible TI fabrication was optimised, by inspecting the transport and structure of these thin films, with optimal fabrication parameters being obtained for different applications and temperatures. The development of flexible FM/TI/FM trilayer systems was also performed, by fabricating this stack systems on two different flexible substrates. The investigation of their electronic and magnetisation dynamics properties was initiated, with the effects of the TI layer being unravelled. From these developments, novel flexible spinorbitronics devices can be created.

Thesis Structure

This thesis is organised in eight chapters, namely an overview, the experimental methods used throughout this thesis, a chapter dedicated to the development of the transport properties measurement setup, four chapters of main results and discussions, and a chapter with the conclusions and future perspectives. The Figure present in the next page shows the outline of the chapters towards the end goal of this thesis, where the interconnection between the results chapters is shown, with Chapter 3 being used to achieve the results of each Chapter.

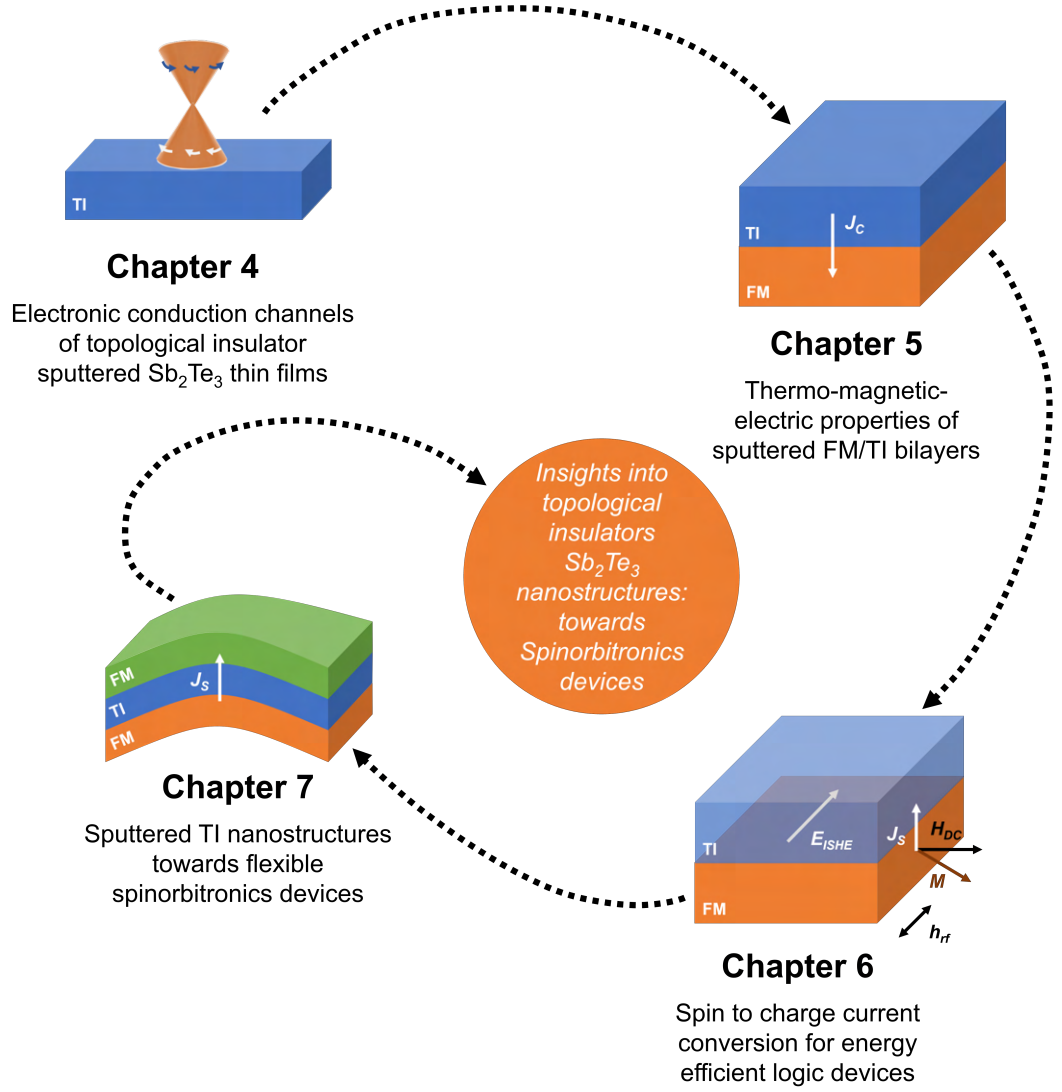
Chapter 1 gives an overview of the current state of topological insulators and of the field of spinorbitronics. It discusses the main basic properties of TIs and the different effects that can occur in these systems, and how these can be exploited for data storage and logic devices, with the current and critical state of the art being discussed.

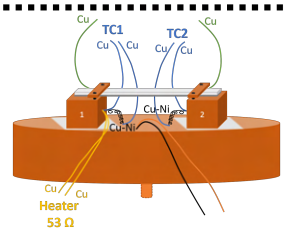
Chapter 2 describes the different experimental methods employed throughout the thesis. The fabrication processes used are explained followed by the description of the different morphological and structural characterisation techniques used. The last two sections of this chapter are devoted to describing the measurements of the transport properties and magnetisation dynamics of the fabricated nanostructures, with a detailed explanation of the implementation of the spin pumping measurements.

Chapter 3 presents the experimental setup developed for the measurement of the resistance and Seebeck coefficient of thin films. It gives an overview of the different constituents of the setup and how the measurements are performed using a closed cycle cryostat. The different measurement methods than can be employed with the setup are also explained. To conclude, the measurements of two types of samples that were used to validate and calibrate the setup are presented.

Chapter 4 is devoted to the structural and transport properties of sputtered topological insulator Sb_2Te_3 thin films of different thicknesses. Their morphological and

structural properties are analysed at great length, followed by the discussion of the resistance, Seebeck coefficient and magnetoconducance of the thin films and how their structure influences the type of conduction.





Chapter 3

Design of a versatile Seebeck and Electrical resistivity measurement setup for thin films

Chapter 5 discusses the fabrication of the simple SOT element based on TIs, namely a bilayer of a TI material with a Ferromagnet (FM) material. The structural characterisation of the sputtered FM/TI bilayers is presented, as well as, their transport properties, giving insights into how the conduction in such type of bilayers occurs. The end of the chapter is dedicated to the magnetisation dynamics of the bilayers at room temperature, obtained by ferromagnetic resonance (FMR) measurements.

Chapter 6 focuses on the spin to charge conversion characterisation in the FM/TI

bilayers. The temperature dependence of the magnetisation dynamics is discussed and the spin current being generated and injected into the TI layer is calculated. Through the spin pumping, where the generated spin current is injected into the Ti layer, the inverse spin hall effect of sputtered Sb_2Te_3 is observed and characterised, leading to the calculation of the spin hall angle and the efficiency of the spin to charge conversion (SCC) for logic devices.

Chapter 7 is dedicated to the development of flexible topological insulators and SOT structures for future flexible spinorbitronics devices. An analysis of the structural and transport properties of the flexible TIs is presented, followed by the characterisation of the transport and magnetisation dynamics properties of FM/TI/FM flexible trilayers.

Chapter 8 outlines the main conclusions of this thesis and concludes with the future perspectives.

List of Contributions

Over the last four years in the framework of this thesis, one research paper was published in peer-reviewed international scientific journals (plus five in preparation and two under collaborations not directly related to this thesis). Fourteen oral presentations were given in national and international conferences and three invited lectures were also given. The work was also recognised by six awards by the American Physical Society (APS), the European Magnetism Association (EMA) and the Portuguese Association of Physics Students (Physis), in collaboration with the Portuguese Physical Society (SPF). A fellowship was also received to attend the fifteenth edition of the Capri Spring School on Transport in Nanostructures in 2019 and a recognition for best input and/or question during the poster sessions was also received during the 2D van der Waals Spin systems workshop organised by SPICE.

Papers in international scientific journals in the framework of this thesis

S. Ferreira-Teixeira, F. Carpinteiro, J. P. Araújo, J. B. Sousa, A. M. Pereira, *Versatile Seebeck and electrical resistivity measurement setup for thin films*, Review of Scientific Instruments (2021), DOI: 10.1063/5.0036817 [9]

S. Ferreira-Teixeira, A. Vanstone, A. L. Pires, W. R. Branford, J. P. Araújo, L. F. Cohen and A. M. Pereira, *Electronic conduction channels engineered in topological insulator sputtered Sb_2Te_3 thin films as a function of thickness*, in preparation

S. Ferreira-Teixeira, A. Vanstone, A. L. Pires, W. R. Branford, J. P. Araújo, L. F. Cohen and A. M. Pereira, *A sputtered topological insulator with large spin to charge current conversion for energy-efficient logic devices*, in preparation

S. Ferreira-Teixeira, A. L. Pires, S. A. Bunyaev, W. R. Branford, J. P. Araújo, G. N. Kakazei, L. F. Cohen and A. M. Pereira, *Insights into the thermo-electric conduction and magnetisation dynamics of sputtered ferromagnetic/topological insulator bilayers*, in preparation

S. Ferreira-Teixeira, A. L. Pires, J. P. Araújo and A. M. Pereira, *Structural and transport properties of sputtered topological insulator thin films towards flexible spintronics devices*, in preparation

S. Ferreira-Teixeira, A. L. Pires, S. A. Bunyaev, G. N. Kakazei, J. P. Araújo and A. M. Pereira, *Mediation of the magnetisation dynamics through a topological insulator on flexible FM/TI/FM sputtered nanostructures*, in preparation

Other papers in international scientific journals

A. L. Pires, I. F. Cruz, J. Silva, G. N. P. Oliveira, **S. Ferreira-Teixeira**, A. M. L. Lopes, J. P. Araújo, J. Fonseca, C. Pereira, and A. M. Pereira, *Printed Flexible μ-Thermoelectric Device Based on Hybrid Bi_2Te_3/PVA composites*, ACS Applied Materials & Interfaces (2019), DOI: 10.1021/acsami.8b18081[10]

S. Ferreira-Teixeira and A. M. Pereira, *Geometrical optimization of a thermoelectric device: numerical simulations*, Energy Conversion and Management (2018), DOI: 10.1016/j.enconman.2018.05.030[11]

Invited lectures in the framework of this thesis

S. Ferreira-Teixeira, A. L. Pires, J. P. Araújo and A. M. Pereira *Spin to charge conversion efficiency of sputtered topological insulators*, Quantum Agora Seminar, Online (Porto, Portugal), 17 February 2022

S. Ferreira-Teixeira, *Spinorbitronics based on Topological Insulators*, Mini-course, Quantum Matter - Materials & Concepts Summer School 2021 (QM-SS 2021), Online and Bragança, Portugal, 10, 15 September 2021

S. Ferreira-Teixeira, A. L. Pires, J. P. Araújo and A. M. Pereira, *My Research*, My Research Talks, PhysikUP, Physics Society of the University of Porto, Online (Porto, Portugal), 29 October 2020

Contributed oral presentations at international and national conferences in the framework of this thesis

1. **S. Ferreira-Teixeira**, A. L. Pires, J. P. Araújo, A. M. Pereira *Magnetoelectric spin-orbit MESO logic devices based on sputtered topological insulators*, MAP-FIs Research Conference, 9 July 2021, Online (Porto, Portugal)

2. **S. Ferreira-Teixeira**, A. L. Pires, J. P. Araújo, A. M. Pereira *Sputtered topological insulators for magnetoelectric spin–orbit MESO logic devices*, 4th Doctoral Congress in Engineering DCE: Engineering Physics Doctoral Symposium, 28 June 2021, Online (Porto, Portugal)

3. **S. Ferreira-Teixeira**, A. Vanstone, A. L. Pires, W. R. Branford, J. P. Araújo, L. F. Cohen, A. M. Pereira *Spin to charge conversion in topological insulator Sb_2Te_3 sputtered thin films towards magnetisation switching devices* [1], JEMS Joint European Magnetic Symposia, 10 December 2020, Online (Lisbon, Portugal)

4. **S. Ferreira-Teixeira**, A. L. Pires, J. P. Araújo, A. M. Pereira *Magneto-thermal-electric transport of sputtered Sb_2Te_3 topological insulator thin films for spintronics applications*, FÍSICA 2020 – 22nd National Physics Conference, 3 September 2020, Online (Lisbon, Portugal)

5. **S. Ferreira-Teixeira**, A. L. Pires, J. P. Araújo, A. M. Pereira, *Insights into the electric transport of sputtered Sb_2Te_3 topological insulator thin films towards spintronics applications*, CMD2020GEFES, 1 September 2020, Recorded, Online (Madrid, Spain)

6. **S. Ferreira-Teixeira**, A. Vanstone, A. L. Pires, W. R. Branford, J. P. Araújo, L. F. Cohen, A. M. Pereira, *Magnetization control of ferromagnetic materials based on topological insulator Sb_2Te_3 sputtered thin films* [2], APS March Meeting 2020, Cancelled due to COVID-19 pandemic, APS - American Physical Society (Denver, United States of America)

7. **S. Ferreira-Teixeira** *The future of spintronics: what role will topological insulators play?*, National Conference of Physics Students ENEF 2020, 20 February 2020, University of Coimbra (Coimbra, Portugal)

8. **S. Ferreira-Teixeira**, A. L. Pires, W. R. Branford, J. P. Araújo, L.F. Cohen, A. M. Pereira, *Spin to charge current conversion in nanostructures based on topological insulators Sb_2Te_3 sputtered thin films*, IFIMUP Talks, 20 January 2020, University of Porto (Porto, Portugal)

9. **S. Ferreira-Teixeira**, A. L. Pires, W. R. Branford, J. P. Araújo, L. F. Cohen, A. M. Pereira, *Observation of Efros and Shklovskii Regime on Sb_2Te_3 nanocrystallites embedded into an amorphous matrix*, CMQM (Condensed Matter and Quantum Materials) Conference 2019, 4 July 2019, University of St. Andrews (St. Andrews, Scotland, United Kingdom)

10. **S. Ferreira-Teixeira**, A. L. Pires, W. R. Branford, J. P. Araújo, L. F. Cohen, A. M. Pereira, *Variable Range Hopping dominated conduction of a Sb_2Te_3 ion beam*

[1] Abstract won the Student Travel Grant.
[2] Abstract won three different awards.

sputtered topological insulator thin film [3], 15th Capri Spring School on Transport in Nanostructures 2019, 10 May 2019 (Anacapri, Italy)

11. **S. Ferreira-Teixeira**, A. L. Pires, W. R. Branford, J. P. Araújo, L. F. Cohen, A. M. Pereira, *Variable Range Hoping conduction dominated Sb_2Te_3 topological Insulator thin films* [4], National Conference of Physics Students ENEF 2019, 28 February 2019, Instituto Superior Técnico (Lisbon, Portugal)

12. **S. Ferreira-Teixeira**, A. L. Pires, W. R. Branford, J. P. Araújo, L.F. Cohen, A. M. Pereira, *Topological Insulator fingerprints in Sb-Te thin films*, IFIMUP Talks, 25 September 2018, University of Porto (Porto, Portugal)

13. **S. Ferreira-Teixeira**, A. L. Pires, J. P. Araújo, A. M. Pereira, *Bi-Te and Sb-Te Topological Insulator Materials: from first principle calculations towards nanostructures fabrication*, International Conference of Physics Students ICPS 2018, 12 August 2018, University of Helsinki (Helsinki, Finland)

14. **S. Ferreira-Teixeira**, A. L. Pires, J. P. Araújo, A. M. Pereira, *From ab-initio calculations towards Topological Insulators nanostructures by Ion Beam Sputtering Deposition*, International Conference on Nanoscience + Technology ICN+T 2018, 25 July 2018, Brno University of Technology, Institute of Physics of the Czech Academy of Sciences (Brno, Czech Republic)

Poster presentations at international and national conferences in the framework of this thesis

1. **S. Ferreira-Teixeira**, A. L. Pires, J. P. Araújo, A. M. Pereira, *Sputtered topological insulators for Spinorbitronics logic devices*, LaPMET Workshop, 23 - 24 September, 2021, Online

2. **S. Ferreira-Teixeira**, A. Vanstone, A. L. Pires, W. R. Branford, J. P. Araújo, L. F. Cohen, A. M. Pereira, *Spin to charge conversion on topological insulator Sb_2Te_3 sputtered thin films* [5], National Conference of Physics Students ENEF 2020, 20 February 2020, University of Coimbra (Coimbra, Portugal)

3. S. Ferreira-Teixeira, **A. L. Pires**, W. R. Branford, J. P. Araújo, L.F. Cohen, A. M. Pereira*The Topological Surface State on a Variable Range Hopping conduction dominated Sb_2Te_3 sputtered thin film*, 3rd Doctoral Congress in Engineering DCE: Engineering Physics Doctoral Symposium, 28 June 2019, (Porto, Portugal)

[3] Fellowship awarded to participate.
[4] Awarded Best Work in Condensed Matter Physics.
[5] Awarded Best Poster Presentation.

Awards received in the framework of this thesis

International awards

Student Grant, JEMS 2020, European Magnetism Association (EMA), 2020

Best Question/Input on a Poster, 2D van der Waals Spin Systems Workshop, SPICE, Johannes Gutenberg Universität Mainz, Germany, 2020

Distinguished Student, Forum on International Physics (FIP), American Physical Society (APS), 2020

Student Travel Award, Topical Group on Magnetism and its Applications (GMAG), American Physical Society (APS), 2020

Ovshinsky Honorable Mention Travel Award, Division of Material Physics (DMP), American Physical Society (APS), 2020

Fellowship, 15th Capri Spring School on Transport in Nanostructures, Capri, Italy, 2019

National awards

Best Poster Presentation, National Conference of Physics Students ENEF, University of Coimbra, Coimbra, Portugal, Portuguese Association of Physics Students (Physis), under collaboration of Portuguese Physical Society (SPF), 2020

Best Presentation in Condensed Matter Physics, National Conference of Physics Students ENEF, Instituto Superior Técnico, Lisbon, Portugal, Portuguese Association of Physics Students (Physis), under collaboration of Portuguese Physical Society (SPF), 2019

CHAPTER 1

Introduction

1.1 Spintronics

Conventional electronic devices are based on non-magnetic semiconductors, where the control of the electric charges is used to process information. The development of these devices allowed for several advancements of technologies, which led to the devices that we use nowadays. These advancements were extremely fast, with the growth rate having been expressed by Moore in 1975[2], when he predicted that the number of transistors per silicon chip would roughly double every other year, which led to an increase in the calculations per second and a decrease in the price of devices as shown in Figure 1.1.(a). This occurred due to the miniaturisation of the different elements of an electronic chip, possible due to the advent of nanotechnology. However, we are currently living in the Era of the Internet of Things (IoT) (Figure 1.1.(b)), in which our demands for faster and reliable devices, with more computational power, are increasing, since more elements of our lives now depend on these electronic devices. As such, the limit of the simple conventional electronic devices is being reached, due to several issues such as overheating, power dissipation and miniaturisation limits of the electronic materials[3]. Therefore, innovative solutions must be found.

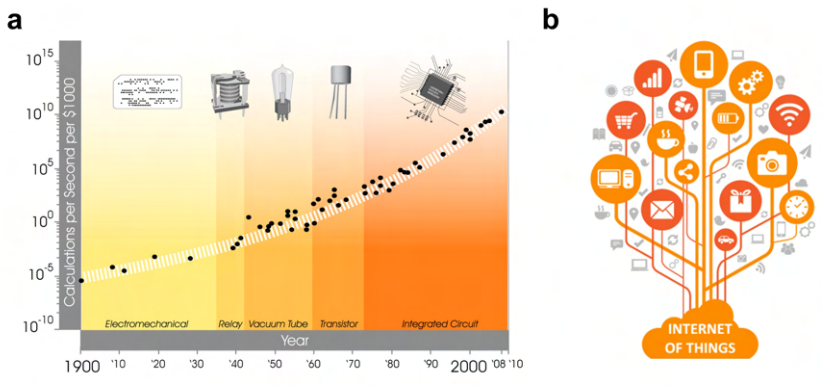


Figure 1.1 – Moore's Law and the Era of the Internet of Things (IoT). (a) The Moore's law predicted that the number of transistor per chip would double every other year, which led to the increase in the possible calculations per second and decrease in the price of devices. (b) The era of the Internet of Things (IoT), in which every aspect of our lives is interconnected through and uses electronic devices. Adapted from[12].

New materials and concepts are thus the focus of scientific efforts to find new electronic standards. One such concept is the use of the other degree of freedom of the electrons: the spin. By considering the spin in the creation of devices, several advantages can be attained, such as reduction in the power consumption, improved data processing speed, and higher density of integration when compared with the conventional electronic devices. Thus, the field of Spintronics (spin electronics) has emerged as one possible solution for the needed development of novel devices[13].

Spintronics had its start with the discovery of the giant magnetoresistance (GMR) in 1988, for which Albert Fert and Peter Grünberg were awarded the Nobel Prize in Physics in 2007[5,6]. Since this first breakthrough, several phenomena and structures have been the object of studies, such as the interplay of charge and spin transport[14], spin dynamics in magnetic and non magnetic systems[15,16], and nanostructured magnetic systems[17]. Moreover, it is remarkable to note that spintronics also delivered large-scale industrial and commercial applications extremely fast since its inception, due to the GMR effect being employed in the read heads in magnetic data storage a decade after its first observation[18]. The wide usage of spintronics and its success boosted the field forward and, nowadays, spintronics is and can be employed in a wide range of applications, from data storage and information sensing, to logic operations and energy harvesting[19–21].

With this fast expansion, the field of spintronics is rapidly giving rise to new subfields, where the electron spin is coupled to other properties of a certain material[22]. Fields such as ultrafast spin photonics, which couple spin and photons, or spincaloritronics, coupling the spin and heat are prime examples. In this thesis, the focus is the emergent field of spinorbitronics, which utilises the spin-orbit coupling (SOC).

1.2 Spinorbitronics

Spinorbitronics exploits the interplay between the charge and spin currents that the spin-orbit coupling (SOC) of non-magnetic systems enables. It can be considered as spintronics being realised without magnetic fields, since a spin current can be generated in non-magnetic systems. This idea was first proposed by Dyakonov and Perel in 1971[23,24], being later experimentally demonstrated[25,26]. Through the SOC, spin to charge interconversion (SCI) can be achieved through two effects in a wide range of materials and employed in different devices.

1.2.1 Spin to charge interconversion

The two phenomena that are the basis of the SCI are the Spin Hall Effect (SHE) and Edelstein Effect (EE), and the respective inverse effects, Inverse Spin Hall Effect (ISHE) and Inverse Edelstein Effect (IEE). The SHE is present at the bulk of materials, whereas the EE occurs at surfaces and interfaces. In both cases, a spin current is created, in

spite of in the EE a flow of a charge current creating a transverse spin density through the EE, which is then diffused to an adjacent material as a spin current.

1.2.1.1 Spin Hall Effect

The Spin Hall effect (SHE) is a spin orbit related effect that allows the charge to spin (direct effect) or spin to charge (inverse effect) current conversion to occur in the bulk of a non-ferromagnetic material. It was first described by Mikhail Dyakonov and Vladimir Perel in 1971[23,27]. Soon later, the inverse effect was observed for the first time[28,29]. The name was coined by Hirsch in 1999[30], by analogy with the ordinary Hall effect.

The spin-dependent deflection of carriers in non-magnetic materials is the cause of SHE, with different spins deflecting to different directions, as shown in Figure 1.2. However, as opposed to the ordinary Hall effect, and due to it occurring in non-magnetic materials, this deflection of spin up and spin down does not create a charge accumulation, and thus no Hall voltage is observed. However, spin accumulation is created at the edges, which can give rise to a spin current[31].

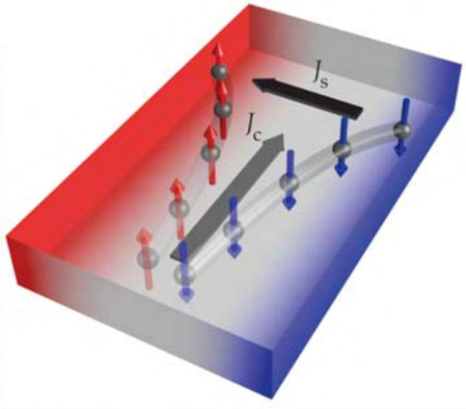


Figure 1.2 – The Spin Hall effect. The spin-dependent deflections generate a spin current $\mathbf{J_S}$ transverse to the flowing charge current $\mathbf{J_C}$, due to the spin-orbit coupling. Adapted from[32].

The spin Hall effect can be characterised by the spin hall angle θ_{SH}, which is a material dependent property. As such, the SCI by (I)SHE can be characterised by this propriety. The spin hall angle θ_{SH} links the flowing and generated charge and spin currents as described in equation 1.1, where σ is the spin polarization unit vector, and $\mathbf{J_C}$ and $\mathbf{J_S}$ are the charge and spin currents, respectively.

$$\mathbf{J_C} = \theta_{SH}\, \mathbf{J_S} \times \sigma \tag{1.1}$$

Two contributions to the SHE exist, namely an intrinsic and extrinsic one. The intrinsic contribution is related to the anomalous velocity of the carriers. On the other hand, the extrinsic contribution is due to skew or side-jump scattering on impurities in the presence of spin orbit coupling.

1.2.1.2 Edelstein Effect

The Edelstein effect is also a spin orbit related effect, where a 2D charge current is converted to spin accumulation, with the inverse effect being the Inverse Edelstein effect (IEE). It is an intrinsic mechanism, which was predicted in 1990 by V.M. Edelstein[33], being demonstrated experimentally later in 2013[34].

EE occurs due to the presence of spin-polarised surface or interface states[35]. These states could be Rashba states that are created by a structural inversion symmetry breaking, which breaks the spin degeneracy of the energy bands, locking the spin polarisation to the momentum in each branch of energy dispersion[36]. Thus, a charge current flowing in these states, generates a spin accumulation, with the effect being called the Rashba-Edelstein effect (REE). Another instance of the EE can be attained by using topological surface states, which are spin-splitted surface states[36]. The energy dispersion in these topological states is linear and has spin-texture, and thus, as for the Rashba states, there is spin accumulation when a charge current flows through these materials.

The EE has been observed up until now only in 2D systems, and as such, the generated spin (or charge) accumulation is bi-dimensional. This is in opposition to the SHE, where the conversion occurs in the bulk of the material. Due to this 2D nature of the EE/IEE effects, the EE/IEE length λ_{EE} is the parameter that describes the SCI based on this effect, being given by equation 1.2, where j_S is the magnitude of 2D spin current and J_C the magnitude of the 3D charge current[35,36].

$$\lambda_{EE} = \frac{j_S}{J_C} \tag{1.2}$$

To draw a comparison between the SHE and EE spin to charge interconversions, an effective length can be obtained for the SHE, which is given by the spin Hall angle θ_{SH} times the spin diffusion length λ_{SD}. From these parameters, materials with one or both effects can be compared and optimised for the wide applications the SCI effects can have.

1.2.2 Data storage and logic devices

The discussed SCI effects are able to create spin currents. These can exert spin orbit torques (SOT) on the magnetisation of neighbouring magnetic materials and also convert a spin current flowing through them into an electric charge signal. Thus, there is a growing interest in utilising and optimising these effects for efficient data storage and logic devices, such as SOT magnetic random access memories (SOT-MRAMs)[7] and spin-logic devices, such as the magnetoelectric Spin-orbit (MESO) device recently proposed by Intel[8].

MRAM technology is already present at the industrial scale, through the spin transfer torque (STT) MRAMs. In these memories, the state is read by measuring the magneti-

sation through tunnelling magnetoresistance (TMR) and the writing is achieved by STT. Thus, both the read and write are achieved using the same conduction path, as shown in Figure 1.3. It offers several advantages in terms of speed and density when compared to the typical RAM memories. However, because the read and write processes have the same path, the magnetisation switching, which is the write process, could also be done during the reading process. The speed is also injured because of the two terminal configuration, due to the shared conduction path[37,38]. A solution to these problems are the SOT MRAMS. These are based on the generation of SOTs through SOC materials. Due to the geometry of the SCI effects, they are three terminal MRAMs, where the writing and reading paths are separated, as it can be seen in both the schematic and Transmission Electron Microscopy (TEM) cross section image of Figure 1.3. This increases the writing speed, while reducing the current density and power needed[39,40]. The writing path in SOT-MRAMs is therefore composed of a SOT element, with the SOC material below the free magnetic layer as shown in Figure 1.3, with the switching of the magnetisation of this free layer being achieved by the spin accumulation created by SHE or EE on the SOC material. Advancements to this SOT-MRAMs are still needed for industrial usage, but due to their reliability and high performances, they can be used where these aspects are key, such as cache memory[41]. The development of the SOC materials is at the forefront of advancing these memories, especially with the goal of achieving field free switching[42].

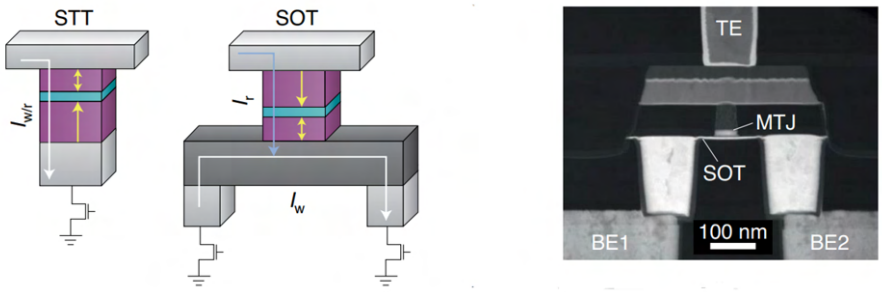


Figure 1.3 – MRAM technology: schematic of two-terminal STT MRAM, for fast and dense implementations, but with write latencies, and of a three-terminal SOT MRAM, which allows for faster operations with high endurance. The Transmission electron microscopy (TEM) cross section image of a field free SOT MRAM cell, where the write current is injected from BE1 to BE2 and read from TE to BE2. Adapted from[20].

Logic devices can also be envisaged based on the SCI effects. In Figure 1.4, the recently proposed MESO logic device is depicted. Each part is composed of a magnetoelectric (ME) and a SOC elements. The ME element is used to switch the ferromagnetic layer, through the coupling of a FM material with, typically, a ferroelectric or piezoelectric material. The SOT element is then used to convert the magnetisation of the FM material into a electric charge signal, by the flow of a current through it, as shown in Figure 1.4. The SOT element is constituted by the FM layer and the SOC material, and a spin injection layer (SIL) can also be added to assist the spin flow from the FM to

the SOC material. This set of elements is then inserted in a cascade where the signal of the SOT element of the previous set is used for the ME switching of the following set. Optimised SCI efficiency is crucial for the conversion of the magnetisation to an electric signal. However, the output voltage also needs to be adequately high for the switching of the following ME set, and thus high resistivities of the SOC material are needed. Thus, the optimal SOC material for the MESO device has both a high SCI conversion and electrical resistivity. The proposed MESO device offers the possibility of a progressive miniaturisation, reduced energy for switching, and ultra low standby power, specially when compared to CMOS logic. Preliminary results in the advancement of the ME and SOC materials are now being obtained and new materials are being developed and applied.

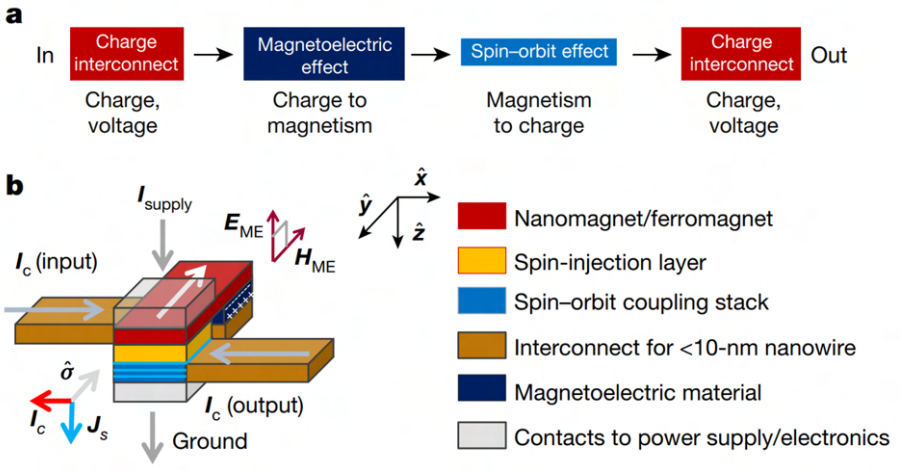


Figure 1.4 – Magnetoelectric spin-orbit logic (MESO) device. (a) transduction of state variable for the cascadable charge-input and charge-output logic device. The magnetoelectric effect transduces the input information to magnetism, and the spin-orbit effect transduces the magnetic state back to a charge. (b) the constituents of a MESO device, namely the magnetoelectric capacitor and SOT element. Besides the ferromagnetic and SOC materials, a spin injection layer can be inserted in the SOT element. Adapted from[8].

1.2.3 Materials for spin-orbit torque applications

After the observation and demonstration of the SCI effects, efforts were focused on increasing the SCI efficiencies by studying and tuning a wide range of materials. Since the SHE and EE effects occur due to spin orbit effects, materials with high spin orbit coupling (SOC) have been the focus.

Heavy metals are the prototypical materials, having been extensively studied due to their large spin hall angles[43–45]. They have been used to achieve the switching of ferromagnets, as Figure 1.5 shows. Here, the switching of a Co FM layer was observed by applying a pulsed current to the adjacent Pt layer[43]. From this simple structure, a reprogrammable magnetic switch was created, which could be integrated into memory and logic architectures, proving the potential for in-plane current switching using heavy

metals.

Nonetheless, through the intrinsic ISHE effects, the Spin Hall angle of the heavy metals is proportional to their resistivity, which can hinder certain application such as the SOT-MRAMs, where low resistivity values are important to achieve switching with less power. Moreover, the spin diffusion length can be smaller than other SOC materials, which reduces the effective efficiency of the SCI effects.

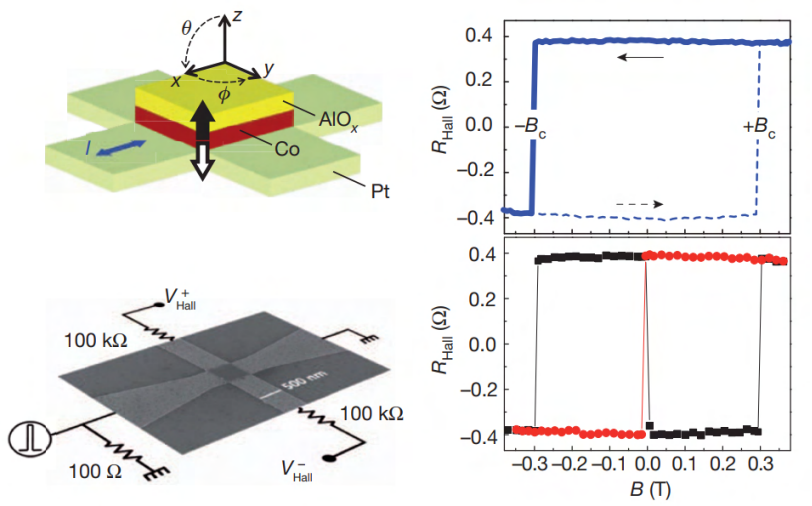


Figure 1.5 – Magnetisation switching via SHE of platinum. An Hall cross geometry was used, with Pt as the SOC material and Co as the ferromagnetic material. The scanning electron micrograph shows the hall bar structure of the sample, with the electric circuitry. The magnetisation reversal of the Co layer measured by the Hall resistance and sweeping the magnetic field, when no current is applied in the Pt layer (top) and with a pulse current, either positive or negative, applied to the Pt layer (bottom). The switching of the magnetisation is visible. Adapted from [43].

Recently, other materials and structures have also been explored. Van der waals heterostructures based on 2D materials have been used to obtain an enhanced room-temperature SCI[46]. This SCI occurred in graphene driven by the proximity of WS_2. The SCI efficiencies could also be tailored by electrostatic gating, both in magnitude and sign, peaking near the charge neutrality point of graphene, with efficiencies being comparable with the large efficiencies observed in Heavy metals. This tailoring by the electric-field thus offered a building block for spin generation free from magnetic materials and for ultra compact MRAM technologies.

Another novel structure for magnetisation switching was obtained in all-oxide heterostructures based on ferromagnetic transition metal oxide and an oxide with strong SOC, namely $SrIrO_3/SrRuO_3$[47]. Depending on the magnetocrystalline anisotropy of $SrRuO_3$, which was controlled by the orientation of the STO substrates, magnetic-field-free switching was achieved, which can further aid the advancements of SOT-MRAMs.

1.3 Topological Insulators

Topological Insulators are a new class of quantum materials. They exhibit a metallic surface state that is protected by time-reversal symmetry and has spin momentum-locking, with these properties occurring in some materials due to their high SOC. As such, the combination of the topological surface state (TSS) with their high SOC, gives TIs a high potential for spinorbitronics applications.

The first 3D topological insulator to be discovered was the bismuth antimony alloy Bi_xSb_{1-x}. It was discovered in 2008[48] by an Angle resolved Photoemission Spectroscopy (ARPES) experiment, with the exotic band structure being obtained. After the discovery of the Bi_xSb_{1-x} alloy, a set of materials was uncovered to also host the TSS: the Bi_2Se_3 semiconductor family. These materials are known for applications as thermoelectric materials[49]. Through ARPES measurements combined with first principle calculations, their topological insulator properties were unveiled[50–52]. They are constituted by quintuple layers and are characterised by having one almost ideal Dirac cone as the TSS, as it can be seen in Figure 1.6.(a) and (b). They only have one Dirac point, and have a large band gap, which allows the TSS properties to be harvested at room temperature.

Due to the exotic properties the TIs present, they can be used in a wide range of applications, with interest in them for spinorbitronics applications growing. TIs have shown θ_{SH} values 10 to 1000 times higher than the HMs values[53,54], which fuelled this interest.

The focus of this thesis is the Sb_2Te_3 TI, which belongs to the Bi_2Se_3 semiconductor family. Sb_2Te_3 presents a distorted TSS Dirac cone and has a smaller band gap, thus being the less explored material of this family. Moreover, its band structure properties lead to the presence of bulk conduction states, as it can be seen in Figure 1.6.(b). As such, it is not yet clear if it is a good material for SOT applications, with very few reports of the SCI on these material being presented[55,56].

1.3.1 Electronic properties of 3D Topological insulators

The electronic and spintronic properties of topological insulators and the TSS, in particular, can be analysed via the measurement of their transport properties, such as the Seebeck coefficient[58–60] and magnetoresistance[57,61].

At low magnetic fields, the weak antilocalisation (WAL) effect can appear as a consequence of the topological surface state characteristics[62–64]. Due to the strong spin orbit effect and to the spin polarisation of the surface state, the WAL effect is visible at low magnetic fields on the magnetoresistance, as shown in Figure 1.6.(c) for a roughly 30 nm thin film of Bi_2Te_3. From the Hikami-Larkin-Nagaoka (HLN) model[65,66], the number of coherent conduction channels and the phase coherence length L_ϕ can be calculated by fitting the data, with fits to this model shown as solids lines in Figure 1.6.(c). A quadratic

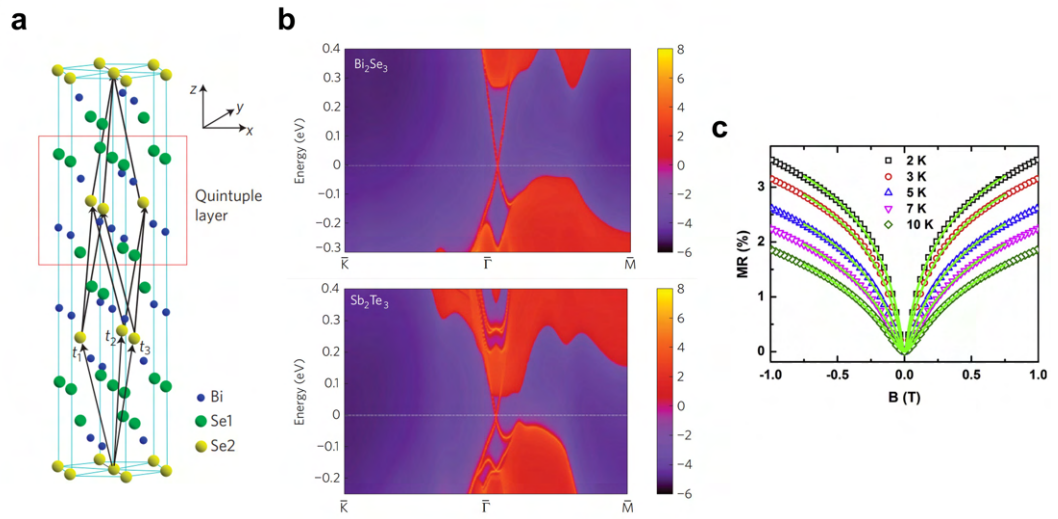


Figure 1.6 – The electronic properties of the Bi_2Se_3 topological insulators family. (a) Crystal structure of Bi_2Se_3 family with three primitive lattice vectors denoted as $t_{1,2,3}$. A quintuple layer is indicated by the red square. (b) Band structure of Bi_2Se_3 (top) and Sb_2Te_3 (bottom). The red regions correspond to bulk energy bands and blue regions to bulk energy gaps. The surface states are seen around the Γ point as red lines dispersing in the bulk gap. (c) Magnetoresistance of a Bi_2Te_3 30 nm thin film measured at low temperatures. The green lines are the theoretical fita given by the HLN model. Adapted from [52,57].

field dependence of the magnetoconductance has also been observed on certain TIs, from which the spin-orbit relaxation length can be calculated [61].

The detection of the TSS conduction without the presence of magnetic field can be achieved, however, by inspecting the Seebeck coefficient (S) of the material. The polarity of S reflects what are the majority charge carriers, being positive for p-type semiconductors and negative for n-type semiconductors. Moreover, the identification of the carriers as metallics or semiconductors can be obtained through the temperature dependence. Metallic carriers have a linear temperature dependence, whereas semiconducting materials show a nonlinear dependence. As such, considering that the TSS is a metallic state, its contribution to S should appear as linear and negative, whereas the bulk states of the typical 3D TIs are semiconducting in origin. Through this method, the different conduction channels and their contributions have been disentangled in Bi_2Se_3, BSTS ($(Bi_{1-x}Sb_x)_2(Te_{1-y}Se_y)_3$, and BST ($(Bi_{1-x}Sb_x)_2Te_3$) [58–60].

1.3.2 Spin to charge interconversion in topological insulators

Topological insulators have been the focus of recent studies of spin to charge interconversion for efficient spinorbitronics devices. Due to their bulk with high SOC, and the existence of the TSS, both SHE and EE can be present in TIs.

Bi_2Se_3 is one of the widely studied TIs, which has already been employed to switch ferromagnets through SHE [67,68]. Generated charge currents via ISHE have also been measured [61,69–71], as it can be seen in Figure 1.7. Related materials such as BST

$((Bi_{1-x}Sb_x)_2Te_3)$ yielded outstanding performances in the charge to spin conversion [54,72].

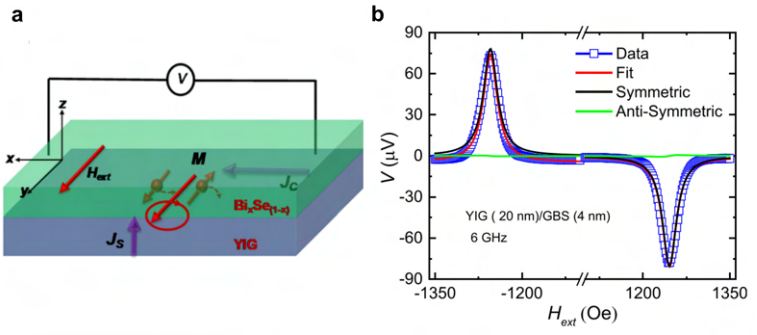


Figure 1.7 – Spin to charge conversion by sputtered Bi_2Se_3 thin film. (a) schematic of the spin to charge conversion (SCC) measured through spin pumping at the ferromagnetic resonance and (b) the measured spin pumping voltage. Adapted from [70].

The disentanglement of the spin Hall effects from the Edelstein effects is not straightforward in TIs, with both effects contributing to the SCI. A possibility to verify what effect is occurring is through angular dependence measurements of the spin to charge conversion, through, for example, spin pumping. Moreover, measurements of TIs with different thicknesses is one of the available methods, since it allows to observe the surface effects versus the bulk contributions. However, the fabrication of TI thin films over a wide range of thicknesses can be an issue, since the structure of the thin films can be altered. Throughout thesis, it will be considered that the SHE is the only effect present, due to the high thicknesses of the nanostructures investigated.

In this thesis, TI nanostructures based on sputtered thin films of Sb_2Te_3 are explored with the objective of investigating the different contributions to its electronic and spintronic conduction, allowing for their exploitation. Magnetoconductance measurements were combined with the temperature dependence of the Seebeck coefficient and resistance to understand the several conduction channels present in these TI thin films. By combining these sputtered films with magnetic materials, insights into the behaviour and efficiency of basic elements of spinorbitronics devices were attained. The magnetisation dynamics and SCI of ferromagnetic materials (FM) and TI bilayers (FM/TI) and spin-valve like stack trilayers (FM/TI/FM) were explored through ferromagnetic resonance and spin pumping measurements. These results can aid the development and usage of TIs in novel data storage and logic devices.

CHAPTER 2

Methods

In this chapter, the employed techniques in the fabrication and study of the topological insulator nanostructures will be described. In the first part, the thin film deposition techniques will be explored. This section will be followed by the description of the structural and morphological instrumental methods used on the produced samples. The last sections are devoted to the electrical and magnetic characterisations techniques for inspecting the nanostructures.

2.1 Nanostructures fabrication

Physical vapour deposition (PVD) is an atomistic deposition process based on the vaporisation of a solid or liquid source. The vaporised atoms or molecules are transported through vacuum or low pressure gaseous (plasma) environment to the substrate, where they are condensed[73]. PVD techniques are used to deposit thin films with thicknesses in the range of a few to thousands of nanometres and allow for uniform deposition of large areas with the intended stoichiometry. Two PVD techniques were used throughout this work: Ion Beam Sputtering and DC Magnetron Sputtering. In these techniques, the vaporisation of the target material is achieved by the impact of high energy inert gas particles.

2.1.1 Ion Beam Sputtering

The nanostructures studied in this thesis were produced by Ion Beam Sputtering (IBS). The system used was the commercial system from Commonwealth Scientific Corporation, which exists in the clean room unit (MNTEC) of Centro de Materiais da Universidade do Porto (CEMUP).

The IBS system of Porto is schematically represented in Figure 2.1. The basic IBS system is constituted by a vacuum chamber, an ion source, a target and a substrate holder. The ions are created in the ion source and accelerated towards the target. Here, the high energy ions remove material, which is then directed to the substrate on the substrate holder, where it is deposited[74]. Besides the basic components, the system at CEMUP also has a shutter and a second ion source. The two ion sources of the system

are 3 cm diameter Kauffman DC ion sources. The main one is used for deposition, where a tungsten filament is heated, thus generating ions due to the collision of inert gas atoms (Argon) with electrons extracted from the filament. This ion-source is placed 10 cm away from the target, which is at a 45º angle relative to the direction of the ion beam. The second ion source can be used for assisting the deposition or for ion-milling, and it was not used throughout this work. The system allows four targets to be inside the deposition chamber at a certain time, through a system that rotates and exposes the intended target for a certain deposition. As such, depositions of up to four different materials can occur without breaking vacuum in between depositions, which was the method used for fabrication of some of the nanostructures studied in this work. The shutter is used to prevent deposition of material when the deposition conditions are not yet fully set or during the pre-cleaning process. It is located in front of the substrate holder and can be opened on demand, thus preventing cross contamination and guaranteeing a greater control of the deposition process. All these components are cooled by an internal water circuit, with a temperature between 10 and 14 ºC, except for the ion sources, which are cooled by air.

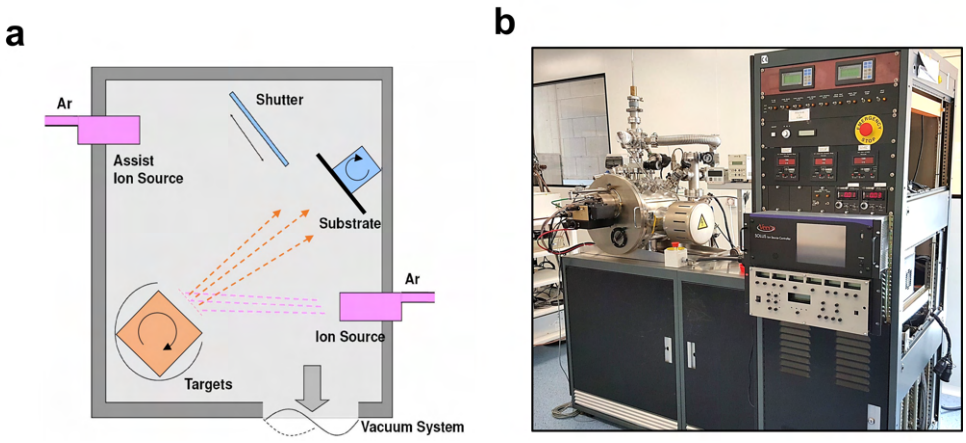


Figure 2.1 – Ion Beam Sputtering. (a) Schematic representation of the deposition chamber (adapted from[75]) and (b) the IBS system at MNTEC-CEMUP.

The depositions are controlled by several parameters, which are either fixed or set and monitored during deposition. The substrate holder rotates at a certain velocity to improve the uniformity of the films, and throughout this work it was kept at 70 rpm. The pressure within the deposition chamber also greatly influences the deposition. A base pressure of $P_B \approx 10^{-7}$ Torr is used for deposition. It is achieved through a rotative pump that reaches $\sim 10^{-3}$ Torr, followed by a turbo-molecular pump, reaching $\sim 10^{-5}$ Torr. A cryogenic pump is then used to reach P_B. For the deposition to occur, the chamber, after reaching P_B, is filled with Argon until a certain pressure. This is the working pressure P_W, which is kept constant during deposition and had the same value for all the fabrication processes, namely 1.4×10^{-4} Torr. This pressure ensures that the incident ions and sputtered atoms preserve their energy and directionality due to their high mean free

paths inside the chamber.

The creation and acceleration of the ions is also controlled. A discharge current is applied to the tungsten filament, controlling the electron ionisation procedure. It is maintained at the value of 2.0 A and monitored during the deposition. The Beam Voltage V_{Beam} controls the energy of the ions when impacting on the target. Thus, it controls the energy of the removed material, which is going to be deposited on the substrates. The V_{Beam} can have values between 300 and 1200 V, with an optimisation procedure having to be carried out to determine which value should be used for a certain material and application. With these parameters, IBS can be used to fabricated metallic or semiconducting thin films. However, oxides and insulators can also be deposited with this IBS system by using a neutraliser current, which is also controlled during deposition.

Three different materials were deposited as single thin films, bilayers and trilayers throughout this thesis: antimony telluride (Sb_2Te_3), permalloy (Py) of nickel and iron ($Ni_{20}Fe_{80}$), and an alloy of cobalt and iron ($Co_{50}Fe_{50}$). The Sb_2Te_3 target was a commercial target acquired at Semiconductor Wafer, Inc. All the targets had a diammeter of $3''$ and a thickness of 3 mm. Capping of certain thin films was achieved with manganese oxide (MgO), tantalum (Ta) and aluminium (Al). For the deposition of MgO, the neutraliser current was employed, as previously explained. With these materials, several thin films and nanostructures were fabricated, which can be found on Table 2.1. The depositions occurred at room temperature in different types of substrates: amorphous rigid glass (fused silica), and flexible polyimide (Kapton®) and Polyethylene terephthalate (PET) substrates. Prior to the deposition, the substrates were rigorously cleaned by three five minutes ultrasonic baths of acetone, isopropanol and deionised water, in this order, followed by drying under nitrogen airflow[76]. Prior to deposition, a cleaning process of the target surface was achieved by setting the deposition conditions and sputtering the target with the shutter closed to prevent deposition. This process ensures that any oxidation on the target surface is removed prior to deposition. In Table 2.1, the different beam voltages and thicknesses of the fabricated nanostructures are also presented.

2.1.2 DC Magnetron Sputtering

DC magnetron sputtering is another type of PVD technique, based on the sputter of material from a target. In DC magnetron sputtering, the target material serves as the cathode and the substrates are placed on the anode, as it can be seen in Figure 2.2. Between these two elements, a voltage of the order of hundreds of volts is applied. A magnetic field, as illustrated in Figure 2.2.(b), is also applied near the cathode region where the target material is placed, trapping the electrons being emitted. These electrons ionize the Ar atoms present in the chamber, forming a plasma near the cathode region, i.e. the target. Due to the voltage being applied between the target and substrate, Ar^+ ions are accelerated, colliding with the target. Through the momentum

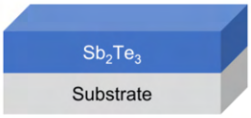
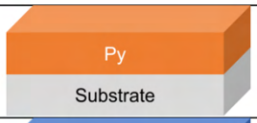
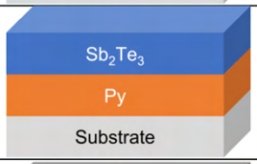
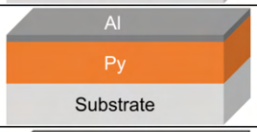
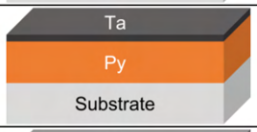
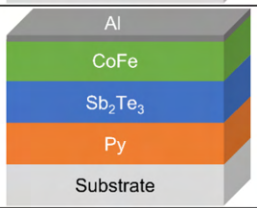
Materials	Nanostructure	Substrate	Beam Voltage V_{Beam} (V)	Thickness (nm)	Name
Sb_2Te_3		Glass	700	35	ST(35)
				51	ST(51)
				66	ST(66)
				100	ST(100)
				200	ST(200)
				300	ST(300)
		Kapton ®	500	188	flexST(500)
			600	263	flexST(600)
			700	338	flexST(700)
			800	413	flexST(800)
			900	488	flexST(900)
			1000	563	flexST(1000)
Py		Glass	1000	10	Py(10)
				100	Py(100)
Py/Sb_2Te_3		Glass	1000/700	10/100	Py(10)/ST(100)
				50/50	Py(50)/ST(500)
				100/10	Py(100)/ST(10)
				100/100	Py(100)/ST(100)
Py/Al		Glass	1000	10/4	Py(10)/Al
Py/MgO/Ta		Glass	1000	10/2/3	Py(10)/MgO/Ta
Py/Ta		Glass	1000	10/3	Py(10)/Ta
$Py/Sb_2Te_3/CoFe/Al$		Glass Kapton ® PET	1000/700/1000	10/30/10/4	Py/ST(30)/CoFe
			1000/700/1000	10/60/10/4	Py/ST(60)/CoFe

Table 2.1 – Fabricated nanostructures.

transfer, atoms from the target are evaporated and deposited on the substrate placed in the anode region. The depositions occur for gas pressures of $\sim 5 \times 10^{-3}$ Torr. The DC Magnetron Sputtering system by BOC Edwards, Scancoart six, found at the IFIMUP facilities, was used to deposit gold electrical contacts for measurements of the transort properties of some of the Sb_2Te_3 thin films. Three depositions of 300 s each at a voltage of 850 V were made to have gold contacts with an approximate thickness of 100 nm.

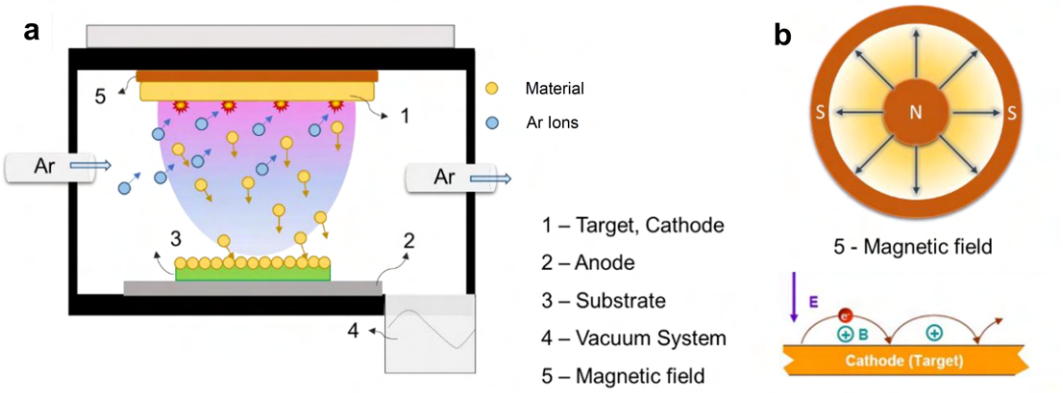


Figure 2.2 – (a) Schematic representation of the DC magnetron sputtering and (b) the configuration of the DC Magnetron sputtering magnet. Adapted from [77].

2.2 Morphological and Structural Characterisation

Following the fabrication of the nanostructures as discussed in the previous section, their morphological and structural characterisation was performed. To study the morphology of the samples, Scanning Electron Microscopy (SEM), high resolution Transmission Electron Microscopy (HRTEM), Atomic Force Microscopy (AFM) and X-ray Reflectivity (XRR) measurements were performed. The structure of the samples was further studied by Energy Dispersive Spectroscopy (EDS), X-ray Diffraction (XRD) and Raman Spectroscopy.

2.2.1 Scanning Electron Microscopy (SEM)

Scanning electron microscopy (SEM) was used to study the morphology of the samples. This technique shows remarkably high spatial resolution, ranging from a few millimetres down to 5 nm both for organic and inorganic materials [78]. SEM not only has the capability of obtaining 3D-like images of the surface of the sample, but also allows the study of the cross-section of the corresponding samples.

SEM is a microscopy technique where the sample surface is irradiated by a beam of electrons. The basic components of a SEM system are illustrated in Figure 2.3. The electrons are generated through emission from an electron source (cold field, thermionic or Schottky), creating a beam with energies of up to 30 keV [80]. Upon the creation of

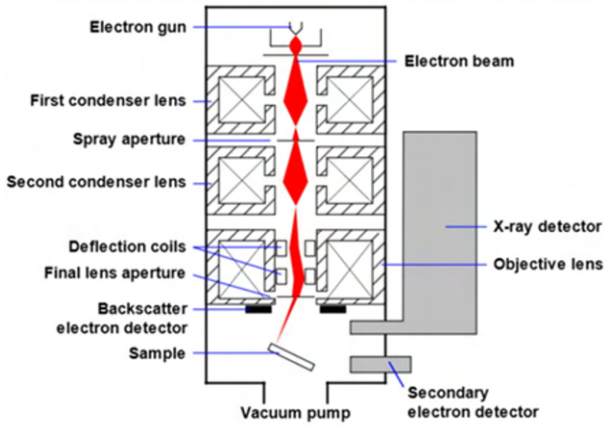


Figure 2.3 – Schematic diagram of the scanning electron microscope (SEM). Adapted from[79].

the electrons, they are focused by a set of electromagnetic lenses complemented by apertures, creating a focused beam of electrons. The lenses are also used to move the beam across the surface, row by row, in order to form a full image of the sample. The electron detection is performed by two detectors, namely the secondary and backscattered, which are also inside the sample chamber, which is in vacuum.

The detection and recreation of the sample surface image is possible due to the different type of interactions between the electrons and the sample. The electrons upon hitting the surface of the sample, interact with it, and several electrons and photons are emitted by the sample. Secondary electrons are produced by the inelastic interactions with the sample's electrons. These are used to form 3D images of the surface due to their low energy being intimately related to the interaction depth, allowing for an investigation of the topography of the samples. The backscattered electrons are the beam electrons that experience elastic backscattering with the sample electrons or nuclei, having a wider volume of interaction within the sample. Thus, they allow an inspection of the topography but also provide information regarding the sample composition. A contrast effect is formed based on the mean atomic number of the spot, which is related to the number of backscattered electrons, the larger the atomic number, the brighter the image of the spot will be[80,81].

In this thesis, the SEM system used was the Phillips-FEI/Quanta 400 FEG of CEMUP. SEM images were obtained of the thin films surface and cross section and the bilayer sample cross section. Before the characterisation of the samples, the face of the SEM sample holder was gently polished, and then a double carbon tape was used to fix the sample to the SEM sample holder.

2.2.2 Energy Dispersive X-ray Spectroscopy (EDS)

Energy Dispersive X-ray Spectroscopy (EDS or EDX) is a technique that consists of irradiating a sample with a high-energy focused electron beam on a selected region of the sample surface, being usually coupled with a SEM system. It is used to identify and

quantify the elemental composition of a small sample (up to a few cubic micrometers)[82].

EDS measures the wavelengths of X-rays that are created by the interaction of the electron beam with the sample. The incident electron beam can remove core electrons from the atomic electronic inner shell, leaving a hole behind. To return to the ground state, electrons from upper states decay to fill the hole, emitting a photon during the process. The energy of this photon is characteristic of each atomic transition and, thus, by analysing the energy of the emitted photons and the quantity of photons, the mass and atomic percentage of each element can be known[83].

In this work, the EDS system employed is coupled with the CEMUP SEM system mentioned in Section 2.2.1, belonging to the EDAX Genesis X4M unit. The composition of the Sb_2Te_3 thin films was obtained with this technique.

2.2.3 High resolution Transmission Electron Microscopy (HRTEM)

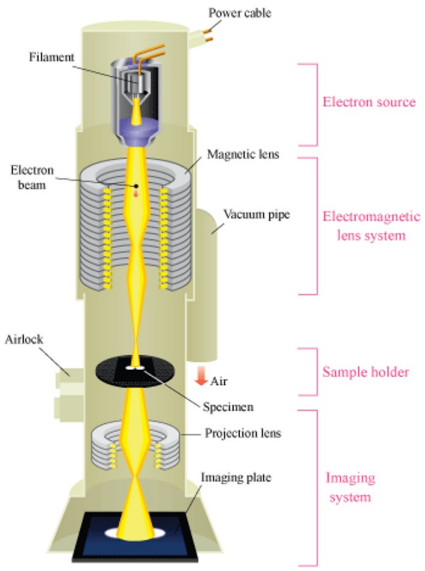


Figure 2.4 – Overview of the basic components of a TEM system. Adapted from[84].

High resolution Transmission Electron Microscopy (HRTEM) was also employed to study the morphology, structure and composition of the samples. TEM is similar to SEM, as it is constituted by similar elements, namely an electron source and electromagnetic lenses and apertures to control the electron beam, all in a vacuum chamber, as represented in Figure 2.4. The main difference is the type of electrons that are detected. As the name indicates, in TEM, the resulting image is formed by the electrons transmitted through the sample, in contrast with the scattered electrons detected in SEM. Due to this, the sample preparation is more detailed for a TEM measurement, since the thickness of a sample should not be higher than 100 nm and the image only depicts two dimensions. However, TEM has a higher resolution, usually smaller than 1 nm and, as such, it can provide information regarding the internal composition and crystallographic

structure of the sample, such as the existence of grains and their size and orientation. Moreover, to ensure that the electrons are able to cross the sample, the electrons are accelerated by a much higher voltage than in SEM, with value of up to 300 kV[85].

In this work, the structure of the Sb_2Te_3 thin films was studied by HRTEM. The system used was the JEOL JEM 2100 80-200 kV of the International Iberian Nanotechnology Laboratory (INL), having a point resolution by of 0.24 nm at 200 kV. The Focused Ion Beam (FIB) FEI Helios NanoLab 450S DualBeam - FIB with UHREM FEG-SEM system was used for the preparation of the thin films for TEM measurements.

2.2.4 Atomic Force Microscopy (AFM)

Atomic Force Microscopy (AFM) is a microscopy technique that probes the surface topography of a sample with nano-metric precision. In this technique, an extremely fine tip (the order of 20 nm) on a cantilever is brought close to the proximity of the surface of a sample. By measuring the interaction between the surface of the sample and the tip, a topographical image of the surface structure can be obtained[86].

There are two main measurement modes. In contact mode (Figure 2.5.(a)), the tip is in contact with the surface of the sample. It allows for high resolutions but if the sample is fragile, it can damage it. The second mode is called tapping mode (Figure 2.5.(b)). Here, the cantilever is vibrated near its resonance frequency close to the surface. Due to the vibration of the cantilever, it oscillates, coming into contact with the surface intermittently. A feedback loop is used to ensure that the interaction forces between the tip and the sample are constant during the scan of the surface. By recording the changes in amplitude needed to keep the interaction constant, a topographical image of the surface is created. It also has a high resolution, without the risk of damage as in the contact mode. The deflection of the cantilever in both modes is usually measured by a laser and a photodiode, as also depicted on Figure 2.5.

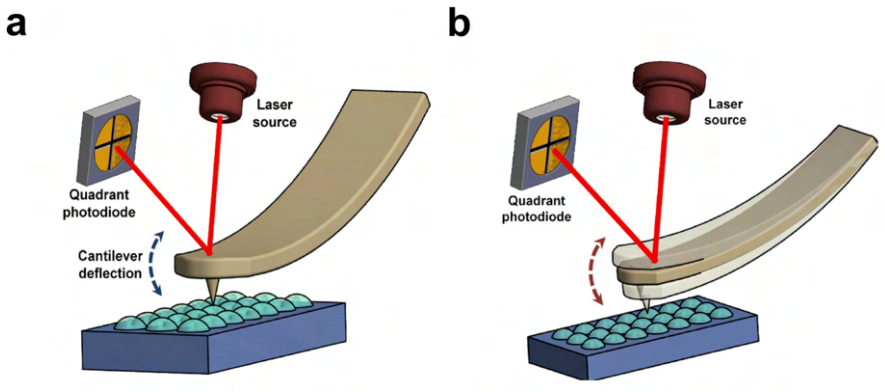


Figure 2.5 – The AFM working modes: (a) contact mode and (b) tapping mode. Adapted from[87].

The AFM system Veeco Metrology Multimode/Nansoscope IVA found at CEMUP facilities was used to obtain the roughness of a Sb_2Te_3 thin film and its glass substrate.

The roughness is obtained by calculating the local variation in height over the analysed area of thin film. The measurements were performed in tapping mode.

2.2.5 X-Ray diffraction (XRD)

X-ray diffraction (XRD) is a powerful non-destructive technique used to characterise the crystallinity of materials. From an XRD measurement, information about the structure, phases, preferential crystal orientations, grain sizes and crystal defects, among others, can be obtained, due to the comparable wavelength of x-rays to inter-planar distances in crystalline materials.

The most common x-ray measurement technique can de described by the XRD picture presented in Figure 2.6. The atoms in a periodic lattice scatter the incident X-rays. If the scattered waves add coherently, it creates a diffraction pattern with minima and maxima intensities. To have this constructive interference, considering a crystal with a set of atomic planes, the path difference of the x-rays, both the incident and scattered paths, must be equal to an integral multiple of the wavelength. This was first stated by Bragg and is described by equation 2.1, where D_{hkl} is the inter-plane distance of the family of atomic planes normal to the *hkl* direction, λ is the wavelength, and θ is the angle at which there is an intensity peak in the diffraction pattern. With this, the spacing between atomic planes determines the peak position in the θ axis[88].

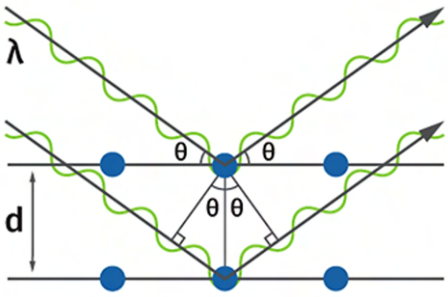


Figure 2.6 – Schematic representation of the Bragg's relation. Adapted from[89]

$$n\lambda = 2D_{hkl}\sin(\theta) \tag{2.1}$$

An XRD equipement is constituted by three basic elements: an x-ray tube, a sample holder and an x-ray detector. The x-rays are generated by a cathode ray tube, where a filament, usually tungsten (W), is heated to produce electrons. These electrons are accelerated by a voltage (typically in the 30 - 50 kV range), bombarding a target material, usually Copper (Cu). If the electrons are energetic enough, they can dislocate inner shell electrons of the target material, generating x-rays with well defined wavelengths (in the range 0.1 - 50 Å), in a process quite similar to the one described in section 2.2.2, for the EDS measurements. The x-rays hitting the sample surface must be monochromatic and focused, which is obtained by using optical systems made of slits and monochromators.

XRD measurements were performed using the SmartLab Rigaku diffractometer found at the IFIMUP facilities. A Bragg-Brentano $\theta/2\theta$ configuration was used, having a range of 2θ from 10º to 100º. The x-rays were obtained using Cu K_α radiation with a wavelength of λ = 1.540593 Å. The system operates at a 9 kW power, 45 kV and 200 mA. All the measurements were performed at room temperature. The Scherrer analysis was performed to obtain the mean grain size of a certain reflection, by using equation 2.2, where d_{hkl} is the grain size, K a constant dependent on the shape of the crystallite, being 0.9 a good approximation for non-detailed shape information, β the full-width at half-maximum (FWHM) of the reflection peak, and θ its angle of reflection[90].

$$d_{hkl} = \frac{K\lambda}{\beta \cos(\theta)} \tag{2.2}$$

2.2.6 X-Ray reflectivity (XRR)

X-ray Reflectivity (XRR) is a technique that has a similar principle to XRD described in section 2.2.5, allowing to characterise the structure of samples constituted by thin film layers, namely their thickness and roughness. Here the x-ray beam is incident on the sample surface at small angles. When it is incident at extremely small angles, it does not penetrate the sample and it is totally reflected. Up to a critical angle θ_C, the detected intensity of the reflection is at its maximum and is approximately constant, appearing as a plateau on the intensity versus angle curve. For angles higher than θ_C, the x-ray beam penetrates the sample surface and the intensity of the reflected wave decreases drastically, by what it is called Fresnel reflectivity. Due to the interference of the waves reflected at the difference interfaces existing in the sample (air/thin film interface and thin film/substrate or film/film interfaces), several oscillations are also observed in the reflectivity spectrum, which are called the Kiessig fringes. Figure 2.7.(a) presents a typical spectrum of a single substrate, with the characteristic behaviour of the Fresnel reflectivity, and Figure 2.7.(b) shows the usual Kiessig fringes for a single thin film on the substrate.

By a simple analysis of the Kiessig fringes, the thickness of the layers of the sample can be obtained, following equation 2.3[91], where m is the order of the fringes, θ_m the angle of the maximum of the m^{th} fringe and t the total thickness.

$$m = -\frac{1}{2} + \frac{2t}{\lambda}\sqrt{\cos^2(\theta_C) - \cos^2(\theta_m)} \tag{2.3}$$

By plotting the order of the fringes as a function of $F(\theta_m) = \sqrt{\cos^2(\theta_C) - \cos^2(\theta_m)}$ and performing a linear fit, the thickness can be calculated.

The system used was the same as in section 2.2.5, namely the SmartLab Rigaku at IFIMUP, but in a parallel beam configuration. The Cu Kα was the radiation used, with a wavelength of λ = 1.540593. The 2θ maximum range was from 0º to 8º.

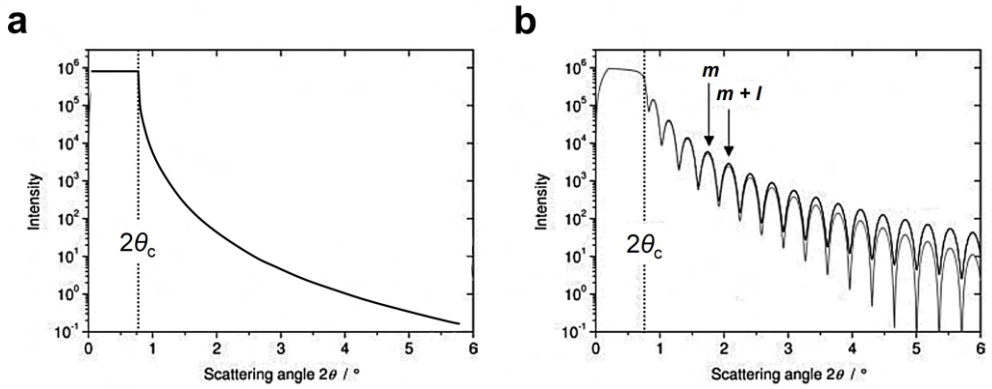


Figure 2.7 – Example of a X-ray reflectivity curve for a substrate and for a thin film deposited on a substrate. Adapted from[92].

2.2.7 Raman Spectroscopy

Raman spectroscopy is used to identify the vibrational modes of a given material. It is based on a non-linear light-matter interaction process, where an incident laser light is absorbed and scattered generating three types of emitted photons, represented in Figure 2.8. The inelastic scattering of light occurs due to the excitation of vibrational modes on the molecules of a sample by the incident light. In anti-Stokes scattering, the molecule is excited to a virtual state and upon returning to the ground state, it emits a more energetic photon than the absorbed one. In contrast, in the Stokes scattering, the molecule is also excited to a virtual state but it emits a photon with a lower energy than the laser light. This difference in energy, either positive or negative, corresponds to the energy of a certain vibrational mode of the sample. As such, by studying the radiation spectrum emitted by the sample, information about the vibrational energy states of the sample is gained, with these energy states being characteristic of each material. The third type of emitted photon is called Rayleigh scattering, where the emitted photon has exactly the same energy as the absorbed one[93].

A simple Raman spectroscopy system is constituted by a laser and a light detector, with optics used to direct the laser beam and emitted light. After the laser light beam is incident on the sample, the emitted light is directed towards a monochromator, to remove the emitted photons corresponding to the Rayleigh scattering, since it gives no information regarding the sample. After this removal, the remaining light is dispersed using a grating onto a detector, which counts the photons received at each wavelength. From this count, the intensity is plotted as a function of the wavelength difference between the laser and emitted light and the spectrum of the vibrational modes is obtained. In this thesis, the Raman spectra were recorded in a backscattering geometry at room temperature, using a 100× objective lens of a Leica microscope. The 633 nm He-Ne laser line was used for excitation and the scattered light was analysed by a Renishaw inVia Qontor spectrometer, with a resolution better than 1.5 cm^{-1}.

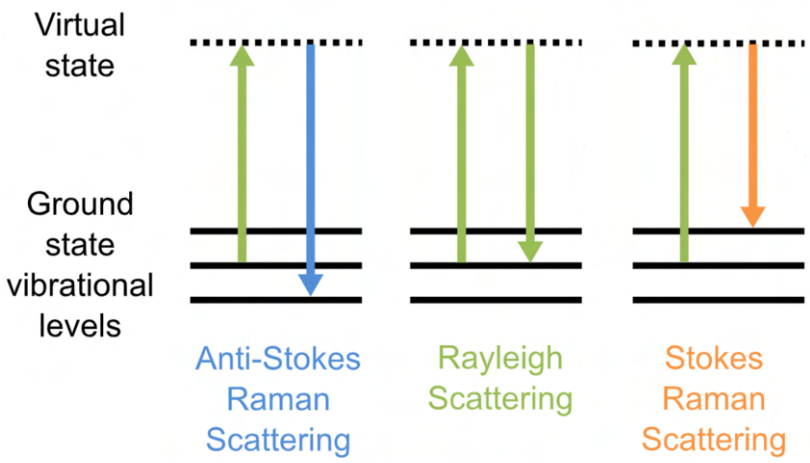


Figure 2.8 – Semi-classical representation of Raman scattering. A molecular structure is excited by light to a virtual energy state and radiation with the same energy (Rayleigh scattering) or a different energy (Stokes and anti-Stokes scattering) is emitted by the sample. The difference in energies corresponds to the excitation energy of a vibrational state. Adapted from [93].

2.3 Transport Properties

To understand the electronic conduction of the studied nanostructures, several transport properties were measured, namely the electrical resistance, the Seebeck coefficient (presented in Chapter 3), the magnetoresistance and the Hall effect. The combination of these measurements, besides characterising the transport in the nanostructures, also allowed the study of the influence of the topological surface state on the conduction of the thin films and its interplay with the ferromagnetic layers in the bilayer and trilayer systems.

2.3.1 Electrical Resistance

The electrical resistance of the fabricated samples was measured as a function of temperature using a closed cycle cryostat (APD Cryogenics Inc. system, HC-4 MK1 compressor). The maximum temperature range was 7 – 310K and all the resistivity measurements were carried out at IFIMUP. Two types of resistance measurements were performed. The first one is described in this section (four-probe method) and the second one (two-probe method, using the developed measurement setup in the scopus of this thesis) is described in Chapter 3.

In Figure 2.9, the experimental setup for the four-probe measurement is presented, showing all elements of the electrical resistance measurement and an assembled sample. To perform the measurements, a cylindrical Cu block acted as a sample holder, which can be mounted on the cryostat. The sample is placed on its surface and to electric isolate it from the Cu block, while maintaining good thermal conduction, a thin leaf of shroud paper embedded in GE-varnish is placed between the sample and the surface of the block. The varnish is also used to glue the sample to the block.

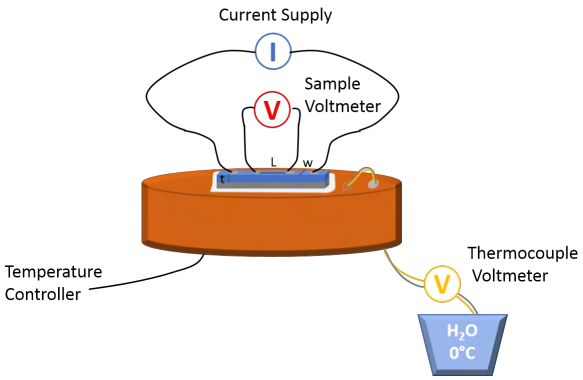


Figure 2.9 – Experimental assembly for electrical resistivity measurements using the 4-probe technique.

The electrical measurements are performed with the standard four linear contacts (four probes). Four wires are inserted into the metallic sample holder. The two outer most wires are used to feed current (I) to the sample, while the inner most wires are used to measure the voltage (V), as shown in Figure 2.9. The electrical contact between these four wires and the sample is made using a silver paste. In order to ensure a stable measurement throughout all temperatures, for some samples, four linear gold contacts were sputtered on to the surface, as described in section 2.1.2 and then the silver ink was used to make the electrical contact between the sputtered contacts and the four wires.

The temperature control is performed using a Lakeshore 331 coupled with a diode sensor inserted at the cryostat. With this controller, the linear time rate of the temperature can be settled. Having defined the rate, the temperature controller automatically sets the PID parameters in order to have a linear temperature variation at the intended rate. The used rate was 0.5 K/min to ensure thermal equilibrium and to have the accuracy needed for these measurements [94].

For a reliable temperature measurement, a differential thermocouple is also placed at the sample holder block, near the sample. The voltage drop across this thermocouple, using as reference 0ºC (ice), is measured with the assistance of a nanovoltmeter (Agilent 3458A 8½ Digit Multimeter). A prior calibration of the thermocouple curve is used to obtain the sample holder block temperature, which is considered to be the same temperature of the sample, due to the ensured good thermal conduction referred previously.

To perform the measurements automatically, an IEEE 488.2 GPIB communication bus was used, allowing all the instruments to interface with a computer, where a custom developed NI LabVIEW program automates the procedures and collects the measurement results. The temperature was controlled and the measured data could be monitored graphically in real time. The voltage *V* was measured using a nanovoltmeter (Keithly 2182 or Agilent/HP 314420) and the current *I* was applied using the DC Time Electronics Current Source 9818. All the measurements were performed in DC mode, by applying a constant value current. For the thin film samples, the resistivity was cal-

culated using equation 2.4, where R is the measured resistance, given by $\frac{V}{I}$ with w the width of the sample, L the distance between the voltage contacts and t the thickness of the films.

$$\rho = \frac{Rwt}{L} = \frac{V}{I}\frac{wt}{L} \tag{2.4}$$

2.3.2 Magnetotransport

2.3.2.1 Magnetoresistance

The magnetoresistance was measured using four probes, either with four-linear contacts, represented in Figure 2.10.(a), or in a square geometry using the van der Pauw method, represented in Figure 2.10.(b). The electrical contact between the probes and the sample was made using silver paste, and, for some samples gold contacts were sputtered as described in section 2.1.2. The magnetic field was applied out of plane (OP) for the Sb_2Te_3 thin films and both contact geometries were used. For the bilayer measurements, both OP and in plane (IP) fields were applied, with the measurements being performed with four-linear contacts. In the IP configuration, both magnetic field perpendicular and parallel to the applied current was used.

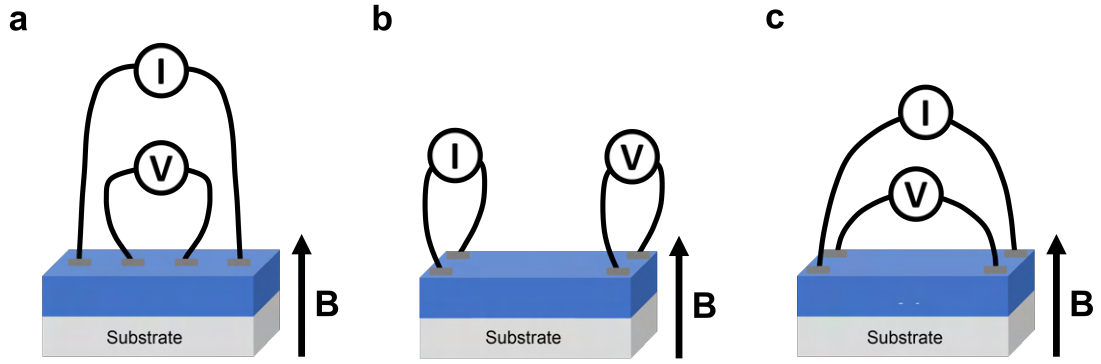


Figure 2.10 – Magnetotransport contact geometries. (a) Four-linear contacts resistance measurement, (b) Van der Pauw contacts resistance measurements. (c) Van der Pauw contacts Hall effect measurement.

The magnetoresistance was obtained at several cryogenic temperatures for the thin films (2 - 10 K) and up to room temperature for the bilayers. The magnetic field was applied up to 7 T, with a step of 0.1 T. The measurements were performed in an AC mode at 23 Hz and the data acquisition was done using a home-made developed software. The measurements were executed at Imperial College London, using a Cryogen Free Measurement System (CFM) from Cryogenic Limited of the Experimental Solid State Group.

2.3.2.2 Hall effect

The Hall effect was measured using the Van der Pauw geometry, as represented in Figure 2.10.(c). As for the magnetoresistance, the electrical contacts were made using silver paste. The measurement was performed with a constant applied magnetic field, while varying the temperature. A closed cycle cryostat (APD Cryogenics Inc. system, HC-4 MK1 compressor) was also used, having a maximum temperature range of 10 – 300 K. The maximum applied field was 1 T. The measurements were performed at IFIMUP.

2.4 Ferromagnetic Resonance Spectroscopy (FMR)

Ferromagnetic Resonance (FMR) spectroscopy is a versatile experimental technique that can be used to characterise the high-frequency behaviour of ferromagnet materials. It takes advantage of the precession of the magnetisation around an applied external DC field, when the system is perturbed by a small RF field. From FMR, several material parameters can be obtained, such as the effective damping, saturation magnetisation and magnetic anisotropies.

The first theory of FMR absorption was given by Kittel[95]. In a FMR experiment, an external DC magnetic field H is applied, defining the initial magnetisation direction of the ferromagnetic (FM) material. Following this definition, a weak RF magnetic field, having a microwave frequency, is applied perpendicular to the external DC magnetic field. In this situation, the resonant absorption process occurs when the angular frequency of the RF field is equal to the frequency of the magnetisation precession of the FM material. From this experimental observation and its deviation from the Lamor frequency, Kittel explained the absorption by considering the internal fields of the FM material, such as the demagnetising field. The resonance frequency is thus given by equation 2.5, the Kittel equation for an in plane magnetic field, where M_S is the saturation magnetisation and H_k is the anisotropy field.

$$f = \frac{\gamma \mu_0}{2\pi} \sqrt{(M_S + H_K + H)\,(H_K + H)} \tag{2.5}$$

In this description, however, the magnetisation precesses about the effective field indefinitely, which is not the case in real materials. To account for energy dissipation, first Landau and Lifshitz and then Gilbert proposed a phenomenological damping parameter, analogous to a viscous drag. The spin dynamics of a material is then given by the Landau-Lifshitz-Gilbert (LLG) equation 2.6, with γ the gyromagnetic ration, $\mathbf{m}$ the unit magnetisation vector of the material, $\mathbf{H}_{eff}$ the effective magnetic field, which includes internal and external magnetic fields, and α the dimensionless Gilbert damping[96,97].

$$\frac{d\mathbf{m}}{dt} = -\gamma \left[\mathbf{m} \times \mathbf{H}_{eff}\right] + \alpha \left[\mathbf{m} \times \frac{\partial \mathbf{m}}{\partial t}\right] \tag{2.6}$$

With this approach, we are able to describe phenomenologically the precession of the magnetisation, using the Gilbert damping α. Several mechanisms contribute to α, which can be divided into intrinsic and extrinsic mechanisms[98]. Intrinsic contributions consider the fundamental physics of the material system, whereas the extrinsic contribution relate to additional secondary contributions, such as inhomogeneities of the sample and angular-momentum dissipation associated with non-magnetic layers in bilayer systems. As such, the measurement of α gives insights into the precession of the magnetisation and also the mechanisms of energy dissipation within a system. It can be obtained from a FMR measurement, by analysing the linewidth of the absorption peak, when measuring in frequency domain. The linewidth ΔH is taken as the full width at half maximum (FWHM) of the absorption peak, being given by an intrinsic damping contribution, ΔH_0, and the extrinsic contribution depending on the Gilbert damping α, as described in equation 2.7, where f is the RF frequency[99].

$$\Delta H = \Delta H_0 + \frac{4\pi\alpha}{\gamma} f \tag{2.7}$$

2.4.1 Vector Network Analyser Ferromagnetic Resonance (VNA-FMR)

A common technique for FMR measurements is through the use of a Vector Network Analyser (VNA). A VNA is a radio frequency (RF) equipment that is able to output and monitor RF signals of variable frequency and power. It combines a microwave generator with a lock-in amplifier, thus providing phase-sensitive detection of its signals, by measuring the amplitude and phase of the microwaves. With two ports, one acting as an emitter (port 1) and the other as a receiver (port 2), the four S parameters of the scattering matrix can be measured using the VNA, namely S_{11} and S_{22}, corresponding to reflection, and S_{12} and S_{21}, corresponding to the transmission.

By inducing an RF signal in the sample and measuring its transmission, the VNA allows for FMR measurements across a wide frequency range. The RF signals are induced in the sample via a coplanar waveguide (CPW), which consists of a coplanar layer with a ground-signal-ground configuration. To apply the RF signals, the sample is placed face-down on the CPW. When the microwaves are directed through the sample, the absorption at the ferromagnetic resonance is detected through the reduction of the transmission S_{21} measured by the VNA. As such, the combination of these two equipments allows for measurements as a function of frequency over a wide range (up to few tens of GHz) and of the applied magnetic field[100].

Measurements at room temperature were performed using a home-made VNA-FMR system which uses a commercial VNA device (Anritsu 37247D), at IFIMUP. The system can operate over a frequency range up to 20 GHz and has a resolution that depends on the range of the working frequencies. In measurements that span up to 20 GHz, a resolution of a few MHz is achieved. The external static DC magnetic field is applied by an electromagnet. A schematic of the VNA-FMR system of IFIMUP is represented

in Figure 2.11.

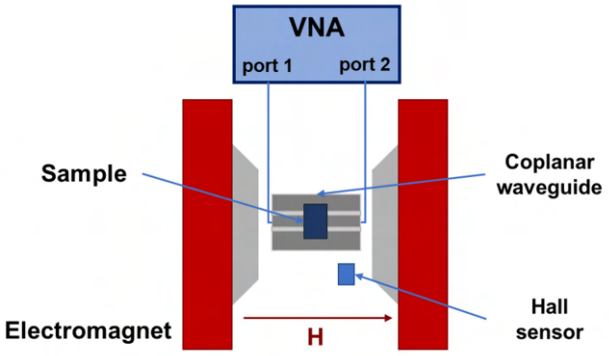


Figure 2.11 – A schematic of VNA-FMR system. The sample is mounted on top of the CPW. Adapted from [101].

The measurements were carried out by sweeping the frequency in the desired range with a fixed DC magnetic field and repeating this sequence for different applied fields. Due to this, the linewidth of the absorption peak obtained by the VNA is a frequency linewidth, which may not directly correspond to the field linewidth that is needed for the calculation of the damping as described in equation 2.7. The field linewidth is obtained from the frequency linewidth by using the identity of equation 2.8 [102].

$$\Delta f = \Delta H \frac{\partial f(H)}{\partial H}\Big|_{H=H_{res}} \tag{2.8}$$

Considering the Kittel equation for in plane applied DC magnetic field (equation 2.5), the field linewidth is thus given by equation 2.9.

$$\Delta H = \frac{\Delta f}{\frac{\gamma\mu_0}{2\pi}\sqrt{1+\left(\frac{\gamma\mu_0 M_S}{4\pi f_{res}}\right)^2}} \tag{2.9}$$

The absorption peak obtained from the imaginary component of S_{21} is fitted to a variation of an asymmetric Lorentzian, given by equation 2.10, where K and X_0 are the scalling and offset parameters and φ, the phase shift adjustment in degrees. From these fits, the resonance frequency and frequency linewidth are obtained, allowing for the calculation of the damping and other parameters as previously described.

$$S_{21} = K\frac{(f_{res}^2 - f^2)\cos(\varphi) + \Delta f_{res} f \sin(\varphi)}{(f_{res}^2 - f^2)^2 + \Delta f_{res}^2 f^2} + X_0 \tag{2.10}$$

2.4.2 Lock-in amplifier Modulated Ferromagnetic Resonance (LIA-FMR)

Ferromagnetic resonance measurements were performed as a function of temperature by using lock-in detection and a modulated external applied field. As in the VNA-FMR measurements described in the previous section, the RF field is induced through a CPW. However, a pair of Helmholtz coils connected to an AC source (490 Hz) generate a small

field h_{ac} parallel to the applied DC magnetic field H_{DC}, as shown in Figure 2.12.(a). This extra component modulates the FMR response, with the intensity (I) of S_{21} varying as $\frac{dI}{dH}$. This modulated response is recovered using the lock-in after an RF diode is used to eliminate the RF of the signal, with the AC source acting as the reference signal. With this method, the measured signal, namely the output of the lock in, will not be the direct absorption peak, being its derivative trace. As such, the output signal, obtained by varying the external DC field at constant RF frequency, can be fitted by a derivated asymmetric Lorentzian function, given by equation 2.11, with K_1 and K_2, scaling of the symmetric and asymmetric components, respectively, and X_0 an offset. From this fit to the modulated signal, the linewidth and resonance fields can be obtained, which are then used to calculate the damping α and the other parameters as previously discussed.

$$(S_{21})_{mod} = K_1 \frac{(\Delta H/2)\,(H - H_{res})}{\left((H - H_{res})^2 + (\Delta H/2)^2\right)^2} + K_2 \frac{(\Delta H/2)^2 - (H - H_{res})^2}{\left((H - H_{res})^2 + (\Delta H/2)^2\right)^2} + X_0 \qquad (2.11)$$

The modulated measurements were performed using a NanOsc Instruments Cry-oFMR system in a Quantum Design Physical Properties Measurement System (PPMS) at Imperial College London. The samples were mounted face-down on the CPW and secured in place with kapton tape. The CPW is placed in the CryoFMR probe insert for the PPMS, which is represented in Figure 2.12.(b), where the Helmholtz coils used for the modulation are also visible, as well as the temperature sensor. The studied temperatures were between 2 and 300 K.

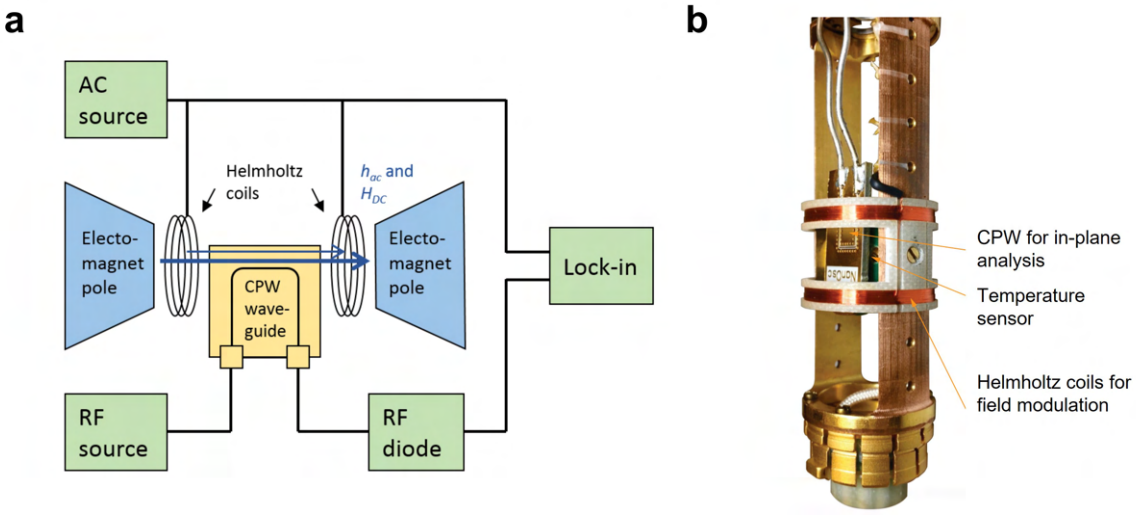


Figure 2.12 – Lock-in amplifier modulated FMR system. (a) Schematic of experimental setup of the CryoFMR system with lock-in detection of NanoOsc Instruments[103]. (b) CryoFMR probe insert for the PPMS, with the CPW and the Helmholtz coils for field modulation. Adapted from[104].

2.4.3 X-Ray Detected Ferromagnetic Resonance (XFMR)

X-ray detected ferromagnetic resonance (XFMR) is a synchrotron-radiation-based tool that is used to study the element-selective magnetisation dynamics[105]. Magnetic and chemical contrast in XFMR is obtained by X-ray magnetic circular dichroism (XMCD), which allows for layer specific measurements when each layer has a different chemical composition. As such, it is a powerful technique to study the magnetisation dynamics and the generation and transmission of spin currents in systems with two or more FM materials, as it is the case of the trilayer systems investigated in this thesis. Time-dependent XFMR can thus be used to measure the amplitude and phase of the spin precession of each FM material layer, using stroboscopic measurements, by utilising the time structure of synchrotron x-rays. The RF field used to achieve the magnetisation precession is synchronised with the X-ray pulses of the synchrotron. As such, each x-ray pulse measures the magnetisation cone at precisely the same point in the cycle, which when introducing phase delays, allows for the study of the full cycle of precession.

Static XMCD is obtained as the difference between X-ray absorption spectra corresponding to the parallel and antiparallel helicity vectors of the circular polarised X-rays to the applied magnetic field[106]. In contrast, time-resolved XFMR measures the small periodic oscillations in the magnetisation direction with fixed circular polarisation. The stroboscopic measurements are performed in multibunch mode and the typical spot size of the X-ray beam on the sample is $200 \times 20\ \mu m^2$.

Figure 2.13 shows the XFMR setup in a transverse geometry used for the typical measurements at the Diamond Light Source. As in the previous FMR techniques, the sample is mounted face-down on a coplanar waveguide (CPW) and it is driven by the external radio frequency (RF) field, h_{rf}, while under the DC magnetic field, H_{DC}. H_{DC} is applied using a vector magnetic system which can apply a field of up to 0.9 T in any direction. The applied h_{rf} field needs to be a harmonic of the X-ray pulse frequency, which at Diamond is roughly 500 MHz. By previously characterising the samples via VNA-FMR, the frequency of h_{rf} is then decided considering the resonance of the FM materials and as a multiple of the X-ray pulse frequency. This is achieved by using an RF comb generator (Atlantic Microwave) driven by the master oscillator clock of the synchrotron x-ray pulses. The phase delay is introduced by a programmable delay line (Colby instruments), which enables the phase shifting of the RF oscillation with respect to the X-ray pulses, with a step resolution of roughly 0.5 ps. The pulse width of the x-rays is approximately 35 ps at Diamond.

The x-rays are incident on the sample through a small hole on the signal line of the CPW. The detection of the x-ray absorption is typically done in transmission as depicted in Figure 2.13. After the x-rays pass through the sample, the transmitted x-rays are detected through the x-ray excited optical luminescence (XEOL) emerging from the luminescent substrate. The optical luminescence is then detected by a photodiode place behind the sample, as shown in figure 2.13. The typical substrate for these measurements

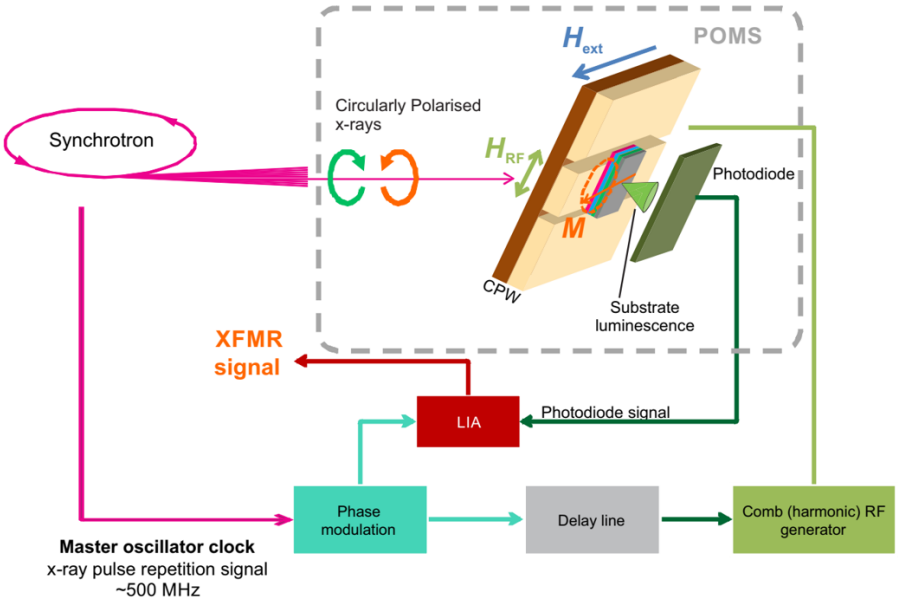


Figure 2.13 – Schematic of the XFMR setup in transverse geometry. The sample is placed face-down on a CPW within POMS (portabvle octupole magnet system) and incident circularly polarised x-rays pass through the hole in the signal line. The applied field H_{DC} is perpendicular to both x-ray beam direction and h_{rf}. The different components of the XFMR electronic signal circuitry, RF excitation circuit, and x-ray detection system are also shown. The delay line enables the phase shifting of the RF oscillation with respect to the x-ray pulses. Adapted from[107].

is MgO, but in this work, the trilayer samples were deposited on the flexible substrates (PET and Kapton). Due to this, for the samples studied in this work, the detection of the x-ray absorption was not performed in transmission but in reflection, and the excitation of the resonance was achieved with an out of plane field, for the measurements in the reflection geometry to be possible.

The XFMR signal is measured by a lock-in amplifier (LIA), with 180º-phase modulation, where the LIA measures the difference between directions of opposite phase during the procession cycle, with this modulation giving a larger signal. Prior to the measurements, XMCD is measured to select the suitable fixed photon energy for each element. The XFMR signal is then recorded with circular polarisation X-rays of fixed photon energy, which leaves only two free scanning parameters, namely the delay time between the X-ray pulses and H_{DC}. In the preliminary measurements presented in this work, time-delay scans were used to record the signal at a constant H_{DC} by sweeping the delay time. By normalising to the XMCD previously obtained, the amplitude of the time-delay signal can be obtained per atom for each different chemical element of the sample, which allows for a quantitative decomposition of the resonance features of each layer.

The preliminary measurements of the trilayer systems were performed in collaboration with Prof. Throsten Hesjedal's group at the University of Oxford and at the Diamond Light Source, on beamline I10. The measurements were made by Dr. David Burn.

2.5 Implementation of Spin Pumping measurements

Besides the aforementioned techniques and procedures, a key point and development throughout this thesis was to deploy and explore for the first time the method of spin pumping measurements at the group of professor Lesley Cohen at Imperial College London. The employed system was the FMR system presented in the subsection 2.4.2, the NanOsc Instruments CryoFMR, and a special ISHE-CPW developed by NanOsc, which can be inserted into a Physical Properties Measurement System (PPMS).

Spin pumping

The spin to charge interconversion mechanisms, such as ISHE and IEE described in Chapter 1, can be studied by several techniques such as lateral spin valves[25], second harmonic measurements[108] and ST-FMR[109], among others. One other technique can be employed, namely spin pumping by FMR. In this technique, spin injection is obtained by using the precession of the magnetisation at the FM resonance. This spin injection was first demonstrated in the 80s by Silsbee and Johnson[110] , being followed by the development of the spin pumping theory by Tserkobniak, Brattas *et al.*[111–113] and Mizukami *et al.*[114] in 2002. These works demonstrated a damping enhancement associated with the spin injection at resonance. The detection of the spin to charge conversion from spin injection was, however, only demonstrated in 2006 by Saitoh *et al.*[24] and Costache *et al.*[115], first in Platinum. Since this first demonstration, spin pumping has become a widely used method to observe spin to charge current conversion by ISHE and/or IEE and to determine the efficiency of this conversion, namely the spin hall angle, spin diffusion length and inverse Edelstein lengths.

In this section, the origin of the spin pumping current will be derivated using the Tserkovniak and Bratas theory, followed by the calculation of the injected spin current and the converted charge current and how it is measured through electrical detection of the FMR. The implementation of these measurements using the NanOsc Instruments CryoFMR system with the ISHE-CPW will be described, from the observation of the spin pumping voltage and ISHE, confirmation of the observation via Lock-in detection and consequent measurements as a function of temperature of the ISHE conversion using a nanovoltmeter.

2.5.1 Injection of the spin current

Spin injection due to spin pumping by a ferromagnetic resonance can be thought of as the reciprocal effect of a spin torque. When a spin current is injected from an adjacent layer into a FM layer, there is a transfer of its angular momentum, which causes the magnetisation to be put out of equilibrium and start precessing. This torque is actually the basis of spin torque MRAMs, where if enough angular momentum is transferred, the switching of the magnetisation is achieved. The reciprocal situation occurs when

the magnetisation of a FM layer is precessing. It losses its angular momentum, through the transfer of a spin current from the FM material to the adjacent layer. As such, a spin current exerts a finite torque on the FM magnetisation and a precessing magnetisation loses torque by emitting a spin current[116].

The spin pumping process is thus associated with loss phenomena, which can be evaluated through the damping parameter of the magnetisation precession. If the FM material is adjacent to a non-magnetic (NM) layer, the total damping will be the sum of the Gilbert damping of the FM material α_{FM}, and the extra damping, $\Delta\alpha$ present due to spin pumping[113]. Due to this simple sum, the extra damping due to spin pumping can be evaluated by performing FMR measurements of two samples with and without the adjacent layer to where the spin current is being injected. Thus, the measurement of a single FM layer gives us the reference damping value, α_{FM}, and the measurement of the FM/NM sample, $\alpha_{FM/NM}$, allows us to calculate $\Delta\alpha = \alpha_{FM/NM} - \alpha_{FM}$. The estimation of the damping parameters is as such of the utmost importance for a good quantification of spin pumping phenomena, evidencing the importance of the FMR measurements previously discussed. Moreover, to correctly estimate the reference damping value, the FM sample is usually capped, to prevent other effects, such as oxidation of the surface of the FM thin film layer, which ”artificially” increases the damping value.

Having estimated the extra damping due to spin pumping, the instantaneous spin pumping current can be calculated following equation 2.12[111,112]. From this equation, the instantaneous spin current is perpendicular to both the magnetisation and its derivative, and it leads to a build-up of a spin accumulation inside the NM layer.

$$\mathbf{J}_{S,0} = \frac{\hbar}{4\pi}\frac{g^{\uparrow\downarrow}}{M_S^2}\mathbf{M}\times\frac{d\mathbf{M}}{dt}\left(\frac{2e}{\hbar}\right) \tag{2.12}$$

The parameter $g^{\uparrow\downarrow}$ is the real part of the spin mixing conduction and it indicates the global spin transmission. It is given by equation 2.13[111,112], being proportional to $\Delta\alpha$, with t_{FM} the thickness of the FM layer. These equations describe the spin pumping phenomena without considering any back-flow, being only valid if there is no spin flip scattering or if the thickness of the NM material is big when compared to its spin diffusion length, which is the case throughout this thesis. As such, these are the equations used in this work.

$$g^{\uparrow\downarrow} = \frac{4\pi M_S t_{FM}}{g\mu_B}\Delta\alpha \tag{2.13}$$

Equation 2.12 describes the instantaneous AC current. However, the measurements are performed by relying on a DC current measurement. To obtain the DC spin current, the integration over the full precession of the magnetisation vector must be performed. In equation 2.12, the only time dependent term is the magnetisation, and thus all the magnetisation components need to be calculated and integrated over its full precession, which can be found in[115]. Considering these calculations and in the approximation of

small precession angle, the DC spin current J_S is given by equation 2.14. From this equation, it can be seen that the spin current can be calculated following a FMR measurement of bilayer and reference samples. Moreover, this spin current is proportional to the out of equilibrium magnetisation at the resonance. Therefore, the field dependence of the current follows the asymmetric Lorentzian shape of the FMR absorption peak.

$$J_S = \frac{g^{\uparrow\downarrow}\gamma^2\hbar\left(\mu_0 h_{rf}\right)^2}{8\pi\alpha^2_{FM/NM}}\left[\frac{\mu_0 M_s\gamma + \sqrt{\left(\mu_0 M_s\gamma\right)^2 + 4\omega^2}}{\left(\mu_0 M_s\gamma\right)^2 + 4\omega^2}\right]\left(\frac{2e}{\hbar}\right) \tag{2.14}$$

2.5.2 Evaluation of the spin to charge conversion

Following the calculation of the spin current, the spin to charge conversion can be evaluated by measuring the current charge being created from J_S. In the NM layer, either due to ISHE or IEE, an electric field arises perpendicular to both the spin current and the external applied DC magnetic field due to the generated charge current, as depicted in Figure 2.14, with Sb_2Te_3 as the NM and Py as the FM materials. In an open circuit condition, the created electric field, generates a current that is equal in amplitude but opposite to the generated charge current. As such, by measuring the voltage drop across the sample, the generated charge current can be calculated, following Ohm's law.

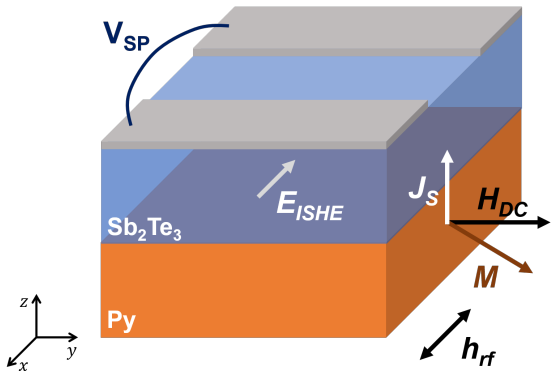


Figure 2.14 – A schematic representation of the spin pumping in a FM/TI bilayers, namely Py/Sb_2Te_3. At resonance, a spin current is injected from the Py layer into the Sb_2Te_3 layer. An electric field corresponding to the ISHE (or IEE) is generated in the bulk (or surface).

From the measured spin pumping voltage V_{SP} the efficiency of the SCC can thus be calculated. However, these effects are not the only ones arising from spin pumping. The anisotropic magnetoresistance (AMR), the anomalous Hall effect (AHE) and Planar Hall effect (PHE) originating in the FM layer could also be picked up by V_{SP}. In the geometry present in Figure 2.14, these effects appear as asymmetric components of the V_{SP}, whereas the ISHE/IEE appear as symmetric. Furthermore, thermoelectric effects can also be presented due to heating of the sample at resonance. These effects are asymmetric regarding the direction of the external applied field, which is the opposite of

the ISHE/IEE effects, due to their symmetry. As such, thermoelectric effects can also be removed by measuring V_{SP} for both directions of the external applied DC magnetic field.

The voltage corresponding to either ISHE or IEE can then be obtained from V_{SP}. Considering a material with only ISHE, the spin diffusion in the bulk of the samples needs to be accounted and the spin current will have a dependence on the z direction of Figure 2.14[117]. As such, the total charge current created due to ISHE is obtained by integrating along the z direction, for all the thickness of the NM film. Following this integration, ISHE can be evaluated by the corresponding ISHE voltage V_{ISHE}, given by equation 2.15, where w is the width of the sample (along the y direction of Figure 2.14), R the resistance of the bilayer system, of both the FM and NM layers, and t_{NM} the thickness of the NM layer.

$$V_{ISHE} = wR\lambda_{SD}\theta_{SH}J_S \tanh\left(\frac{t_{NM}}{2\lambda_{SD}}\right) \tag{2.15}$$

From equation 2.15, the spin Hall angle θ_{SH} times the spin diffusion length λ_{SD} can be obtained from a single sample, or both independently for samples with different NM layer thicknesses. Thus, a spin pumping measurement is a powerful technique, allowing for the observation of the ISHE (or IEE) and also for the calculation of the efficiency of the SCC caused by these effects.

2.5.3 Measurements of spin pumping voltage

The spin pumping voltage V_{SP} was measured using the FMR system presented in the subsection 2.4.2, the NanOsc Instruments CryoFMR. A special ISHE-CPW developed by NanOsc, which can also be placed in the PPMS insert, was used and is shown in Figure 2.15.(a). With these capabilities, measurements as a function of temperature, for temperatures between 2 and 300 K were optimised and performed at Imperial College London.

2.5.3.1 Observation of the Inverse Spin Hall Effect

The ISHE-CPW has two additional ISHE contact pads which run parallel to the CPW, having a center-to-center separation of 3.5 mm. Each pad has five raised bumps which help facilitate the electrical contact with the sample, as seen in Figure 2.15.(a). To further improve the contact, silver paste contacts were also drawn on top of the bilayer samples, as shown in Figure 2.15.(b), for a test sample. The sample is then placed faced down on the CPW as for the FMR measurements, and held in place with tightly wounded kapton tape. The voltage is then picked up through the contact pads, which are connected to the two pins numbered 10 and 12 on Figure 2.15.(a), which correspond to pins 10 and 12 of the PPMS puck insert.

This voltage is then routed to the ISHE input BNC on the front panel of the CyoFMR instrument. With this method, the spin pumping voltage is measured using the same lock-in amplifier as described in section 2.4.2, for the LIA-FMR method. There are two modes available for this measurement. The first mode modulates the external applied DC field, as also described for the LIA-FMR measurements, and as such it measures the field derivative of V_{SP}. The second mode available chops the V_{SP} DC signal to create a square wave for the lock-in detector to measure. Figure 2.15.(c) shows the V_{SP} signal measured using the modulated mode for the Py(10)/ST(100) bilayer, and also the corresponding measured FMR resonance, with both signals closely following each other.

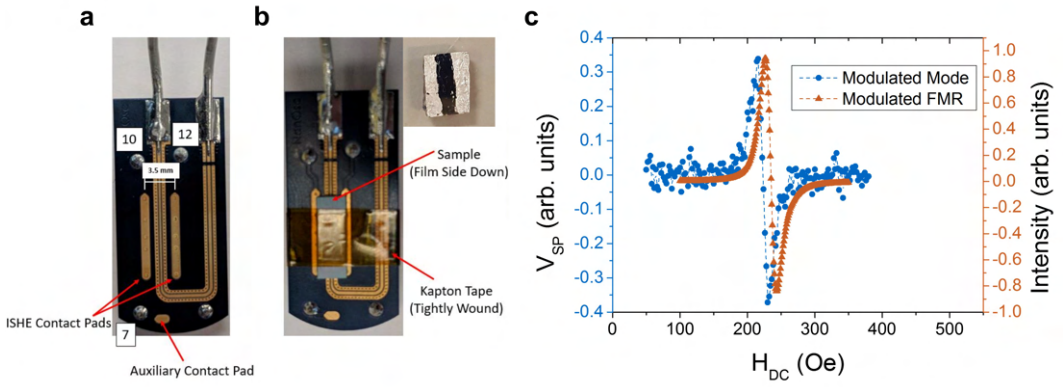


Figure 2.15 – NanOsc CryoFMR spin pumping measurements. (a) The coplanar waveguide for spin pumping measurements (ISHE-CPW). The pads for the electrical contact are at a center-to-center distance of 3.5 mm, and the pins 10 and 12 correspond to the pads are also marked. There is also an extra auxiliary contact pad numbered 7. (b) The sample mounted on the CPW, with the film side down, and secured in place by tightly wound kapton tape. Silver paste contacts were drawn as seen in the photograph of a test sample. Adapted from [118]. (c) Spin pumping voltage V_{SP} and FMR intensity as a function of the external applied DC field H_{DC} at 4 GHz. Both these measurements were performed in the modulated modes offered by the CryoFMR system.

With this method, it is possible to observe the V_{SP} and as such ISHE through the symmetric component of the signal. However, information about the DC voltage is lost for both measurement modes, and as such, these methods do not allow the characterisation of the SCC efficiency.

2.5.3.2 External Lock-in detection

An external lock-in was also employed to verify the measurement automatically performed by the NanOsc system. The input to the external lock-in was the same as the input into the front panel of the CryoFMR equipment. Both measurements with the external lock-in and the CryoFMR system, could not be performed at the same time. As such, the external lock-in measurement was made while an FMR measurement was performed by the CryoFMR. The external lock-in output was connected to the AUX input in the CryoFMR system, which guarantees synchronisation of the FMR and Lock-in measurements. Following the external Lock-in measurement, the modulated measurement

mode was also employed to compare and verify both outputs. All these measurements were performed as frequency sweeps, with the field kept constant at 200 Oe.

Figure 2.16 shows the signals obtained for the measurements described above for the Py(10)/ST(100) sample. It is verified that both signals have the exact same dependence with field, namely the derivated asymmetric Lorentzian, as expected when exciting the resonance with a modulated field. It was verified that the signal measured by either the internal (CryoFMR) and external lock-in have the expected field dependence, confirming that measurements with only the CryoFMR are valid.

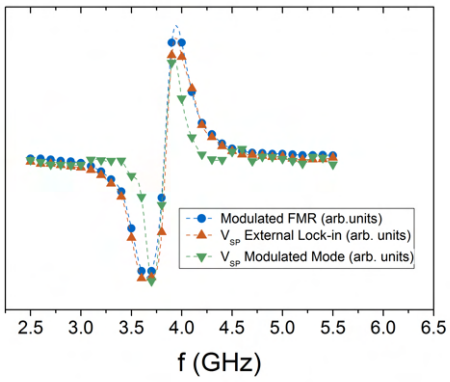


Figure 2.16 – Spin pumping measurement comparison between the CryoFMR system and an external Lock-in.

2.5.3.3 Open voltage nanovoltmeter measurements

To obtain the DC values of V_{SP}, the previous two methods could not be employed, as previously discussed. As such, an external nanovoltmeter had to be used to measure the DC Voltage. As for the external lock-in measurements, the voltage input into the CryoFMR was taken as the input for the nanovoltmeter. The measured voltage was then collected by the AUX input of the CryoFMR system, guaranteeing the synchronisation of the measurements. The measurements were performed while inducing the FMR of the samples. A Keithley 2182A Nanovoltmeter was used to perform these measurements.

Figure 2.17 shows the measured DC V_{SP} and its comparison with the signal obtained by the modulated mode offered by the CryoFMR system for the Py(10)/ST(100) sample. The nanovoltmeter measurement appears as the direct asymmetric Lorentzian. Despite this, the linewidth and resonance fields are extremely similar for both signals.

From the DC signal measured with the nanovoltmeter, the V_{ISHE} can be obtained from the symmetric part of the V_{SP} signals. The symmetric part of the signal is calculated by performing the fit to the data with an asymmetrtic Lorentzian, as described in equation 2.16. V_{sym} and V_{asym} correspond to the symmetric and asymmetric components of V_{SP}, with ΔH and H_{res} the linewidth and resonance fields of the ferromagnetic resonance, and

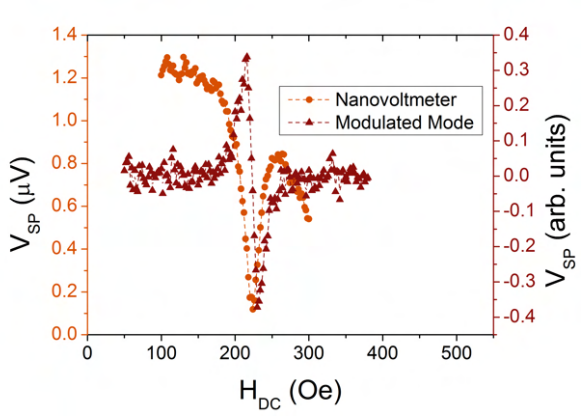


Figure 2.17 – Spin pumping measurement comparison between the CryoFMR system and the nanovoltmeter.

V_0 a possible offset. With these nanovoltmeter measurement and analysis methods, the SCC was measured as function of temperature.

$$V_{SP} = V_{sym}\frac{(\Delta H/2)}{(H-H_{res})^2+(\Delta H/2)^2} + V_{asym}\frac{H-H_{res}}{(H-H_{res})^2+(\Delta H/2)^2} + V_0 \qquad (2.16)$$

CHAPTER 3

Design of a versatile Seebeck and Electrical Resistivity measurement setup for thin films

In this chapter [1] design, implementation and testing of a versatile measurement setup of the Seebeck coefficient for thin films at temperatures in the range [10 – 300] K is performed. A dynamic differential method is employed to obtain a fast measurement of the Seebeck coefficient as a function of temperature. Moreover, a steady and/or quasi-steady state method can also be employed. Using the same apparatus, the resistivity can also be measured by a two-probe method, within the same range of temperatures. Finally, the details of the instrumentation and implementation are described and to validate the reliability and accuracy of the setup, test measurements on certain materials were performed.

3.1 Introduction

The thermoelectric effects (Seebeck and Peltier) are phenomena that convert heat into electricity or vice-versa[119], respectively. Even though these effects have been discovered several years ago, contemporary thermoelectric materials are gaining more attention due to their possible applications in power generation, heat recovery and electronic refrigeration, besides the common application to temperature measurements[120–124]. Moreover, by being effects solely based on non-equilibrium carrier transport, their study also allows for insights into novel materials such as topological insulators[125], 2D materials[126,127], and magnetocaloric materials[128,129]. These can be key materials for several breakthroughs in, for example, energy harvesting and spintronics[130,131], among others. All these applications and ground-breaking materials research create the need of a reliable, fast and easy to perform measurement of the Seebeck coefficient (thermopower) S, given by $S = -\lim_{\Delta T \to 0} \frac{\Delta V}{\Delta T}$.

[1] Adapted from S. Ferreira-Teixeira, F. Carpinteiro, J. P. Araújo, J. B. Sousa, A. M. Pereira, *Versatile Seebeck and electrical resistivity measurement setup for thin films*, Review of Scientific Instruments, 92.4 (2021): 043904.[9] S. Ferreira-Teixeira contribution to the publication: development of the measurement procedures, and calibration and validation of the measurement setup. Responsible for the main manuscript preparation.

For applications in energy harvesting, the thermoelectric materials are also evaluated by the figure of merit ZT, $ZT = \alpha T/k$, with k the thermal conductivity and α the power factor given by $\alpha = S^2/\rho$, with ρ the resistivity. Thus, the coupling of S and ρ measurements is crucial. Having the power factor, the output power of thermoelectric materials can be assessed without performing the complex measurement of the thermal conductivity[49,132]. Moreover, by combining the measurements of these two transport properties, insights into the band structure of the material can be obtained. By these means, the study of novel exotic materials is attained by measuring these two properties, creating the demand for a simple resistivity and Seebeck coefficient measurement.

However, even though the measurement of the thermopower and of the resistivity seem to be simple processes, obtained by applying a temperature difference or current and measuring the generated voltage, the realisation and production of reliable results is still difficult, especially as a function of temperature for low temperatures[132–138]. Two Seebeck coefficient measurement techniques have been widely studied and explored: the differential and the integral method[139]. In the differential method, several small temperature differences (ΔTs) are applied to the sample and the corresponding thermoelectric voltage is obtained. Usually, this method is employed in a steady-state, where each voltage measurement is only performed after a ΔT stabilisation, which is time consuming for measurements as a function of temperature[140,141]. These measurements can also be performed in a quasi-steady state, without waiting for ΔT to stabilise. In the integral method, one end of the sample is kept at a fixed temperature and the opposite end temperature is varied continuously, with the Seebeck coefficient being calculated from the generated voltage[142].

Most measurements of the Seebeck coefficient and resistivity of a thin film are also achieved by drawing contacts on top of the thin film. This can be achieved either manually[143,144] or by using complex processes, such as lithography[145–148] and wire bonding[135,137,149–151]. By drawing manually, several issues can arise. The size of the contacts is one of the biggest issues for measurements of metallic thin films' resistivities. The use of lithography solves this issue and allows the creation of differential thermocouples and local heaters for a Seebeck coefficient measurement. On the other hand, lithography can also be too time consuming and expensive. Thus, the measurement of these transport properties in thin films is still a challenge.

3.2 Principle and Setup

3.2.1 Measurement apparatus

The measurement apparatus is represented in Figure 3.1.(a). A closed cycle cryostat (APD Cryogenics Inc. system, HC-4 MK1 compressor) with operating temperatures between 10 and 300 K is used. The measurement setup described in the next subsection could also be used in other cryostats and/or ovens with operating temperatures between

5 K and 473.15 K. The sample chamber is evacuated prior to any measurements to a pressure of 9 $\times 10^{-6}$ mbar using an oil diffusion pump backed up by a rotary mechanical pump. At the end of the second stage copper cold head, the homemade sample holder, which contains the measurement setup, can be mounted. Indium foil is used for better thermal contact with the cold head. To this second stage, a Chromel/AuFe thermocouple (TCA) and heater are attached and are connected to a Lakeshore 331 temperature controller, which allows for a PID feedback control loop of the temperature of the second stage and ultimately of the sample holder.

A primary radiation shield, polished to mirror finish both on the inner and outer surfaces, attaches to the second stage copper cold head. A secondary radiation shield is mounted on the first stage of the cold head. All probe wires are twisted around the first and second stages of the cold head and held with Teflon tape, to ensure good thermal anchoring. This electrical feedthrough of the cryostat is connected to all the instrumentation devices via a twisted air round cable.

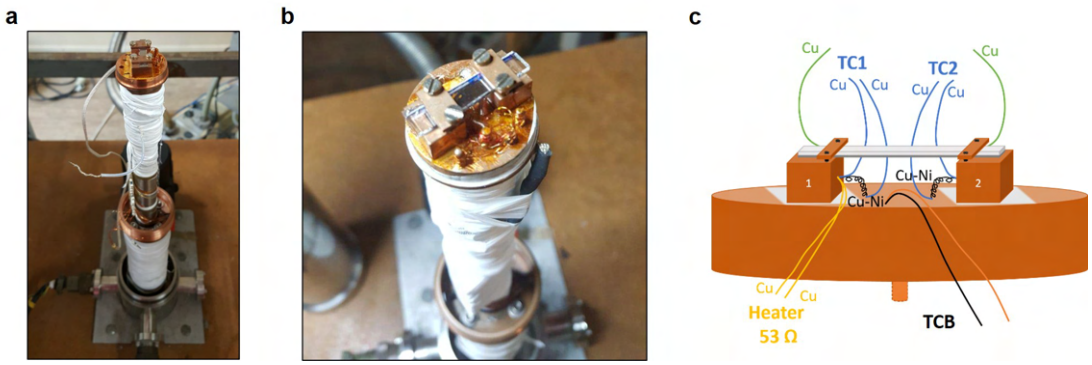


Figure 3.1 – Setup and Sample Holder. (a) A photograph of the sample holder and the setup mounted onto the cryostat without the radiation shields. (b) Detailed photograph of the setup. (c) Sketch of the side view of the setup.

3.2.2 Measurement setup

A digital photograph and sketch of the measurement setup is represented in 3.1.(b), and (c). The measurement setup is mounted on a copper sample holder. In this holder, two copper blocks are assembled on top of GE varnish embedded shroud paper. This guaranties a good thermal contact and at the same time electric insulation. The ΔTs can be generated by Joule heating of a copper (Cu) 53 Ω resistance inside the copper blocks. Two probe wires are coupled to the blocks. One corresponds to the differential thermocouples (Type T) of each block (TC1 and TC2), having as reference the copper sample holder temperature. The other probes (Cu wires), one on each block, measure the voltage generated across the sample and feed the current for resistivity measurements. The sample is placed on top of the two blocks, which hold an empty space of 2.5 $\times$ 0.5 cm, corresponding to the maximum size of a sample to be measured. Two copper bars held together by two screws each are also attached to hold the sample to the

blocks and to ensure the electrical pressured contact of the sample with the probes. A Chromel/AuFe thermocouple (TCB), having 0 ºC as reference, is inserted into the sample holder after its installation in the second stage cold head. It measures the sample holder temperature, which is the blocks and sample temperature if no ΔTs are applied, due to the ensured good thermal contacts.

The voltage across the sample and the differential thermocouple voltage of one block (TC2) is measured by a Keithley 2182 Nanovoltmeter, using Channel 1 and 2, respectively. The differential thermocouple voltage of the other block (TC1) is measured by a Keithley 182 Nanovoltmeter. The thermocouple voltage of the sample holder (TCB) is measured by an Agilent 3458A 8½ Digit Multimeter. The current for generating a temperature difference and for the resistivity measurements is applied using a Time Electronics Current Source 9818. Using an IEEE 488.2 GPIB communication bus, all the instruments interface with a computer, where custom developed NI LabVIEW programs automate the procedures and collect the measurements results.

3.3 Measurement Procedure

The setup described in the previous section allows for the measurement of both the Seebeck coefficient and Electrical Resistivity as a function of temperature in the range [10 – 300] K.

3.3.1 Seebeck coefficient measurement

The Seebeck coefficient is measured in a two-probe arrangement, with the versatility of measuring in a dynamic or a steady and/or quasi-steady differential method.

3.3.1.1 Dynamic measurement

For a faster and reliable Seebeck coefficient measurement, the dynamic method can be used, except in the case of materials with phase transitions. In this method, the temperature of the sample holder is varied at a constant rate of 0.5 K/min, with each thermal cycle lasting 20 hours, and it is monitored by the TCA and TCB thermocouples. A constant current is applied to the heating resistance of Block 1 to establish the ΔT. The temperature of Block 1, which is the temperature of one side of the sample, is measured by the thermocouple TC1. In these conditions, the temperature of Block 2 is kept equal to the temperature of the sample holder (TC2 = TCB) and varied at the same rate. By applying a current, the temperature of Block 1 will always remain higher than TCB. ΔT (equal to the difference between TC1 and TC2) does not remain constant during the measurement, due to the temperature dependence of the thermal conductivity of copper and of the sample. In Figure 3.2, the variation of ΔT as a function of the sample

holder temperature is presented as an example for an applied current of 0.1 A and for a measurement performed with a Specular Spin Valve (SV)[152].

The voltage across the sample and the thermocouple voltages (TC1, TC2, TCA, TCB) are instantaneously acquired at intervals of 2 s. The Seebeck coefficient is instantly calculated to be the measured voltage divided by the instant temperature difference.

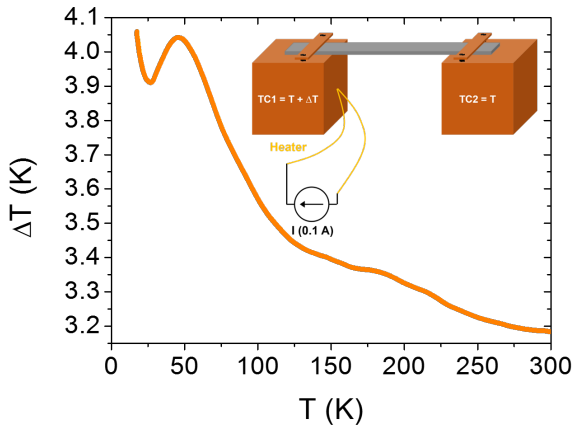


Figure 3.2 – The applied temperature difference ΔT to a specular spin valve (SV) as a function of the sample holder temperature T. The inset shows the generation of ΔT by applying a constant current (0.1 A) to the resistance inside Block 1, changing its temperature TC1 to $T + \Delta T$. The temperature of the Block 2, TC2, is kept equal to T.

3.3.1.2 Quasi-steady differential measurements

Using this setup, quasi-steady differential measurements of the Seebeck coefficient can also be performed. In this method, the sample holder is kept at a constant temperature. Currents are applied to the heater resistance inside the copper block, increasing the temperature of that block while keeping the other block at the same temperature of the sample holder. The voltages and temperatures are simultaneously acquired while the applied current varies. In Figure 3.3.(a) the temperature difference and the generated voltage are represented as a function of time during a quasi-steady measurement of the SV. Figure 3.3.(b) presents the voltage across the SV as a function of ΔT at different temperatures. The Seebeck coefficient is calculated from the slope of the linear dependency of the voltage on the temperature difference, being also represented in Figure 3.3.(b).

3.3.2 Resistivity measurement

The resistivity is measured in a two-probe method. The current is fed through the two probes, with a probe in each Block of Figure 3.1. The generated voltage is measured at the terminals of the probes. If a 4-probe measurement is necessary, an extension can be achieved by wire bonding two additional contacts into the sample. For measurements

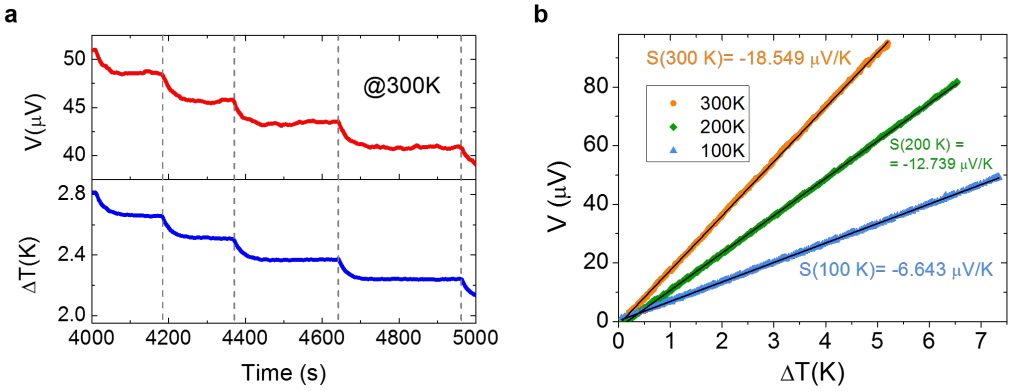


Figure 3.3 – Seebeck coefficient measurements by the quasi-steady differential method. (a) Temperature difference and the generated thermoelectric voltage as a function of time. The voltage change due to a variation of the temperature difference is clearly visible. (b) The Voltage across the sample as a function of the applied temperature difference. The expected linear relationship is observed.

as a function of temperature, a constant current is applied. The current value is decided by considering that the generated power should not be higher than 500 mW and the resistance of the sample. The temperature is varied, either increasingly or decreasingly, at a rate of 0.5 K/min. The value of the voltage and temperature of the sample holder are acquired instantaneously every 2 s, corresponding to roughly acquiring values every 20 mK.

To verify the response of the system, different currents were applied to the SV sample, obtaining the corresponding I-V curves. The measured voltage and the applied current as a function of time are represented in Figure 3.4.(a), showing the linear response of the system, in accordance with Ohm-law. These are represented in Figure 3.4.(b) for different temperatures.

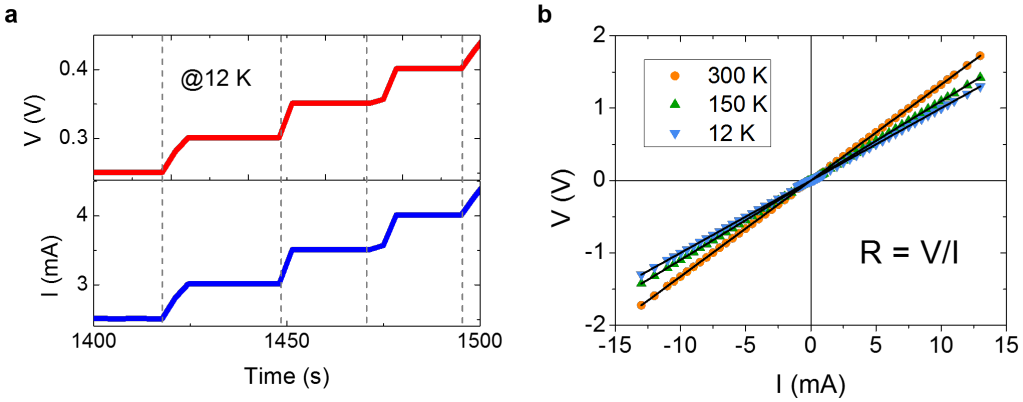


Figure 3.4 – I-V curve resistance measurements. (a) Applied current and measured voltage as a function of time. The voltage change due to a variation of the current is visible. (b) The I-V curve of a specular spin valve, namely the voltage across the sample as a function of the applied current . The expected linear relationship characteristic of an ohmic behaviour is observed.

3.4 Validation of the measurement setup and method

In order to study the reliability and accuracy of the experimental setup, Seebeck measurements were performed, using the dynamical differential method, of commercial niobium foil and of a Specular Spin Valve (SV), previously measured[152,153].

3.4.1 Commercial Niobium foil

The $S(T)$ of the niobium foil (Alfa Aesar, 99.8 - metals basis, annealed) measured utilizing this setup is represented in Figure 3.5.(a), as well as a reference measurement of a polycrystalline rod of niobium (> 99.99) from John Matthey, annealed at 1100ºC[154]. At high temperature (T > 150 K), there is a total overlap between the measured and reference values. By further cooling the sample, the temperature dependence of the Seebeck coefficient follows the same trend, decreasing in magnitude and becoming positive until reaching a maximum of 0.7 μV/K, and then decreasing until it has negative values again. The temperatures at which these behaviours occur for the reference sample are different from the ones obtained with this measurement setup. This can be due to different sample characteristics, namely the purity of the niobium measured[154] or the degree of oxidation in the samples annealed at different temperatures.

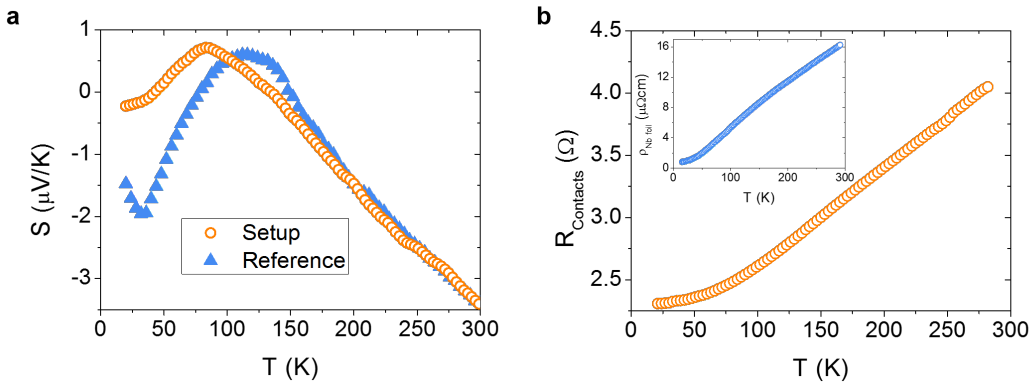


Figure 3.5 – Measurements of the commercial niobium foil and contact resistance of the setup. (a) Seebeck coefficient as a function of temperature of the commercial niobium foil obtained using the above described setup and compared with reference[154]. (b) Contact resistance of the described setup obtained by measuring the resistance of the niobium foil. The inset shows the resistivity of the niobium foil measured with a four-probe method as a function of temperature. The contact resistance was calculated using this measured resistivity.

To characterise the contact resistance of the setup, the niobium foil resistance was measured using the setup and a four-probe arrangement as a function of temperature. From the four-probe measurement, the resistivity ρ_{Nb} of the niobium foil was obtained, and it is shown in the inset of Figure 3.5.(b). The obtained values are in accordance with the expected commercial values. Having obtained the resistivity of the niobium foil, the contact resistance was calculated following equation 3.1, where $R_{Nb@setup}$ corresponds to the resistance of the Niobium foil measured using the setup, R_{Nb} is the resistance of

the niobium foil, *l* is the length between the two contacts of the setup (1.5 cm), and *w* and *t* are the width and thickness of the niobium foil. The obtained contact resistance is thus represented in Figure 3.5.(b) as a function of temperature. A characteristic metallic behaviour is observed, where the resistance decreases with cooling, being 4.04848 Ω at room temperature. This value and the obtained behaviour are in accordance with what is expected for a two-probe method using this type of contacts, namely the resistance of the two copper blocks.

$$R_{contacts} = R_{Nb@setup} - R_{Nb} = R_{Nb@setup} - \rho_{Nb}\frac{l}{wt} \tag{3.1}$$

3.4.2 Specular Spin Valve

The measured $S(T)$ of the Specular Spin Valve is presented in Figure 3.6.(a), normalised to its value at 300 K. A comparison is performed with previous reported results[152]. Both measurements have the same temperature dependence and the Seebeck coefficient values are in accordance with each other, showing that the described setup can be used to obtain precisely the Seebeck coefficient as a function of temperature. The temperature dependence of the resistivity was also obtained using this apparatus. It is represented as a function of temperature in Figure 3.6.(b), normalised to its value at 300 K. Previously reported results are also presented in this figure[153]. Like the Seebeck coefficient, both curves have the same temperature dependence characteristic of metals, with an increase of the resistance with heating, and the values of resistance measured by the setup within a 3% error of the reference values.

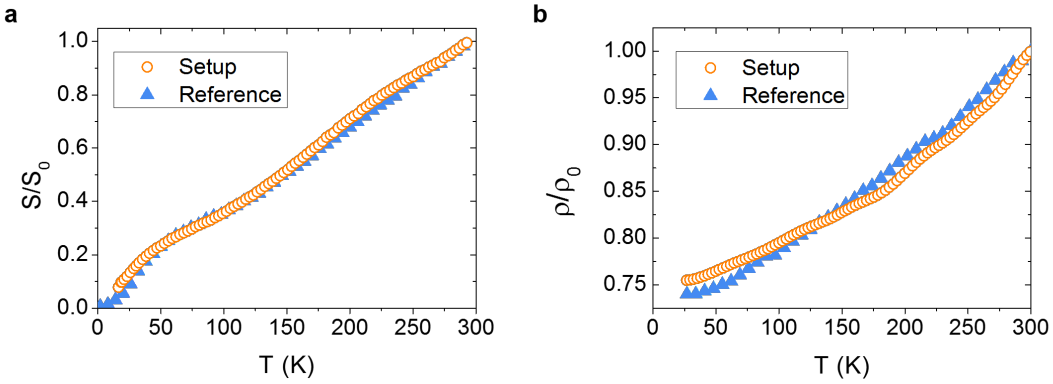


Figure 3.6 – Measurements of the Specular Spin Valve. (a) Seebeck coefficient normalised by its value at $S_0 = S(300\ K)$ as a function of temperature of the Specular spin valve obtained using the above described setup and compared with reference[147], which was measured using manual made electric contacts and a differential method. (b) Resistivity normalised by its value at $\rho_0 = \rho(300\ K)$ as a function of temperature of the Specular spin valve obtained using the above described setup and compared with reference[148], which was measured using a standard 4 linear probe method.

3.5 Conclusion

In this chapter, a setup developed for measurements of the Seebeck coefficient and Resistivity of thin films as a function of temperature between 10 and 300 K was presented. The apparatus and measurement setup were fully described, as well as the different procedures employed to perform the measurements. The Seebeck coefficient is measured using a two-probe arrangement and either a dynamic or steady/quasi-steady differential method, where resistive heaters create the temperature differences. A full measurement between 10 K and 300 K of the Seebeck coefficient is achieved in 10 hours. The Resistivity is obtained using a two-probe arrangement, with a contact resistance between roughly 2 and 4 Ω. The results obtained of commercial (niobium foil) and previously measured material (Specular Spin Valve) have a great agreement (within 3%) with references measured using a more complex and time-consuming measurement technique and setup.

CHAPTER 4

Electronic conduction channels of topological insulator sputtered Sb_2Te_3 thin films

This chapter [1] focuses on the study of the transport properties of sputtered Sb_2Te_3 TI thin films. Sb_2Te_3 belongs to the Bi_2Se_3 family of semiconductors, which was discovered to host the TSS in 2009[52]. It has not been as extensively explored due to its smaller band gap when compared to other members of the Bi_2Se_3 family and distorted TI surface state[155]. As such, unravelling the contributions to conduction remain challenging in this material. By combining magnetoconductance and the Seebeck coefficient, we verify that the conductance channel dominance and carrier type can be controlled by thin film thickness in these nanocrystalline films. Moreover, we show that the TI state survives in all films robustly and independently of film thickness.

4.1 Introduction

Spinorbitronics has emerged in recent years as one of the developments that has the potential to bring widespread uptake of spintronics, for logic and memory[20,156,157]. Spinobitronics is based on the spin to charge inter-conversion, exploiting the high spin-orbit coupling (SOC) of certain non-magnetic materials, such as heavy metals, like Pt, W and Ta[44,158,159], and, more recently, 2D Van der Waals structures, for example Graphene/WS_2. A new class of quantum materials, topological insulators (TIs) exhibit a metallic topological surface state (TSS), hosting spin-momentum locking[46]. By combining the TSS properties with their high SOC, outstanding performances in spin to charge inter-conversion have been achieved[54,67].

The promise offered by TIs for spintronics applications, nonetheless, faces outstanding challenges. The electrical conduction of a TI material presents several parallel chan-

[1] Adapted from S. FerreiraTeixeira, A. Vanstone, A. L. Pires, W. R. Branford, J. P. Araújo, L. F. Cohen and A. M. Pereira, *Electronic conduction channels engineered in topological insulator sputtered Sb_2Te_3 thin films as a function of thickness*, in preparation. S. Ferreira-Teixeira contribution to the publication: fabrication of the samples, structural and morphological analysis, measurement of the resistivity, Seebeck Coefficient, Hall effect and magnetoconductance and data analysis. Responsible for the main manuscript preparation.

nels, including bulk conduction, surface effects, and the TSS. These are hard to disentangle, making it difficult to properly take advantage of the TSS and/or bulk properties. Manipulation of the surface states and control of the dominant conduction channel have been achieved in Bi_2Te_3 [160] and $BiSbTe_3$ [161] using gating. Alternatively, positioning the Fermi level between the bulk conduction and valence bands, in the band gap, has been achieved by controlling the stoichiometry of a TI thin film during MBE growth [72]. Nevertheless, alternative methods to control the conduction channel dominance that neither require external gate control nor highly sophisticated growth methods requiring ultra-high vacuum technology would be desirable for scalable application.

In this chapter, Sb_2Te_3 thin films with thicknesses ranging from 35 to 300 nm were fabricated using ion beam sputtering deposition on glass substrates. Their morphology and structure was inspected using the different microscopy and x-ray techniques, and Raman spectroscopy. The conduction was investigated by measuring the resistivity and Seebeck coefficient of the thin film as a function of temperature. Insights into the electronic and spintronic transport were obtained through magnetotransport measurements at low temperatures, with conduction coming from the TSS being observed.

4.2 Morphology and structure of the sputtered films

4.2.1 Structural characterisation

Figure 4.1 shows the obtained SEM image of the 100 nm Sb_2Te_3 thin film. There is good surface coverage and the thin film is uniform at this magnification. Small defects are observed which correspond to the amorphous glass substrate. The inset shows the EDS spectrum, where elements corresponding to the fused silica glass are visible, as well as the Sb and Te elements. The chemical stoichiometry of these elements was calculated to be near the 2:3, which is the nominal composition of Sb_2Te_3. Thus, during the sputtering process the chemical stoichiometry of the target is preserved. This shows that IBS is able to deposit uniform thin films with the intended stoichiometry over a large area, which is crucial for several device applications.

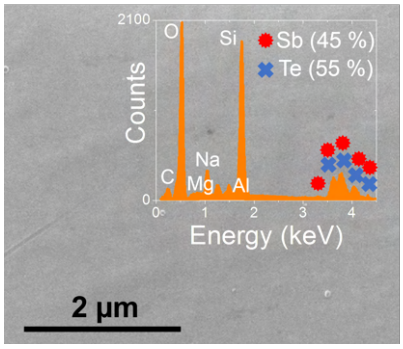


Figure 4.1 – SEM top image of the 100 nm Sb_2Te_3 thin film , with the EDS spectrum of the same film as an inset.

The diffraction pattern from XRD analysis is presented in Figure 4.2. Two reflections are observed at 24.7º and 51.7º in all thin films, which can be indexed by the planes (1 0 2) and (2 0 5), respectively[162]. These correspond to the Sb_2Te_3 phase, with a rhombohedral crystal geometry (R-3m). This shows that the thin films are polycrystalline. The observed broadness of the peaks indicates that the thin films are constituted by small size nanocrystallites (of the order of 10 - 20 nm, from Scherrer analysis). Moreover, there is a broad reflection centred at 26º, which is due to the amorphous glass substrate.

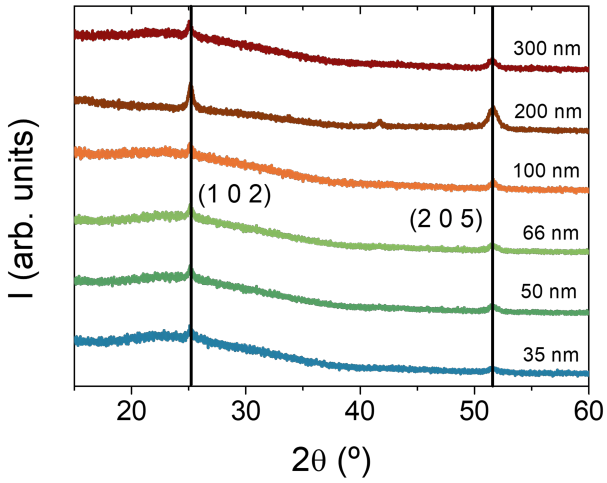


Figure 4.2 – XRD patern of the Sb_2Te_3 thin films with the identified peaks as solid lines.

The Raman spectrum is represented in Figure 4.3 for the films with thicknesses between 35 and 200 nm. There are two optical phonon modes of Sb_2Te_3 active in the range of 100 and 180 cm^{-1}. These are the E_g^2 and A_{1g}^2 modes, at approximately 120 and 165 cm^{-1}, respectively[163]. These two modes can be identified in all the thin films, which corroborates the crystalline structure obtained from XRD and the 2:3 stoichiometry. However, all samples also exhibit a new peak at approximately 140 cm^{-1}. This peak has been previously attributed to a Raman active mode of Te[163,164], having been explained by the existence of segregated particles of Te within a polycrystalline Sb_2Te_3 matrix. In these sputtered films, these particles would be small, since no peaks corresponding to Te are observed in the XRD patterns. The broadness of this Te-Te mode also overlaps with the A_{1g}^2 mode, turning the later into a more broad hump, as it was observed in previously semiconducting Sb_2Te_3 thin films[163]. However, it is noted that the overall peaks are broad, which would signify that there is the presence of defects or amorphisation, which corroborates with the XRD results. These defects could be the aforementioned Te particles and their agglomeration and/or the nanocrystallite grains also expected from the XRD analysis.

High resolution TEM (HRTEM) was also employed to provide insights into the atomic structure. Two samples were analysed by HRTEM, namely the 100 and 35 nm films, with

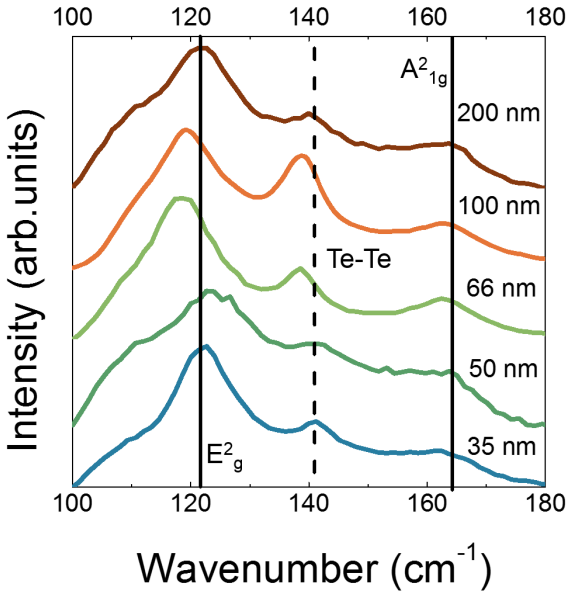


Figure 4.3 – Raman spectra of the Sb_2Te_3 thin films. The Sb_2Te_3 Raman active E^2_g and A^2_{1g} modes are identified as solid lines, and the Te-Te mode as a dashed line.

the bright field images taken in-plane view shown on Figure 4.4.(a) and (b), respectively. Both films show crystalline nanometer sized grains. The films are also revealed to be constituted by two layers, namely a top layer with lighter contrast, of approximate 10 nm thickness in both thin films, and the bottom bulk of the film. The bulk displays large grains that grow along the height of the thin films, with grain thicknesses of up to 80 nm (in the 100 nm thin film) and sizes of 10 – 20 nm, which are in accordance with the XRD Scherrer analysis (10 – 20 nm).

Inverted Fast Fourier Transform (FFT) was performed of the red squared areas of Figure 4.4.(a) and (b). It is depicted as insets of these images and confirms that these grains are crystalline for both thin films. The interatomic distances were calculated to be approximately 3.6 and 1.5 Å, which also correspond to the (1 0 2) and (2 0 5) peaks identified from XRD, respectively. From FFT, it was also possible to verify that these grains, even though they are crystalline, grew along the film thickness but at slightly different small angles. In Figure 4.4.(c), the grains of the region shown in Figure 4.4.(a) of the 100 nm thin film are marked with different colours in accordance with their orientation, with the FFT marked with corresponding-coloured arrows in the inset of Figure 4.4.(a). The space between these grains appears to, however, be amorphous. It is thus displayed that the films are constituted by nanocrystallites of different orientations within an amorphous matrix. Moreover, these grains are also visible within the lighter top layer previously identified, showing that it also has a degree of crystallinity. Despite this, the concentration of these crystallites is smaller within this region.

Elemental maps from EDS analysis were also obtained for the 35 nm thin film. Figure 4.4.(d) depicts one of these maps, showing the distribution of the Sb and Te elements. In Figure 4.5, the normalised quantity of these elements and the Si from the substrate

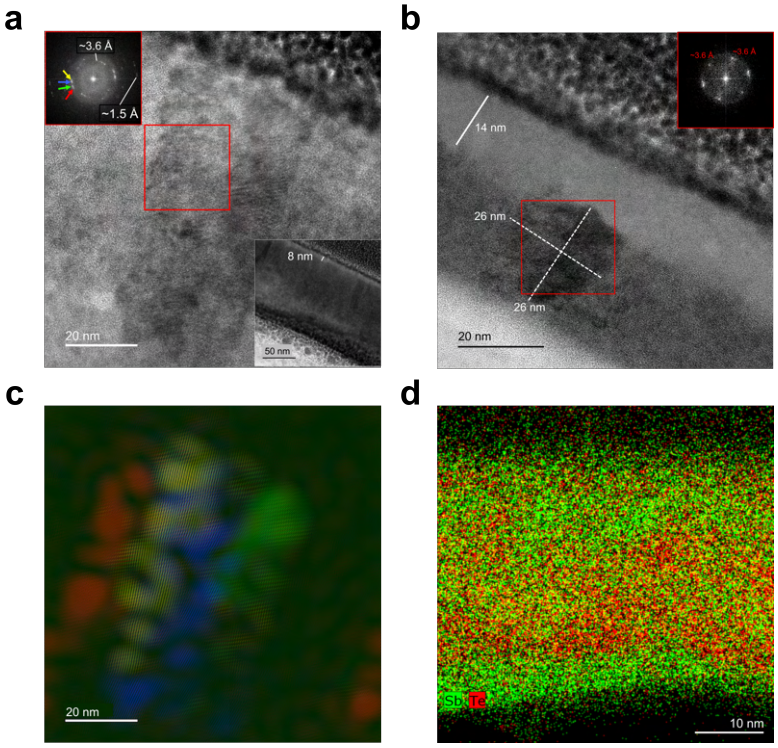


Figure 4.4 – HRTEM analysis of the nanostructure of the Sb_2Te_3 thin films. (a) and (b) HRTEM cross section images of the 100 and 35 nm thin films, respectively. Both have as an inset the FFT analysis of the red squared area with the corresponding identified interatomic distances, which match with the two peaks identified in the XRD. (a) has a zoomed-out image of the 100 nm film as an inset, where a more amorphous surface layer is observed. (b) also shows the size of one of the grains as well as the measured thickness of the surface layer. The nanocrystalline grains of the 100 nm thin film area shown in (a) are highlighted in colour in (c), with the colours corresponding to slightly different growth orientations, also marked as arrows in the FFT analysis in (a). (d) shows an elemental map of Sb and Te of the 35 nm obtained by EDS. A region richer in Sb is noticed at the bottom of the film.

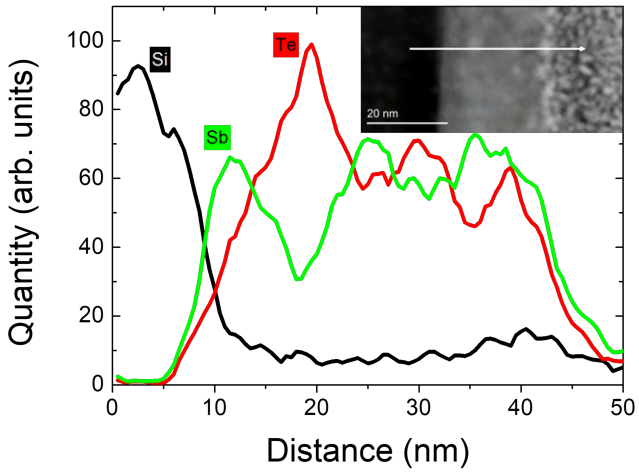


Figure 4.5 – Quantity of Sb, Te and Si obtained through the EDS line scan of the 35 nm thin film shown in the inset. The Si corresponds to the glass substrate. There is a higher concentration of Sb at the bottom of the film in contact with substrate. A region with a higher concentration of Te is also visible, corresponding to the a lighter area region shown in the inset.

is shown along a line scan of the same film. These results demonstrate that there is an accumulation of Sb at the bottom of the film, in contact with the substrate, and that the remainder of the film has a roughly uniform distribution of these elements, with small regions richer in Te. Since the overall EDS results show the presence of these two elements in the 2:3 stoichiometry, this distribution within the film can be explained considering the deposition technique. During the sputtering process, due to the higher vapour pressure of Te comparing with Sb, there is diffusion of the Te deposited on the first film layers through the rest of the film due to the impact of the highly energetic material, leaving the bottom layers depleted of Te, as it is seen in Figure 4.5.(d). This extra Te is thus dispersed in the rest of the film during the deposition, which explains the identified Te-Te vibration mode in the Raman spectra.

4.2.2 Morphological characterisation

The morphology of the sputtered thin films was also analysed, since for a wide range of applications, especially microelectronics, these materials need to be fabricated within several nanostructures, such as thin film stacks, and thus good uniformity and thickness control are of the utmost importance.

An analysis of the uniformity of the the 100 nm thin film was carried out by AFM. The AFM image shown in Figure 4.6.(a) confirms the uniformity of the thin film as it was noted in the SEM image. The root-mean-square (r.m.s.) roughness was calculated to be of ~0.8 nm over a 2×2 μm scanned region. A glass substrate was also analysed, having yelded a r.m.s. roughness of 1 nm over the same size region. The thickness was also inspected by cross-section SEM image of the 100 nm thin film, which is presented in Figure 4.6.(a). The thickness was calculated, revealing a value of 100 ± 5 nm, which is the intended value.

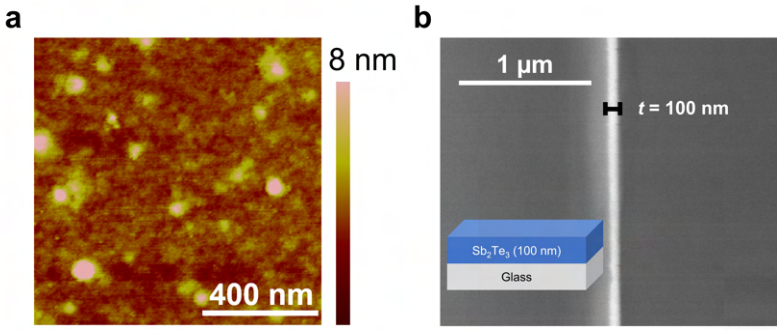


Figure 4.6 – (a) AFM and (b) SEM cross section images of the Sb_2Te_3 100 nm thin film. The calculated thickness from SEM is shown.

XRR was employed to calculate the thickness of the different samples. The results are shown in Figure 4.7, for the 35 to 100 nm thin films. The Fresnel reflectivity decrease is seen as well as the Kiessig fringes, which demonstrates the thickness uniformity of the thin films, corroborating the SEM and AFM results. The periodicity of the fringes

is reduced with the increase in thickness of the films, with the inset on Figure 4.7.(d) showing a zoom into the smaller fringes of the 100 nm film. The angles of the fringes were measured, and the thicknesses were calculated following equation 2.3., with the insets of each panel of Figure 4.7 showing this linear analysis. From the linear fits, the thickness were calculated to be 35.1 ± 0.2 nm, 51.8 ± 0.4 nm, 66.6 ± 0.6 nm, and 98.3 ± 0.2 nm. These thicknesses are in accordance with the expected deposited values, and the 100 nm thin film calculation is in accordance with the SEM cross-section value. Thus, uniform thin films of Sb_2Te_3 can be sputtered over a large area with precise control of their thickness.

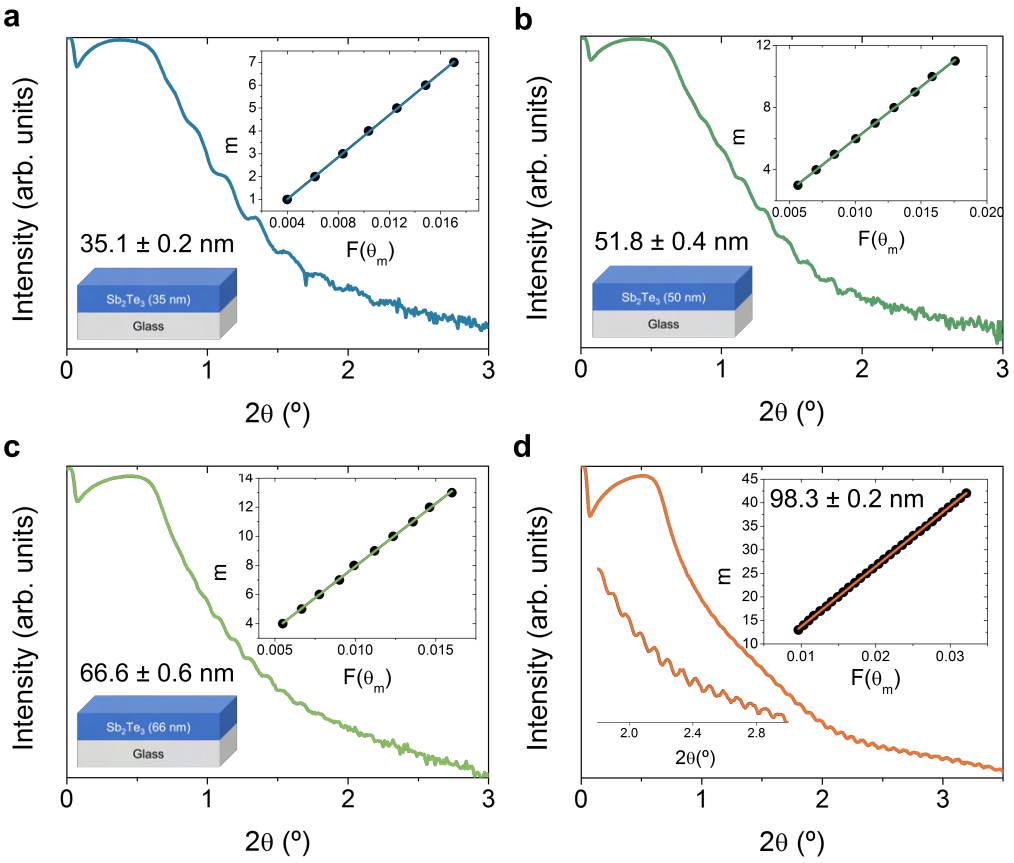


Figure 4.7 – XRR patterns of the Sb_2Te_3 thin films: (a) ST(35), (b) ST(50), (c) ST(66) and (d) ST(100). The insets show the linear analysis of the fringes' order to equation 2.3, used to calculate the thicknesses, which are also shown. (d) also has as an inset a zoom into the Kiessig fringes.

4.3 Electronic transport properties

The resistivity ρ as a function of temperature is represented in Figure 4.8.(a), displaying a semiconductor-like behaviour. The resistivity ρ increases with cooling for all thin film thicknesses, being between 0.072 and 2.03 Ωcm at 300 K and between 2.39 and 183.49 Ωc at 15 K.

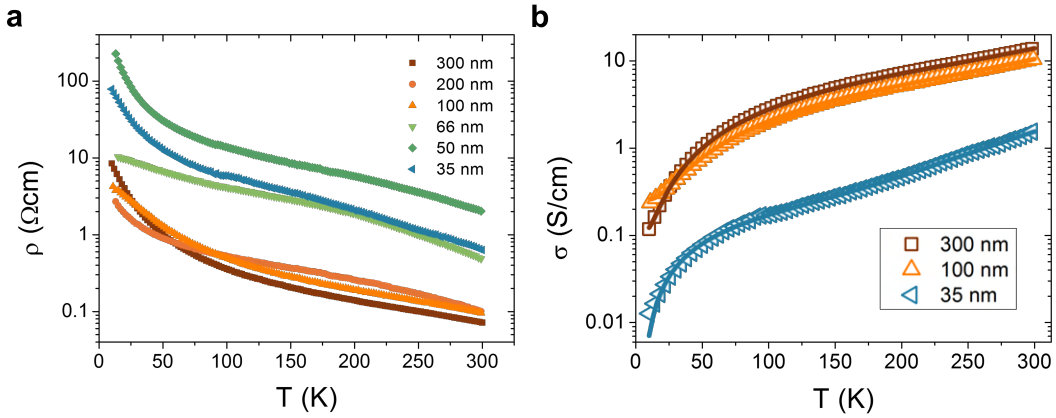


Figure 4.8 – (a) Resistivity as a function of temperature of the Sb_2Te_3 thin films. (b) Conductivity of the 300, 100 and 35 nm thin films, with the fits to equation 4.1 as solid lines.

Another useful transport property to disentangle the different conduction contributions in topological insulators, especially in the absence of magnetic fields, is the Seebeck coefficient (S)[58,59], which was measured as a function of temperature and is displayed in Figure 4.9.(a). S is positive for all the thin films at room temperature, with values ranging from 38 μV/K to 125 μV/K, similar to previously reported values for Sb_2Te_3 thin films[148] and as expected for undoped Sb_2Te_3. As the temperature decreases, S starts to decrease in the thinner films, eventually changing sign. S reaches very high absolute values at the lowest temperatures for the thinnest films. From these results, the temperature at which the change from positive to negative S occurs (T_{pn}) can be identified. T_{pn} decreases with the increase in film thickness, being close to room temperature, 264 K, for the 35 nm thin film, and 80 K for the 100 nm thin film. For the 200 nm thin film, S is always positive within the range of temperatures studied, as it is found in the bulk[163].

Figure 4.9.(b) shows the absolute values of S as a function of the temperature normalised to the T_{pn} of each thin film. The behaviour of $|S|$ with the normalised temperature is approximately the same for the different thin films. This indicates that the transport properties characteristics are common to all films. They have a combination of n-type and p-type conduction, with a thickness controlled T_{pn} value. Thus, by changing the thickness of these sputtered thin films, it is possible to change the type of dominant conduction, from p-type to n-type. This is explained by considering the structure of the thin films revealed by HRTEM. The surface layer has a roughly constant thickness for the different films, being independent of the thickness of the whole film. Moreover, the bulk layer is richer in Sb than the rest of the film. Thus, the different films have the same conduction mechanisms coming from both their bulk and surface layer, with a contribution that depends on the ratio between the n-type surface layer versus the p-type bulk. Thus, by changing the thickness of these sputtered thin films, we can control the input into the overall conduction coming from the surface layer versus the bulk, and, as such,

the overall type of dominant conduction at a certain temperature, either p-type or n-type, due to the manipulations of the T_{pn} value.

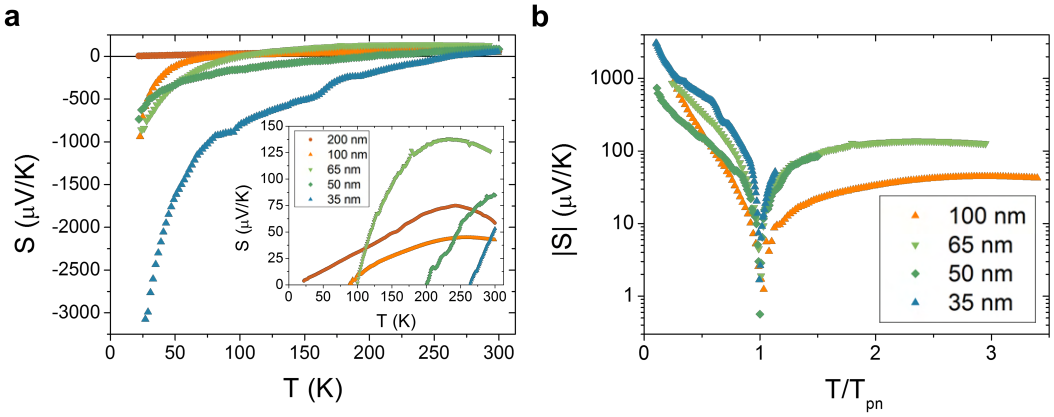


Figure 4.9 – (a) The Seebeck coefficient as a function of temperature of the Sb_2Te_3 thin films, with a zoom into the positive coefficient temperature ranges as an inset. (b) The absolute value of the Seebeck coefficient as a function of the temperature normalised to T_{pn}.

Inspecting these two coefficients, the trend of the conduction with thickness and as a function of temperature of these sputtered thin films, although semiconductor-like, is complex and could not be described with a simple activation energy semiconductor law. Moreover, it cannot be described by other used models, such as variable range hopping[165]. A change in the majority charge carrier is also seen on the Seebeck coefficient, reinforcing the degree of complexity of the electrical transport. Two-layer conduction models have been employed to explain qualitatively other topological insulators[59,166,167]. As such, considering the structure of the thin film in two layers, a two-channel model of semiconductor conductivity was employed to fit the data: a surface term, which corresponds to a n-type semiconductor, and a bulk term being a p-type semiconductor, both conducting in parallel. This difference in the type of conduction can be explained by considering the concentration of Sb at the bottom of the film, which would act as an acceptor. Equation 4.1 can be used to fit the data, where ΔE_S and ΔE_B are the surface and bulk activation energies, respectively, a_S and a_B are the exponents, which are close to 1.5 and arise from the effective density of states function for an intrinsic semiconductor, and A_S an A_B, constants. All the conductivities curves were fitted to this equation and in Figure 4.8.(b), the fits to the 35, 100 and 300 nm thin films can be found. Figure 4.10.(a) depicts the model used, where the thin film can be divided into three sections that conduct in parallel: a bulk section, with the Fermi level closer to the bulk valence bands (BVB) of Sb_2Te_3, a surface section which has the Fermi level much closer to the bulk conduction band (BCB) and the expected TSS of Sb_2Te_3. Thus, by increasing the thickness of the thin films, there is more contribution from the bulk and thus the conduction is dominated by the p-type state, which has a Fermi level closer to the BVB. In equation 4.1 no contributions from the TSS were added, since at this range of temperatures, no contributions consistent with a TSS could be observed.

$$\sigma = A_S (k_B T)^{a_S} \exp\left(-\frac{\Delta E_S}{k_B T}\right) + A_B (k_B T)^{a_B} \exp\left(-\frac{\Delta E_B}{k_B T}\right) + \sigma_0 \quad (4.1)$$

In Figure 4.10.(b), the conductivity and Seebeck coefficient analysis are combined, with the temperature T_{pn} being plotted as a function of the surface activation energy ΔE_S. A correlation between these two parameters is observed, with the T_{pn} decreasing with an increase in ΔE_S. For the 35 nm thin film, which shows the highest T_{pn}, the surface activation energy is 48 ± 6 meV, increasing to 147 ± 3 for the 100 meV, with a T_{pn} equal to 80 K. This indicates that by reducing the thickness of the thin film, the energy required to activate the surface conduction is lowered and thus the n-type conduction is more dominant within the studied temperature range, which is in accordance with the two-layer structure of the films.

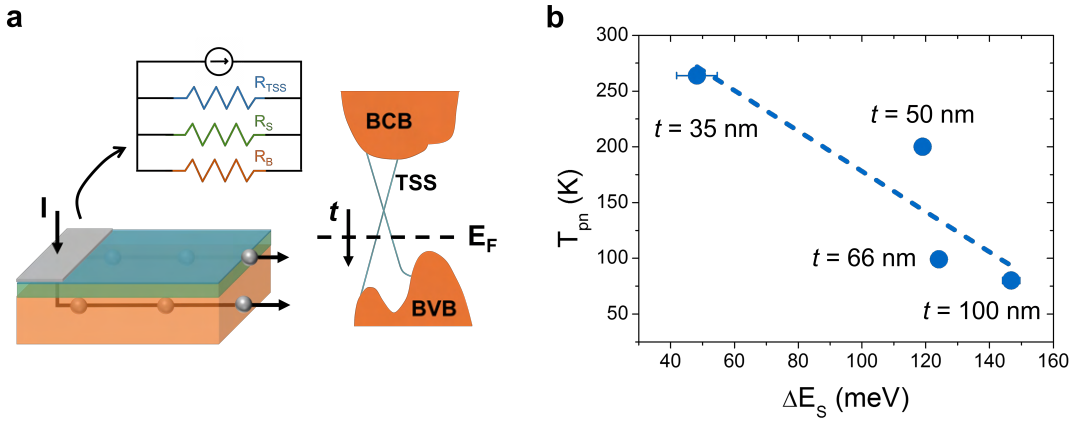


Figure 4.10 – The electronic conduction of the Sb_2Te_3 thin films. (a) Schematic representation of the surface and bulk conduction model used, with the three resistances conducting in parallel, and where the surface has n-type conduction, and the bulk has p-type conduction, with the type of conduction becoming more p-type with an increase in thickness. (b) The temperature at which the Seebeck Coefficient changes from positive to negative values, T_{pn}, as a function of the surface activation energy ΔE_S obtained from the conductivity fits to equation 4.1.

These results demonstrate that the interplay between the different types of conduction can be controlled by changing the thickness of the sputtered thin films without having to resource to gate voltages or doping, having achieved a p-type thin film at all the studied temperatures (200 nm) or a n-type thin film at almost room temperature. Moreover, the resistivity values are high when compared to similar TIs, even at high temperatures, which are needed for applications such as the proposed MESO device[8].

4.4 Magnetotransport

Magnetotransport measurements were carried out to further investigate the electronic and also spintronics transport properties of the Sb_2Te_3 thin films.

4.4.1 Hall effect

The Hall coefficient of the ST(100) sample measured at 1 T as a function of temperature is presented in Figure 4.11. It remains constant and positive from 300 K until approximately 100 K, when it starts to decrease, and then becoming negative at 30 K. Two regimes can then be identified. For temperatures higher than 100 K, the thin film behaves as p-type doped semiconductor with a constant acceptor sheet density of 2.15×10^{10} cm^{-2}. For temperatures lower than 100 K, the hole density starts to decrease, and the majority carriers are electrons. Below 30 K, the Hall coefficient is purely negative and increases in magnitude, as the temperature is lowered. This behaviour is consistent with the Seebeck coefficient shown in Figure 4.9. The change in sign of the Hall coefficient in this type of materials has previously been explained by a parallel conduction model of a VHR-Mott bulk insulator component and a metallic[166]. It has also been observed in $(Bi_xSb_{1-x)2}Te_3$ (BST) and $(Bi_xSb_{1-x)2}(Te_xSe_{1-x)3}$ (BSTS) and attributed[167,168] to the ageing of the sample when exposed to atmosphere which causes the surface to be doped with electrons. This is consistent with our model proposed in the previous section, schematically represented in Figure 4.10.(a).

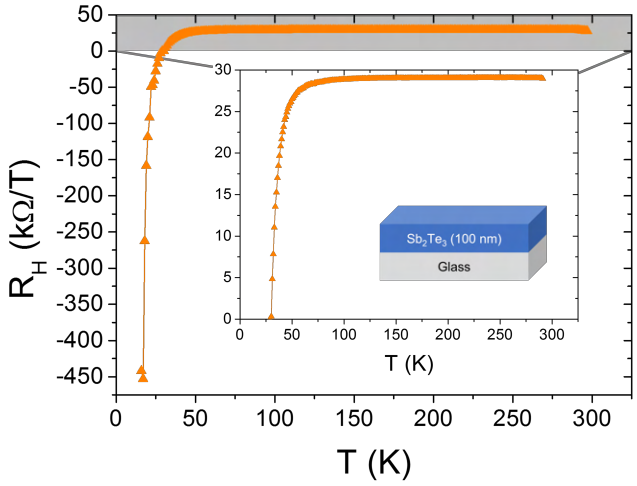


Figure 4.11 – Hall resistivity of Sb_2Te_3 100 nm thin film as a function of temperature. A zoom into the higher temperature positive resistance is shown.

4.4.2 Magnetoconductance

Figure 4.12.(a) shows the magnetoconductance $\left(\frac{\Delta G(B)}{G(0T)} = \frac{G(B)}{G(0T)} - 1\right)$ as a function of applied perpendicular magnetic field of the 100 nm thin film. All measured temperatures have a similar behaviour. At low magnetic fields, ΔG is negative, showing Weak Antilocalisation (WAL) effect cusps, and decreases until a certain applied field. For higher fields, ΔG starts to increase and, for temperatures in the range [2 – 5] K, becomes positive.

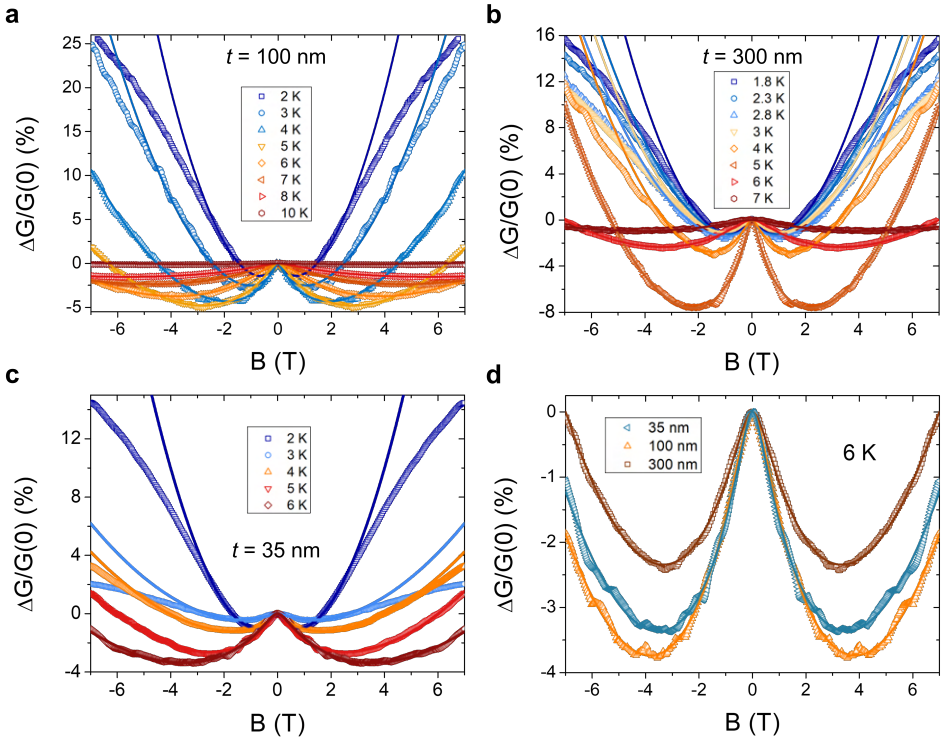


Figure 4.12 – Magnetoconductance of the Sb_2Te_3 thin films as a function of the out of plane applied magnetic field for temperature in the range of 1.8 and 10 K: (a) ST(100), (b) ST(300) and (c) ST(35). The fits to equation 4.2 are shown as solid lines. (d) Magnetoconductance at 6 K, for the 35, 100 and 300 nm films studied, with the corresponding magnetoconductance fits as solid lines.

In materials with high SOC, the magnetoconductance ΔG can be described by the Hikami-Larkin-Nagaoka (HLN) model, describing the WAL effect, combined with a quadratic background term due to scattering[61], which are presented in equation 4.2:

$$\Delta G(B) = -\alpha \frac{e^2}{\pi h} \left[\psi \left(\frac{1}{2} + \frac{\hbar}{4eL_\phi^2} \frac{1}{B} \right) - \ln \left(\frac{\hbar}{4eL_\phi^2} \frac{1}{B} \right) \right] + \beta B^2 \tag{4.2}$$

ψ is the digamma function and L_ϕ is the phase coherence length, which characterises the mesoscopic electron interference, with e the electron charge, h the Planck constant and ħ the reduced Planck constant. The constant α describes the number of coherent conduction channels present and it is 0.5 when a single 2D surface state exists on a thin film (symplectic case) or 1 for a thin film with top and bottom 2D surface states (orthogonal case)[169]. α becomes 0 if the coherent conduction channels are non-existing (unitary case). β is the quadratic term coefficient that can be due to scattering and have a classical and quantum contribution[61].

The experimental data was fitted to this model, and the obtained fits are represented as full lines in Figure 4.12.(a) for ST(100), (b) for ST(300) and (c) for ST(35) for all the studied temperatures. Figure 4.12.(d) shows the magnetoconductance of the 35, 100 and 300 nm thin films at 6 K, with the corresponding fits as solid lines. The three different thicknesses thin films have a similar behaviour, with the WAL cusp evident at low magnetic fields and the quadratic component being dominant at higher magnetic fields. The 100 nm and 35 nm thin films have similar WAL cusp magnitudes, whereas the 300 nm thin film has a smaller WAL cusp.

The magnetoconductance parameters, α, L_ϕ and β were obtained from the fits. The temperature dependence of the α parameter is shown in Figure 4.13.(a). At the lowest temperature, values close to 0.5 are obtained for the 35 and 100 nm thin films indicative of the existence of a 2D surface state conduction channel coupled to bulk conduction, where the electrons scatter off the surface channel into the bulk, creating an effective conduction channel, corresponding to a symplectic case following time-reversal symmetry[61,169]. The α parameter decays exponentially for the 100 nm thin film as the film is warmed, whereas the 35 nm thin film α value remain roughly constant. This situation is also similar to the temperature dependence of the electrical resistivity and Seebeck coefficient. Here, parallel conduction between a bulk channel and a surface channel takes place, as illustrated schematically in Figure 4.10. These measurements combined suggest a scenario whereby in these polycrystalline Sb_2Te_3 thin films, three different types of conduction are present: a 2D surface state, a n-type surface conduction and a p-type bulk conduction channel. The α values are also consistent with previous descriptions of Sb_2Te_3 thin films, with values of 0.6 and 0.01 being obtained and its temperature dependences being influenced by transport disorder caused by the granular nature of the thin films[170,171]. For the 300 nm thin film, the behaviour is different. The α values are small, indicating that the coherent conduction of the 2D state on the surface is overshadowed by the bulk and surface semiconductor conduction. However, above 5 K,

an exponential decay also starts to appear, similar to the behaviour of the 100 nm thin film. This demonstrates that the coupling of the surface and bulk conductions is more prominent in the thicker films, with the bulk overpowering the conduction.

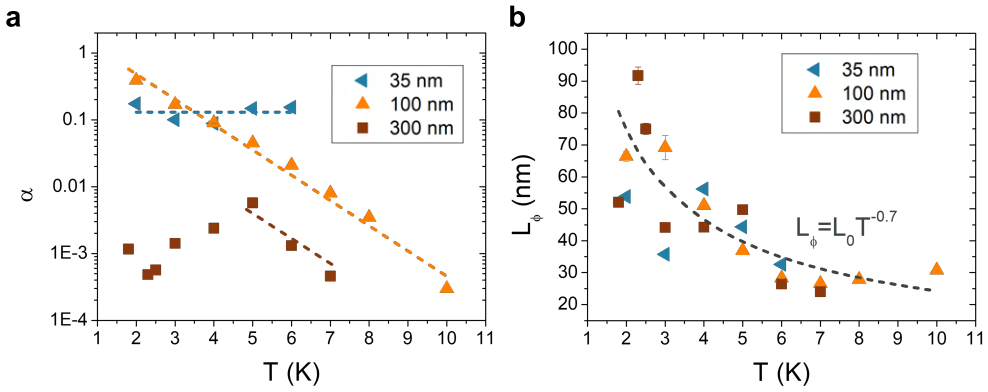


Figure 4.13 – Magnetoconductance WAL parameters of the Sb_2Te_3 thin films. (a) α parameter, which describes the number of coherent conduction channels on the thin films surface, as a function of temperature for the 35, 100 and 300 nm thin films. (b) Phase coherence length L_ϕ of the three studied thin films as a function of temperature, with the power law describing the temperature dependence as a dashed line.

Concerning the coherence length L_ϕ, represented in Figure 4.13.(b), values between 62 and 90 nm are obtained around 2 K for all the films. With heating, the coherence length decreases to values between 25 nm to 35 nm, following a temperature power law of $T^{-0.7}$. The coherence length presents the same behaviour for the three different thickness thin films, which shows that this is independent of the thin film thickness, as expected for the WAL effect due to a TSS. On the other hand, the obtained values are smaller than previously reported, with values of 400 nm presented for a MBE fabricated 21 nm thick thin film, for example[172]. However, recently, it has been verified that nanocrystallinity reduces the coherence length, with values between 20 and 80 nm being reported for granular[171] and nanocrystalline films[170] at temperatures close to 2 K, consistent with our obtained values. Moreover, the obtained power law is similar to previously reported behaviours for Sb_2Te_3 thin films and similar TIs[57,168,170,172] and it is consistent with an expected predominant electron-electron scattering in 2D weakly disordered systems as it is the case for the expected 2D TI surface state. The TSS is thus coupled to the p-type bulk and n-type surface conduction channels. The WAL cusps coming from the TSS are observed at these low temperatures due to the freezing of the other mechanisms, thus dominating the conduction.

Figure 4.14.(a) shows the quadratic parameter β as a percentage for all the studied thin films, as a function of temperature. All the thin films follow a similar temperature dependence, namely an exponential decay with heating, with values around 1 %/T^2 around 2 K and 0.003 % /T^2 at 10 K. Moreover, the values are similar for the different thin films, which demonstrate that the effect is independent of the thickness and of the same nature for all the studied thin films.

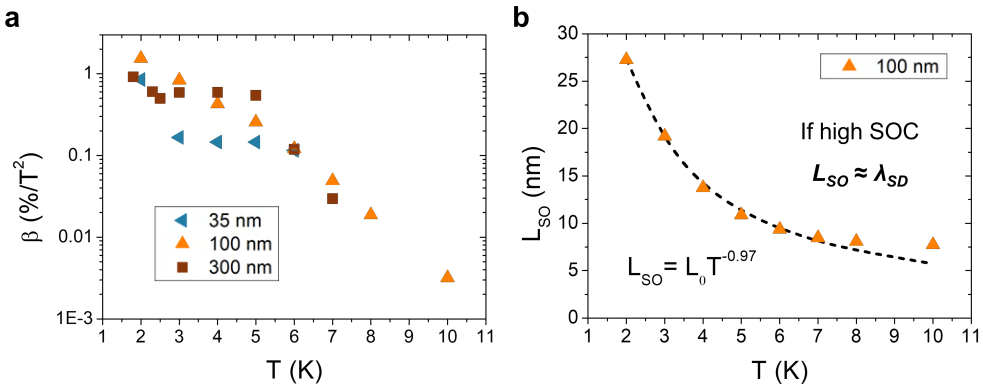


Figure 4.14 – Magnetoconductance parameters a) quadratic component β as a function of temperature for the 35, 100 and 300 nm thin films. b) Spin-orbit relaxation length L_{SO} of the three studied thin films as a function of temperature, with the power law describing the temperature dependence as a dashed line. If the material has a high spin orbit coupling (SOC), the spin-orbit relaxation length is a good approximation of the spin diffusion length λ_{SD}.

The nature of this quadratic component, as previously mentioned, can be due to scattering, with β having a classical and quantum contribution[61]. It can thus be given by equation 4.3. The classical cyclotronic contribution depends on the Hall mobility μ_H and on the conductance at zero magnetic field $G(0)$. The quantum part, originating from spin-orbit and elastic scattering, depends on the magnetic fields B_{SO} and B_e, which are given by $B_{SO} = \frac{\hbar}{4eL_{SO}^2}$, where L_{SO} is the spin-orbit relaxation length, and by $B_e = \frac{\hbar}{4eL_e^2}$, where L_e is the electron mean free path, being approximately 10 nm for the Sb_2Te_3 family of semiconductors[61].

$$\beta = -\mu_H^2 G(0) - \frac{e^2}{24\pi h}\left[\frac{1}{B_{SO}+B_e}\right]^2 + \frac{3e^2}{48\pi h}\left[\frac{1}{(4/3)B_{SO}+B_\phi}\right]^2 \qquad (4.3)$$

From this equation, it is thus possible to calculate the spin-orbit relaxation length. This calculation was performed for only the 100 nm thin film, since the Hall mobility could only be calculated for this sample. The results are shown in Figure 4.14.(b). It is 27.3 ± 0.1 nm at 2 K, decreasing with temperature until 7.736 ± 0.004 nm at 10 K. A temperature power law was fitted to the data, and the fit can be seen as a dashed line in Figure 4.14.(b). It is verified that the L_{SO} is proportional to $T^{-0.97}$ within this range of low temperatures, which is indicative of spin relaxation by lattice scattering via spin-orbit coupling[173]. This relaxation length, in materials where the predominant source of spin scattering is the spin-orbit coupling, can be taken as a good approximation of the spin diffusion length λ_{SD}[61,174].

4.5 Conclusion

The transport properties of the Sb_2Te_3 ion beam sputtered thin films show the presence of the 2D TI surface state and exotic temperature and thickness dependences that can

be exploited. The thin film conduction can be subdivided into three types of conduction: a bulk p-type semiconductor, a surface n-type semiconductor layer and a 2D TI surface state conduction. Usually, to control the type of conduction, gate voltages are used, or the stoichiometry of the thin films must be controlled precisely. However, for these sputtered thin films, the interplay between these types of conduction channels can be controlled by film thickness, achieving a p-type thin film at all the studied temperatures (200 nm) representative of the bulk or a n-type thin film where the surface layer dominates in thin films, existing almost to room temperature (35 nm). Besides this interplay, the magnetoconductance shows the evidence of the 2D TI state. The trademark WAL cusps are visible in all thin films due to the TSS presence and dominance at lower temperatures.

Moreover, when fabricated as a thin film, this family of materials are either epitaxial and have very high conductivity values, which decrease with heating, or are amorphous-like, with variable range hopping conduction and at lower temperatures the TI surface state conduction. In contrast, the nanocrystalline sputtered thin films studied here, show semiconductor electrical conduction dominated by activation energies, with high resistivity values even at high temperatures, and the presence of the TI surface states. Thus, even though the conduction of this sputtered Sb_2Te_3 thin films is complex, the TI surface states are robust, paving the way for a wide range of technological applications requiring a protected surface topological state using large area, scalable deposition methods.

CHAPTER 5

Thermo-magneto-electric properties of sputtered ferromagnetic/topological insulator bilayers

This chapter [1] is dedicated to the analysis of ion beam sputtered FM/TI bilayers. These nanostructures are made of permalloy (Py), which is a FM material widely used in spintronics, and Sb_2Te_3. The structural and morphological properties of these bilayers are analysed via x-ray diffraction and reflectometry, showing the uniformity of the film layers and the conservation of the structure of each material when fabricated as bilayers. Through the transport properties, namely electrical resistance and Seebeck coefficient, a conduction model explaining the shunting effect in these bilayers is proposed. This model is further confirmed through the magnetoresistance of the bilayers, which at low temperatures shows the magnetoresistance effects coming from the TSS of Sb_2Te_3. From ferromagnetic resonance (FMR) measurements, the magnetisation dynamics of these bilayers is compared with the Py dynamics and an increase in the Gilbert damping is noticed, which considering the structural properties of the bilayers, can be explained by spin pumping occurring into the TI layer.

5.1 Introduction

Spintronics, aims to be one of the fields that answers the current technological demands, by offering innovative devices that outperform the classical semiconductor electronics on the scaling, power consumption and data processing speed[20]. One way the spin and charge can be controlled is through the spin to charge interconversion (SCI), which can be achieved by taking advantage of the strong Spin Orbit Coupling (SOC) of certain materials. Due to this, a sub-field called Spinorbitronics has recently emerged, devoted to the study and development of materials and devices based onthe SCI[156,157]. Several

[1] Adapted from S. Ferreira-Teixeira, A. L. Pires, S. A. Bunyaev, W. R. Branford, J. P. Araújo, G. N. Kakazei, L. F. Cohen and A. M. Pereira, *Insights into the thermoelectric conduction and magnetisation dynamics of sputtered ferromagnetic/topological insulator bilayers*, in preparation. S. Ferreira-Teixeira contribution to the publication: fabrication of the samples, structural and morphological analysis, measurement of the resistivity, Seebeck Coefficient, and magnetoconductance and data analysis. Responsible for the main manuscript preparation.

advancements have been made, namely in the progress of data storage via non-volatile magnetic memories[159,175], and logic devices, such as the MESO device recently proposed[8]. At the basis of an SCI device is the SCI element, which in its most basic form is a bilayer of a ferromagnetic (FM) material and a SOC material. As such, the study of this element is key for the development of innovative devices.

Research into SOC materials is at the basis of improving the SCI element. The prototypical SOC materials are the Heavy metals (HM), having been widely explored and used, namely Pt, W and Ta[44,158,159]. However, Topological Insulators (TIs) have recently gathered attention due to their unique properties[130,176]. Being insulating in their bulk, they host protected metallic surface states (TSS) that exhibit spin-momentum locking[177]. The combination of the TSS with their high SOC have led to outstanding highly efficient SCI[54,67–69], based on either the Spin Hall Effect (SHE) and/or the Edelstein Effect introduced in Chapter 1. Thus, the improvement of SCI elements constituted by TIs is driving forward the development of novel devices.

Nonetheless, challenges still exist in the creation of FM/TI structures. Several issues regarding the interface of the two materials have arisen, because they can damage the flow of charge and/or spin currents. For example, the existence of magnetic dead layers[178,179] and intermetallic alloying[180] can reduce the spin transparency of the interface. This is harmful for the SCI, since the created or converted spin currents are not able to flow from one layer to the other, which blocks the practical and efficient application of SCI in the above mentioned data storage and logic devices. To prevent this issue, the interface could be engineered, with this approach having been followed by several groups. Bonell *et. al*[181] introduced a spacer layer of several non magnetic (NM) materials, such as Al, Ag and Te, and not only verified that material intermixing is reduced but that there is a dramatic enhancement of the field-like torque created by the TI acting on the magnetisation of the FM layer, which can be explained by the suppression of spin memory loss. Another approach is by *in situ* deposition, where there is no vacuum break between the deposition of each layer. This is achieved by using the same fabrication system for both layers or having an interlocked system. Bi_2Se_3/Fe bilayers have been fabricated using a single MBE system[182], with a enhanced SOT efficiency and large spin mixing conductance being obtained, which was attributed to a thinner interfacial layer when compared to *ex situ* fabrication, enhancing the spin transparency of the interface.

Another challenge stems from the mismatch of the electrical resistance of the FM and TI materials. As mentioned above, TIs are insulating or semiconducting materials, having resistivity values orders of magnitude higher than the usual FM materials. Due to this, shunting is expected to occur in the bilayer systems[183,184]. However, the shunting effects in the electronic and spintronic properties of the FM/TI systems and their SCI are not yet fully understood and described. With TIs offering great promising for SCI applications, the complete understanding and solution of these issues is critical for the creation of efficient devices based on TIs.

To explore and disentangle these effects, ion beam sputtered FM/TI bilayers are inspected in this chapter. The fabrication is performed *in situ* using the same IBS system and without breaking vacuum between the deposition of each layer, which is expected to improve the interface between the two materials. The structure and morphology of the bilayer systems are examined. Moreover, the electronic properties were explored, with a shunting model of the conduction being proposed, explaining how the charge carriers flow in these nanostructures. The magnetisation dynamics was then probed at room temperature, to analyse the flow of the generated spin current.

5.2 Morphological and Structural Properties of the FM/TI bilayers

Figure 5.1 shows the cross-section SEM images of the bilayers. For the Py(50)/ST(50) and Py(100)/ST(100) samples, each layer of the structures can be identified, having a smooth interface within the measurement capabilities of SEM. The thicknesses were obtained, being 48 ± 5 and 55 ± 5 nm for the Py and ST layer, respectively, for the Py(50)/ST(50) sample. They were 91 ± 5 and 95 ± 5 nm for the Py and ST layer, respectively, of the Py(100)/ST(100) samples. These are the nominal values within the uncertainty. The images also show that each layer is uniform, leading to a good uniformity of the overall bilayers. For the remaining samples, with films of different thicknesses, it was not possible to individually identify each layer, due to the SEM limitations. In spite of this, the total thicknesses of the bilayer structures are in agreement with the expected values: 108.7 ± 5 nm for Py(10)/ST(100), and 110.1 ± 5 nm for Py(100)/ST(10). The structures are also overall uniform.

XRR was employed to calculate the thickness and analyse the overall structure of the bilayers. Figure 5.2 shows the XRR curves of the Py(10)/ST(100) and Py(100)/ST(10) bilayers. The Fresnel reflectivity decrease is seen as well as the Kiessig fringes corresponding to each layer, with the thicker film in each bilayer having a smaller oscillation period. This demonstrates the good uniformity of each thin film layer and of their interface, in accordance with what was observed in the SEM images for the other bilayers. By measuring the fringe angles of the two layers, the thicknesses can be calculated following equation 2.3. This linear analysis is presented as the respective insets of Figure 5.2. From the linear fits, the Py and ST thicknesses were calculated to be 8.54 ± 0.07 nm and 102.83 ± 0.08 nm, respectively, for the Py(10)/ST(100) and 97.60 ± 0.08 nm and 11.9 ± 0.2 nm for the Py(100)/ST(10).

XRR was also performed on the bilayers with layers of the same thickness, with the results being shown in Figure 5.3. For the Py(50)/ST(50) sample, two sets of superimposed fringes are detected. Being the thickness of each layer similar, the two oscillations corresponding to each layer overlap and each fringe appears to have two smaller fringes. These superimposed Kiessig fringes have a similar behaviour to a beat-

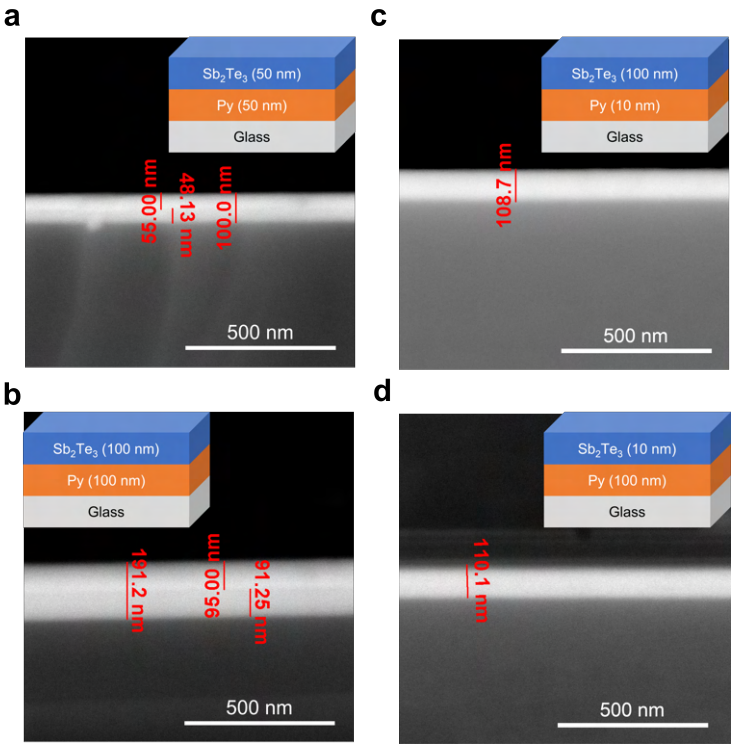


Figure 5.1 – SEM cross sectional imaages of the bilayers: (a) Py(50)/ST(50), (b) Py(100)/ST(100), (c) Py(10)/ST(100), (d) Py(100)/ST(10).

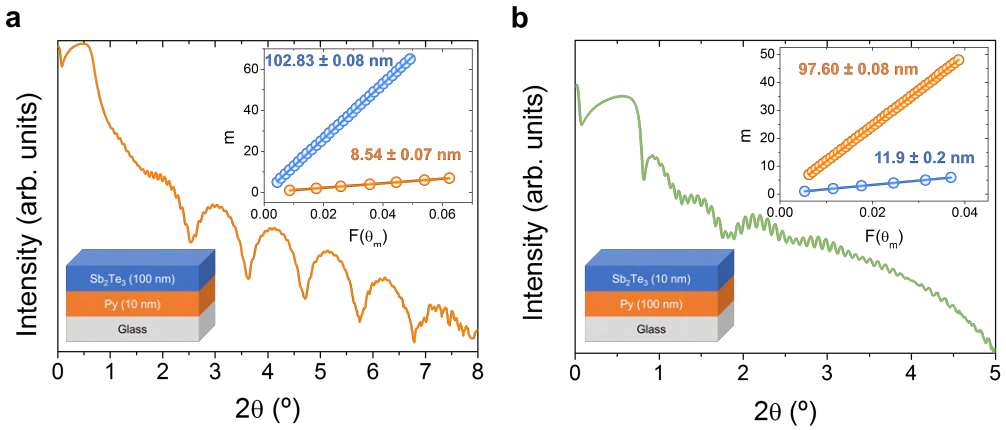


Figure 5.2 – XRR of the bilayers: (a) Py(10)/ST(100), (b) Py(100)/ST(10). The inset are the linear fit analysis of the fringes' order following equation 2.3, showing the respective calculated thicknesses.

ing effect of two interfering sound waves. The detected wave is a superposition of the x-rays reflected at the interface between the ST and Py layers and at the bottom of the Py layer. These two reflections, corresponding to different layers, yield different intensities at different angles, according to their thickness. When interfered, they produce the beating pattern observed. This also demonstrates the good uniformity of each layer, as it was also seen in the SEM image. The average thickness for each layer was also calculated using equation 2.3 and one of the set of fringes, with the inset of Figure 5.3.(a) showing the analysis. The thickness of 47.1 ± 0.1 nm was obtained for both sets of fringes. These values are in accordance with the thicknesses obtained from SEM.

The XRR pattern of the Py(100)/ST(100) bilayer is depicted in Figure 5.3.(b). Only one set of Kiessig fringes can be identified. For thicknesses higher than roughly 100 nm, it is not possible to detected any fringes. With the Sb_2Te_3 layer having a thickness of roughly 100 nm, it is not possible to detect the signal corresponding to the Py layer. The analysis was thus performed to this single set, having yielded a thickness of 89.0 ± 0.2 nm. As for the previous bilayer, the thicknesses obtained from XRR and SEM are in agreement.

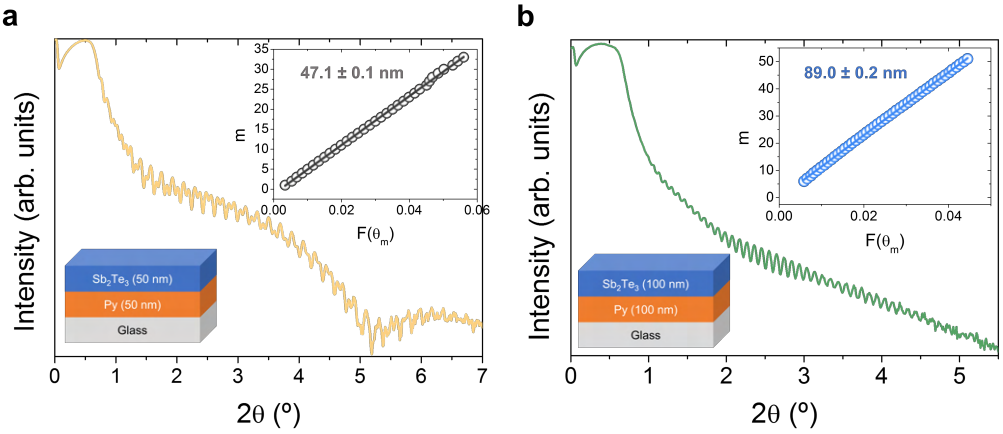


Figure 5.3 – XRR of the bilayers: (a) Py(50)/ST(50), (b) Py(100)/ST(100). The inset are the linear fit analysis of the fringes' order following equation 2.3, showing the respective calculated thicknesses.

Figure 5.4 shows the XRD pattern of all the bilayers and the 100 nm thin films of Sb_2Te_3 and Py and the identified reflections as lines. The bilayers show two reflections at 24.7º and 51.7º (solid lines). These are also seen in the pattern of ST(100) and can be indexed by the planes (1 0 2) and (2 0 5) of the Sb_2Te_3 phase, with a rhombohedral crystal geometry (R-3m)[162]. This indicates that the structure of Sb_2Te_3 in the bilayers is identical to that of the single thin films and as such the TSS should still be present. Three other peaks are seen in both the bilayers and the Py(100) films. These correspond to the $Ni_{80}Fe_{20}$ FCC phase (dashed lines), with the peak at 44º corresponding to the (1 1 1) plane, the peak at 92º to the (3 1 1) plane and the peak at 96º to the (2 2 2) plane[185]. The intensity of the peaks coming either from ST or Py depends on the thickness of each layer, with for example the intensity of the Py peaks being smaller for the Py(50)/ST(50)

bilayer than the Py(100)/ST(100).

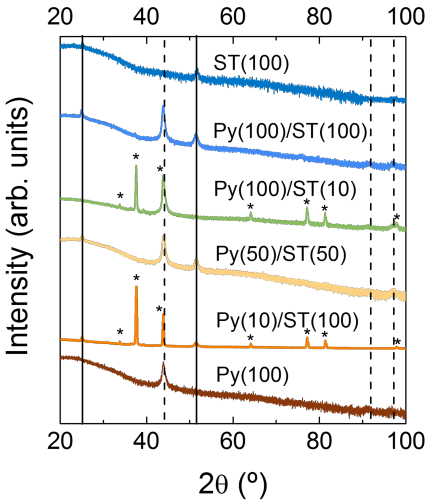


Figure 5.4 – XRD patterns of the bilayer structures and of the Py and ST thin films, both with a thickness of 100 nm. The solid lines identify the two ST observed peaks, whereas the dashed lines are the Py peaks. The peaks marked by an asterisk correspond to sample holder peaks and the broad peak centred at 26º is from the glass substrate.

5.3 Electronic Properties of the FM/TI bilayers

5.3.1 Resistivity and Seebeck Coefficient

The resistance as a function of temperature of the bilayers and Py thin films is shown in Figure 5.5.(a). The resistance of all these samples increases with heating, which is expected for the temperature dependence of the resistance of Py[186] and as previously measured for Py thin films ion beam sputtered on Si/SiO_2 substrates using the same IBS system[187]. This indicates that the conduction is dominated by the Py film of the bilayers. Furthermore, the resistance of the Py(10) is higher than the Py(100). However, the decrease in thickness is not enough to explain this effect, since it should only be 10 times higher. This can be explained by the increase of the resistivity with a reduction of the Py thin film thickness, which occurs due to a combination of grain boundary and surface (Fuchs size effect) scattering[188,189], with the results being consistent with previous measurements of thin films of Py fabricated with the same system[187].

In all the range of measured temperatures, the resistance also increases with the presence of the Sb_2Te_3 layer. For example, both bilayers with a 100 nm thick Py layer have similar values of resistance, with the Py(100)/ST(10) resistance being slightly higher. This is justified by the decrease in thickness, which increases the resistance, but also by the resistivity of the Sb_2Te_3 layer increasing with a reduction in thickness, as presented in the previous chapter. The resistance of the other bilayers is higher, both due to a combination of the decrease and increase of the thickness of the Py and ST

layer, respectively. Moreover, for the lowest Py thickness bilayer, Py(10)/ST(100), an increase in resistance at the lowest temperatures, below 40 K, is also noted, showing the presence of conduction through the Sb_2Te_3 due to the highest ratio between the thickness of Sb_2Te_3 and Py layers.

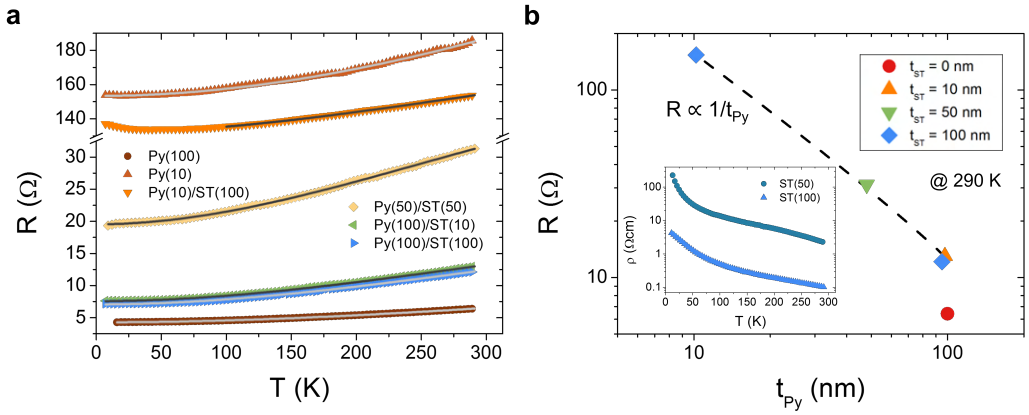


Figure 5.5 – Resistance of the bilayers (a) as a function of temperature and (b) at 290 K as a function of the Py thickness. The solid lines in (a) are the fits following equation 5.1 to the resistance of the Py films and bilayers. The dashed line in (b) corresponds to the resistance dependence on the inverse of the Py layer thickness. The resistivity of the ST(100) and ST(50) thin films is shown as the inset in (b).

The resistance of Py can be explained considering different scattering phenomena[190]. Since Py is constituted by transition metals, scattering between the s-d electrons is expected, which leads to a cubic dependence on temperature of the resistivity of Py. A quadratic dependence on temperature can also appear due to magnon-electron interactions at low temperatures relative to the Curie temperature of the Py[191]. As such, the resistance of the Py films can be described by equation 5.1, with R_0 being the residual resistance not dependent on temperature, occurring due to electron scattering with defects (impurities, grain boundaries, interfaces) and alloy disorder[186], and Q and C the quadratic and cubic temperature dependence coefficients. The resistance of the single Py thin films and of the bilayers were fitted to this equation and the fits are shown as solid lines in Figure.5.5.(a).

$$R = R_0 + QT^2 + CT^3 \tag{5.1}$$

Equation 5.1 describing the resistance of the Py thin film, also describes well the bilayers resistance, and the obtained parameters are shown in Figure 5.6. Focusing on the samples with a Py thickness of 100 nm, the residual resistance increases due to the Sb_2Te_3 layer, as it would be expected due to the added source of resistance from conduction occurring through this layer. Moreover, this residual resistance is higher for the bilayer with 10 nm film of Sb_2Te_3 than with 100 nm, which can be explained by the reduced thickness and increase in resistivity of the Sb_2Te_3 layer. Considering the resistance coefficients, the cubic coefficient is approximately zero, which indicates that

scattering between the s-d electrons is negligible. On the other hand, the quadratic coefficient increases for the bilayers. This shows that the magnon-electron interaction is enhanced with the existence of the Sb_2Te_3 layer.

Considering the samples with 10 nm of Py, the fit to the Py(10)/ST(100) was not performed to the full range of temperatures studied due to the increase in the resistance at low temperatures previously noted and attributed to the Sb_2Te_3 100 nm layer. This fit, nonetheless, described well the resistance of the bilayer at the highest temperatures. From the two fits, it is calculated that the residual resistance and quadratic coefficient decrease for the Py(10)/ST(100) bilayer from the bare film values, which is the opposite behaviour of the Py(100) bilayers. The residual resistance decrease can be explained considering that the Py(10) sample is not capped and as such, there could be oxidation of the surface leading to an increase of the non-temperature dependent resistance. This was not seen in the Py(100) film since the surface contribution to the resistance of this film is smaller due to the film having a higher thickness. The opposite behaviour of the quadratic coefficient when compared with the Py(100) bilayers, however, shows that for the 10 nm thin film, the Sb_2Te_3 decreases the magnon-electron scattering.

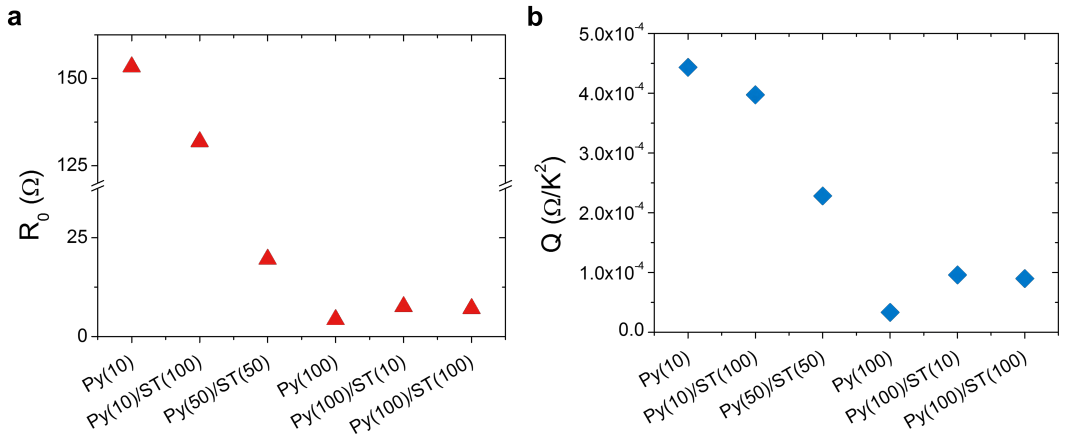


Figure 5.6 – Permalloy resistance parameters. (a) The residual resistance R_0 and (b) quadratic component Q calculated from the fits of equation 5.1 to the resistance of the Py thin films and bilayers.

To fully explain the conduction in these bilayers, Figure 5.5.(b) shows the resistance of the bilayers at 290 K as a function of the thickness of the Py layer, in logarithmic scale. A dependence of the resistance on the inverse of the Py layer thickness is observed. It is also independent of the thickness of the Sb_2Te_3 layer. The inset shows the resistivity of the ST(100) and ST(50) thin films. As discussed in Chapter 4, the Sb_2Te_3 resistivity ρ_{ST} decreases with cooling, having high values even at room temperature. This is in contrast with the Py resistivity ρ_{Py}, with ρ_{ST} being between four or five orders of magnitude higher than the ρ_{Py} at room temperature, with this difference increasing with cooling. As such, this demonstrates again that the conduction is dominated by the permalloy.

Figure 5.7 shows the Seebeck coefficient S as a function of temperature for the bilayers and the Py thin films. The Seebeck values are negative, as expected for metals.

They decrease in magnitude with cooling from between -20 and -30 μV/K at room temperature to -2 μV/K at 20 K, similar to previously reported values for Py[192–194]. This is in contrast with the Seebeck coefficient temperature dependence of ST determined in the previous Chapter. The Sb_2Te_3 thin films' Seebeck coefficient is positive at room temperature, being approximately 150 μV/K, and decreases with cooling until becoming negative and reaching values around -1000 μV/K at 20 K. These values are orders of magnitude higher than the Py values. However, in the bilayer system, the Seebeck coefficient is identical to Py films coefficient. This is indicative that most of the conduction is happening through the Py layer and not the ST layer.

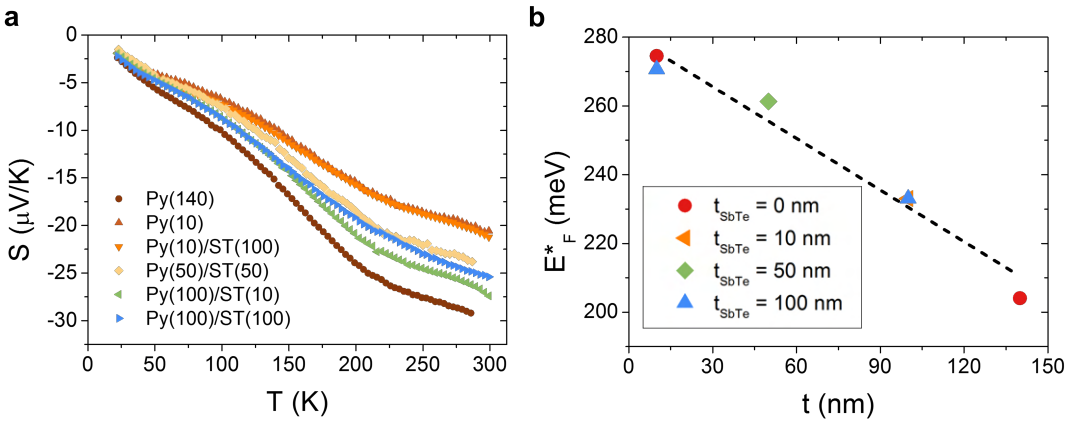


Figure 5.7 – Seebeck coefficient of the bilayers. (a) *S* as a function of temperature. (b) The effective Fermi level calculated from the Seebeck linear fit at low temperatures as a function of the Py thickness.

At low temperatures, below 50 K, the *S* curves of both thin films and bilayers have a linear dependence on temperature. In metals, this linear dependence can be described by equation 5.2[191]. Following this equation, linear fits were performed to the Seebeck coefficient of the thin films of Py but also to the bilayers. From the fits, the effective Fermi energy E_F^* was calculated, and it is plotted as a function of the Py layer thickness in Figure 5.7.(b). A linear dependence can be observed, being independent of the thickness of the ST layer. Thus, it corroborates the resistance results, where it was verified that most of the conduction occurs though the Py layer in the bilayer systems.

$$S = -\frac{\pi^2}{3}\left(\frac{k_B^2}{eE_F}\right)T \tag{5.2}$$

For temperatures between 50 and 200 K, however, there is a deviation from this linear behaviour. A bump is observed at these temperatures, which has been previously attributed to phonon drag in transition metal structures[195]. This effect is more noticeable for the thinner Py film and bilayers, showing that it has a dependence on the thickness of the films. On the other hand, at the highest temperatures (250 - 300 K), a linear behaviour returns. Linear fits were performed and the slope is independent of the thickness of the Py (and also of the presence and thickness of Sb_2Te_3). Considering

this, the effective Fermi energy thickness dependence can be explained by the phonon drag. At room temperature, the Seebeck coefficient linear behaviour is independent of the thickness. However, with cooling, the phonon drag, which is dependent on the Py thickness, deviates the curves from the expected linear dependence. Thus, at the lowest temperatures, because the Seebeck at 0 K must be equal to zero, the slopes of the retrieved linear dependence are different and have the thickness dependence shown in Figure 5.7.(b). As such, the curves of the Seebeck coefficient depict surface versus bulk effects in the Py, with the phonon drag being more prominent in the thinner Py layers.

The simplest model of transport in a bilayer system would be a parallel conduction model, which would be dominated by the Py conduction due to the difference in resistivities. However, when calculating the bilayer resistances from the resistivities of each material, the calculated conductance following the parallel resistances model is always higher than the bilayer conductance. Moreover, the Seebeck coefficient is also dominated by the Py layer and does not show anything similar to the ST temperature dependence of the Seebeck coefficient. As such, the simple parallel conduction model does not explain the bilayers conduction. Due to the high difference in resistivity, shunting effects are expected to occur, with the current being directed towards the metallic layer to avoid the Sb_2Te_3 layer. From this concept, the conduction could be taking place through three resistances in series: the Py layer resistance, and two volumes within the Sb_2Te_3 layer of equal cross sectional area A and a length equal to the Sb_2Te_3 layer thickness t_{ST}, as seen in the inset of Figure 5.8. This model would allow for a minimisation of the conduction paths via the Sb_2Te_3 layer and thus effectively reduce the overall resistance of the bilayer. Thus, considering the effective volume that conducts, the bilayer resistance is described by equation 5.3 where L is the length between the contacts, w the width of the samples, t_{Py} the thickness of the Py layer, and ρ_{Py} and ρ_{ST} the resistivities of the Py and Sb_2Te_3 layers, respectively.

$$R = \rho_{Py}\frac{L}{wt_{Py}} + 2\rho_{ST}\frac{t_{ST}}{A} \tag{5.3}$$

This model shows that the resistance is proportional to the inverse of the Py layers thickness, corroborating the results shown in Figure 5.5.(b). It can also explain why there is no contribution from the Sb_2Te_3 layer to the Seebeck coefficient since the Sb_2Te_3 conductions paths do not experience any temperature differences. From this model, using equation 5.3, it is possible to calculate the cross-sectional area of the conduction paths in the Sb_2Te_3 layer. This area, as a function of temperature, is presented in Figure 5.8. It increases with cooling for the four bilayers, which signifies that the second term in equation 5.3, the resistance coming from the Sb_2Te_3 layer, reduces with cooling. This shows that due to the increase in the ρ_{ST} with cooling, the shunting effect is more prominent. Moreover, the area enlarges when the Py layer thickness is higher, which corresponds to a lower resistance of the Py layer, and/or the Sb_2Te_3 layer thickness decreases, having a higher resistance, i.e. when the ratio between the resistance of the

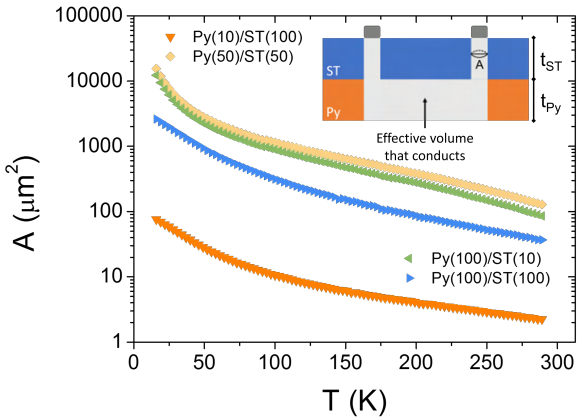


Figure 5.8 – The calculated cross-sectional area *A* of the Sb_2Te_3 shunting conduction path as a function of temperature. The inset shows the shunting conduction path model proposed for these bilayers.

ST layer and Py layer increases, the area of the conduction path also increases.

5.3.2 Magnetoresistance

To further understand the electronic transport and the shunting effects in these basic SCI elements, magnetoresistance measurements were performed of the Py(10)/ST(100) and Py(100)/ST(100) samples as a function of temperature and in different field and current configurations: out of plane (OP) magnetic field, and in plane magnetic field, either perpendicular (IP: $I \perp B$) or parallel (IP: $I \parallel B$) to the applied current.

5.3.2.1 Temperature dependence of the Magnetoresistance

Figure 5.9 shows the magnetoresistance (MR) curves of the two samples at room temperature and in the three configurations measured. The magnetoresistance is defined as $MR(B) = \frac{R(B)-R(0T)}{R(0T)}$. For each geometry of the field and current, the curves of the two different samples have a similar appearance. They all present a maximum or minimum at zero magnetic field, saturating or decreasing upon application of the field. This behaviour is consistent with previous reports for the MR of Py[187,196]. As such, the MR, like the other transport properties analysed here, shows that the conduction is dominated by the Py layer.

The MR of a FM material closely follows its magnetisation[187,196]. Since the coercive field of Py is of the order of 1 mT[196] for the easy axis, the magnetisation saturates at small applied magnetic fields, which changes the resistance status. For example, for the IP: $I \perp B$ measurements, in saturation, the magnetisation is perpendicular to the current, resulting in a low resistance. For the in plane measurements, the MR at 0 T is either the maximum of the minimum of the curve for the perpendicular or parallel field measurements, respectively, which is consistent with the anisotropic magnetore-

sistance (AMR)[187]. The zero-field state is a state of either high or low resistance, as the magnetisation is parallel or perpendicular to the current due to the anisotropy. The OP measurements, however, do not saturate as opposed to the IP MR. This indicates that the preferred orientation of the magnetisation is in plane for both Py thin films, which is consistent with previous Py thin films with in plane orientation of the magnetisation, having a saturation field of approximately 1.05 T for the OP direction[196]. Moreover, OP MR shows an approximate parabolic behaviour with the field. This is expected considering AMR and when the magnetisation rotates coherently[196]. The peaks observed at 0 T illustrates that there was a small misalignment of the magnetic field with the OP direction, which induces a small IP rotation of the magnetisation, leading to peaks as in the IP-MR[196].

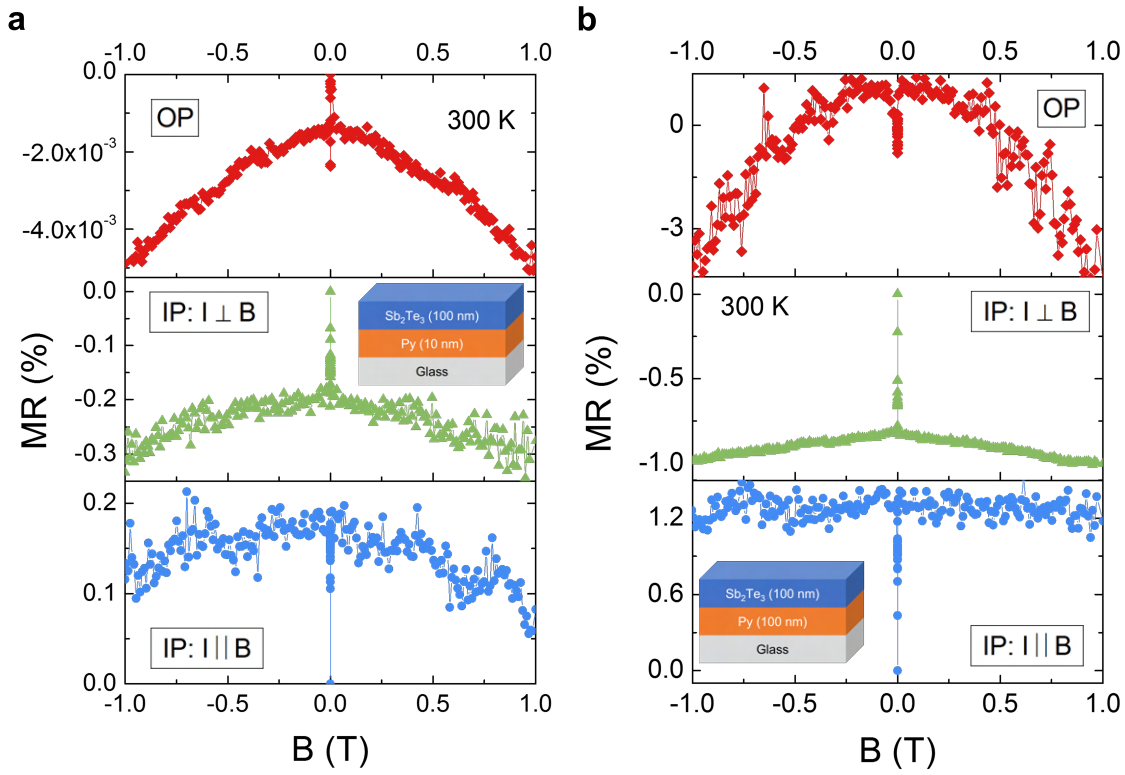


Figure 5.9 – Magnetoresistance of the bilayers (a) Py(10)/ST(100) and (b) Py(100)/ST(100) for the three different orientations of the magnetic field field with the applied current at room temperature.

The magnetoresistance was also measured at other temperatures. The dependence on the magnetic field was approximately maintained with cooling, being the same as shown in Figure 5.9. The temperature dependence of the MR magnitude was calculated and it is depicted in Figure 5.10, for a field of 1 T. The magnitude of the thicker Py bilayer is roughly one order of magnitude higher, with this dependence on the thickness of the Py film having been reported[196]. However, both samples show a similar behaviour, namely the MR magnitude increasing with a decrease in temperature. This has been observed previously and it is due to the magnetisation temperature dependence, which at this range of temperatures for Py, follows the Bloch-law[197]. In spite of

this, at the lowest temperatures, the MR has a sharp increase for the IP-MRs and decrease for the OP-MR for both samples. This could be due to the presence of the Sb_2Te_3 layer, since it is at this temperatures that the magnetoconductance of the Sb_2Te_3 films becomes significant, as discussed in Chapter 4. To fully understand this increase, the magnetisation dependence on temperature ought to be explored.

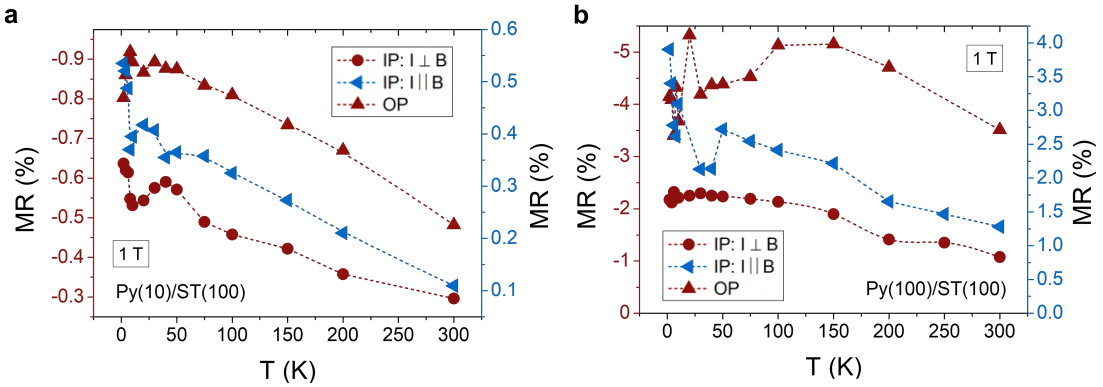


Figure 5.10 – Temperature dependence of the magnetoresistance of the bilayers (a) Py(10)/ST(100) and (b) Py(100)/ST(100) for the three different orientations of the magnetic field with the applied current at 1 T.

5.3.2.2 Magnetoresistance at low temperatures

To fully disentangle the conduction at the lowest temperatures, where the TSS conduction of Sb_2Te_3 should be active, Figure 5.11 shows the dependence of the resistance with the applied magnetic field for the IP configuration with the field applied perpendicular to the current for both measured bilayers at 2 K. The Py(10)/ST(100) has the same form as the MR at 300 K. However, the Py(100)/ST(100) MR does not saturate, with the resistance increasing with the magnetic field. This behaviour is similar to the magnetoresistance of Sb_2Te_3, namely the Weak Antilocalisation (WAL) effect correction at low fields, which was thoroughly analysed in Chapter 4.

To verify if this exotic magnetoresistance is present due to the Sb_2Te_3 TSS conduction, the magnetoconductance was analysed and it is shown in Figure 5.12. The obtained data was smoothed and symmetrised and the peak of the Py MR was removed, with the result being shown in Figure 5.12.(a) for both the 2 K and 4 K magnetoconductance. The data were fitted to equation 4.2, which includes the WAL term and the quadratic background. The α and β parameters cannot be calculated since the conductance has the contribution of the Py layer, being much higher than Sb_2Te_3. However, L_ϕ can be calculated since it is not a proportionality constant. The values obtained were 62.5 ± 0.7 nm at 2 K and 58 ± 1 nm and at 4 K, which corresponds to a error of 7% and 14% from the values calculated from the single Sb_2Te_3 100 nm thin film measurements. The values are in agreement, which indicates that the MR behaviour is being influenced by the the Sb_2Te_3 layer, i.e. dominated by the topological surface state of Sb_2Te_3.

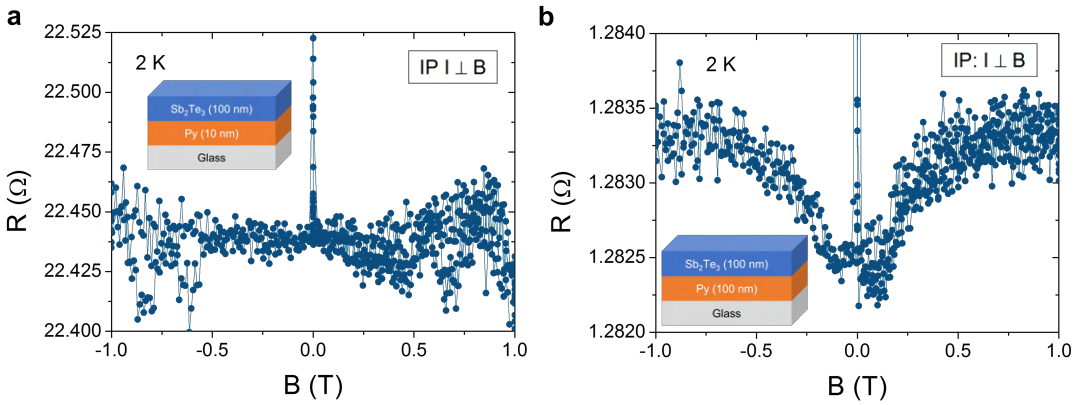


Figure 5.11 – Magnetoresistance of the bilayers (a) Py(100)/ST(10) and (b) Py(10)/ST(100) bilayers with an in plane applied magnetic field perpendicular to the applied current at 2 K.

In contrast, the MR performed under different geometries and of the Py(10)/ST(100) bilayer does not show such behaviour, being dominated again by the Py conduction. This agrees with the aforementioned interpretation regarding the shuting model proposed to explain the transport properties under the absence of B. When considering B applied in plane but perpendicular to the applied current, the field is perpendicular and out of plane to the current flowing in the Sb_2Te_3 layer, due to the conduction paths created by the shunting in the Sb_2Te_3 layer, as shown in Figure 5.12.(b). It is also at this geometry (out of plane field) when these effects are more prominent and were measured in Chapter 4. However, this contribution from the TI state of the Sb_2Te_3 layer is negligible in the Py(10)/ST(100). Figure 5.8 shows that the cross-sectional area of the Sb_2Te_3 conduction path is smaller in this bilayer, which can explain why the MR contribution is also smaller.

5.4 Magnetisation dynamics at room temperature

Having explored the transport properties of the bilayers, their magnetisation dynamics was studied through Ferromagnetic Resonance (FMR) measurements. VNA-FMR, as described in Chapter 2 was employed to obtain the magnetisation dynamics parameters of the bilayer structures and also of the proposed capped samples.

5.4.1 FM/TI bilayers

Figure 5.13.(a) shows the resonance frequency as a function of the applied DC field for the four Py/ST bilayers at room temperature, obtained from the FMR absorption peaks. The resonant frequency and field should follow the Kittel formula given by equation 2.5. The data were fitted to this equation and the obtained fits are plotted as solid lines on Figure 5.13.(a). From these fits, the Saturation Magnetisation M_S and the anisotropy field H_k were obtained. The gyromagnetic ration γ was fixed for all the analysis to the

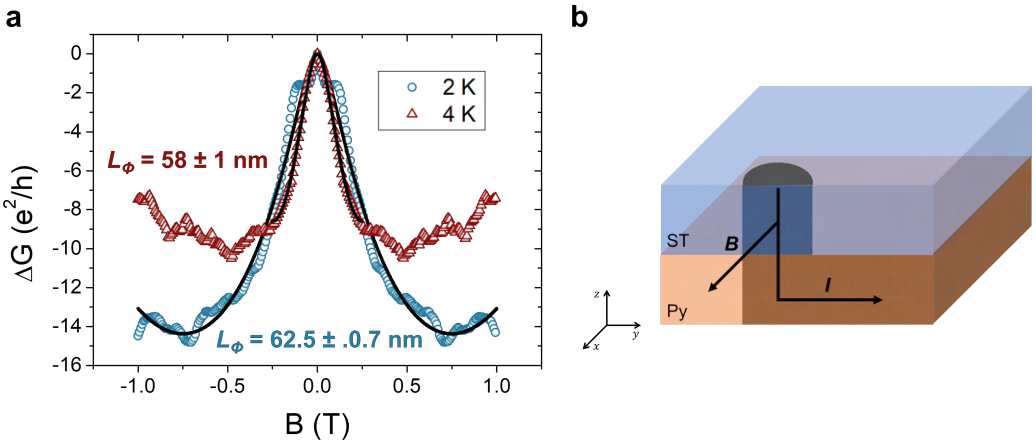


Figure 5.12 – The shunting effect on the magnetoresistance. (a) The magnetoconductance at the lowest temperature of Py(100)/ST(100) and the respective fit to the expected ST contribution to the magnetoconductance, which is given by equation 4.2. (b) A schematic of the magnetoresistance measured with an in plane field perpendicular to the applied current. The shaded area corresponds to the volume that conducts considering the shunting model proposed in the previous section. From this model, it can be seen that for the ST layer conduction path, the magnetic field is effectively out of plane.

value of 2.96 MHz/Oe, which corresponds to the Py value[198]. The obtained parameters are displayed on Table 5.1.

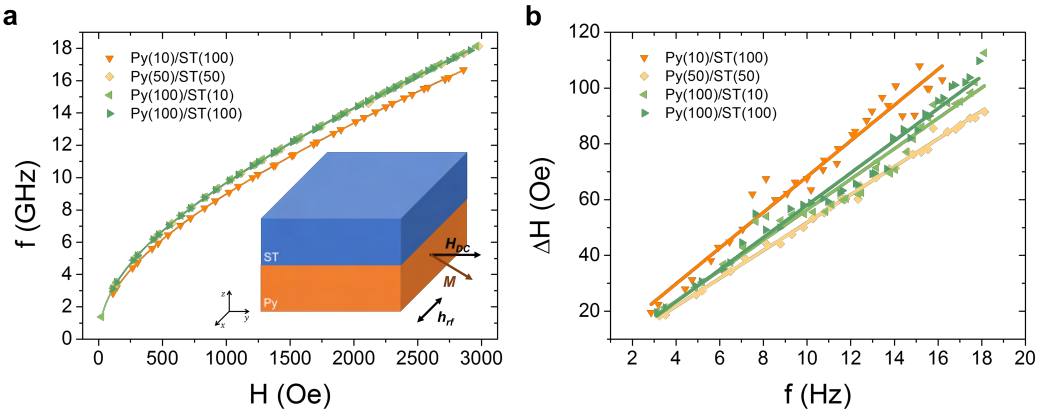


Figure 5.13 – Magnetisation dynamics of the bilayers. (a) FMR frequency as a function of the resonance magnetic field for all the studied bilayers. The solid lines are the Kittel fits to the experimental data. The inset shows the FMR measurements geometry. (b) Linewidth of the FMR peaks as a function of the frequency. The solid lines are the linear fits to the data used to calculate the Gilbert damping.

From the absorption peaks, the Gilbert Damping can also be obtained. Following equation 2.7, the linewidth ΔH of the peaks is proportional to the resonant frequency, with the slope being proportional to α. Figure 5.13.(b) depicts the field linewidth as a function of the frequency, with the linear fits to equation 2.7 as solid lines. The obtained damping values are on Table 5.1, and are between 7 and 9×10^{-3}, being close to other reported values, which confirms the good quality of the Py layers[199,200]. In general,

they are also higher for the sample with a thinner Py film, which is in agreement with previous reports, where it was showed that the damping is inversely proportional to the thickness of the Py[199].

5.4.2 Reference FM capped thin films

To fully characterise the magnetisation dynamics of the bilayer samples and quantify the influence of the Sb_2Te_3 layer on Py, reference values for the damping ought to be obtained. This can be achieved from measuring single Py thin films. However, single Py thin films are prone to several defects, such as oxidation, which even in small amounts can affect greatly the damping. As seen in Chapter 2, the damping is a very important parameter, needed to fully explain the magnetisation dynamics of these materials and structures. Taking this issue into consideration, several Py cappings were investigated by FMR.

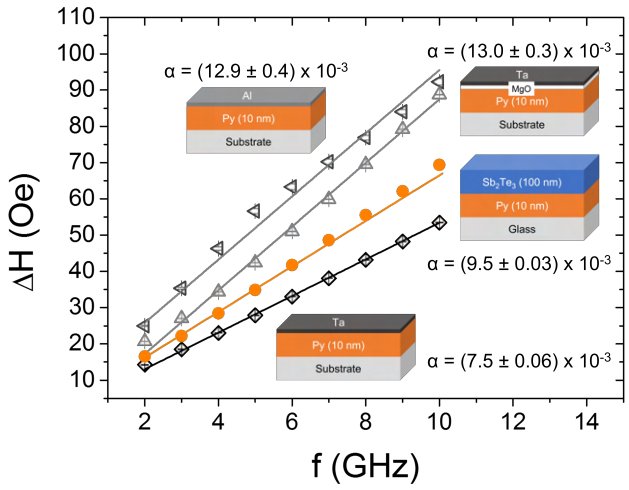


Figure 5.14 – Capped FM Py thin films magnetisation dynamics, namely the linewidth of the FMR peaks as a function of the frequency. The solid lines are the linear fits to the data. The Gilbert damping for each nanostructure is also shown.

The linewidth as a function of the resonance frequency is displayed in Figure 5.14 for the three capped Py 10 nm thin films. The Al capped Py has the highest linewidth values, whereas the Ta capped sample showcases the lowest. All the capped films have higher values than the Py(10)/ST(100) bilayer, except for the Ta capped sample. The linear fits were performed to the linewidth frequency dependence, being presented as full lines. The high ΔH values can be partially attributed to the intrinsic linewidth contribution ΔH_0, which is given by the intercept at the origin. This intrinsic parameter does not depend on the frequency, being related to inhomogeneities present in the FM or caused by the interface. Since the Py thin films were grown under the same conditions, on the same substrate and have the same thickness for all the nanostructures present in Figure 5.14, the Al and MgO/Ta capping have negatively influenced the magnetisation dynamics of

Sample	M_S (Oe)	H_k (Oe)	α (10^{-3})
Py(10)/Ta	8923 ± 2	-7.41 ± 0.07	7.47 ± 0.06
Py(10)/ST(100)	8233 ± 7	-2.0 ± 0.7	9.5 ± 0.3
Py(50)/ST(50)	9600 ± 15	4 ± 1	7.40 ± 0.08
Py(100)/Ta	9663 ± 7	8.1 ± 0.3	7.8 ± 0.3
Py(100)/ST(10)	9720 ± 6	0.4 ± 0.4	8.1 ± 0.3
Py(100)/ST(100)	9607 ± 6	4.5 ± 0.5	8.5 ± 0.2

Table 5.1 – Magnetisation dynamics parameters of the FM/TI bilayers at room temperature.

the Py layer. The deposition of the MgO layer on top of the Py film could have oxidized it, which would lead to the observed increase. On the other hand, the deposition of the Al capping can also lead to intermixing between the Py and Al at their interface, as it has been previously observed for sputtering of Al[201], which also negatively affects the magnetisation of the Py layer. As such, the presence of alumina from Al intermixing and oxidisation could also explain this increase. For the Py/ST bilayer and the Ta capped sample, the intrinsic contribution is roughly the same, which indicates that this capped sample can be taken as the reference sample.

The damping of the capped samples was calculated form the slope of the linear dependence of ΔH on the frequency, and it is shown in Figure 5.14. As for the intrinsic linewidth, the damping of the Al and MgO/Ta capped samples is the highest, being the same within uncertainty. It is also higher than both the bilayer and Ta capped sample. However, the Py film capped with Ta has the lowest value, being even lower than the bilayer value. Considering the expected effect of the presence of the Sb_2Te_3 layer on the Py magnetisation dynamics, namely the presence of spin pumping into the ST layer, which would increase the damping, the behaviour observed with these two samples is expected. Considering the lower damping value and the intrinsic linewidth discussion, the optimal reference sample from the available ones is the Ta capped sample, and as such, the Ta capping was the approach for also the Py(100) thin film.

On Table 5.1 the parameters of the magnetisation dynamics of both the Py/ST bilayers and the reference samples are thus summarised. The saturation magnetisation M_S has similar values for the same thickness of Py, having lower values for the thinner Py samples. The anisotropy field H_k is also similar for samples with the same Py layer. It is negative for 10 nm of Py, being higher in magnitude for the capped sample. On the other hand, it increases becoming positive for thicker Py samples, showcasing the change in the anisotropy of the films with a reduction of the Py thickness. For the 100 nm Py nanostructures, the capped sample also has the higher value.

Furthermore, α is substantially higher in the bilayer systems with ST than the reference samples, with an increase in 27% for the Py(10)/ST(100) bilayer, for example. There are several mechanisms that lead to a greater damping, from intrinsic mechanisms of the ferromagnetic material itself, to extrinsic contribution due to structural inhomogeneity and grain boundaries, among others[113,200]. Another mechanism is an

added magnetic relaxation channel via spin pumping. From the morphological characterisation previously discussed, the extrinsic contribution to the damping increase in the bilayers should be minimal, whereas the reference values obtained herein confirm the good quality of the Py. As such, an increase due to spin pumping is the most likely, as it has been previous observed in TI systems[202,203] and other bilayers systems[200,204]. This implies that a spin current is being inject into the ST from the Py layer, which, as previously reported in TIs, could be transformed in a charge current via the inverse spin hall effect (ISHE)[69,205] and/or the inverse Rashba-Edelstein effect (IREE)[70,71,206].

5.4.3 Generated spin currents

From the results of the previous section, and as described in Chapter 2, the generated spin current J_S can be calculated from the parameters present in Table 5.1, namely M_S and α. The spin current is created in the Py layer and can then be injected intot he adjacent layer, which in this case is Sb_2Te_3. It is described by equation 2.14, and it is proportional to the spin mixing conduction $g^{\uparrow\downarrow}$, which is given by equation 2.13. The spin mixing conduction depends on the difference of the Gilbert damping of the bilayer system and of the reference sample, which from the previous section is taken as the Ta capped sample.

Figure 5.15 displays the $g^{\uparrow\downarrow}$ and J_S calculated for each bilayer with the corresponding reference FM sample. Both the spin mixing conduction and spin current increase with the thickness of the Py layer and of the ST layer. The increase due to the Py thickness can be explained by considering that the spin current is generated due to the precession of the magnetisation. Since the thicker Py samples have a higher saturation magnetisation, this increase in the current can be attributed to it. Regarding the ST thickness dependence, it can be explained if ST is a good spin sink, i.e. the injected current propagates into the Sb_2Te_3 layer, where, if Sb_2Te_3 is an efficient spin sink, it can be absorbed. This was previously noted in trilayer system of FM/TI/FM with the TI being Bi_2Se_3 by VNA-FMR and XFMR[207]. As such, this could explain the increase with the Sb_2Te_3 layer thickness. The obtained values for $g^{\uparrow\downarrow}$, between 9×10^{18} and 4×10^{19} m^{-2}, are also higher or comparable with previously reported values for FM/TI nanostructures based on Bi_2Se_3[61,207] at room temperature.

5.5 Conclusions

We have successfully fabricated bilayers of Py and ST topological insulator thin films using ion beam sputtering deposition. The fabricated bilayers are uniform, and the structure of each material's layer is maintained from the single thin film form. As the TSS of the ST layer was previously observed in thin films deposited on glass, this indicates that it should also be present in these bilayers.

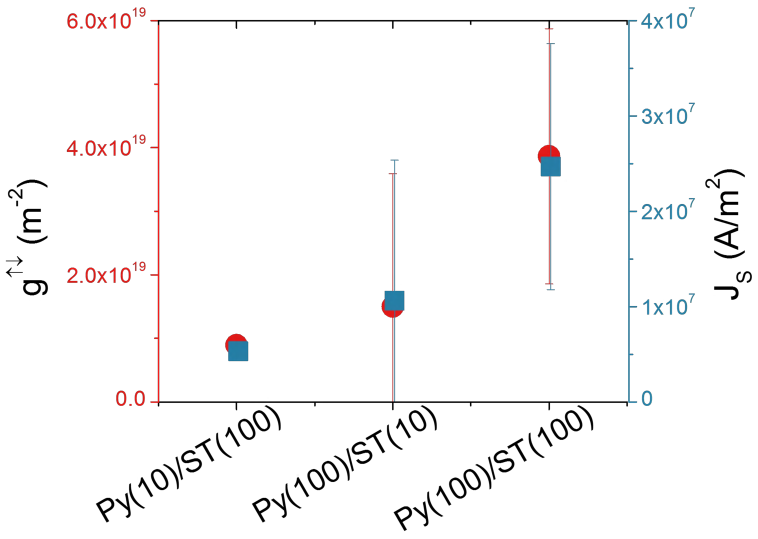


Figure 5.15 – The spin mixing conduction and generated spin current of the Py/ST bilayers.

The electrical conduction is dominated by the metallic Py layer, as observed through the magnetotransport and Seebeck coefficient. From the electrical resistance and considering the temperature dependence of the Seebeck coefficient, a shunting conduction model was proposed. Herein, the conduction does not follow a simple parallel resistance model, but is equivalent to three resistances in series, namely the Py layer resistance and two more conduction paths on the ST layer. This model showed that as the temperature decreases, the cross-sectional area of the ST conduction paths increased, thus reducing the overall resistance, which corresponds to an increase in the shunting effect. Moreover, an increase in the ratio between thickness and resistance of each layer also promoted an increase of the shunting effect. Despite the conduction being dominated by the Py layer due to shunting, at low temperatures, the WAL contribution to the magnetoresistance from the ST TSS was observed, further proving the shunting model introduced and confirming the presence of the TSS as foreseen from the structural properties.

The magnetisation dynamics of the bilayers was also analysed via FMR and compared with reference capped Py samples. These results showed an overall increase in the Gilbert damping with the presence of the ST layer, such as an increase of 27% for the Py(10)/ST(100) sample. Considering the structural properties, this increase must be due to spin pumping occurring into the ST layer, indicating that ST could be a material of interest for the development of devices based on the SCI and that this bilayer structure could also be taken as the basic SCI element. The spin pumping effect in these bilayers is the subject of the next chapter (Chapter 6).

CHAPTER 6

Spin to charge current conversion for energy-efficient logic devices

This chapter [1] will focus on the research conducted on the spin to charge conversion in Sb_2Te_3 as well as its efficiency for applications in logic devices, such as the magneto-electric spin-orbit (MESO) logic device[8]. Sb_2Te_3 is a TI material, which has not been thoroughly explored due to its smaller band gap and distorted TI surface state[155], and as such it is not yet clear if it is a noteworthy spin-orbit coupling (SOC) material. The spin to charge conversion (SCC) of Sb_2Te_3 was evaluated through spin pumping experiments in sputtered Py/Sb_2Te_3 on glass as a function of temperature from room to cryogenic temperatures. By combining the low temperature studies with the electronic transport measurements and structural characterisation of Chapter 4 and 5, we aim to understand the underlying physical effects of the spin to charge conversion in Sb_2Te_3 at room temperature. The results herein obtained present Sb_2Te_3 as a prominent SOC material, paving the way for future progress in beyond CMOS logic devices.

6.1 Introduction

Spintronics has seen advancements in the last few decades due to the generation and manipulation of spin currents based on ferromagnets. By combining these effects that revolutionised our use of technology with new developments, such as Spinorbitronics, novel devices can be devised. Spinorbitronics is based on efficient spin to charge interconversion (SCI) due to high spin orbit coupling (SOC) in non-magnetic materials[156,157]. The charge to spin conversion can be achieved via the two effects previously mentioned:

1. The spin Hall effect (SHE) converts a charge current into a transverse spin current in the bulk of a material[31].

[1] Adapted from S. Ferreira-Teixeira, A. Vanstone, A. L. Pires, W. R. Branford, J. P. Araújo, L. F. Cohen and A. M. Pereira, *A sputtered topological insulator with optimised spin to charge current conversion for energy efficient logic devices*, in preparation. S. Ferreira-Teixeira contribution to the publication: fabrication of the samples, partial measurements of the FMR and Spin pumping, and data analysis. Responsible for the main manuscript preparation.

2. The Edelstein Effect (EE) occurs in Rashba systems where the spin degeneracy is lifted in surfaces or interfaces, with the spin becoming locked with momentum, due to SOC. A two-dimensional (2D) charge current flowing in such a system generates a transverse spin density through the EE, which, by diffusing into an adjacent three-dimensional (3D) system, generates a spin current[33].

The spin to charge conversion (SCC) can be achieved through the reciprocal effects, namely the Inverse Spin Hall Effect (ISHE) and Inverse Edelstein Effect (IEE)[25,34].

The SCIs are described by certain figures of merit, which can be optimised for greater conversion efficiency. The spin Hall angle θ_{SH} of the SHE/ISHE effects defines this conversion, whereas, due to the 2D nature of the EE/IEE conversion, the IEE length λ_{IEE} is the parameter to optimise. By taking the product of θ_{SH} and the spin diffusion length λ_{SD}, the SCC can be evaluated by taking λ_{IEE} or $\theta_{SH}\lambda_{SD}$ as figure of merit[208]. For the efficiencies to be improved, research and development of novel SOC materials is necessary. Heavy metals, which exhibit SHE/ISHE, are the staple SOC materials, having been widely investigated[158,209] and employed[44,159,210], with moderate θ_{SH} values. New types of structures are also being developed, like van der Waals, such as Graphene/WS_2[46], and oxide heterostructures, such as $SrIrO_3$/$SrRuO_3$[47], with promising performances, similar to Heavy Metals. A novel set of materials are also the Topological Insulators (TIs)[211]. They are a new class of quantum materials, which exhibit a metallic surface state with spin-momentum locking[52,177]. Due to its high SOC, this TI property can be combined with the SHE/ISHE and EE/IEE effects in the bulk and surface, respectively, allowing for exceptional θ_{SH}[68,212] and λ_{IEE}[71,213]. Bi_2Se_3 is one of the widely studied TIs, having already been employed to switch ferromagnets[67]. $(Bi;Sb)_2Te_3$ (BST) TIs have also yielded outstanding performances[54,72].

By employing these materials and controlling the SCI effects, wide applications are foreseen. The generation of spin currents via SCC by SHE and EE can be used to manipulate ferromagnetic materials through the Spin Orbit Torque (SOT), allowing for a wide range of applications in data storage[159,175,214]. Logic devices can also be developed based on SOC materials that could improve the current standards and go beyond CMOS technology[215]. Manipatruni, Nikonov[8] have recently introduced a Magneto-electric Spin-Orbit (MESO) non-volatile device which promises lower switching voltage, enhanced logic density and superior switching energy than the current CMOS technology. To achieve these MESO performances, the SOC material is required to be highly resistive (ρ > 10 mΩcm) and have an equivalent λ_{IEE} higher than 5 nm. Despite the well-established performances of Heavy Metals and the promising properties of novel structures, their outputs are not yet qualified for the MESO device. TIs could be the SOC material employed, having higher resistivities. However, their performance is not yet optimal and most studied TIs are currently crystalline and fabricated in single-crystal substrates by using Molecular Beam Epitaxy[54,67,72,212]. This prevents fabrication scalability and real performance analysis for widespread MESO applications. This chapter

is devoted to the study of the SCC in Sb_2Te_3 sputtered nanostructures through spin pumping measurements.

6.2 Temperature dependence of the magnetisation dynamics

6.2.1 Ferromagnetic resonance as a function of temperature

The magnetisation dynamics was studied as a function of temperature through FMR. The derivatives of the absorption peaks obtained at 8 GHz and for different temperatures in the range [2 - 300] K are represented in Figure 6.1.(a) for the Py(10)/ST(100) bilayer and (b) the reference capped sample (Py(10)/Ta(3)), as discussed in Chapter 5. It can be remarked that there is a shift in the resonance to lower values with cooling for both samples. However, the range of resonance fields H_{res} is higher for the bilayer sample, with higher fields at room temperature but lower H_{res} at the lowest temperatures than the capped sample. Moreover, the peaks also appear to be wider for the bilayer sample at all temperatures, being indicative of spin pumping occurring at all temperatures, as previously discussed for room temperature in Chapter 5.

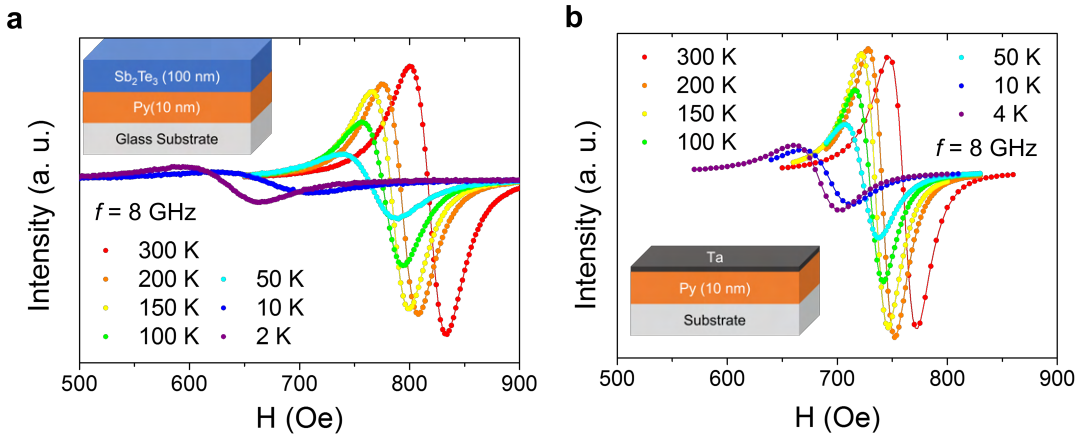


Figure 6.1 – Ferromagnetic resonance absorption as a function of temperature for (a) the Py(10)/ST(100) bilayer and (b) reference capped Py(10 nm) sample (Py(10)/Ta(3)). The solid lines correspond to the derivated asymmetric Lorentzian fits, given by equation 2.11

The peaks were fitted to the derivated asymmetric Lorentzian of equation 2.11, and the fits are also present in Figure 6.1.(a) and (b) as full lines. From the fits, the resonance field H_{res} and linewidth ΔH were obtained and their frequency dependence can be found in Figure 6.2 and Figure 6.4, respectively.

The frequency dependence on H_{res} is shown in Figure 6.2.(a) and (b) for the bilayer and capped sample, respectively. It follows the expected behaviour described by Kittel, with the full lines being the fits made to the Kittel equation (equation 2.6). Moreover, as it was previously noted, the resonance field decreases with cooling. From the Kittel

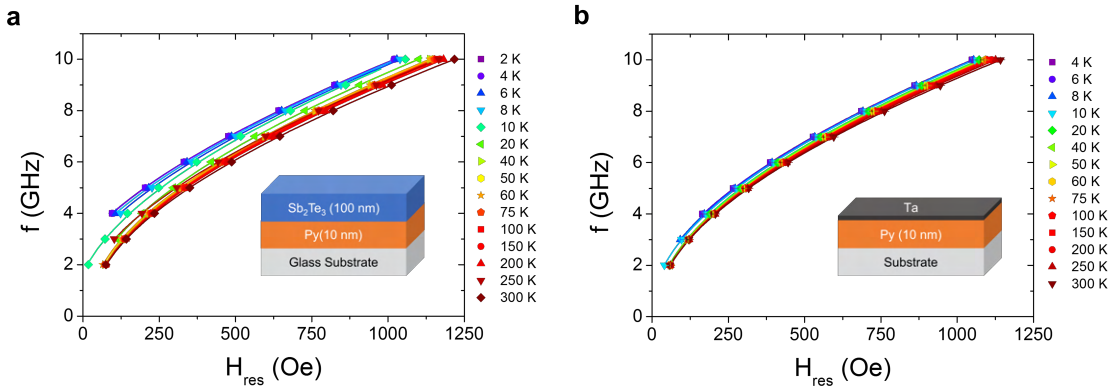


Figure 6.2 – Resonance field H_{res} frequency dependence for (a) the Py(10)/ST(100) bilayer and (b) reference capped Py(10 nm) sample. The fits to Kittel equation (equation 2.6 are shown as solid lines for the different temperatures.

fits, the saturation magnetisation of the permalloy M_S and the anisotropy field H_k were calculated and are represented in Figure 6.3 for both samples. The bilayer temperature dependence of these parameters is the same as the capped sample, confirming that the capped sample can be taken as a suitable reference, as it was verified in the previous Chapter. The M_S decreases under heating, arising from thermal fluctuations, as it has been observed for Py thin films FMR measurements[199]. It is also in accordance with the magnetoresistance (MR) dependence on temperature discussed in the previous Chapter, which corroborates that the MR depends on the M_S. The anisotropy field is negative until approximately 20 K. By further cooling, the anisotropy field increases exponentially as it has been reported, becoming positive at the lowest temperatures, indicating that there is a change in the preferential direction of the thin film magnetisation[216,217], which is in accordance with the decrease observed in M_S at the lowest temperatures.

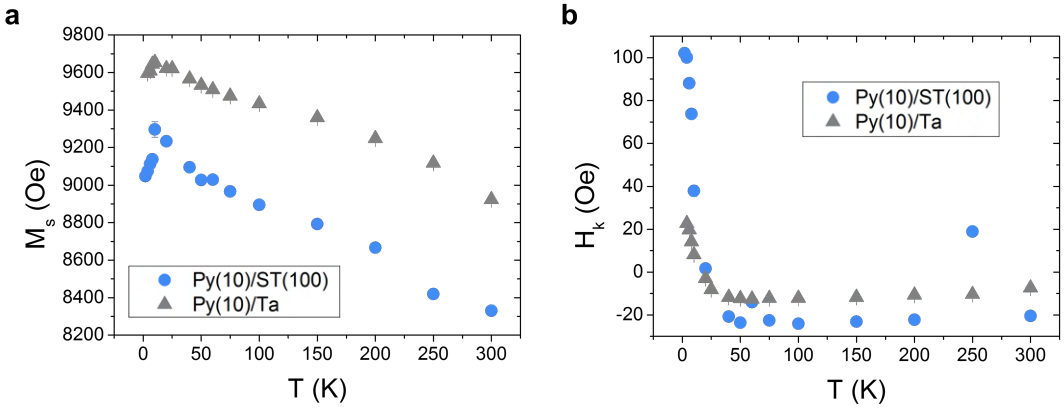


Figure 6.3 – (a) Magnetisation M_S and (b) Anisotropy field H_k dependence on temperature.

The linewidth ΔH is present in Figure 6.4.(a) and (b) as a function of temperature for the bilayer and capped sample, respectively, showing a linear dependence on fre-

quency, as described by equation 2.7. It generally increases with cooling, as it was also previously noted, except for temperatures below 10 K, when it decreases. Moreover, the bilayer linewidths have higher values than the reference sample for the whole range of temperatures studied here. As it was explored in the previous Chapter, this can be due to the presence of spin pumping into the TI Sb_2Te_3 layer. However, it is also due to an increase in the inhomogeneuous linewdith ΔH_0. ΔH_0 increases with cooling for both samples, but it reaches much higher values for the bilayer. From the XRR results explored in Chapter 5, this increase could be explained by the interface between the Sb_2Te_3 and Py layers, as it was discussed in the previous Chapter structural and morphological analysis.

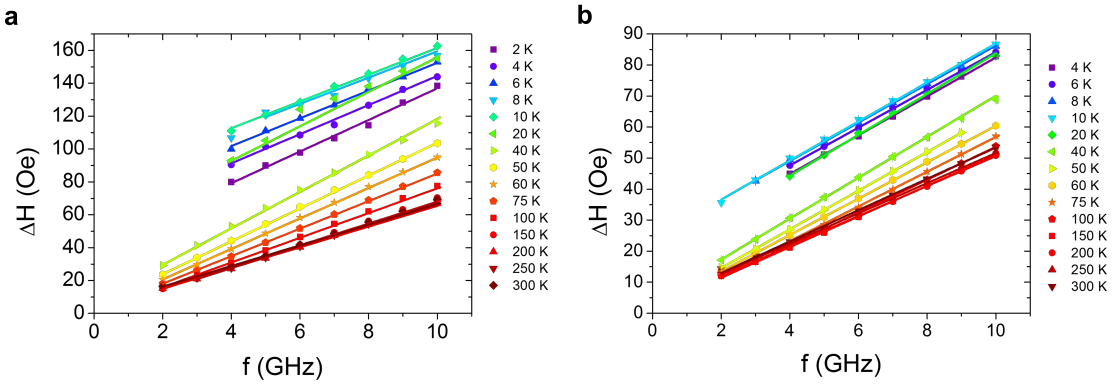


Figure 6.4 – The Ferromagnetic resonance linewidth ΔH as a function of the frequency for (a) the Py(10)/ST(100) bilayer and (b) reference capped Py(10 nm) sample. The linear fits of the different temperatures are shown as solid lines.

Linear fits were performed to the linewidth frequency dependence and are also represented on Figure 6.4, as solid lines. Following equation 2.7, the Gilbert damping was calculated, and it can be found on Figure 6.5 as a function of temperature for both the bilayer and reference sample. The damping is higher at all temperatures for the bilayer than for the capped Py reference sample. This behaviour is related with an additional damping source, which can be due to intrinsic mechanisms of the ferromagnetic material itself or to extrinsic contributions due to structural inhomogeneity and grain boundaries of the Py, among others. Another mechanism that can lead to an increase in the damping is an added magnetic relaxation channel via spin pumping[113,200], which as been previously observed in TI systems[202,203] and other bilayers systems[200,204]. Thus, the increase in damping from the reference value is expected to occur due to spin pumping.

Despite the difference in values, a similar temperature dependence of the reference and bilayers damping is seen. Until approximately 40 K, the damping increases with cooling. Below this maximum, the damping decreases following the reference samples behaviour except at the lowest temperatures. In this regime, the bilayers exhibit a damping increase by further cooling. This increase is 20 % from 8 K to 2 K for the Py(10)/ST(100) bilayer. This added damping increase with cooling indicates that spin injection is further enhanced at these temperatures. As it was previously discussed in

Chapter 4 for sputtered Sb_2Te_3, at low temperatures, the TI states are prominent and as such, this enhancement could be caused by their presence.

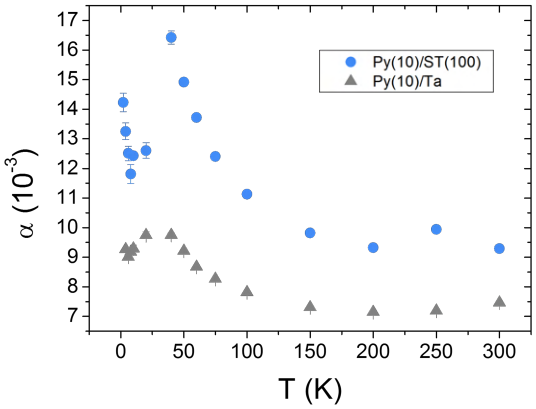


Figure 6.5 – Temperature dependence of the Gilbert Damping for the the Py(10)/ST(100) bilayer and reference capped Py(10 nm) sample (Py(10)/Ta(3)).

6.2.2 Characterisation of the generated spin currents

The spin current J_S created in the Py layer can be injected into the Sb_2Te_3 layer due to the magnetisation precession of Py as analysed in Chapter 2. This spin current can be determined through the FMR behaviour of the bilayers, being given by 2.14. It is proportional to the spin mixing conduction $g^{\uparrow\downarrow}$ (equation 2.13), which is in turn proportional to the difference between the damping of the bilayer and of the Py reference sample.

The spin mixing conduction $g^{\uparrow\downarrow}$ is represented in Figure 6.6.(a) as a function of temperature. It indicates the global spin transmission in the bilayer system from the Py to the Sb_2Te_3 layer. It has a value of $(1.13 \pm 0.06) \times 10^{19}$ m^{-2} at room temperature, increasing with cooling until 40 K, reaching a value of $(3.3 \pm 0.1) \times 10^{19}$ m^{-2}. With further cooling it decreases, until reaching its minimum value between 8 and 10 K. It has a slight increase for the lowest measured temperatures, being $(2.0 \pm 0.2) \times 10^{19}$ m^{-2} at 4 K. These values are comparable with previously reported values for Bi_2Se_3/Py bilayers[61] at room temperature, for example, and two to three times higher at lower temperatures.

The temperature dependence of $g^{\uparrow\downarrow}$ is similar to the damping behaviour of the bilayer seen in Figure 6.5, having a maximum at 40 K, and then an increase at low temperatures. Since $g^{\uparrow\downarrow}$ is proportional to the difference between the damping of the bilayer and the reference sample, this indicates the spin mixing through the interface between the Sb_2Te_3 and Py layers is increased with cooling, specially around 40 K and at the lowest temperatures. As previously noted, at low temperatures, the presence of the TSS state, verified through the magnetoconductance, could be improving this intermixing. Moreover, for the 100 nm thin film of Sb_2Te_3, below 80 K, the type of conduction changes, with electrons becoming the majority charge carrier. This change could possibly aid

the transmission of the spins through the interface, leading to the sharper increase in cooling observed in $g^{\uparrow\downarrow}$ below 80 K.

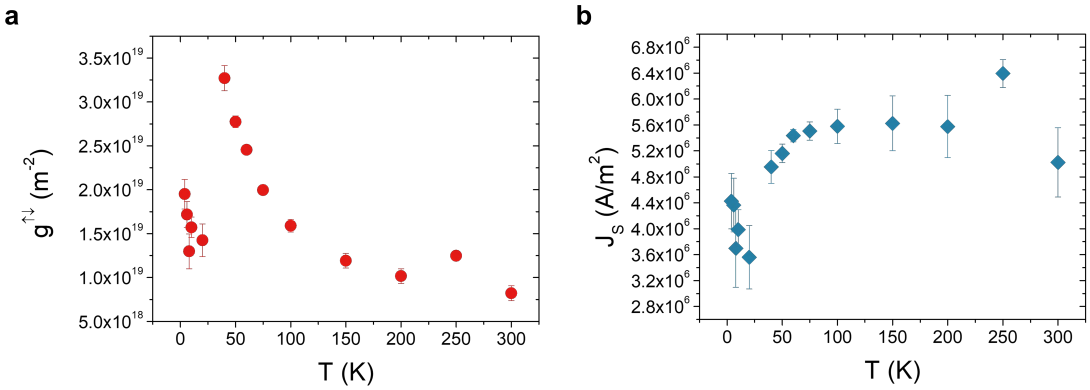


Figure 6.6 – (a) The Spin mixing conduction $g^{\uparrow\downarrow}$ and (b) the spin current J_S as a function of temperature.

With $g^{\uparrow\downarrow}$ calculated, the spin current J_S was obtained and it is shown in Figure 6.6.(b) as a function of temperature. It has a different behaviour when compared to $g^{\uparrow\downarrow}$. It is approximately constant from room temperature until 100 K, with a value of $(5.5 \pm 0.2) \times 10^6$ Am^{-2}. Below 100 K it decreases until 10 K, when it reaches its minimum value of $(3.6 \pm 0.5) \times 10^6$ Am^{-2}. As it was seen in the α and $g^{\uparrow\downarrow}$ temperature dependences, it then increases with cooling, having a value of $(4.4 \pm 0.4) \times 10^6$ at 4 K. This behaviour with temperature can be explained due to J_S being proportional to $g^{\uparrow\downarrow}$ and having approximately a dependence on the inverse of M_S.

6.3 Spin pumping in the FM/TI bilayers

Having the magnetisation dynamics characterised as a function of temperature, the spin to charge conversion in Sb_2Te_3 can be examined by spin pumping experiments. As discussed in Chapter 2, in a spin pumping experiment, like in the FMR experiments, an RF magnetic field h_{rf} excites the magnetisation dynamics of the system, inducing the precession of the magnetisation **M** in the Py layer. This precession at the resonance field creates a 3D spin current J_S that is injected into the above Sb_2Te_3 layer. Due to the strong spin orbit coupling of Sb_2Te_3, the spin current can be converted to a charge current through the Inverse Spin Hall effect (ISHE) of the bulk. This current can be detected through the measured voltage V_{SP} and calculated from the symmetric part of the output signal.

Figure 6.7.(a) shows the obtained V_{SP} signal at 300 K and 2 K and at 4 GHz with negative and positive applied magnetic fields for the Py(10)/ST(100) bilayer. The symmetric part of the measured signals at positive and negative field has opposite signs, which is the expected behaviour if the spin current is converted into the charge current through ISHE, due to the different spin directions[69,218]. Moreover, the signal has an opposite

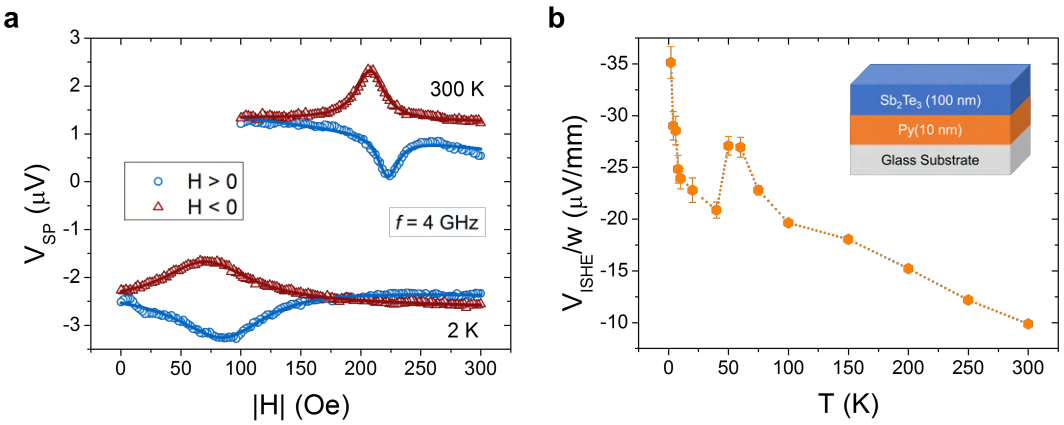


Figure 6.7 – Spin pumping as a function of temperature in the Py(10)/ST(100) bilayer. (a) Spin pumping voltage V_{SP} as a function of the applied magnetic field for positive and negative fields, measured at 4 GHz and at 300 and 2 K. The asymmetric Lorentzian (equation 2.16) fits to the peaks are shown as full lines. (b) The ISHE voltage V_{ISHE} normalised to the width of the sample as a function of temperature.

sign to the field, being positive for negative applied magnetic fields and vice-versa.

Besides the ISHE contribution, the measured signal can have three other sources: the anisotropic magnetoresistance (AMR) and anomalous Hall effect (AHE) of the Py layer, and the Seebeck effect[61,71,205]. In this measurement configuration of a 90º degree angle between the rf and applied magnetic fields[205], the AMR and AHE signals have an asymmetric Lorentzian shape[61]. Moreover, the Seebeck effect is an odd function of the applied magnetic field. Considering all these components, the measured data was fitted to the sum of the symmetric and asymmetric Lorentzian function, given by equation 2.16, and shown as solid lines in Figure 6.7.(a). To calculate V_{ISHE}, the possible Seebeck effects are removed by averaging the positive and negative magnetic field symmetric component of V_{SP}, V_{sym}:

$$V_{ISHE} = \frac{V_{sym}(+H) - V_{sym}(-H)}{2} \tag{6.1}$$

Figure 6.7.(b) shows the calculated V_{ISHE} normalised by the width of the sample as a function of temperature. V_{ISHE}/w is $-9.9 \pm 0.3\ \mu$V/mm at room temperature and it increases in magnitude with cooling. It has a local peak, between 50 and 60 K, but with further cooling, it continues to increase until reaching its maximum value of $-35 \pm 2\ \mu$V/mm at 2 K. This dependence is similar to the behaviour of the damping and the spin mixing conduction previously observed. With cooling from 10 K until 2 K, V_{ISHE} has a sharp increase, increasing 45.8%. This is also similar to the behaviour at low temperatures of the damping, indicating that it is directly connected to the damping and to the increase in the injection of the spin current into the ST layer, as seen in the spin mixing conduction. This increase also occurs when the TI surface state conduction is active, and thus the influence of the TSS could also explain this increase at low temperatures.

To further estimate the spin to charge conversion efficiency, spin pumping measure-

ments of the Py(100)/ST(100) bilayer were also carried out at room temperature and at 4 GHz, being shown in Figure 6.8.(a), for positive and negative applied magnetic fields. As for the Py(10)/ST(100) sample, the positive and negative field signals have opposite signs, with the positive magnetic field signal producing a negative signal. However, the signal is much more asymmetric than the thinner Py bilayer signal. V_{ISHE}/w was also calculated, being –4.42 ± 0.06 μV/mm. It is approximately half the value obtained for the Py(10)/ST(100) bilayer, which can be explained by the lower bilayer resistance and also by the lower value of the spin current calculated in Chapter 5.

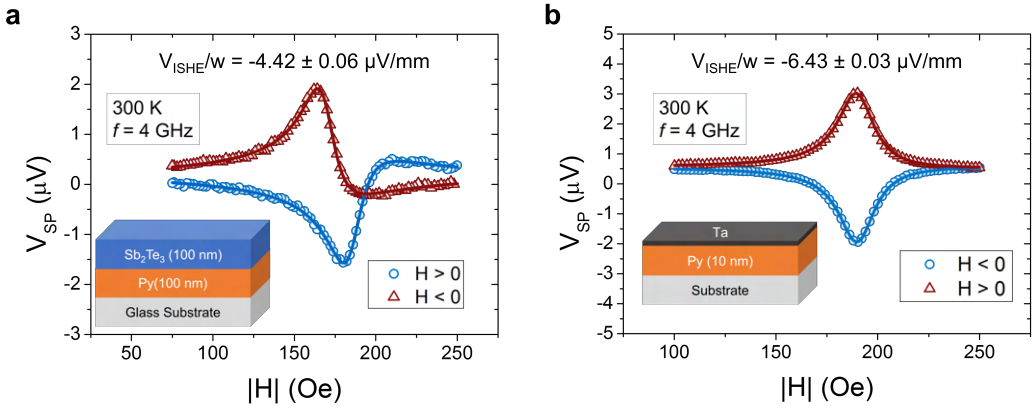


Figure 6.8 – Spin pumping at room temperature. Spin pumping voltage V_{SP} as a function of the applied magnetic field for positive and negative fields, measured at 4 GHz for (a) the Py(100)/ST(100) bilayer and (b) reference capped Py(10 nm) sample (Py(10)/Ta(3)). The asymmetric Lorentzian (equation 2.16) fits to the peaks are shown as full lines. The calculated normalised V_{ISHE}/w is also shown for the two samples.

Spin pumping on the reference Py capped sample (Py(10)/Ta(3)) was also evaluated at room temperature and 4 GHz and it is shown in Figure 6.8.(b). It follows the same trend as observed for the Sb_2Te_3 bilayers, with opposite signs for opposite applied magnetic fields. The signals are symmetric as for the Sb_2Te_3 bilayer, which indicates that the magnetoresistance effects from the Py thin film layer are negligible. The calculated V_{ISHE}/w is –6.43 ± 0.03 μV/mm. It is smaller than the Py(10)/ST(100) voltage, but it is a significant value. Since Ta is a well known Heavy metal, the observed signal could be due to the ISHE of the Ta capping, as previously observed[219,219].

6.4 Spin to charge conversion efficiency of Sb_2Te_3

To characterise the SCC of Sb_2Te_3 based on ISHE, the spin hall angle θ_{SH} can be calculated from V_{ISHE}. Considering equation 2.15, all the dependencies of V_{ISHE} have been obtained except for the spin diffusion length λ_{SD}. To directly measure this parameter, several bilayer structures with different thickness of the Sb_2Te_3 layer would need to be fabricated, optimised and their spin pumping measured. However, an estimation of λ_{SD} can be obtained from the magnetoconductance measurements presented in Chapter

4. In materials where the predominant source of spin scattering is the spin-orbit coupling, the spin diffusion length λ_{SD} is dominated by the spin orbit relaxation length L_{SO}. From this consideration, it can be assumed that these parameters are approximately equal[220]. Since Sb_2Te_3 has high spin orbit coupling, the spin orbit relaxation length can be taken as λ_{SD}, as previously noted for Bi_2Se_3[61]. The λ_{SD} calculated from the magnetoconductance fits discussed in Chapter 4 is presented in Figure 6.9.(a) as a function of temperature. At 2 K, its value is approximately 27 nm, almost twice as high than previously reported values at low temperatures[61]. λ_{SD} decreases to approximately 7.7 nm at 10 K. A temperature power law was fitted to the data, and the fit can be seen as a full line in Figure 6.9.(a). It is verified that λ_{SD} is proportional to $T^{-0.97}$ within this range of low temperatures. Previous reports show a decrease of the λ_{SD} with heating for similar materials[61], but a similar temperature dependence as the one observed here has not yet been reported to the best of our knowledge. The decrease with heating demonstrates that a propagating spin current is dissipated faster by heating the sample from 2 K to 10 K. Thus, an injected spin current into Sb_2Te_3 propagates more into its bulk by cooling, as the inset of Figure 6.9.(a) shows. This is in accordance with the FMR damping behaviour at low temperatures, with the increase of 20 % of the damping from 8 K to 2 K and it explaines the increase seen on Figure 6.6 of J_S at the lowest temperatures. It can also explain the sharp increase at low temperatures of V_{ISHE}, since V_{ISHE} is approximately proportional to λ_{SD}, for this 100 nm Sb_2Te_3 layer. With these considerations, the ISHE generated electric field E_{ISHE} is overall decreased with heating, leading to the decrease in the voltage picked up through the spin pumping voltage, which is represented in the inset of Figure 6.9.(a).

With the spin diffusion length calculated, the spin hall angle θ_{SH} of Sb_2Te_3 can be obtained as a function of temperature from the Py(10)/ST(100) bilayer results and also at room temperatures from the Py(100)/ST(100) measurement. The spin diffusion length λ_{SD} for temperatures higher than 10 K is assumed to be constant, taking the value of 5 nm, which has been obtained for similar TIs[61]. Thus, θ_{SH} takes the value at room temperature of -0.0033 ± 0.0004 and -0.003 ± 0.002 for the Py(10)/ST(100) and Py(100)/ST(100), respectively. This value is equal within the uncertainty as expected since the Sb_2Te_3 film is the same on both bilayers.

The temperature dependence of the apparent spin hall angle θ_{SH} obtained from the Py(10)/ST(100) measurements is depicted in Figure 6.9.(b). By cooling the sample, θ_{SH} increases monotonously with this behaviour having been previously observed in a similar system[61]. However, it has a local maximum peak at 50 K. This corresponds to the maximum of the damping and also of the spin mixing conduction and V_{ISHE}. Thus, it can be concluded that this peak observed in these two parameters is due to the ISHE of Sb_2Te_3. After the local peak, the θ_{SH} value at 40 K is smaller but, with further cooling, it increases, reaching its maximum value of -0.018 ± 0.008 at 20 K. At the lowest temperatures it has a sharp decrease, which is due to the increase seen in λ_{SD}.

Performing a comparison between the herein obtained results with the current state

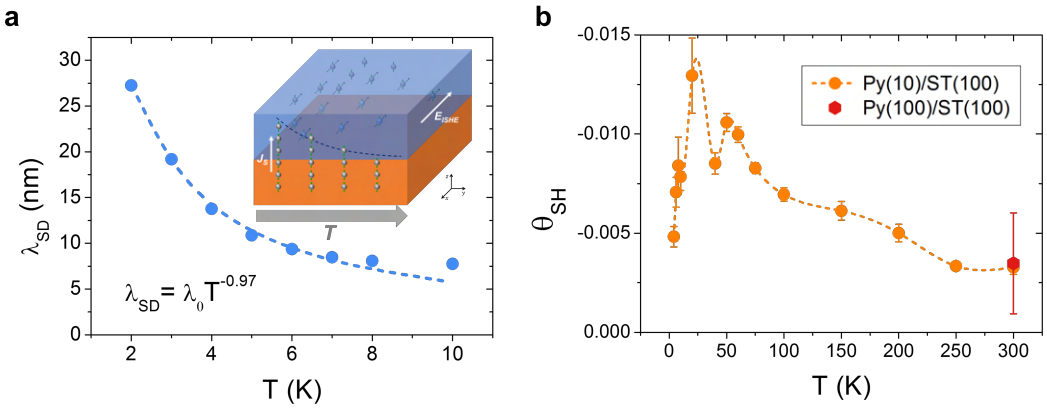


Figure 6.9 – Spin to charge conversion properties of Sb_2Te_3. (a) Spin diffusion length λ_{SD} calculated from the magneconductance results discussed in Chapter 4 as a function of temperature with a schematic of the spin and electronic transport in the Py/Sb_2Te_3 bilayers at low temperatures as an inset. (b) the spin Hall angle θ_{SH} as a function of temperature calculated from the spin pumping measurements.

of the art, Figure 6.10.(a) shows the θ_{SH} for different materials, such as TIs, Heavy Metals and new novel SOC materials like 2D TMDCs materials and STO, among others, and the values obtained in this work. A wide range of spin Hall angle values can be seen, with the TIs having surpassed the widely studied and employed heavy metals, reaching values as high as 52 for a more metallic TI[212]. The latest results show that novel materials also have a very good performance, reaching a value of 0.79[221], higher than the typical value for heavy metals. Our outcome for sputtered Sb_2Te_3 positions it among the typical TIs, with θ_{SH} being similar to other TIs.

However, concerning the technological applications, the spin Hall angle is not the only parameter of importance for SOT applications. For materials with the Inverse Spin Hall effect, the product of the spin hall angle times the spin diffusion length λ_{SD} is a parameter to be optimised. This product is equivalent to the Inverse Edelstein Effect length λ_{IEE} in materials where IEE is the predominant effect[208]. Furthermore, the resistivity of the different SOC materials is also an important parameter. The figure of merit of these materials can thus be taken as he equivalent λ_{IEE} and the resistivity. Taking these parameters into consideration, Figure 6.10.(b) shows the Ashby plot of $\theta_{SH}\lambda_{SD}$ or λ_{IEE} as a function of the resistivity ρ of the analysed materials from different reports. The Heavy metals have the lowest resistivities and lengths. Novel Materials and TIs are well equated, having a wide range of length values. However, TIs have the highest resistivities. The Sb_2Te_3 studied in this work presents the highest resistivity, positioning it quiet well for applications such as the MESO device proposed by Intel[8]. For an optimal performance of this device, a resistivity higher than 10 mΩcm and a λ_{IEE} higher than 5 nm is needed, corresponding to the grey shaded area in Figure 6.10.(b). It is then verified that the studied Sb_2Te_3 is a well positioned material towards future applications.

This promising efficiency of Sb_2Te_3 could be explained based on its structure. DC *et al.*[68] have demonstrated that the charge to spin conversion efficiency is improved due

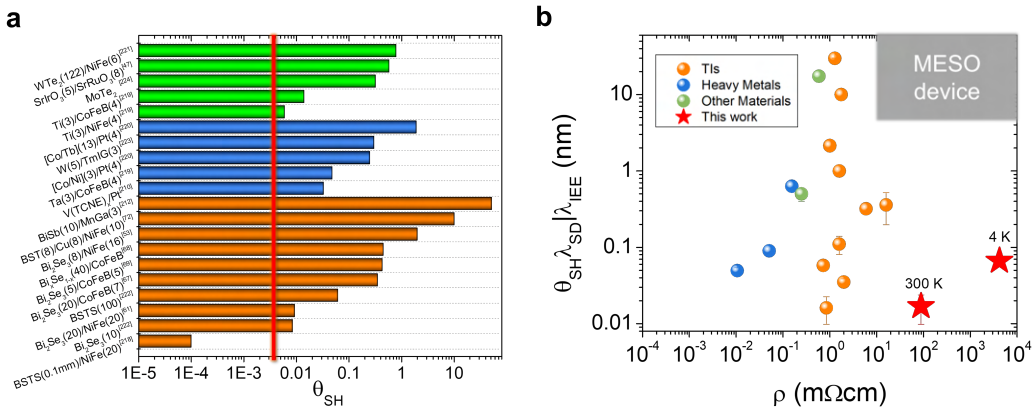


Figure 6.10 – State of the art of SOC materials. (a) Spin Hall angle θ_{SH} at room temperature for different types of materials: Topological Insulators (TIs) (orange)[53,67–69,72,212,218,222], Heavy Metals (Blue)[210,219,220,223] and other materials (TMDCs, STO, etc...)[47,219,221,224] (green). The lines in red depict θ_{SH} at room temperature of Sb_2Te_3 obtained in this work for both bilayers at room temperature. (b) Ashby plot of θ_{SH} times the spin diffusion length λ_{SD} (the equivalent to the IEE length λ_{IEE}) or λ_{IEE} of several materials and of their conductivity: Topological Insulators (orange)[53,61,67–72,213,222], Heavy metals (blue)[209,210,223], and other materials[221,225]. These parameters can be taken as the figure of merit of SOT materials. Very high resistivities and lengths are needed for applications in logic devices like the MESO device, corresponding to the shaded area.

to quantum confinement. This quantum confinement can occur in grains of sputtered thin films, with DC *et al.* having verified that this effect is enhanced by reducing the grain size. Our ion beam sputtered Sb_2Te_3 thin films have grain sizes of roughly 20 nm as observed by the TEM and XRD crystallie determination discussed in Chapter 4. These grains can enhance the intrinsic and expected spin to charge conversion of Sb_2Te_3. Moreover, the temperature dependence of the resistivity is indicative of a semi-amorphous semiconductor behaviour, being caused by the amorphous and grain structure of the thin films. Thus, the grain structure of the sputtered thin films also improved the resistivity, leading to the obtained promising results.

6.5 Conclusions

Through spin pumping measurements, the study of Sb_2Te_3 as a SOC material, when combined with ferromagnetic Py thin films, was achieved. The magnetisation dynamics of a Py(10)/ST(100) bilayer was obtained as a function of temperature for low temperatures, having yielded high Gilbert damping resonance values when compared to capped Py samples, which is indicative of the occurrence of spin pumping into the Sb_2Te_3. Moreover, the behaviour at low temperatures could be explained by the activation of the TSS conduction at the cryogenic temperatures previously discovered in the sputtered Sb_2Te_3 thin films. The spin mixing conduction and spin current were calculated, with values being close to reported values for similar bilayers. The spin current temperature dependence showed, however, that it is roughly constant at high temperatures, with an increase at low temperatures, which can be explained by the temperature dependence

of the bilayer and capped sample damping and saturation magnetisation.

The inverse spin Hall effect was observed through the spin pumping measurements. The corresponding voltage, V_{ISHE}, which corresponds to the charge current converted from the spin current, was obtained as a function of temperature for the Py(10)/ST(100) bilayer and at room temperature for the Py(100)/ST(100) bilayer. V_{ISHE} roughly increases with cooling, reaching its maximum value at the lowest measured temperature. From these measurements, the apparent spin Hall angle was calculated, also showing an increase with cooling, which could also be explained by the change in the electronic properties of the Sb_2Te_3 thin films.

The SCC efficiency was obtained for the studied Sb_2Te_3 bilayer, with competitive values being achieved, specially when considering applications in logic devices, such as the MESO device proposed by Intel. The results presented and discussed in this Chapter discovered that sputtered Sb_2Te_3 is a material of interest for SOT applications, opening the door to further studies and implementations of this TI for spinorbitronics applications.

CHAPTER 7

Sputtered topological insulator nanostructures towards flexible spintronics devices

This chapter [1] [2] is devoted to the development of flexible nanostructures with the end goal of spinorbitronics flexible devices. First, the structural and electronic transport properties of flexible thin films of Sb_2Te_3 are analysed. The thin films are deposited by ion beam sputtering, a technique already present in the semiconducting and spintronics industry. The depositions occurred on Kapton ® polyimide substrates, which is a flexible material. The effects of the sputtering plasma voltage and thickness on the structural and transport properties are discussed, namely its resistivity and Seebeck coefficient. Through the combination of these studies, the influence of the fabrication parameters on the thin films and the different contributions to the electronic conduction are unravelled, paving the way for further research into flexible TIs and their implementation in flexible spinorbitronics devices.

Following these studies, the structural and electronic properties of flexible FM/TI/FM trilayers are dissected. Preliminary studies of their magnetisation dynamics, employing not only the usual VNA-FMR technique, but the layer specific XFMR, were also used to gain insights into the propagation of spin currents and their effects on neighbouring FM materials.

[1] Adapted from S. Ferreira-Teixeira, A. L. Pires, J. P. Araújo and A. M. Pereira, *Structural and transport properties of sputtered topological insulator thin films towards flexible spintronics devices*, in preparation. S. Ferreira-Teixeira contributions to the publication: structural and morphological analysis, measurement of the resistivity and Seebeck Coefficient, and data analysis. Responsible for the main manuscript preparation.

[2] Adapted from S. Ferreira-Teixeira, A. L. Pires, S. A. Bunyaev, G. N. Kakazei, J. P. Araújo and A. M. Pereira *Mediation of the magnetisation dynamics through a topological insulator on flexible FM/TI/FM sputtered nanostructures.*, in preparation. S. Ferreira-Teixeira contributions to the publication: sample fabrication, structural and morphological analysis, measurement of the resistivity and Seebeck Coefficient, and data analysis. Responsible for the main manuscript preparation.

7.1 Introduction

The Era of the Internet of Things (IoT) demands adaptable and alternative devices, which can be achieved by using flexible and stretchable electronics. By integrating electronic systems with flexible substrates, materials, and structures, a wide range of attractive applications can be realised, from wearable devices to flexible displays[226–230]. To fully attain a wide usage, innovative spintronic devices should also be developed based on flexible materials to obtain novel data storage and logic devices. Towards this goal, several efforts have been made, such as studying the strain effects on perpendicular magnetic anisotropy[231] and exchange bias[232], and the development of memory elements[233].

In the last few years, a lot of research within spintronics has been dedicated to Spinorbitronics, which is based on the spin to charge interconversion, exploiting the high spin-orbit coupling (SOC) of certain non-magnetic materials. These materials are commonly heavy metals, like Pt, W and Ta[44,158,159]. Moreover, 2D Van der Waals structures, for example, Graphene/WS_2[46], have also been explored. A new class of quantum materials, topological insulators (TIs), which exhibit a metallic topological surface state (TSS), and host spin-momentum locking[177], have also shown outstanding spin to charge inter-conversion performances[54,67]. One set of materials which exhibit the TSS is the Bi_2Te_3 family of semiconductors, having been discovered in 2009 as TI materials[52].

Due to the demand of adapting and creating flexible devices, the control of spin currents via SOC has already been the subject of studies for the development of flexible spintronics[234–236]. Fe/Pt/Fe trilayers were grown on flexible mica substrates and their SCI was investigated, having observed a tunable charge to spin conversion with the application of compressive strain, with over 50% enhancement of the spin hall angle being obtained for a 6.26% strained film[234]. Pt/Co bilayers were also investigated, having shown that the frequency of the ferromagnetic resonance can be tuned using purely mechanical strain, with the device being reversibly manipulated over 10^4 cycles, which demonstrates robustness for flexible devices[235].

Despite these efforts and developments, these studies focused only on Heavy Metals, namely Pt. As such, the integration of TIs in flexible SOC devices has not yet been explored. Though they have gained great attention due to their TI properties, these materials have also been extensively studied as thermoelectric materials[237–239]. With the end goal of implementation of flexible thermoelectric devices, advancements in the structural and electronic properties of flexible TI materials have been obtained[10,240–242]. However, these studies have not yet been translated into the exploitation of TIs for SCI applications, and thus the creation of spinorbitronic flexible devices based on TIs needs to be developed.

In this chapter, insights into the realisation of flexible TIs are achieved through the structural and electronic studies of sputtered Sb_2Te_3 thin films on kapton flexible sub-

strates. The interplay between the thickness and structure of the thin films will be explained through transport measurements and XRD characterisation, which yields what should be the optimal fabrication parameters and what are the transport characteristics of the optimised film. The flexible TI thin films are then implemented in flexible trilayer FM/TI/FM nanostructures to study what is the role of the TI in the spin pumping and transmission of spin currents in a stack structure. FMR is employed to verify the dependence of the magnetisation dynamics of the FM materials on the TI layer, with preliminary results showing that the TI can act as an efficient spin sink.

7.2 Flexible Sb_2Te_3 topological insulator thin films

7.2.1 Structural and Morphological characterisation

The flexible Sb_2Te_3 thin films were fabricated using ion beam sputtering, in depositions of one hour. The thickness of the thin films is shown in Figure 7.1.(a) as a function of the beam voltage V_{Beam} used for deposition. The thickness of the thin films increases linearly with V_{Beam}, at a rate of 0.75 nm $V^{-1}h^{-1}$, being 192 and 555 nm for the thin films deposited with 500 and 1000 V, respectively.

Figure 7.1.(b) displays the XRD diffractograms obtained for the different thin films presenting several diffraction peaks. The peak at 14.38º marked with an asterisk is due to the Kapton substrate. The broad plateau until roughly 35º also comes from the amorphous contribution of the polymeric chain of the Kapton substrate, being most prominent for the lower V_{Beam} thin films, which is explained by their lower thickness.

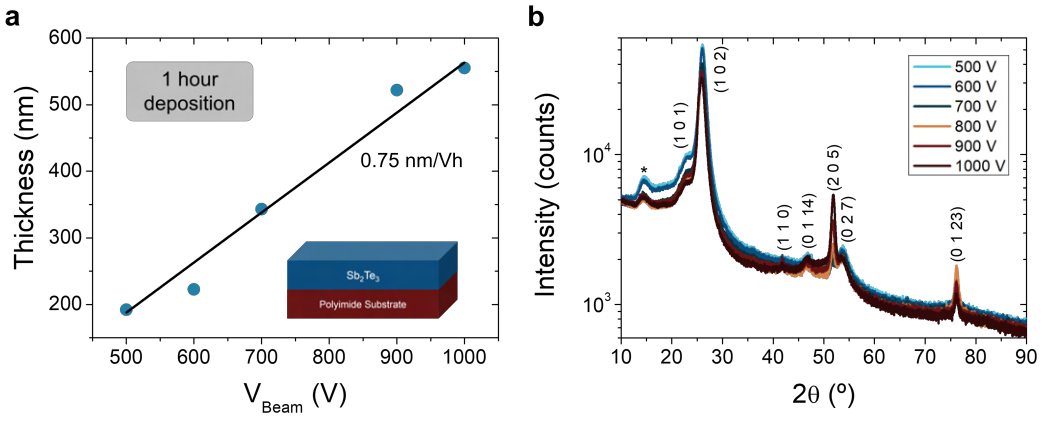


Figure 7.1 – Structural characterisation of the flexible thin films. (a) The thickness of the thin films as a function of the beam Voltage for a deposition of one hour. (b) The XRD diffractogram of the flexible Sb_2Te_3 thin films deposited at the different voltages. The peak marked with * corresponds to the substrate.

The other observed peaks can be attributed to different reflections of the Sb_2Te_3 phase, with a rhombohedral crystal geometry (R-3m)[162]. The peak angles and the corresponding attributed planes are the following: 22.8º, (1 0 1); 26.0º, (1 0 2); 41.9º, (1

1 0); 46.8º, (0 1 14); 51.7º, (2 0 5); 53.7º, (0 2 7); 76.1º, (0 1 23). From the wide range of indexed planes, it can be concluded that the thin films are polycrystalline.

Since the only variation between measurements are the thin films thickness and beam voltage V_{Beam}, with the substrate and measurement conditions being the same, the intensity of the peaks can be directly compared between different samples. With this consideration, the biggest reflection occurs for the (1 0 2) plane, with the smaller V_{Beam} thin films having the higher intensity even when considering the substrate background. Moreover, the (0 2 7) peak is more prominent for the films deposited with smaller V_{Beam} whereas the intensity of the (2 0 5) peak increases with V_{Beam}. The two peaks at 41.9º and 46.8º have the lowest intensity, with the (1 1 0) reflection being sharper for the films deposited with higher V_{Beam}. The last identified peak, indexed by the (0 1 23) phase, is sharper than other peaks and has the highest intensity for the 800 V deposited thin films, decreasing both for higher and lower voltages. These changes in intensity and peak width indicate that by increasing the V_{Beam}, the intrinsic structure of the thin films is changing, with certain directions beings favoured over others with a higher or lower V_{Beam}.

Fits to the diffractograms were performed for all the studied samples and for angles higher than 35º. These can be found in Figure 7.2. For angles below 35º, the influence of the substrate, which cannot be properly removed, does not allow to perform these fits.

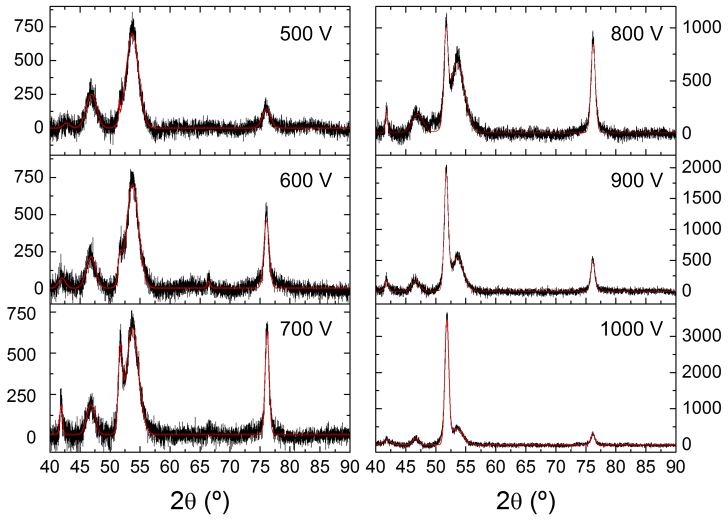


Figure 7.2 – XRD diffractograms of the flexible Sb_2Te_3 thin films with the background subtracted and the respective fits as a solid red line.

From the fits, Scherrer analysis as described in equation 2.2 of Chapter 2 was employed to obtain the grain sizes *d* of each peak, except the (1 0 1) and (1 0 2). In Figure 7.3, the sizes obtained for the fitted peaks are shown as a function of V_{Beam}, with the (1 1 0) grain size being shown in Figure 7.7. These range from 3 nm to 20 nm, depending on the peak and beam voltage. The peak with the highest grain size corresponds to the

(1 1 0) reflection and the lowest to the (0 2 7) reflection. These results show that the flexible films are constituted by nanocrystallites of different crystalline orientation, with varying sizes.

Considering the structural analysis present here and the structure of the Sb_2Te_3 thin films deposited on glass discussed in Chapter 4, it can be inferred that these flexible films are also constituted by the nanocrystalline grains of different orientation within an amorphous matrix. Moreover, it can be expected a similar V_{Beam} influence on the structure as an increase in thickness. By depositing for a longer time, i.e. a higher thickness film, there was diffusion of Te through the film. In contrast, here the deposition time of the flexible films was always one hour. However, by increasing the V_{Beam}, the energy of the incident materials is higher. Thus, the Te diffusion effect could be enhanced, due to the higher energy and consequently higher temperature of the film after the impact of the materials. These effects can explain the different observed directions in the XRD and their change with V_{Beam}. As such, a change in V_{Beam} changes the structural properties of the films, namely the orientation and size of the nanocrytalline grains.

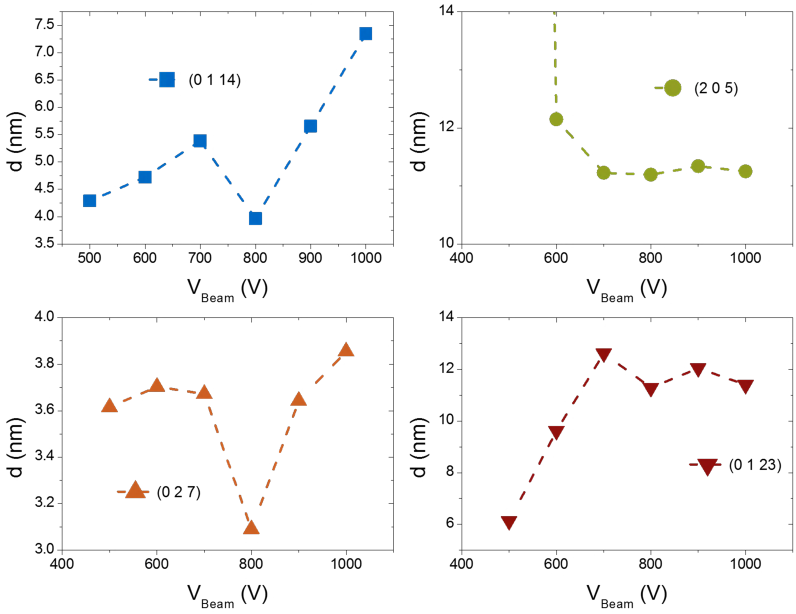


Figure 7.3 – The grain sizes of the flexible Sb_2Te_3 thin films as a function of the Beam voltage V_{Beam} obtained from the FWHM of the corresponding XRD peaks by using Scherrer's analysis. The dashed lines are guides to the eye.

7.2.2 Electronic properties

The resistivity ρ as a function of temperature is shown in Figure 7.4.(a). The resistivity increases with cooling for all samples, having a semiconducting behaviour. The ρ values range between 8.34×10^{-2} and 1.2 Ωcm at 280 K and 3.43×10^{-1} and 2.49 Ωcm at 15 K. These ρ values are much higher than previously reported values for Sb_2Te_3 [148,243],

being similar to insulating/semiconducting BSTS[59,167], BTS[166] and Sn-BSTS[244].

The thin films deposited with lower V_{Beam} present a larger increase in ρ at lower temperatures, roughly below 50 K. This could be explained considering the dependence of the thickness of the film on V_{Beam}. In Chapter 4, the Sb_2Te_3 films deposited on glass substrates showed that the resistivity generally increases for thinner films. Thus, since lower V_{Beam} films also have lower thicknesses, this effect should indeed be more prominent for lower V_{Beam} films. This sharp increase results in a variation of roughly three orders of magnitude for the lower V_{Beam} films, whereas the 900 and 1000 V film ρ increases only one order of magnitude with cooling.

To further understand the V_{Beam} influence on the conduction, Figure 7.4.(b) shows the V_{Beam} dependence of ρ at 280 K and 15 K. There is an increase of three orders of magnitude with a decrease in temperature for V_{Beam} smaller than 800 V. For higher V_{Beam}, the increase with temperature is smaller, becoming less than one order of magnitude at 1000 V. Each temperature also has a similar V_{Beam} dependence. First, ρ decreases from 500 to 600 V. Then it increases until its maximum value, either at 700 V at 15 K or 800 V at 280 K. By further increasing V_{Beam}, ρ becomes smaller, having its lowest value at 1000 V.

This behaviour could be explained by a combination of thickness and structural effects. By increasing V_{Beam} from 500 to 600 V, the structural properties are not effectively altered while the thickness is increased, as discussed in the previous subsection. As seen in Chapter 4, thicker films have lower resistivity values. By further increasing V_{Beam}, the thickness also increases but the structural properties are altered. As seen from the XRD analysis, the structure does not change monotonously with V_{Beam}, with for example the (0 1 23) peak having the highest intensity for the 800 V films. Moreover, the grain sizes associated with each reflection also have a change of behaviour at 800 V, either increasing (reflection (0 1 14)) or remaining roughly constant (reflection (0 1 23)) for higher beam voltages, as seen in Figure 7.3.

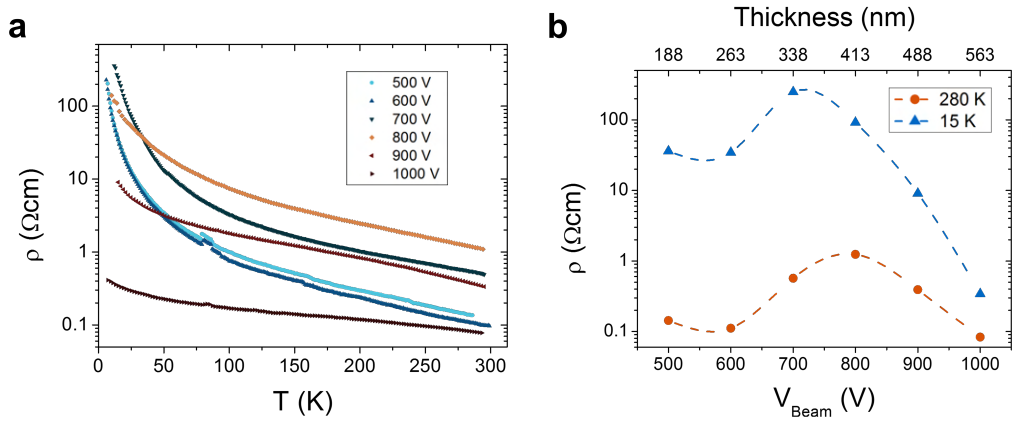


Figure 7.4 – Electrical resistivity of the flexible Sb_2Te_3 thin films. Resistivity as a function of (a) temperature for the thin films deposited at the different V_{Beam} and (b) V_{Beam} at 15 K and 280 K. The dashed lines are a guide to the eye.

The Seebeck coefficient *S* was also measured as a function of temperature, being displayed in Figure 7.5.(a). This transport property can be an effective tool to disentangle the different conduction contributions in TIs thin films in the absence of magnetic fields[58,59]. *S* is positive for all the thin films at room temperature, having values between 52.5 μV/K and 78 μV/K at 280 K, which are within previously reported values for Sb_2Te_3 thin films[148,243] and as expected for undoped Sb_2Te_3. By cooling the films, the highest V_{Beam} samples show a nonlinear *T* dependence of *S*, with an increase until reaching a maximum value around roughly 260 K. This behaviour has previously been ascribed to hole carriers being generated in a valence band of a semiconductor via thermal excitations of electrons to an upper impurity trapping level[59]. From the structural properties, we can see that due to the polycrystalline nature of the films, the different grain sizes can create additional bands, which could create this effect.

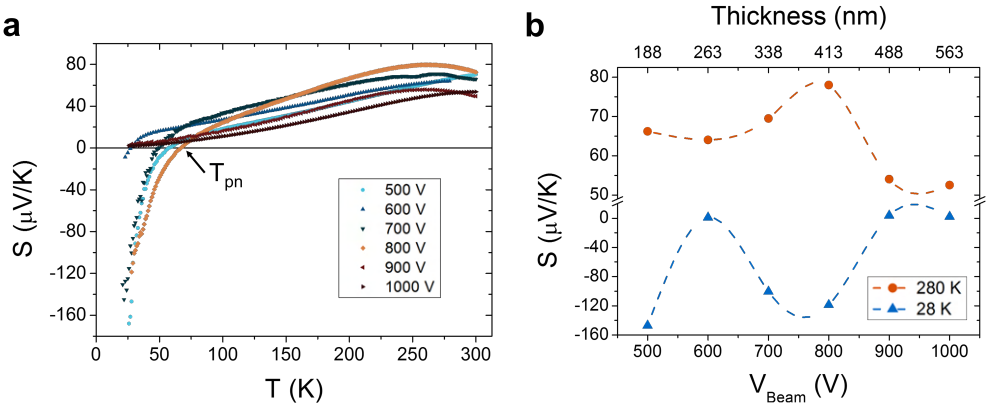


Figure 7.5 – Seebeck Coefficient of the flexible Sb_2Te_3 thin films. (a) The Seebeck Coefficient as a function of temperature for the thin films deposited at the different V_{Beam}. The temperature at which the transition from p-type conduction (positive Seebeck values) to n-type conduction (negative Seebeck values) Tpn is marked for the sample deposited at 800 V. (b) Seebeck coefficient as a function of V_{Beam} at 28 K and 280 K. The dashed lines are a guide to the eye.

With further cooling, *S* starts to decrease, eventually changing sign for the lower V_{Beam} films while always being positive for the 900 and 1000 V films, as reported for bulk Sb_2Te_3[163] and previously for the thicker Sb_2Te_3 films in Chapter 4. The sign of *S* indicates what are the majority charge carriers. As such, at high temperatures, the positive sign shows that holes are the majority charge carrier and that all the films are p-type semiconductors. However, when it becomes negative for the lower V_{Beam} films, electrons become the majority charge carrier. Thus, there is a change from p-type to n-type conduction. This has been previously observed in BSTS thin films, where the change in sign of *S* and majority charge carriers is attributed to surface conduction, which is n-type, versus bulk conduction being p-type[59]. Previous measurements of the Hall coefficient have also seen similar changes in charge carriers on BSTS and BST, which were also explained by n-type surface conduction and a p-type bulk[166,167]. In Chapter 4, this was also observed for the Sb_2Te_3 films fabricated with the same method on glass substrates, which was explained by a parallel model of a surface n-type conducting in

parallel to the bulk p-type.

Upon becoming negative, S reaches the highest absolute values at the lowest temperatures for the films fabricated with 500, 700 and 800 V. However, the 600 V film, which also shows the change in sign, reaches much smaller values when compared to the other films, having a behaviour closer to the 900 and 1000 V films. This is in accordance with the behaviour of ρ, where the resistivity of the 600 V is closer to that of the 900 V and 1000 V films.

Figure 7.5.(b) shows the V_{Beam} dependence of S at 280 K and 28 K. Like previously mentioned, at 280 K, S is positive for all films. However, at 28 K, it is only positive for the 900 and 1000 V films, with the 600 V value being negative but extremely small when compared with the other films. Moreover, S behaves like ρ at both temperatures when considering its V_{Beam} dependence. First, it decreases in magnitude from 500 to 600 V, but then increases until the maximum, which occurs at 800 V for both temperatures. It then decreases again until reaching the lowest values for the 900 and 1000 V. This can also be described by a combination of thickness and structural changes similar to the behaviour of ρ with V_{Beam}.

To better understand the electronic conduction in these flexible thin films, the model of the conductivity for the thin films deposited on glass substrates presented in Chapter 4 was employed. This model describes the conduction of Sb_2Te_3 films as three resistances conducting in parallel: the p-type semiconductor bulk, a n-type semiconductor surface and the TSS, previously observed through magnetoconductance in the sputtered thin films on glass. In this model, for the measured temperatures in this work, the electrical conductivity is described by equation 7.1, where ΔE_S and ΔE_B are the surface and bulk semiconductor activation energies, respectively, a_S and a_B are the exponents, which are close to 1.5 and arise from the effective density of states function for an intrinsic semiconductor, and A_S and A_B, constants. At these temperatures, no traces of the TSS conduction were and are observed and as such, it is not included in this equation. All the conductivities of the flexible thin films were fitted to this equation. The fits describe well the data and can be found in Figure 7.6.(a), where the conductivity of the thin films is presented as a function of temperature. From the conductivity fits, the different parameters were calculated. The obtained surface activation energy ΔE_S is plotted in Figure 7.7 as a function of V_{Beam}, having values between 84 and 150 meV. It is worthy to note that a value of 140 meV as activation energy in the semiconducting/insulating Sn-BSTS sample has been reported[244], showcasing that this flexible Sb_2Te_3 thin films conduction follows a similar mechanism to the extremely insulating Sn-BSTS semiconductor films.

$$\sigma = A_S \left(k_B T\right)^{a_S} \exp\left(-\frac{\Delta E_S}{k_B T}\right) + A_B \left(k_B T\right)^{a_B} \exp\left(-\frac{\Delta E_B}{k_B T}\right) + \sigma_0 \tag{7.1}$$

Concerning the Seebeck Coefficient, the critical temperature at which the change from positive to negative S occurs (T_{pn}) can be identified, as seen in Figure 7.5.(a) for

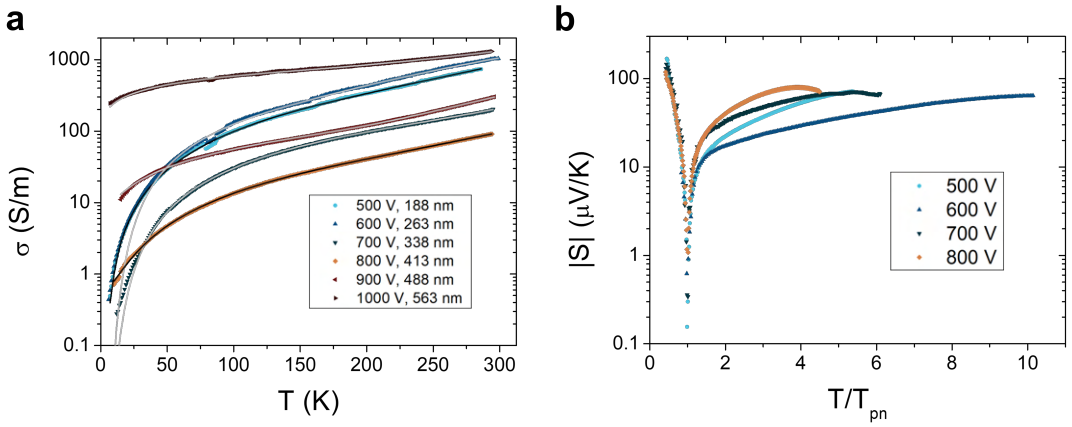


Figure 7.6 – Analysis of the transport properties of the flexible Sb_2Te_3 thin films. (a) The electrical conductivity of the flexible thin films as a function of temperature and the respective fits to equation 7.1 as solid lines. (b) The absolute value of the Seebeck coefficient as a function of the temperature normalised to T_{pn}.

the 800 V sample. Figure 7.6.(b) displays the absolute values of S as a function of the temperature normalised to T_{pn}. $|S|$ has a similar T_{pn} dependence for the different films, which shows that the conduction effects are common to all films. Moreover, by changing V_{Beam} and the thickness, control of T_{pn} and of the type of conduction is achieved.

Figure 7.7 shows T_{pn} as a function of V_{Beam}, having been assumed a T_{pn} equal to 13 K for the 900 and 1000 V, since, if it exists for this samples, it will have a value between 0 and 26 K. Previously, T_{pn} has been reported to decrease with an increase in thickness[244] and this tendency was also observed in Chapter 4. This is identified for the films fabricated with 500 and 600 V, but it does not show this behaviour for the other thin films.

Since the different structural and transport properties cannot be fully explained considering just the thickness of the films, in Figure 7.7 the grain size obtained from XRD of the (1 1 0) peak is also shown. It is remarkable to note that similar tendencies are observed for the surface activation energy ΔE_S, T_{pn} and the grain size $d_{(110)}$. These tendencies are the same as previously seen and discussed for ρ and S. They decrease in value from the 500 V to the 600 V deposited thin films. Then, they increase until reaching the maximum between 700 and 800 V, which is the area signalled in grey in Figure 7.7. With a further increase in V_{Beam}, the films' parameters decrease. From this an explanation similar to the ρ and S discussion above can also be valid here. Thickness plays the most important role in the thin films fabricated with V_{Beam} below 600 V. Here, the structural properties are very similar, as seen through the grain size of the (1 1 0) reflection, for example, which even though it does reduce from 500 to 600 V, it has a very similar value when compared to the other films. As such, the thickness of the film has the greatest influence on the transport properties for these smaller V_{Beam}.

However, the situation changes by increasing V_{Beam}. In Chapter 4, it was noted that for thicknesses higher than 200 nm, Sb_2Te_3 films have very similar behaviours,

closer to the bulk. Moreover, the grain size $d_{(110)}$ has a variation between 67 and 75 % from the peak value at 800 V and its value at 600 and 1000 V, respectively. Thus, the crystalline properties have the greatest influence for the films fabricated with V_{Beam} higher than 600 V. As previously discussed, by increasing V_{Beam}, certain XRD peaks increase in intensity while others become less prevalent, with the (0 1 23) peak reaching a maximum intensity at 800 V, for example. Moreover, the grain sizes also change behaviour between 700 and 800 V. Thus, the type of nanocrystallites and their respective size control the electronic conduction in this flexible sputtered TI thin films.

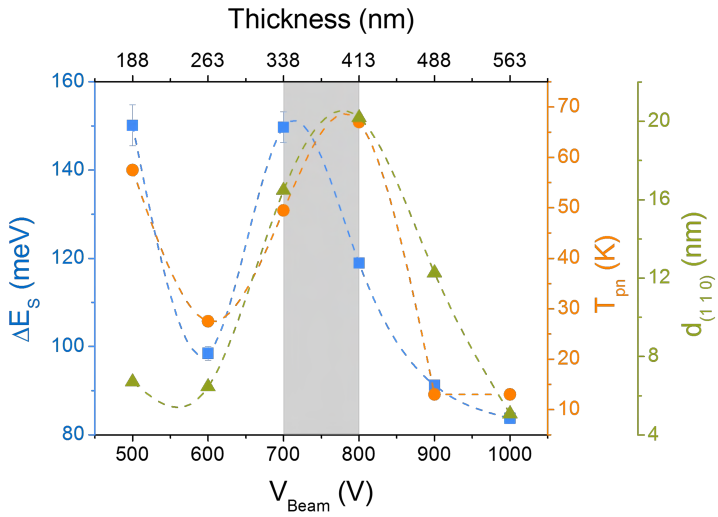


Figure 7.7 – Structural and transport parameters of the Sb_2Te_3 thin films. The Surface activation energy ΔE_S (blue squares), obtained from the resistivity, the critical temperature at which the change from p to n-type temperature occurs, T_{pn} (orange circles), obtained from the Seebeck Coefficient, and the grain size $d_{(110)}$ of the (1 1 0) XRD peak (green triangles) as a function of V_{Beam}. The dashed lines are guides to the eye and the grey area marks the V_{Beam} values at which the maximums of these parameter occur.

These results show that the type of conduction required for the development of Spinorbitronics flexible devices based on Sb_2Te_3 TI can be directly chosen by the sputtering conditions, by controlling both the thickness and V_{Beam}. For certain applications, such as the MESO device recently proposed[8], high resistivities are needed for an optimal output performance, and thus the films deposited with V_{Beam} between 700 V and 800 V are more suitable. However, to reduce shunting effects in charge to spin conversion elements[245], a lower resistivity of the SOC material is needed, and thus thicker films and/or films deposited with higher V_{Beam} should be used. Another interesting application is also for thermoelectric device design. As previously discussed, Sb_2Te_3 is one of the prototypical thermoelectric materials and as such its transport properties are also of interest for the development of flexible thermoelectric devices. From these two applications and their diverse requirements, ion beam sputtering is a versatile technique that allows for the fabrication of flexible Sb_2Te_3 thin films which could be employed in the future of flexible devices.

7.3 Flexible FM/TI/FM trilayers

Having flexible TI thin films, the fabrication and analysis of nanostructures for SOT applicatiosn can be envisaged. Trilayer nanostructures of ferromagnetic materials and Sb_2Te_3 as the TI material, with a FM/TI/FM structure, were sputtered on flexible substrates. The flexible trilayers allow for the analysis of the generation of the spin current, as discussed in Chapter 6, but also their transmission through the TI layer and their interaction with the second FM layer, further developing the creation of novel spinorbitronics devices.

The thickness of the FM materials was chosen to be the typical thicknesses used for the magnetisation dynamics studies, namely 10 nm. The Sb_2Te_3 deposition voltage for these flexible trilayers was 700 V because it was noted in the previous section that it yields the highest values of resistivity of the flexible thin films, which is needed for application such as the MESO device. Moreover, the thin films deposited on glass discussed in the previous Chapters were also fabricated at 700 V. The thicknesses of Sb_2Te_3 were chosen considering the temperature dependence of the conduction of the TI thin films, with a thickness of 30 and 60 nm having been chosen.

7.3.1 Structural and Morphological Characterisation

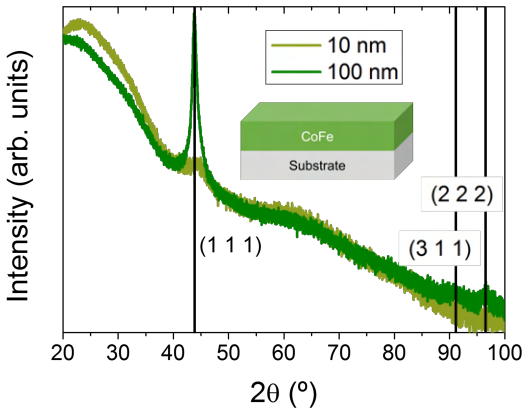


Figure 7.8 – XRD diffractogram of the CoFe thin films.

The sputtered trilayers have Py and CoFe as the FM materials. The CoFe and Py thin films were fabricated using previous optimised sputtering parameters obtained at IFIMUP. The structural properties of the Py sputtered thin films and layers were explored in Chapter 5. The structure of the CoFe thin film layers is presented here. Figure 7.8 shows the XRD diffractogram of the CoFe 10 and 100 nm thin films deposited on glass. Three peaks can be identified in the thicker film, which correspond to the $Co_{50}Fe_{50}$ FCC phase[246]. These are shown as solid lines of Figure 7.8 and correspond to the (1 1 1) peak at 44º, the (3 1 1) peak at 91º and the (2 2 2) peak at 96º. It has the same structure

as the Py thin films. The (1 1 1) peak at 44º and the (2 2 2) peak at 96º can also be identified in the 10 nm thin film, with the (1 1 1) peak being broader for this thinner film.

The XRD analysis of the trilayers is shown in Figure 7.9.(a) for the Py/ST(30)/CoFe trilayer deposited on glass and (b) on Kapton. The (1 0 2) and (2 0 5) peaks of the Sb_2Te_3 layer are identified on both samples at 26º and 51.7º as solid lines. On the trilayer deposited on Kapton, the (1 0 1) peak of Sb_2Te_3 can also be seen at 22.8º. The peak at 44º on both bilayers corresponds to both the Py and/or CoFe layer. On the Kapton trilayer, the peak at 92º of these two materials is also observed, with the peaks of these materials being shown as dashed lines. Moreover, the flexible trilayer also presents a peak corresponding to its substrate, Kapton, marked as an asterisk, and a peak corresponding to the (1 1 1) plane of the aluminium capping at 38.5º[247], shown as a dotted line. From these results, it can be concluded that the different materials maintain their structure when deposited as a trilayer structure. On the XRD diffractogram of the trilayer deposited in PET, only peaks corresponding to the substrate were identified.

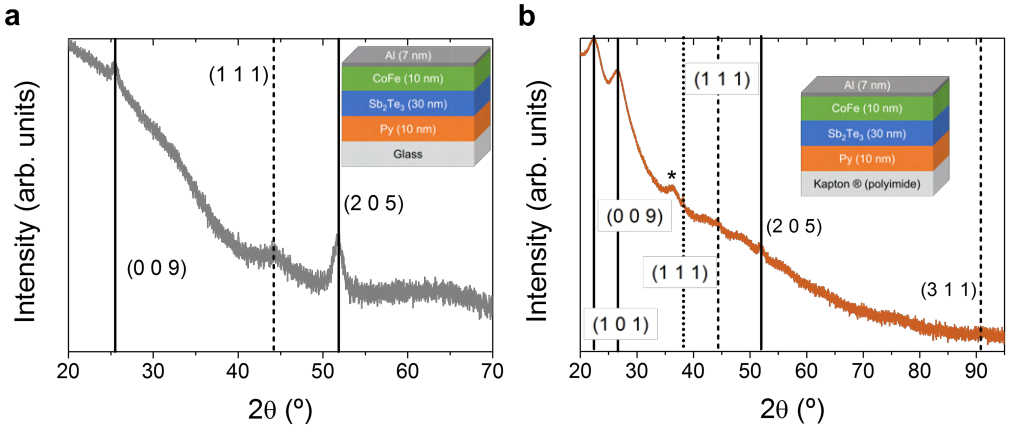


Figure 7.9 – XRD diffractogram of the trilayer samples deposited on (a) glass and (b) Kapton substrates.

XRR was employed to study the trilayer morphology. First, XRR was performed on the trilayer deposited on the glass substrate, due to it being a rigid substrate, allowing for a first analysis of the deposition of the capped trilayer system. The XRR pattern of this sample is shown in Figure 7.10.(a), where several Kiessig fringes can be observed: smaller in period which correspond to the Sb_2Te_3 high thickness layer, and broader fringes, encompassing roughly three of the smaller fringes, which can correspond to the both the Py and CoFe layers, due to these layers having the same thickness. The fringe order analysis was performed to these two sets to calculate the corresponding layer thicknesses. The fringe order and corresponding linear fit of the two sets of fringes is represented in Figure 7.10.(b). The circle data blue points correspond to the Sb_2Te_3 layer, having yielded a thickness of 36.6 ± 0.2 nm, while the triangle grey data points correspond to the FM layers, having an average thickness of 10.7 ± 0.4 nm. Fringes corresponding to the Al capping were not identified. This analysis shows that the tri-

layer materials can be grown in this stack nanostructure with good morphology and well defined independent layers, with good interfaces.

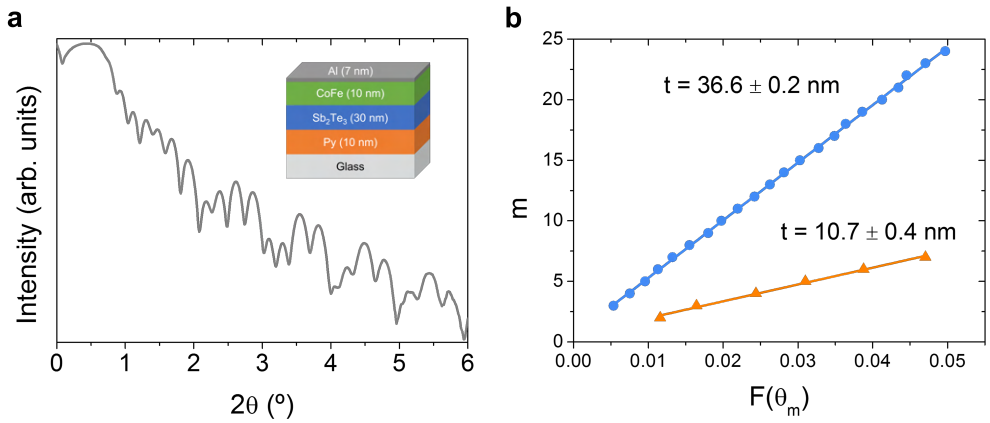


Figure 7.10 – XRR of the trilayer sample deposited on glass. (a) XRR pattern and (b) linear fit analysis of the fringes' order following equation 2.3, with the respective calculated thicknesses.

XRR was also performed on the flexible trilayers. However, due to the flexible nature of the substrate, the reflections are less intense, which makes the analysis via XRR of the trilayer structure difficult. As such, no proper signal was obtained by measuring the trilayers deposited on Kapton. However, for the PET trilayers, viable reflectivity patterns were obtained, being represented in Figure 7.11.(a) for the P:Py/ST(30)/CoFe trilayer and (b) P:Py/ST(60)/CoFe. On both samples, the XRR shows a high Fresnel reflectivity decrease. For the thinner Sb_2Te_3 film trilayer, only one set of fringes can be observed, with only seven fringes being noted. The inset of Figure 7.11.(a) shows the linear fit analysis, which produced a thickness of 30 ± 1 nm, corresponding to the Sb_2Te_3 layer. Focusing on the XRR pattern of the P:Py/ST(60)/CoFe sample, two sets of fringes can be roughly estimated, namely four small fringes corresponding to the Sb_2Te_3 layer, and four wider fringes, which, as in the sample deposited on glass, correspond to one or both the FM layers. From the linear fit analysis, represented in the inset of Figure 7.11.(b), thicknesses of 62 ± 4 nm and of 11.2 ± 0.2 nm were obtained which correspond to the Sb_2Te_3 layer and the Py and/or CoFe layers, respectively. As for the glass sample, no fringes corresponding to the capping are visible

7.3.2 Electronic properties

The resistance of the trilayer systems was measured as a function of temperature, being depicted in Figure 7.12, as well as the resistance of the Py(10) and CoFe(10) thin films on glass substrates. The resistance increases with heating for all the samples, following the same tendency as the FM thin films. This was the behaviour observed in the Py/Sb_2Te_3 bilayers, which indicates that all the conduction is carried by the metallic layers. However, since the trilayers are capped with a 7 nm film of Al, this should be the main contribution to the conduction, which is also observed, since the temperature

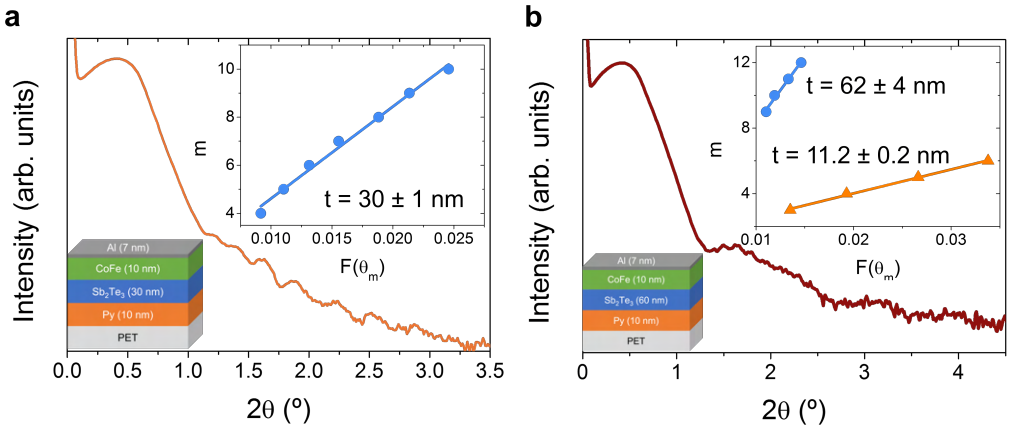


Figure 7.11 – XRR of the trilayer samples deposited on the flexible PET substrate. (a) XRR pattern of the P:Py/ST(30)/CoFe trilayer with an inset of the linear fit analysis of the fringes' order with the calculated thickness. (b) XRR pattern of the P:Py/ST(60)/CoFe trilayer with an inset of the linear fit analysis of the fringes' order with the calculated thicknesses.

dependence does not follow either the Py or CoFe behaviour.

Furthermore, the resistance is higher for the trilayers with the thinner Sb_2Te_3 layer. This is anticipated considering the simple conduction parallel mode, with a decrease in the thickness increasing the resistance. It can also happen because the resistivity of the TI material increases with a reduction in thickness, as it was discussed in Chapter 4 and on the first part of this Chapter.

There is also a substrate influence. The trilayers deposited on PET have a higher resistance than their counterparts deposited on Kapton. This can indicate that the structure of the layers is altered when deposited on PET, but no definite conclusions can yet be given, since the XRD measurements yielded no results due to only peaks of the PET substrate being identified.

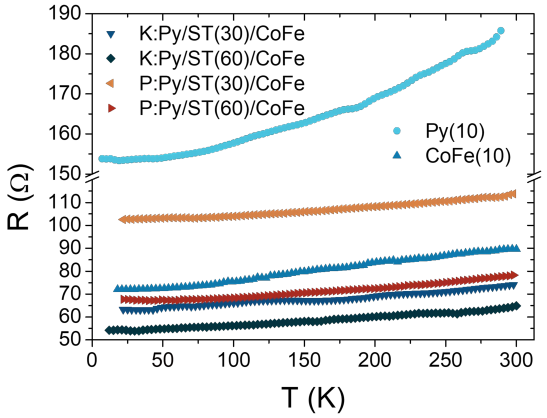


Figure 7.12 – Resistance of the trilayer samples and bare Py and CoFe 10 nm thin films as a function of temperature.

The Seebeck coefficient of the trilayers was also measured as a function of temperature, which is shown in Figure 7.13. The Seebeck coefficient of the Py(10) and

CoFe(10) thin films is also shown. As for the bilayers in Chapter 5, there is no contribution to the Seebeck coming from the Sb_2Te_3 layer, with the thermopower being negative within the range of temperatures studied and decreasing in magnitude with cooling. The temperature dependence is similar to the Py and CoFe thin films, but the values are much smaller in magnitude, especially at room temperature. Aluminium also has negative thermopower at this range of temperatures, but has much smaller values, with S being roughly -2.6 μV/K at room temperature[248]. Since the transport properties are measured through the Al capping, it is expected that the conduction is dominated by this film, which is observed in the Seebeck dependence on temperature of these capped trilayer samples.

Moreover, there appears to be no dependence of the Seebeck coefficient on the Sb_2Te_3 layer thickness, which further confirms that the measured thermopower is dominated by the Al capping. Concerning the substrate dependence, the samples deposited on PET have slightly smaller values of the thermopower. However, at the lowest temperatures, all the curves overlap, and appears to be no influence on both the substrate and thickness.

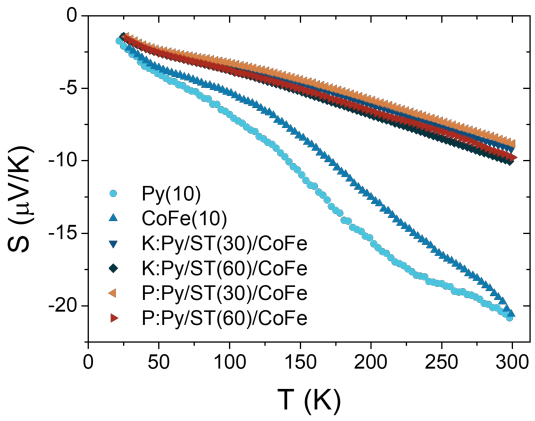


Figure 7.13 – Seebeck coefficient of the trilayer samples as a function of temperature.

7.3.3 Magnetisation dynamics

The magnetisation dynamics of both FM materials of the trilayer samples was measured at room temperature through VNA-FMR. Figure 7.14.(a) displays the absorption peaks of the Py/ST(30)/CoFe trilayer deposited on Kapton, obtained at H_{DC} of 1312.05 Oe in a frequency sweep. Two peaks are observed at different resonance frequencies. From previous FMR characterisation, one is identified as the Py layer resonance and the other as the resonance of the CoFe layer. The CoFe resonance peak has an higher intensity, which is due to it being closer to the origin of the induced RF field, since the sample is placed face down on the CPW. The data was fitted to a sum of asymmetric Lorentzians (equation 2.10) with the fit being presented as a full line. From the fits performed to the

Sample	K:Py/ST(30)/CoFe	K:Py/ST(60)/CoFe	P:Py/ST(30)/CoFe	P:Py/ST(60)/CoFe
Py M_S (Oe)	7693 ± 9	8130 ± 50)	6850 ± 20	6920 ± 20
Py H_k (Oe)	0.5 ± 0.7	-7 ± 3	3 ± 2	-12 ± 2
Py α (10^{-3})	11 ± 1	11 ± 1	21 ± 2	22.9 ± 0.9
CoFe M_S (Oe)	15500 ± 50	14600 ± 200	15830 ± 30	15300 ± 90
CoFe H_k (Oe)	-1 ± 2	30 ± 10	-18 ± 1	-21 ± 3
CoFe α (10^{-3})	11.8 ± 0.8	19 ± 2	13.2 ± 0.6	15.8 ± 0.6

Table 7.1 – Magnetisation dynamics parameters of the flexible FM/TI/FM trilayers at room temperature.

data at different applied magnetic fields, the resonance frequency and linewidth were calculated.

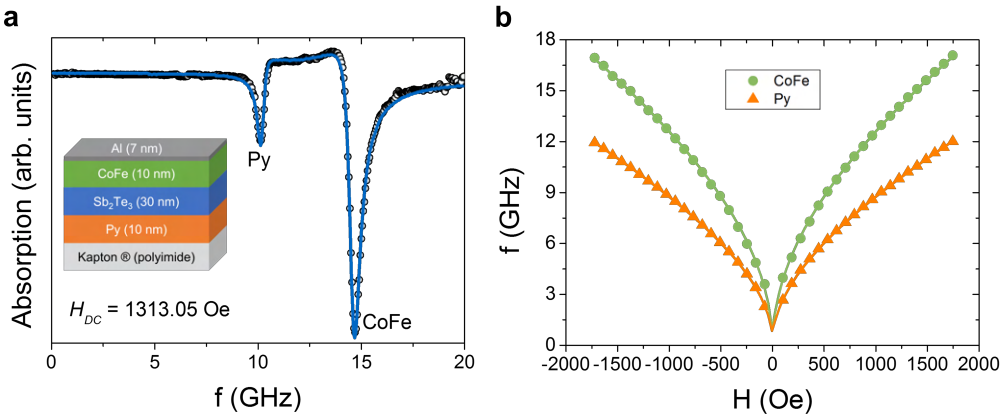


Figure 7.14 – Ferromagnetic resonance of the K:Py/ST(30)/CoFe trilayer. (a) representative ferromagnetic resonance absorption measured by VNA-FMR in frequency sweep at a H_{DC} of 1312.05 Oe. (b) Resonance frequency f_{res} as a function of the applied magnetic field H_{DC} for both the Py and CoFe resonances. The fits to the Kittel equation 2.5 are shown as solid lines.

Figure 7.14.(b) shows the frequency of the Py and CoFe resonances as a function of the applied field, for both positive and negative applied magnetic fields. The frequency dependence on the field is well described by the Kittel equation (equation 2.5), as it can be seen by the fits represented as solid lines. From the fits, the saturation magnetisation M_S and anisotropy field H_k were calculated, being shown in Table 7.1.

Focusing on the Py parameters, the deposition of the Py layer directly on top of the flexible substrate affects the saturation magnetisation, reducing it when compared to the Py reference value of the Py capped sample deposited on glass, presented in Chapter 5. This effect is greater for the PET substrate, with M_S decreasing roughly 1500 Oe, from the reference value. The roughness of PET and Kapton substrates has been reported to

be 46 and 44 nm[249], respectively, whereas the roughness of the glass substrates was obtained in Chapter 4 to be 1 nm. As such, the decrease in the saturation magnetisation can be explained by the roughness of the flexible substrates. The anisotropy is negative for the trilayers with the thicker Sb_2Te_3.

Considering the dynamics of the CoFe layer, M_S also decreases when compared to reference values of a previous report of capped sputtered CoFe[250]. However, in contrast to the Py case, this decrease seems to be independent of the flexible substrate used, but dependent on the thickness of the Sb_2Te_3 layer, since both samples with a Sb_2Te_3 thickness of 30 nm have a M_S higher approximately 500 Oe than the 60 nm samples. This could be explained by the presence of interface defects or magnetic dead layers at the interface between Sb_2Te_3 and CoFe. However, it was verified in Chapter 4 that there is no change in the structure of the Sb_2Te_3 thin films with different thicknesses. Thus, a structural effect is probably not the cause.

From the calculated linewidth, using equation 2.9 and 2.7, the damping corresponding to each layer could be calculated and it is also presented in Table 7.1. The damping of each FM material in the trilayer system is always higher than reference values, namely the ones reported for Py in Chapter 5 and approximately 6×10^{-3} for CoFe[250]. As discussed in the previous chapters, this can be due to extrinsic effects, such as the interface between each layer, and the presence of spin pumping. From the decrease of the saturation magnetisation in the Py layer, the increase in damping could also occur due to interfacial effects between the Py and the substrate. However, the Py damping increase is extremely high, with an increase of 47% for the kapton trilayers and 180% for the PET samples, from the reference value of the capped sample, whereas the magnetisation only decreases by 18%. The cause of this extremely high damping increase could thus be the presence of spin pumping into the Sb_2Te_3 layer and the interaction of a transmitted current flowing through the Sb_2Te_3 layer. For the CoFe layer, the damping parameter has an even higher increase when in the trilayer structure, increasing with the thickness of the Sb_2Te_3 layer. Since the variation of the saturation magnetisation is much smaller for CoFe, this increase could be due to spin pumping into the TI layer.

Previous FM/TI/FM trilayer studies, namely a CoFe(30 nm)/Bi_2Se_3 (4 - 20 nm)/Py(30 nm) trilayer, showed a similar situation, where the damping of both magnetic layers increased with the thickness of the TI layer[207]. Typically, in a trilayer, the damping drops exponentially with the spacer thickness, since scattering within the non-magnetic layer is a much less efficient sink for angular momentum than direct absorption by the second FM[251]. The opposing behaviour noted here thus suggests that not only the TIs in general, and Sb_2Te_3 in particular, are very efficient spin-sinks but that the pure spin current can penetrate some distance into the TI. This propagation of the spin current inside the TI, as observed in Chapter 6, is converted to a charge current, and the scattering of the conduction carriers within the bulk of the TI could provide a mechanism for efficient absorption of the pumped angular momentum[207].

From the previous results, it was verified the damping increase with thickness of

Sb_2Te_3, which can be due to spin pumping occurring out of the FM layers. However, the ability of a TI to absorb and transfer the pure spin current cannot be inferred from these measurements. By taking advantage of the material specific detection of the precession of the magnetisation that XFMR allows to probe, the spin transfer phenomena can be explored due to the high sensitivity of the phase of the magnetisation precession across the resonances. As such, preliminary XFMR measurements of the dynamic signal corresponding to the precession of each FM element of the K:Py/ST(30)/CoFe sample were performed.

The dynamic signal as a function of the delay between the incident x-rays and the RF magnetic field are shown in Figure 7.15 for the three elements, with the Ni signal having been increased $\times 100$. The measurements had to be performed in reflection, with an out of plane field, since the dynamic signal had to be collected at grazing incident X-ray beam, which an in-plane field blocks. However, the field range in this geometry is not optimal, since no resonance was crossed. Thus similar dynamic signals are obtained at all the applied magnetic fields, with the signal in Figure 7.15 being a representative measurement.

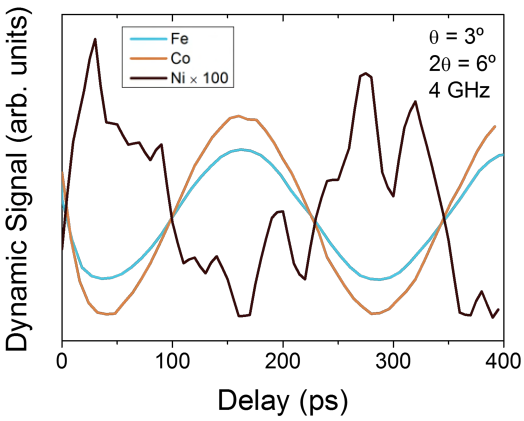


Figure 7.15 – Preliminary measurement of the x-ray detected ferromagnetic resonance of the K:Py/ST(30)/CoFe trilayer.

The Ni signal has the lowest amplitude, which is explained due to the geometry of the measurement, with the sample being placed down on the CPW. On the other hand, the dynamic signal of Fe and Co have the highest amplitude, since it is the layer on top of the sample. Concerning the phase of the signals, the Fe and Co signals are in phase, whereas the Ni signal has a different phase. Thus, there is a phase change in the signal between the layers, which could be indicative of off resonance precession being induced on the Py layer, as it was previously observed for the FM/TI/FM layer with Bi_2Se_3 as the TI material[207]. This would indicate that there could be a coupling between the two layers being mediated by the Sb_2Te_3 layer. However, to fully verify this hypothesis, the XFMR measurements would need to be optimised. Measurements across the resonances of both layers would need to be performed to infer how the spin

current is being transmitted through the Ti, if and how it is being injected into the second FM layer, and its influence on the precession of the FM Py layer.

7.4 Conclusion

Sb_2Te_3 TI thin films were successfully sputtered on flexible Kapton ® polyimide substrates, having transport and structural properties dependences on both thickness and fabrication parameters. The flexible films are polycrystalline, constituted by nanocrystallites of different orientations, with sizes ranging from 3 to 20 nm. By changing the plasma beam sputtering voltage V_{Beam}, the relative size and orientations of these nanocrystallites can be controlled, with 800 V emerging as a critical value V_{Beam}, at which the thickness versus V_{Beam} influence on the films' properties changes.

The transport properties of the flexible thin films are intriguing, with the films being highly resistive, having a semiconducting behaviour. Moreover, a change in the majority charge carriers with a temperature variation was observed through the Seebeck coefficient, being characterised by a critical temperature T_{pn}. This temperature is greatly influenced by the nanocrystalline nature of the films, as the electrical resistivity is. This conduction could be explained by the previously employed model in Chapter 4 of three resistances conducting in parallel, namely a bulk p-type semiconductor, a surface n-type semiconductor and the TSS. Through the control of the fabrication parameters allowed by ion beam sputtering, the studied flexible Sb_2Te_3 TI thin films can be fabricated having in consideration a wide range of applications, paving the way for the future development of logic and data storage flexible spintronic devices based on the spin to charge interconversion, while also being an attractive option for certain applications requiring flexible thermoelectric devices.

Flexible FM/TI/FM trilayer nanostructures were then fabricated based on the flexible Sb_2Te_3 thin films. The structural properties showed that the phase of the different materials is kept when fabricated on flexible substrates and as a stack trilayer structure. From XRR, the morphology was also explored, having been distinguished the different layers of the structure.

The magnetisation dynamics of the trilayers was probed by VNA-FMR and preliminarily by XFMR. It was seen that by introducing the Sb_2Te_3 thin film in the FM/FM stack, the damping of the FM materials increases, which is indicative of Sb_2Te_3 being a great spin-sink, with the spin current being able to propagate far in the TI. From the spin to charge conversion previously observed in Chapter 6, this shows that Sb_2Te_3 can offer a mechanism for efficient absorption of pumped angular momentum. Dynamic FMR signals of the trilayer structure were also observed via the preliminary XFMR measurements. A phase change of the signal of the layers was identified, which could be due to dynamic coupling between the FM layers being mediated by the Sb_2Te_3 layer. However, the measurements must be continued for a full exploration of this effect.

CHAPTER 8

Conclusions and Perspectives

8.1 Conclusions

Throughout this thesis, topological insulator nanostructures towards novel spinorbitronics devices for data storage and logic were investigated, considering the demand for fast information processing with ultra-low power consumption. Out of this endeavour, many scientific relevant insights to the community and society in general have been attained and are summarized in the following points.

Examining the **fabrication of thin film nanostructures**, thin films of topological insulator Sb_2Te_3 were fabricated using ion beam sputtering, which is a fast and scalable technique already present in both the semiconductors and spintronics industry, which was unveiled to be reliable for the fabrication of these films. It was shown that the topological surface state (TSS) conduction is present in all these sputtered TIs due to the existence of the weak antilocalisation (WAL) cusps in magnetoconductance measurements, being well-defined at low temperatures (2 - 10 K). By adjusting the fabrication parameters, such as the beam voltage or thickness, the possibility of tailoring the band structures by tuning the electronic properties was enabled, allowing the control of the type of conduction. This achievement was the ground work for the physical studies carried out throughout this thesis, since it demonstrated that the sputtered nanocrystalline thin films had the TSS, which could make them good candidates for spinorbitronic devices.

Multilayer-magnetic-nanostructures, such as bilayers (FM/TI) and trilayers (FM/TI/FM), were fabricated obtaining structures with crystalline layers and with the desired magnetic properties, i.e. identical to those of the individual thin films. The electronic and spintronic properties of these nanostructures were fully probed, which granted us a better understanding of their conduction, by calculating several transport parameters and coefficients that describe it in the detail. From this knowledge, physical models were created to describe the conduction of the single TI thin films and of the FM/TI systems. The former allowed us to gain knowledge of how the conduction occurs in the sputtered TIs, with the later having critical significance for the realisation of the basic SOT elements and their inclusion in devices.

The **inverse spin hall effect (ISHE)** that generates the spin to charge conversion on

Sb_2Te_3 was also inspected, in the temperature range [2 - 300] K. An effectively spin to charge conversion through the generation of the ISHE voltages was observed. Three main parameters of SOT devices, namely the spin diffusion length λ_{SD}, the spin current J_S, and the spin hall angle θ_{SH} were determined. Considering applications at room temperature, θ_{SH} was calculated to be -0.0033, with the figure of merit for logic applications, $\theta_{SH}\lambda_{SD}$, being 0.0165 nm. By combining the high resistivity of the sputtered thin films, and the comparable $\theta_{SH}\lambda_{SD}$, logic devices, such as the magnetoelectric spin-orbit (MESO) device proposed by Intel could be realised based on sputtered Sb_2Te_3 TI films. The sputtered bilayers have thus shown to be valuable SOT elements for logic devices, with the detailed study of their electronic properties promoting further improvements in the creation of novel SCC elements.

In the light of the ongoing progress of technological applications and the future trends on the field of spintronics, **flexible nanostructures** were also produced, which can lead to the advancement of the emergent flexible spintronics field. These exhibit crystalline and magnetic properties similar to those obtained in bilayers and trilayers on hard substrates. The generation and flow of the spin currents were probed in these flexible nanostructures, with Sb_2Te_3 emerging as an effective spin sink material.

Through an innovative **measurement setup of transport properties** and the **implementation of spin pumping experiments**, not only were the conduction contributions disentangled, including the topological surface state observed in the Sb_2Te_3 thin films, but the spin to charge conversion of Sb_2Te_3 was studied as a function of temperature and its efficiency for logic devices characterised.

The results of this thesis gave insights into the advancement of the field of spinorbitronics based on TIs and the developing world of flexible electronics. Moreover, it produced significant contributions to the emergent thematic line of Quantum Materials at IFIMUP and LapMET, being a step forward for future research in this field.

Lastly, Sb_2Te_3 has also emerged in this thesis as an alternative SOC material, until now not fully considered. It had not been properly explored yet, but the results herein show that it displays essential material properties, which can also be tuned and optimised, for the advancement of fast information processing, bringing us closer to the realisation of devices such as MESO logic.

8.2 Perspectives

In this section, future perspectives will be addressed, first within the framework of this thesis and at a later part on a more general note, by considering the results attained here.

Considering the **fabrication of nanostructures**, fabrication of other Sb_2Te_3 thin films can be performed and optimised. Temperature control during deposition, such as the substrate temperature, can be implemented, which could increase the crystallinity

degree of the films. Doping and other stoichiometries are also used to control the conduction in these materials, and such studies could be implemented for these materials. Moreover, ion beam sputtering can be employed to fabricate other TI systems. Ferromagentic/TI bilayers can be produced with other FM materials, such as the typical CoFe and CoFeB, which are also widely used in spintronics, due to their magnetic anisotropy. Other materials can also be employed which could optimise the SCC, such as the ferrimagnet YIG (Yttrium iron garnet, $Y_3Fe_5O_{12}$), which has been used in bilayers with TIs[252] due to being an insulator, reducing the shunting effects for data storage applications.

Engineering of the FM/TI interface could also be achieved with the ion beam sputtering, by introducing spacer layers of nonmagnetic and more conductive materials, which could assist the flow of the spin current through the interface, as it was previously demonstrated[181].

To fully characterise the SCC on the **flexible systems**, bilayer structures could also be sputtered on the flexible substrates already studied in this thesis. Further TI optimisation could also be attained by adding steps to the fabrication process, such as annealing of the thin films. This type of procedure has been previously employed in our group for thin films of Sb_2Te_3 with the end goal of thermoelectric applications, and great control of the structure was achieved for flexible substrate thin films.

As a major perspective, different classes of nanostructures could also be created based on the TIs studied here. **Antiferromagnetic spintronics** is gaining a lot of attention nowadays, due to the shorter time scales of AFM materials, which can be potentially used in ultrafast devices. AFMs have been combined with heavy metals for the detection of generated spin currents through spin pumping measurements[253,254]. With the observation that the sputtered Sb_2Te_3 of this thesis exhibit the inverse spin hall effect, they could be combined with AFM materials for applications of SCC at high-frequencies.

Considering the **flexible TI thin films**, magnetoconductance of the flexible TI films could be measured, to verify the existence of the TSS and calculate the conduction parameters, such as the λ_{SD} of flexible films. Moreover, the **interface of the Py/ST bilayers** could be probed by TEM, to have insights into the morphology of the interface, which is important for a full characterisation of these bilayers as SOT elements. Moreover, the temperature dependence of the **inverse spin hall effect** could also be studied for the other bilayers, or any other fabricated bilayer, which could help identify which would be the optimised pair of FM/TI for the SCC applications. The spin pumping measurements could also be performed on the above-mentioned flexible bilayers. The XFMR measurements initiated in this thesis can be optimised and finished, to fully characterise the flow of the spin current in the trilayer stack.

Addressing the **charge to spin conversion** through the spin hall effect could also be analysed. By performing magneto-optic Kerr effect (MOKE)[67] or pump-probe measurements, the inverse of SCC could be characterised, which is at the basis of magnetic memories applications.

Focusing on future **technological applications**, magnetisation state read-out devices have been created based on SOC materials, using focused electron beam. However, it is expected that the usage of TIs in this device could further improve them[255]. Thus, the sputtered TIs used in this thesis could be employed within this device. Moreover, the basic SOT elements studied here could also be integrated with the other elements of the proposed MESO device[8]. The material properties for a certain efficiency of the MESO device were calculated, and as discussed in Chapter 6, our sputtered TIs have the needed resistivity and comparable SOT efficiency values, and as such, the integration of the basic SOT elements with the remaining MESO components and the realisation of this logic device could be further advanced.

Bibliography

[1] M. T. Bohr, I. A. Young, Cmos scaling trends and beyond, IEEE Micro **37** (6) (2017) 20–29. doi:10.1109/MM.2017.4241347.

[2] G. E. Moore, Progress in digital integrated electronics, in: Electron devices meeting, Vol. 21, Washington, DC, 1975, pp. 11–13. doi:10.1109/N-SSC.2006.4804410.

[3] M. M. Waldrop, The chips are down for moore's law, Nature News **530** (7589) (2016) 144. doi:10.1038/530144a.

[4] ICT, Ict energy strategic research agenda, Tech. Rep. 611004, ICT Energy (Oct. 2016).

[5] M. N. Baibich, J. M. Broto, A. Fert, F. N. Van Dau, F. Petroff, P. Etienne, G. Creuzet, A. Friederich, J. Chazelas, Giant magnetoresistance of (001)fe/(001)cr magnetic superlattices, Physical Review Letters **61** (1988) 2472–2475. doi:10.1103/PhysRevLett.61.2472.

[6] G. Binasch, P. Grünberg, F. Saurenbach, W. Zinn, Enhanced magnetoresistance in layered magnetic structures with antiferromagnetic interlayer exchange, Physical Review B **39** (1989) 4828–4830. doi:10.1103/PhysRevB.39.4828.

[7] K. Garello, F. Yasin, S. Couet, L. Souriau, J. Swerts, S. Rao, S. Van Beek, W. Kim, E. Liu, S. Kundu, D. Tsvetanova, K. Croes, N. Jossart, E. Grimaldi, M. Baumgartner, D. Crotti, A. Fumémont, P. Gambardella, G. Kar, Sot-mram 300mm integration for low power and ultrafast embedded memories, in: 2018 IEEE Symposium on VLSI Circuits, 2018, pp. 81–82. doi:10.1109/VLSIC.2018.8502269.

[8] S. Manipatruni, D. E. Nikonov, C.-C. Lin, T. A. Gosavi, H. Liu, B. Prasad, Y.-L. Huang, E. Bonturim, R. Ramesh, I. A. Young, Scalable energy-efficient magnetoelectric spin–orbit logic, Nature **565** (7737) (2019) 35–42. doi:10.1038/s41586-018-0770-2.

[9] S. Ferreira-Teixeira, F. Carpinteiro, J. P. Araújo, J. B. Sousa, A. M. Pereira, Versatile seebeck and electrical resistivity measurement setup for thin films, Review of Scientific Instruments **92** (4) (2021) 043904. doi:10.1063/5.0036817.

[10] A. L. Pires, I. F. Cruz, J. Silva, G. N. P. Oliveira, S. Ferreira-Teixeira, A. M. L. Lopes, J. P. Araújo, J. Fonseca, C. Pereira, A. M. Pereira, Printed flexible μ-thermoelectric device based on hybrid bi_2te_3/pva composites, ACS Applied Materials & Interfaces **11** (9) (2019) 8969–8981. doi:10.1021/acsami.8b18081.

[11] S. Ferreira-Teixeira, A. Pereira, Geometrical optimization of a thermoelectric device: numerical simulations, Energy Conversion and Management **169** (2018) 217–227. doi:10.1016/j.enconman.2018.05.030.

[12] Kurzweil, Exponential growth of computing (April 9, 2010).
URL https://www.kurzweilai.net/exponential-growth-of-computing

[13] S. Wolf, D. Awschalom, R. Buhrman, J. Daughton, v. S. von Molnár, M. Roukes, A. Y. Chtchelkanova, D. Treger, Spintronics: a spin-based electronics vision for the future, Sci-

ence **294** (5546) (2001) 1488–1495. doi:10.1126/science.1065389.

[14] I. Žutić, J. Fabian, S. Das Sarma, Spintronics: Fundamentals and applications, Rev. Mod. Phys. **76** (2004) 323–410. doi:10.1103/RevModPhys.76.323.

[15] D. D. Awschalom, L. C. Bassett, A. S. Dzurak, E. L. Hu, J. R. Petta, Quantum spintronics: Engineering and manipulating atom-like spins in semiconductors, Science **339** (6124) (2013) 1174–1179. doi:10.1126/science.1231364.

[16] A. V. Chumak, V. I. Vasyuchka, A. A. Serga, B. Hillebrands, Magnon spintronics, Nature Physics **11** (6) (2015) 453–461. doi:10.1038/nphys3347.

[17] A. Brataas, A. D. Kent, H. Ohno, Current-induced torques in magnetic materials, Nature Materials **11** (5) (2012) 372–381. doi:10.1038/nmat3311.

[18] S. Bader, S. Parkin, Spintronics, Annu. Rev. Condens. Matter Phys. **1** (1) (2010) 71–88. doi:10.1146/annurev-conmatphys-070909-104123.

[19] J. Sinova, I. Žutić, New moves of the spintronics tango, Nature Materials **11** (5) (2012) 368–371. doi:10.1038/nmat3304.

[20] B. Dieny, I. L. Prejbeanu, K. Garello, P. Gambardella, P. Freitas, R. Lehndorff, W. Raberg, U. Ebels, S. O. Demokritov, J. Akerman, A. Deac, P. Pirro, C. Adelmann, A. Anane, A. V. Chumak, A. Hirohata, S. Mangin, S. O. Valenzuela, M. C. Onbaşlı, M. d'Aquino, G. Prenat, G. Finocchio, L. Lopez-Diaz, R. Chantrell, O. Chubykalo-Fesenko, P. Bortolotti, Opportunities and challenges for spintronics in the microelectronics industry, Nature Electronics **3** (8) (2020) 446–459. doi:10.1038/s41928-020-0461-5.

[21] E. Y. Vedmedenko, R. K. Kawakami, D. D. Sheka, P. Gambardella, A. Kirilyuk, A. Hirohata, C. Binek, O. Chubykalo-Fesenko, S. Sanvito, B. J. Kirby, et al., The 2020 magnetism roadmap, Journal of Physics D: Applied Physics **53** (45) (2020) 453001. doi:10.1088/1361-6463/ab9d98.

[22] A. Hoffmann, S. D. Bader, Opportunities at the frontiers of spintronics, Physical Review Applied **4** (2015) 047001. doi:10.1103/PhysRevApplied.4.047001.

[23] M. Dyakonov, V. Perel, Current-induced spin orientation of electrons in semiconductors, Physics Letters A **35** (6) (1971) 459–460. doi:https://doi.org/10.1016/0375-9601(71)90196-4.

[24] E. Saitoh, M. Ueda, H. Miyajima, G. Tatara, Conversion of spin current into charge current at room temperature: Inverse spin-hall effect, Applied Physics Letters **88** (18) (2006) 182509. doi:10.1063/1.2199473.

[25] S. O. Valenzuela, M. Tinkham, Direct electronic measurement of the spin hall effect, Nature **442** (7099) (2006) 176–179. doi:10.1038/nature04937.

[26] Y. K. Kato, R. C. Myers, A. C. Gossard, D. D. Awschalom, Observation of the spin hall effect in semiconductors, Science **306** (5703) (2004) 1910–1913. doi:10.1126/science.1105514.

[27] M. I. D'Yakonov, V. Perel, Possibility of orienting electron spins with current, Soviet Journal of Experimental and Theoretical Physics Letters **13** (1971) 467.

[28] J. Chazalviel, I. Solomon, Experimental evidence of the anomalous hall effect in a nonmagnetic semiconductor, Physical Review Letters **29** (25) (1972) 1676. doi:

10.1103/PhysRevLett.29.1676.

[29] A. Bakun, B. Zakharchenya, A. Rogachev, M. Tkachuk, V. Fleĭsher, Observation of a surface photocurrent caused by optical orientation of electrons in a semiconductor, Soviet Journal of Experimental and Theoretical Physics Letters **40** (1984) 1293.

[30] J. E. Hirsch, Spin hall effect, Physical Review Letters **83** (1999) 1834–1837. doi:10.1103/PhysRevLett.83.1834.

[31] J. Sinova, S. O. Valenzuela, J. Wunderlich, C. Back, T. Jungwirth, Spin hall effects, Reviews of Modern Physics **87** (4) (2015) 1213–1260. doi:10.1103/RevModPhys.87.1213.

[32] J. Sinova, T. Jungwirth, Surprises from the spin hall effect, Physics Today **70** (7) (2017) 38–42. doi:10.1063/PT.3.3625.

[33] V. M. Edelstein, Spin polarization of conduction electrons induced by electric current in two-dimensional asymmetric electron systems, Solid State Communications **73** (3) (1990) 233–235. doi:https://doi.org/10.1016/0038-1098(90)90963-C.

[34] J. C. R. Sánchez, L. Vila, G. Desfonds, S. Gambarelli, J. P. Attané, J. M. De Teresa, C. Magén, A. Fert, Spin-to-charge conversion using rashba coupling at the interface between non-magnetic materials, Nature Communications **4** (1) (2013) 2944. doi:10.1038/ncomms3944.

[35] F. Bottegoni, C. Zucchetti, G. Isella, M. Bollani, M. Finazzi, F. Ciccacci, Spin-charge interconversion in heterostructures based on group-iv semiconductors, La Rivista del Nuovo Cimento **43** (2) (2020) 45–96. doi:10.1007/s40766-020-0002-0.

[36] J.-C. Rojas-Sánchez, S. Oyarzún, Y. Fu, A. Marty, C. Vergnaud, S. Gambarelli, L. Vila, M. Jamet, Y. Ohtsubo, A. Taleb-Ibrahimi, P. Le Fèvre, F. Bertran, N. Reyren, J.-M. George, A. Fert, Spin to charge conversion at room temperature by spin pumping into a new type of topological insulator: α-sn films, Physical Review Letters **116** (2016) 096602. doi:10.1103/PhysRevLett.116.096602.

[37] W. Zhao, T. Devolder, Y. Lakys, J. Klein, C. Chappert, P. Mazoyer, Design considerations and strategies for high-reliable stt-mram, Microelectronics Reliability **51** (9) (2011) 1454–1458. doi:https://doi.org/10.1016/j.microrel.2011.07.001.

[38] W. Zhao, Y. Zhang, T. Devolder, J. Klein, D. Ravelosona, C. Chappert, P. Mazoyer, Failure and reliability analysis of stt-mram, Microelectronics Reliability **52** (9) (2012) 1848–1852. doi:https://doi.org/10.1016/j.microrel.2012.06.035.

[39] K. Garello, C. O. Avci, I. M. Miron, M. Baumgartner, A. Ghosh, S. Auffret, O. Boulle, G. Gaudin, P. Gambardella, Ultrafast magnetization switching by spin-orbit torques, Applied Physics Letters **105** (21) (2014) 212402. doi:10.1063/1.4902443.

[40] M. Cubukcu, O. Boulle, N. Mikuszeit, C. Hamelin, T. Brächer, N. Lamard, M.-C. Cyrille, L. Buda-Prejbeanu, K. Garello, I. M. Miron, O. Klein, G. de Loubens, V. V. Naletov, J. Langer, B. Ocker, P. Gambardella, G. Gaudin, Ultra-fast perpendicular spin–orbit torque mram, IEEE Transactions on Magnetics **54** (4) (2018) 1–4. doi:10.1109/TMAG.2017.2772185.

[41] G. Prenat, K. Jabeur, P. Vanhauwaert, G. D. Pendina, F. Oboril, R. Bishnoi, M. Ebrahimi, N. Lamard, O. Boulle, K. Garello, J. Langer, B. Ocker, M.-C. Cyrille, P. Gambardella, M. Tahoori, G. Gaudin, Ultra-fast and high-reliability sot-mram: From cache replacement

to normally-off computing, IEEE Transactions on Multi-Scale Computing Systems **2** (1) (2016) 49–60. doi:10.1109/TMSCS.2015.2509963.

[42] G. Yu, P. Upadhyaya, Y. Fan, J. G. Alzate, W. Jiang, K. L. Wong, S. Takei, S. A. Bender, L.-T. Chang, Y. Jiang, et al., Switching of perpendicular magnetization by spin–orbit torques in the absence of external magnetic fields, Nature Nanotechnology **9** (7) (2014) 548–554. doi:10.1038/nnano.2014.94.

[43] I. M. Miron, K. Garello, G. Gaudin, P.-J. Zermatten, M. V. Costache, S. Auffret, S. Bandiera, B. Rodmacq, A. Schuhl, P. Gambardella, Perpendicular switching of a single ferromagnetic layer induced by in-plane current injection, Nature **476** (7359) (2011) 189–193. doi:10.1038/nature10309.

[44] L. Liu, C.-F. Pai, Y. Li, H. W. Tseng, D. C. Ralph, R. A. Buhrman, Spin-torque switching with the giant spin hall effect of tantalum, Science **336** (6081) (2012) 555. doi:10.1126/science.1218197.

[45] Q. Hao, W. Chen, G. Xiao, Beta (β) tungsten thin films: Structure, electron transport, and giant spin hall effect, Applied Physics Letters **106** (18) (2015) 182403. doi:10.1063/1.4919867.

[46] L. A. Benítez, W. Savero Torres, J. F. Sierra, M. Timmermans, J. H. Garcia, S. Roche, M. V. Costache, S. O. Valenzuela, Tunable room-temperature spin galvanic and spin hall effects in van der waals heterostructures, Nature Materials **19** (2) (2020) 170–175. doi:10.1038/s41563-019-0575-1.

[47] L. Liu, Q. Qin, W. Lin, C. Li, Q. Xie, S. He, X. Shu, C. Zhou, Z. Lim, J. Yu, W. Lu, M. Li, X. Yan, S. J. Pennycook, J. Chen, Current-induced magnetization switching in all-oxide heterostructures, Nature Nanotechnology **14** (10) (2019) 939–944. doi:10.1038/s41565-019-0534-7.

[48] D. Hsieh, D. Qian, L. Wray, Y. Xia, Y. S. Hor, R. J. Cava, M. Z. Hasan, A topological dirac insulator in a quantum spin hall phase, Nature. doi:10.1038/nature06843.

[49] G. J. Snyder, E. S. Toberer, Complex thermoelectric materials, Nature Materials **7** (2) (2008) 105–114. doi:10.1038/nmat2090.

[50] J. Moore, Topological insulators: The next generation, Nature Physics **5** (6) (2009) 378–380. doi:10.1038/nphys1294.

[51] Y. Xia, L. Wray, D. Qian, D. Hsieh, A. Pal, H. Lin, A. Bansil, D. Grauer, Y. Hor, R. Cava, et al., Electrons on the surface of bi_2se_3 form a topologically-ordered two dimensional gas with a non-trivial berry's phase, arXiv preprint arXiv:0812.2078.

[52] H. Zhang, C.-X. Liu, X.-L. Qi, X. Dai, Z. Fang, S.-C. Zhang, Topological insulators in bi_2se_3, bi_2te_3 and sb_2te_3 with a single dirac cone on the surface, Nature Physics **5** (6) (2009) 438–442. doi:10.1038/nphys1270.

[53] A. R. Mellnik, J. S. Lee, A. Richardella, J. L. Grab, P. J. Mintun, M. H. Fischer, A. Vaezi, A. Manchon, E. A. Kim, N. Samarth, D. C. Ralph, Spin-transfer torque generated by a topological insulator, Nature **511** (7510) (2014) 449–451. doi:10.1038/nature13534.

[54] Y. Fan, P. Upadhyaya, X. Kou, M. Lang, S. Takei, Z. Wang, J. Tang, L. He, L.-T. Chang, M. Montazeri, G. Yu, W. Jiang, T. Nie, R. N. Schwartz, Y. Tserkovnyak, K. L. Wang, Magnetization switching through giant spin–orbit torque in a magnetically doped topological

insulator heterostructure, Nature Materials **13** (7) (2014) 699–704. doi:10.1038/nmat3973.

[55] E. Longo, M. Belli, M. Alia, M. Rimoldi, R. Cecchini, M. Longo, C. Wiemer, L. Locatelli, P. Tsipas, A. Dimoulas, G. Gubbiotti, M. Fanciulli, R. Mantovan, Large spin-to-charge conversion at room temperature in extended epitaxial sb_2te_3 topological insulator chemically grown on silicon, Advanced Functional Materials **n/a** (n/a) (2021) 2109361. doi:https://doi.org/10.1002/adfm.202109361.

[56] E. Longo, L. Locatelli, M. Belli, M. Alia, A. Kumar, M. Longo, M. Fanciulli, R. Mantovan, Spin-charge conversion in fe/au/sb_2te_3 heterostructures as probed by spin pumping ferromagnetic resonance, Advanced Materials Interfaces **n/a** (n/a) (2021) 2101244. doi:https://doi.org/10.1002/admi.202101244.

[57] P. H. Le, P.-T. Liu, C. W. Luo, J.-Y. Lin, K. H. Wu, Thickness-dependent magnetotransport properties and terahertz response of topological insulator bi_2te_3 thin films, Journal of Alloys and Compounds **692** (2017) 972–979. doi:10.1016/j.jallcom.2016.09.109.

[58] M. Guo, Z. Wang, Y. Xu, H. Huang, Y. Zang, C. Liu, W. Duan, Z. Gan, S.-C. Zhang, K. He, X. Ma, Q. Xue, Y. Wang, Tuning thermoelectricity in a bi_2se_3 topological insulator via varied film thickness, New Journal of Physics **18** (1) (2016) 015008. doi:10.1088/1367-2630/18/1/015008.

[59] S. Y. Matsushita, K.-K. Huynh, K. Tanigaki, Ultrathin films of three-dimensional topological insulators by vapor-phase epitaxy: Surface dominant transport in a wide temperature range as revealed by measurements of the seebeck effect, Physical Review B **99** (19) (2019) 195302. doi:10.1103/PhysRevB.99.195302.

[60] J. Zhang, X. Feng, Y. Xu, M. Guo, Z. Zhang, Y. Ou, Y. Feng, K. Li, H. Zhang, L. Wang, X. Chen, Z. Gan, S.-C. Zhang, K. He, X. Ma, Q.-K. Xue, Y. Wang, Disentangling the magnetoelectric and thermoelectric transport in topological insulator thin films, Physical Review B **91** (2015) 075431. doi:10.1103/PhysRevB.91.075431.

[61] P. Deorani, J. Son, K. Banerjee, N. Koirala, M. Brahlek, S. Oh, H. Yang, Observation of inverse spin hall effect in bismuth selenide, Physical Review B **90** (9) (2014) 094403. doi:10.1103/PhysRevB.90.094403.

[62] Y. S. Kim, M. Brahlek, N. Bansal, E. Edrey, G. A. Kapilevich, K. Iida, M. Tanimura, Y. Horibe, S.-W. Cheong, S. Oh, Thickness-dependent bulk properties and weak antilocalization effect in topological insulator bi_2se_3, Physical Review B **84** (2011) 073109. doi:10.1103/PhysRevB.84.073109.

[63] H.-T. He, G. Wang, T. Zhang, I.-K. Sou, G. K. L. Wong, J.-N. Wang, H.-Z. Lu, S.-Q. Shen, F.-C. Zhang, Impurity effect on weak antilocalization in the topological insulator bi_2te_3, Physical Review Letters **106** (2011) 166805. doi:10.1103/PhysRevLett.106.166805.

[64] X. Wu, X. Li, Z. Song, C. Berger, W. A. de Heer, Weak antilocalization in epitaxial graphene: Evidence for chiral electrons, Physical Review Letters **98** (2007) 136801. doi:10.1103/PhysRevLett.98.136801.

[65] S. Hikami, A. I. Larkin, Y. Nagaoka, Spin-orbit interaction and magnetoresistance in the two dimensional random system, Progress of Theoretical Physics **63** (2) (1980) 707–710. doi:10.1143/PTP.63.707.

[66] P. Adroguer, W. E. Liu, D. Culcer, E. M. Hankiewicz, Conductivity corrections for topologi-

cal insulators with spin-orbit impurities: Hikami-larkin-nagaoka formula revisited, Physical Review B **92** (2015) 241402. doi:10.1103/PhysRevB.92.241402.

[67] Y. Wang, D. Zhu, Y. Wu, Y. Yang, J. Yu, R. Ramaswamy, R. Mishra, S. Shi, M. Elyasi, K.-L. Teo, Y. Wu, H. Yang, Room temperature magnetization switching in topological insulator-ferromagnet heterostructures by spin-orbit torques, Nature Communications **8** (1) (2017) 1364. doi:10.1038/s41467-017-01583-4.

[68] M. DC, R. Grassi, J.-Y. Chen, M. Jamali, D. Reifsnyder Hickey, D. Zhang, Z. Zhao, H. Li, P. Quarterman, Y. Lv, M. Li, A. Manchon, K. A. Mkhoyan, T. Low, J.-P. Wang, Room-temperature high spin–orbit torque due to quantum confinement in sputtered $bi_xse_{(1-x)}$ films, Nature Materials **17** (9) (2018) 800–807. doi:10.1038/s41563-018-0136-z.

[69] M. Jamali, J. S. Lee, J. S. Jeong, F. Mahfouzi, Y. Lv, Z. Zhao, B. K. Nikolić, K. A. Mkhoyan, N. Samarth, J.-P. Wang, Giant spin pumping and inverse spin hall effect in the presence of surface and bulk spin−orbit coupling of topological insulator bi_2se_3, Nano Letters **15** (10) (2015) 7126–7132. doi:10.1021/acs.nanolett.5b03274.

[70] M. DC, T. Liu, J.-Y. Chen, T. Peterson, P. Sahu, H. Li, Z. Zhao, M. Wu, J.-P. Wang, Room-temperature spin-to-charge conversion in sputtered bismuth selenide thin films via spin pumping from yttrium iron garnet, Applied Physics Letters **114** (10) (2019) 102401. doi:10.1063/1.5054806.

[71] M. DC, J.-Y. Chen, T. Peterson, P. Sahu, B. Ma, N. Mousavi, R. Harjani, J.-P. Wang, Observation of high spin-to-charge conversion by sputtered bismuth selenide thin films at room temperature, Nano Letters **19** (8) (2019) 4836–4844. doi:10.1021/acs.nanolett.8b05011.

[72] K. Kondou, R. Yoshimi, A. Tsukazaki, Y. Fukuma, J. Matsuno, K. S. Takahashi, M. Kawasaki, Y. Tokura, Y. Otani, Fermi-level-dependent charge-to-spin current conversion by dirac surface states of topological insulators, Nature Physics **12** (11) (2016) 1027–1031. doi:10.1038/nphys3833.

[73] D. M. Mattox, Handbook of physical vapor deposition (PVD) processing, William Andrew, 2010.

[74] J. K. Hirvonen, Ion beam assisted thin film deposition, Materials Science Reports **6** (6) (1991) 215–274. doi:10.1007/978-94-011-0077-9_9.

[75] R. Fermento, D. Leitao, J. Teixeira, A. Pereira, F. Carpinteiro, J. Ventura, J. Araujo, J. Sousa, Structural, magnetic and transport properties of ion beam deposited co thin films, Journal of Non-Crystalline Solids **354** (47) (2008) 5279–5281, non-Crystalline Solids 9. doi:https://doi.org/10.1016/j.jnoncrysol.2008.05.077.

[76] L. M. C. Pereira, J. P. Araújo, M. J. V. Bael, K. Temst, A. Vantomme, Practical limits for detection of ferromagnetism using highly sensitive magnetometry techniques, Journal of Physics D: Applied Physics **44** (21) (2011) 215001. doi:10.1088/0022-3727/44/21/215001.

[77] A. L. Pires, New nanogenerators for thermal energy harvesting, Ph.D. thesis, Faculty of Sciences of the University of Porto (2019).

[78] V. Pecharsky, P. Zavalij, Fundamentals of powder diffraction and structural characterization of materials, Springer Science & Business Media, 2008.

[79] Schematic of a scanning electron microscope, nanoscience Instruments (Accessed October 21, 2021).
URL https://www.nanoscience.com/techniques/scanning-electron-microscopy/

[80] J. I. Goldstein, D. E. Newbury, J. R. Michael, N. W. Ritchie, J. H. J. Scott, D. C. Joy, Scanning electron microscopy and X-ray microanalysis, Springer, 2017.

[81] W. Zhou, Z. L. Wang, Scanning microscopy for nanotechnology: techniques and applications, Springer science & business media, 2007.

[82] S. Ebnesajjad, C. Ebnesajjad, Surface treatment of materials for adhesive bonding, William Andrew, 2013.

[83] J. S. Bergstrom, Mechanics of solid polymers: theory and computational modeling, William Andrew, 2015.

[84] Fig. 4 the schematic outline of a tem, atomic World (Accessed October 21, 2021).
URL http://www.hk-phy.org/atomic_world/tem/tem02_e.html

[85] C. Kisielowski, B. Freitag, M. Bischoff, H. van Lin, S. Lazar, G. Knippels, P. Tiemeijer, M. van der Stam, S. von Harrach, M. Stekelenburg, et al., Detection of single atoms and buried defects in three dimensions by aberration-corrected electron microscope with 0.5-Å information limit, Microscopy and Microanalysis **14** (5) (2008) 469–477. doi:10.1017/S1431927608080902.

[86] N. J. DiNardo, Atomic Force Microscopy, John Wiley and Sons, Ltd, 1994, Ch. 3, pp. 118–137. doi:https://doi.org/10.1002/9783527615957.ch3.
URL https://onlinelibrary.wiley.com/doi/abs/10.1002/9783527615957.ch3

[87] B. O. Alunda, Y. J. Lee, Cantilever-based sensors for high speed atomic force microscopy, Sensors **20** (17) (2020) 4784. doi:10.3390/s20174784.

[88] H. A. Wilson, The reflexion of x-rays by crystals, Phys. Rev. **18** (1921) 396–401. doi:10.1103/PhysRev.18.396.

[89] X-ray diffraction from crystal lattice planes (bragg's law), stresstech (Accessed October 14, 2021).
URL https://www.stresstech.com/knowledge/non-destructive-testing-methods/x-ray-diffraction/

[90] U. Holzwarth, N. Gibson, The scherrer equation versus the'debye-scherrer equation', Nature Nanotechnology **6** (9) (2011) 534–534. doi:10.1038/nnano.2011.145.

[91] I. Gomes, B. Almeida, A. Lopes, J. Araújo, J. Barbosa, J. Mendes, Structural and magnetic characterization of lasrmno 3 thin films deposited by laser ablation on mgo substrates, Journal of Magnetism and Magnetic Materials **322** (9) (2010) 1174–1177. doi:10.1016/j.jmmm.2009.06.072.

[92] X-ray diffraction technique, Advanced Laboratory II, Department of Physics and Astronomy of the Faculty of Siences of the University of Porto (2016).

[93] L. Weller, M. Kuvshinov, S. Hochgreb, Gas-phase raman spectroscopy of non-reacting flows: comparison between free-space and cavity-based spontaneous raman emission, Appl. Opt. **58** (10) (2019) C92–C103. doi:10.1364/AO.58.000C92.

[94] A. M. T. Pereira, Rare-earth nanostratified compounds with novel potentialities for refrig-

eration and magnetic sensors, Ph.D. thesis, Faculty of Sciences of the University of Porto (2010).

[95] C. Kittel, On the theory of ferromagnetic resonance absorption, Phys. Rev. **73** (1948) 155–161. doi:10.1103/PhysRev.73.155.

[96] B. Heinrich, J. A. C. Bland, Ultrathin magnetic structures II: Measurement techniques and novel magnetic properties, Vol. 2, Springer Science & Business Media, 2006.

[97] T. Gilbert, J. Kelly, Conference on magnetism and magnetic materials, Pittsburgh, PA (1955) 253.

[98] S. Azzawi, A. Hindmarch, D. Atkinson, Magnetic damping phenomena in ferromagnetic thin-films and multilayers, Journal of Physics D: Applied Physics **50** (47) (2017) 473001. doi:10.1088/1361-6463/aa8dad.

[99] T. D. Rossing, Resonance linewidth and anisotropy variation in thin films, Journal of Applied Physics **34** (4) (1963) 995–995. doi:10.1063/1.1729582.

[100] C. Bilzer, T. Devolder, P. Crozat, C. Chappert, S. Cardoso, P. P. Freitas, Vector network analyzer ferromagnetic resonance of thin films on coplanar waveguides: Comparison of different evaluation methods, Journal of Applied Physics **101** (7) (2007) 074505. doi: 10.1063/1.2716995.

[101] A. S. V. Silva, Ultrafast magnetization dynamicsin multilayered filmsdown to the few-cycle regime, Ph.D. thesis, Universidad de Salamanca (2020).

[102] S. S. Kalarickal, P. Krivosik, M. Wu, C. E. Patton, M. L. Schneider, P. Kabos, T. J. Silva, J. P. Nibarger, Ferromagnetic resonance linewidth in metallic thin films: Comparison of measurement methods, Journal of Applied Physics **99** (9) (2006) 093909. doi:10.1063/1.2197087.

[103] NanOsc, PhaseFMR User Manual (Jan. 2019).

[104] NanOsc, Broadband fmr spectrometers, Flyer (Oct. 2019).

[105] G. van der Laan, Time-resolved x-ray detected ferromagnetic resonance of spin currents, Journal of Electron Spectroscopy and Related Phenomena **220** (2017) 137–146. doi: 10.1016/j.elspec.2016.12.011.

[106] G. Van der Laan, Applications of soft x-ray magnetic dichroism, in: Journal of Physics: conference series, Vol. 430, IOP Publishing, 2013, p. 012127. doi: 10.1088/1742-6596/430/1/012127.

[107] A. Figueroa, A. Baker, L. Collins-McIntyre, T. Hesjedal, G. van der Laan, Spin pumping through a topological insulator probed by x-ray detected ferromagnetic resonance, Journal of Magnetism and Magnetic Materials **400** (2016) 178–183. doi: 10.1016/j.jmmm.2015.07.013.

[108] K. Garello, I. M. Miron, C. O. Avci, F. Freimuth, Y. Mokrousov, S. Blügel, S. Auffret, O. Boulle, G. Gaudin, P. Gambardella, Symmetry and magnitude of spin–orbit torques in ferromagnetic heterostructures, Nature Nanotechnology **8** (8) (2013) 587–593. doi: 10.1038/nnano.2013.145.

[109] L. Liu, T. Moriyama, D. Ralph, R. Buhrman, Spin-torque ferromagnetic resonance induced by the spin hall effect, Physical Review Letters **106** (3) (2011) 036601. doi:

10.1103/PhysRevLett.106.036601.

[110] M. Johnson, R. Silsbee, Spin-injection experiment, Physical Review B **37** (10) (1988) 5326. doi:10.1103/PhysRevB.37.5326.

[111] A. Brataas, Y. Tserkovnyak, G. E. W. Bauer, B. I. Halperin, Spin battery operated by ferromagnetic resonance, Physical Review B **66** (2002) 060404. doi:10.1103/PhysRevB.66.060404.

[112] Y. Tserkovnyak, A. Brataas, G. E. W. Bauer, Spin pumping and magnetization dynamics in metallic multilayers, Physical Review B **66** (2002) 224403. doi:10.1103/PhysRevB.66.224403.

[113] Y. Tserkovnyak, A. Brataas, G. E. W. Bauer, Enhanced gilbert damping in thin ferromagnetic films, Physical Review Letters **88** (2002) 117601. doi:10.1103/PhysRevLett.88.117601.

[114] S. Mizukami, Y. Ando, T. Miyazaki, Effect of spin diffusion on gilbert damping for a very thin permalloy layer in cu/permalloy/cu/pt films, Physical Review B **66** (2002) 104413. doi:10.1103/PhysRevB.66.104413.

[115] M. V. Costache, M. Sladkov, S. M. Watts, C. H. van der Wal, B. J. van Wees, Electrical detection of spin pumping due to the precessing magnetization of a single ferromagnet, Physical Review Letters **97** (2006) 216603. doi:10.1103/PhysRevLett.97.216603.

[116] Y. Tserkovnyak, A. Brataas, G. E. W. Bauer, B. I. Halperin, Nonlocal magnetization dynamics in ferromagnetic heterostructures, Rev. Mod. Phys. **77** (2005) 1375–1421. doi:10.1103/RevModPhys.77.1375.

[117] H. Nakayama, K. Ando, K. Harii, T. Yoshino, R. Takahashi, Y. Kajiwara, K. Uchida, Y. Fujikawa, E. Saitoh, Geometry dependence on inverse spin hall effect induced by spin pumping in $ni_{81}fe_{19}$/pt films, Physical Review B **85** (2012) 144408. doi:10.1103/PhysRevB.85.144408.

[118] QuantumDesign, Application Note 1087-203: Measuring the inverse spin Hall effect (ISHE) using the PPMS/DynaCool/VersaLab (Jun. 2018).

[119] D. M. Rowe, Thermoelectrics handbook: macro to nano, CRC press, 2005.

[120] M. H. Elsheikh, D. A. Shnawah, M. F. M. Sabri, S. B. M. Said, M. H. Hassan, M. B. A. Bashir, M. Mohamad, A review on thermoelectric renewable energy: Principle parameters that affect their performance, Renewable and Sustainable Energy Reviews **30** (2014) 337–355. doi:10.1016/j.rser.2013.10.027.

[121] J.-F. Li, W.-S. Liu, L.-D. Zhao, M. Zhou, High-performance nanostructured thermoelectric materials, Npg Asia Materials **2** (2010) 152. doi:10.1038/asiamat.2010.138.

[122] P. Sundarraj, D. Maity, S. S. Roy, R. A. Taylor, Recent advances in thermoelectric materials and solar thermoelectric generators – a critical review, RSC Advances **4** (87) (2014) 46860–46874. doi:10.1039/C4RA05322B.

[123] D. Zhao, G. Tan, A review of thermoelectric cooling: Materials, modeling and applications, Applied Thermal Engineering **66** (1–2) (2014) 15–24. doi:http://dx.doi.org/10.1016/j.applthermaleng.2014.01.074.

[124] R. E. Bentley, Handbook of Temperature Measurement: Theory and Practice of Thermo-

electric Thermometry, Springer-Verlag Pte. Ltd.: Singapore, 1998.

[125] J. E. Moore, The birth of topological insulators, Nature **464** (7286) (2010) 194. doi: 10.1038/nature08916.

[126] G. Zhang, Y.-W. Zhang, Thermoelectric properties of two-dimensional transition metal dichalcogenides, Journal of Materials Chemistry C **5** (31) (2017) 7684–7698. doi: 10.1039/C7TC01088E.

[127] C.-C. Chen, Z. Li, L. Shi, S. B. Cronin, Thermoelectric transport across graphene/hexagonal boron nitride/graphene heterostructures, Nano Research **8** (2) (2015) 666–672. doi:10.1007/s12274-014-0550-8.

[128] K. R. Hahn, E. Assaf, A. Portavoce, S. Bertaina, A. Charaï, Structural and composition effects on electronic and magnetic properties in thermoelectric $mn_{1-x-y}co_{1+x}ge_{1+y}$ materials, The Journal of Physical Chemistry C **121** (48) (2017) 26575–26586. doi: 10.1021/acs.jpcc.7b04863.

[129] A. M. Pereira, C. Magen, J. P. Araújo, P. A. Algarabel, L. Morellon, M. E. Braga, R. P. Pinto, M. R. Ibarra, J. B. Sousa, Effect of rare earth ion in the thermopower of r5(sixge1-x)4 compounds with x□0.5 and r=gd and tb, Journal of Magnetism and Magnetic Materials **310** (2, Part 2) (2007) e580–e582. doi:https://doi.org/10.1016/j.jmmm.2006.10.543.

[130] D. Pesin, A. H. MacDonald, Spintronics and pseudospintronics in graphene and topological insulators, Nature Materials **11** (5) (2012) 409. doi:10.1038/nmat3305.

[131] H.-H. Fu, D.-D. Wu, L. Gu, M. Wu, R. Wu, Design for a spin-seebeck diode based on two-dimensional materials, Physical Review B **92** (4) (2015) 045418. doi: 10.1103/PhysRevB.92.045418.

[132] K. A. Borup, J. de Boor, H. Wang, F. Drymiotis, F. Gascoin, X. Shi, L. Chen, M. I. Fedorov, E. Müller, B. B. Iversen, G. J. Snyder, Measuring thermoelectric transport properties of materials, Energy I& Environmental Science **8** (2) (2015) 423–435. doi: 10.1039/C4EE01320D.

[133] J. Mackey, F. Dynys, A. Sehirlioglu, Uncertainty analysis for common seebeck and electrical resistivity measurement systems, Review of Scientific Instruments **85** (8) (2014) 085119. doi:10.1063/1.4893652.

[134] X. He, J. Yang, Q. Jiang, Y. Luo, D. Zhang, Z. Zhou, Y. Ren, X. Li, J. Xin, J. Hou, A new method for simultaneous measurement of seebeck coefficient and resistivity, Review of Scientific Instruments **87** (12) (2016) 124901. doi:10.1063/1.4969056.

[135] J. Martin, G. S. Nolas, Apparatus for the measurement of electrical resistivity, seebeck coefficient, and thermal conductivity of thermoelectric materials between 300 k and 12 k, Review of Scientific Instruments **87** (1) (2016) 015105. doi:10.1063/1.4939555.

[136] A. Guan, H. Wang, H. Jin, W. Chu, Y. Guo, G. Lu, An experimental apparatus for simultaneously measuring seebeck coefficient and electrical resistivity from 100 k to 600 k, Review of Scientific Instruments **84** (4) (2013) 043903. doi:10.1063/1.4798647.

[137] J. Liu, Y. Zhang, Z. Wang, M. Li, W. Su, M. Zhao, S. Huang, S. Xia, C. Wang, Accurate measurement of seebeck coefficient, Review of Scientific Instruments **87** (6) (2016) 064701. doi:10.1063/1.4952744.

[138] L. Adnane, N. Williams, H. Silva, A. Gokirmak, High temperature setup for measurements of seebeck coefficient and electrical resistivity of thin films using inductive heating, Review of Scientific Instruments **86** (10) (2015) 105119. doi:10.1063/1.4934577.

[139] J. Martin, T. Tritt, C. Uher, High temperature seebeck coefficient metrology, Journal of Applied Physics **108** (12) (2010) 121101. doi:10.1063/1.3503505.

[140] O. Boffoué, A. Jacquot, A. Dauscher, B. Lenoir, M. Stölzer, Experimental setup for the measurement of the electrical resistivity and thermopower of thin films and bulk materials, Review of Scientific Instruments **76** (5) (2005) 053907. doi:10.1063/1.1912820.

[141] J. Martin, Apparatus for the high temperature measurement of the seebeck coefficient in thermoelectric materials, Review of Scientific Instruments **83** (6) (2012) 065101. doi:10.1063/1.4723872.

[142] C. Wood, A. Chmielewski, D. Zoltan, Measurement of seebeck coefficient using a large thermal gradient, Review of Scientific Instruments **59** (6) (1988) 951–954. doi:10.1063/1.1139756.

[143] B. Dörling, O. Zapata-Arteaga, M. Campoy-Quiles, A setup to measure the seebeck coefficient and electrical conductivity of anisotropic thin-films on a single sample, Review of Scientific Instruments **91** (10) (2020) 105111. doi:10.1063/5.0021715.

[144] C. S. B. Pang, W. Ng, J. Liang, Q. Qu, H. T. M. Chau, M. Niu, M. K. Cheng, I. K. Sou, A simple thermoelectric effect setup for determining the conductivity type of thin film materials, IEEE Transactions on Instrumentation and Measurement **70** (2021) 1–7. doi:10.1109/TIM.2020.3046922.

[145] Z. Luo, J. Tian, S. Huang, M. Srinivasan, J. Maassen, Y. P. Chen, X. Xu, Large enhancement of thermal conductivity and lorenz number in topological insulator thin films, ACS Nano **12** (2) (2018) 1120–1127. doi:10.1021/acsnano.7b06430.

[146] V. Linseis, F. Völklein, H. Reith, K. Nielsch, P. Woias, Advanced platform for the in-plane zt measurement of thin films, Review of Scientific Instruments **89** (1) (2018) 015110. doi:10.1063/1.5005807.

[147] Z. Fan, D. Du, X. Guan, J. Ouyang, Polymer films with ultrahigh thermoelectric properties arising from significant seebeck coefficient enhancement by ion accumulation on surface, Nano Energy **51** (2018) 481–488. doi:https://doi.org/10.1016/j.nanoen.2018.07.002.

[148] S. Zastrow, J. Gooth, T. Boehnert, S. Heiderich, W. Toellner, S. Heimann, S. Schulz, K. Nielsch, Thermoelectric transport and hall measurements of low defect sb_2te_3 thin films grown by atomic layer deposition, Semiconductor Science and Technology **28** (3) (2013) 035010. doi:10.1088/0268-1242/28/3/035010.

[149] A. C. Westerheim, A. C. Anderson, M. J. Cima, Substrate temperature measurements using ultrasonically bonded platinel ii thermocouples, Review of Scientific Instruments **63** (4) (1992) 2282–2287. doi:10.1063/1.1143151.

[150] V. Balakrishnan, T. Dinh, T. Nguyen, H.-P. Phan, T.-K. Nguyen, D. V. Dao, N.-T. Nguyen, A hot-film air flow sensor for elevated temperatures, Review of Scientific Instruments **90** (1) (2019) 015007. doi:10.1063/1.5065420.

[151] P. Kumar, D. V. M. Repaka, K. Hippalgaonkar, Lithography-free resistance thermometry based technique to accurately measure seebeck coefficient and electrical conductivity for

organic and inorganic thin films, Review of Scientific Instruments **88** (12) (2017) 125112. doi:10.1063/1.5012039.

[152] A. M. Pereira, J. M. Teixeira, F. Carpinteiro, J. P. Araújo, R. P. Pinto, M. E. Braga, J. B. Sousa, A. Veloso, P. P. Freitas, Thermopower in specular spin valves, Journal of Alloys and Compounds **423** (1-2) (2006) 240–243. doi:10.1016/j.jallcom.2005.12.097.

[153] J. B. Sousa, J. O. Ventura, M. A. Salgueiro da Silva, P. P. Freitas, A. Veloso, Comparative study of magnetoresistance and magnetization in nano-oxide specular and nonspecular mnir/cofe/cu/cofe spin valves from 10 to 300 k, Journal of Applied Physics **91** (8) (2002) 5321–5324. doi:10.1063/1.1459617.

[154] G. S. Okram, Intrinsic thermoelectric power of group vb metals, AIP Advances **2** (1) (2012) 012178. doi:10.1063/1.3698169.

[155] D. Hsieh, Y. Xia, D. Qian, L. Wray, F. Meier, J. H. Dil, J. Osterwalder, L. Patthey, A. V. Fedorov, H. Lin, A. Bansil, D. Grauer, Y. S. Hor, R. J. Cava, M. Z. Hasan, Observation of time-reversal-protected single-dirac-cone topological-insulator states in bi_2te_3 and sb_2te_3, Physical Review Letters **103** (14) (2009) 146401. doi:10.1103/PhysRevLett.103.146401.

[156] A. Soumyanarayanan, N. Reyren, A. Fert, C. Panagopoulos, Emergent phenomena induced by spin–orbit coupling at surfaces and interfaces, Nature **539** (7630) (2016) 509–517. doi:10.1038/nature19820.

[157] A. Manchon, H. C. Koo, J. Nitta, S. M. Frolov, R. A. Duine, New perspectives for rashba spin–orbit coupling, Nature Materials **14** (9) (2015) 871–882. doi:10.1038/nmat4360.

[158] S. Dushenko, M. Hokazono, K. Nakamura, Y. Ando, T. Shinjo, M. Shiraishi, Tunable inverse spin hall effect in nanometer-thick platinum films by ionic gating, Nature Communications **9** (1) (2018) 3118. doi:10.1038/s41467-018-05611-9.

[159] E. Grimaldi, V. Krizakova, G. Sala, F. Yasin, S. Couet, G. Sankar Kar, K. Garello, P. Gambardella, Single-shot dynamics of spin–orbit torque and spin transfer torque switching in three-terminal magnetic tunnel junctions, Nature Nanotechnology **15** (2) (2020) 111–117. doi:10.1038/s41565-019-0607-7.

[160] F. Xiu, L. He, Y. Wang, L. Cheng, L.-T. Chang, M. Lang, G. Huang, X. Kou, Y. Zhou, X. Jiang, Z. Chen, J. Zou, A. Shailos, K. L. Wang, Manipulating surface states in topological insulator nanoribbons, Nature Nanotechnology **6** (4) (2011) 216–221. doi:10.1038/nnano.2011.19.

[161] F. Lüpke, S. Just, M. Eschbach, T. Heider, E. Młyńczak, M. Lanius, P. Schüffelgen, D. Rosenbach, N. von den Driesch, V. Cherepanov, G. Mussler, L. Plucinski, D. Grützmacher, C. M. Schneider, F. S. Tautz, B. Voigtländer, In situ disentangling surface state transport channels of a topological insulator thin film by gating, npj Quantum Materials **3** (1) (2018) 46. doi:10.1038/s41535-018-0116-1.

[162] N. Sakai, T. Kajiwara, K. Takemura, S. Minomura, Y. Fujii, Pressure-induced phase transition in sb_2te_3, Solid State Communications **40** (12) (1981) 1045–1047. doi:https://doi.org/10.1016/0038-1098(81)90248-9.

[163] D. Das, K. Malik, A. K. Deb, S. Dhara, S. Bandyopadhyay, A. Banerjee, Defect induced structural and thermoelectric properties of sb_2te_3 alloy, Journal of Applied Physics **118** (4) (2015) 045102. doi:10.1063/1.4927283.

[164] B. Torrie, Raman spectrum of tellurium, Solid State Communications **8** (22) (1970) 1899–1901. doi:https://doi.org/10.1016/0038-1098(70)90343-1.

[165] I. Korzhovska, H. Deng, L. Zhao, Y. Deshko, Z. Chen, M. Konczykowski, S. Zhao, S. Raoux, L. Krusin-Elbaum, Spin memory of the topological material under strong disorder, npj Quantum Materials **5** (1) (2020) 39. doi:10.1038/s41535-020-0241-5.

[166] Z. Ren, A. A. Taskin, S. Sasaki, K. Segawa, Y. Ando, Large bulk resistivity and surface quantum oscillations in the topological insulator bi_2te_2Se, Physical Review B **82** (24) (2010) 241306. doi:10.1103/PhysRevB.82.241306.

[167] A. Taskin, Z. Ren, S. Sasaki, K. Segawa, Y. Ando, Observation of dirac holes and electrons in a topological insulator, Physical Review Letters **107** (1) (2011) 016801. doi:10.1103/PhysRevLett.107.016801.

[168] L. Bao, L. He, N. Meyer, X. Kou, P. Zhang, Z.-g. Chen, A. V. Fedorov, J. Zou, T. M. Riedemann, T. A. Lograsso, Weak anti-localization and quantum oscillations of surface states in topological insulator bi_2se_2te, Scientific reports **2** (2012) 726. doi:10.1038/srep00726.

[169] Y.-C. Huang, P. Lee, C. Chien, F. Chiu, Y. Chen, S. R. Harutyunyan, Magnetotransport properties of sb_2te_3 nanoflake, Physica B: Condensed Matter **452** (2014) 108–112. doi:10.1016/j.physb.2014.07.010.

[170] S. Bera, P. Behera, A. K. Mishra, M. Krishnan, M. M. Patidar, R. Venkatesh, V. Ganesan, Weak antilocalization in sb_2te_3 nano-crystalline topological insulator, Applied Surface Science **496** (2019) 143654. doi:https://doi.org/10.1016/j.apsusc.2019.143654.

[171] R. Cecchini, R. Mantovan, C. Wiemer, L. Nasi, L. Lazzarini, M. Longo, Weak antilocalization in granular sb_2te_3 thin films deposited by mocvd, physica status solidi (RRL) – Rapid Research Letters **12** (8) (2018) 1800155. doi:https://doi.org/10.1002/pssr.201800155.

[172] Y. Takagaki, A. Giussani, K. Perumal, R. Calarco, K. J. Friedland, Robust topological surface states in sb_2te_3 layers as seen from the weak antilocalization effect, Physical Review B **86** (12) (2012) 125137. doi:10.1103/PhysRevB.86.125137.

[173] R. J. Elliott, Theory of the effect of spin-orbit coupling on magnetic resonance in some semiconductors, Phys. Rev. **96** (1954) 266–279. doi:10.1103/PhysRev.96.266.

[174] Z. G. Yu, Spin-orbit coupling, spin relaxation, and spin diffusion in organic solids, Physical Review Letters **106** (10) (2011) 106602. doi:10.1103/PhysRevLett.106.106602.

[175] N. Sato, F. Xue, R. M. White, C. Bi, S. X. Wang, Two-terminal spin–orbit torque magnetoresistive random access memory, Nature Electronics **1** (9) (2018) 508–511. doi:10.1038/s41928-018-0131-z.

[176] J. Han, L. Liu, Topological insulators for efficient spin–orbit torques, APL Materials **9** (6) (2021) 060901. doi:10.1063/5.0048619.

[177] M. Z. Hasan, C. L. Kane, Colloquium: Topological insulators, Reviews of Modern Physics **82** (4) (2010) 3045–3067. doi:10.1103/RevModPhys.82.3045.

[178] J. Li, Z. Y. Wang, A. Tan, P. A. Glans, E. Arenholz, C. Hwang, J. Shi, Z. Q. Qiu, Magnetic dead layer at the interface between a co film and the topological insulator bi_2se_3, Physical Review B **86** (5) (2012) 054430. doi:10.1103/PhysRevB.86.054430.

[179] Y. Wang, P. Deorani, K. Banerjee, N. Koirala, M. Brahlek, S. Oh, H. Yang, Topological

surface states originated spin-orbit torques in bi_2se_3, Physical Review Letters **114** (25) (2015) 257202. doi:10.1103/PhysRevLett.114.257202.

[180] L. A. Walsh, C. M. Smyth, A. T. Barton, Q. Wang, Z. Che, R. Yue, J. Kim, M. J. Kim, R. M. Wallace, C. L. Hinkle, Interface chemistry of contact metals and ferromagnets on the topological insulator bi_2se_2, The Journal of Physical Chemistry C **121** (42) (2017) 23551–23563. doi:10.1021/acs.jpcc.7b08480.

[181] F. Bonell, M. Goto, G. Sauthier, J. F. Sierra, A. I. Figueroa, M. V. Costache, S. Miwa, Y. Suzuki, S. O. Valenzuela, Control of spin–orbit torques by interface engineering in topological insulator heterostructures, Nano Letters **20** (8) (2020) 5893–5899. doi:10.1021/acs.nanolett.0c01850.

[182] D. Zhu, Y. Wang, S. Shi, K.-L. Teo, Y. Wu, H. Yang, Highly efficient charge-to-spin conversion from in situ bi_2se_3/fe heterostructures, Applied Physics Letters **118** (6) (2021) 062403. doi:10.1063/5.0035768.

[183] A. K. Reza, X. Fong, Z. A. Azim, K. Roy, Modeling and evaluation of topological insulator/ferromagnet heterostructure-based memory, IEEE Transactions on Electron Devices **63** (3) (2016) 1359–1367. doi:10.1109/TED.2016.2520941.

[184] K. Ando, S. Takahashi, J. Ieda, H. Kurebayashi, T. Trypiniotis, C. H. W. Barnes, S. Maekawa, E. Saitoh, Electrically tunable spin injector free from the impedance mismatch problem, Nature Materials **10** (9) (2011) 655–659. doi:10.1038/nmat3052.

[185] S. Lamrani, A. Guittoum, R. Schäfer, S. Pofahl, V. Neu, M. Hemmous, N. Benbrahim, Microstructure investigation and magnetic study of permalloy thin films grown by thermal evaporation, Eur. Phys. J. Appl. Phys. **74** (3). doi:10.1051/epjap/2016150548.

[186] G. Counil, T. Devolder, J.-V. Kim, P. Crozat, C. Chappert, S. Zoll, R. Fournel, Temperature dependences of the resistivity and the ferromagnetic resonance linewidth in permalloy thin films, IEEE Transactions on Magnetics **42** (10) (2006) 3323–3325. doi:10.1109/TMAG.2006.879718.

[187] D. C. Leitao, J. Ventura, J. M. Teixeira, C. T. Sousa, S. Pinto, J. B. Sousa, J. M. Michalik, J. M. D. Teresa, M. Vazquez, J. P. Araujo, Correlations among magnetic, electrical and magneto-transport properties of NiFe nanohole arrays, Journal of Physics: Condensed Matter **25** (6) (2013) 066007. doi:10.1088/0953-8984/25/6/066007.

[188] A. F. Mayadas, J. F. Janak, A. Gangulee, Resistivity of permalloy thin films, Journal of Applied Physics **45** (6) (1974) 2780–2781. doi:10.1063/1.1663668.

[189] I. Trindade, D. Leitão, R. Fermento, Y. Pogorelev, J. Sousa, Electron scattering characteristics of polycrystalline metal transition films by in-situ electrical resistance measurements, Journal of Magnetism and Magnetic Materials **321** (16) (2009) 2494–2498. doi:https://doi.org/10.1016/j.jmmm.2009.03.014.

[190] P. L. Rossiter, The electrical resistivity of metals and alloys, Cambridge university press, 1991.

[191] I. Campbell, A. Fert, Chapter 9 transport properties of ferromagnets, in: Handbook of Ferromagnetic Materials, Vol. 3 of Handbook of Ferromagnetic Materials, Elsevier, 1982, pp. 747–804. doi:https://doi.org/10.1016/S1574-9304(05)80095-1.
URL https://www.sciencedirect.com/science/article/pii/S1574930405800951

[192] K. Uchida, S. Takahashi, K. Harii, J. Ieda, W. Koshibae, K. Ando, S. Maekawa, E. Saitoh, Observation of the spin seebeck effect, Nature **455** (7214) (2008) 778–781. doi:10.1038/nature07321.

[193] K. Uchida, T. Ota, K. Harii, S. Takahashi, S. Maekawa, Y. Fujikawa, E. Saitoh, Spin-seebeck effects in $ni_{81}fe_{19}$/pt films, Solid State Communications **150** (11) (2010) 524–528. doi:https://doi.org/10.1016/j.ssc.2009.10.045.

[194] M. S. Anwar, B. Lacoste, J. Aarts, Anisotropic magnetothermoelectric power of ferromagnetic thin films, Journal of Magnetism and Magnetic Materials **441** (2017) 542–547. doi:https://doi.org/10.1016/j.jmmm.2017.06.055.

[195] M. Kimura, X. He, T. Katase, T. Tadano, J. M. Tomczak, M. Minohara, R. Aso, H. Yoshida, K. Ide, S. Ueda, H. Hiramatsu, H. Kumigashira, H. Hosono, T. Kamiya, Large phonon drag thermopower boosted by massive electrons and phonon leaking in laalo3/lanio3/laalo3 heterostructure, Nano Letters **21** (21) (2021) 9240–9246, pMID: 34709840. doi:10.1021/acs.nanolett.1c03143.

[196] T. G. S. M. Rijks, S. K. J. Lenczowski, R. Coehoorn, W. J. M. de Jonge, In-plane and out-of-plane anisotropic magnetoresistance in $ni_{80}fe_{20}$ thin films, Physical Review B **56** (1997) 362–366. doi:10.1103/PhysRevB.56.362.

[197] D. C. Leitao, J. Ventura, C. T. Sousa, A. M. Pereira, J. B. Sousa, M. Vazquez, J. P. Araujo, Insights into the role of magnetoelastic anisotropy in the magnetization reorientation of magnetic nanowires, Physical Review B **84** (2011) 014410. doi:10.1103/PhysRevB.84.014410.

[198] B. Khodadadi, J. B. Mohammadi, C. Mewes, T. Mewes, M. Manno, C. Leighton, C. W. Miller, Enhanced spin pumping near a magnetic ordering transition, Physical Review B **96** (2017) 054436. doi:10.1103/PhysRevB.96.054436.

[199] Y. Zhao, Q. Song, S.-H. Yang, T. Su, W. Yuan, S. S. P. Parkin, J. Shi, W. Han, Experimental investigation of temperature-dependent gilbert damping in permalloy thin films, Scientific Reports **6** (1) (2016) 22890. doi:10.1038/srep22890.

[200] S. Martín-Rio, A. Pomar, L. Balcells, B. Bozzo, C. Frontera, B. Martínez, Temperature dependence of spin pumping and inverse spin hall effect in permalloy/pt bilayers, Journal of Magnetism and Magnetic Materials **500** (2020) 166319. doi:https://doi.org/10.1016/j.jmmm.2019.166319.

[201] J. D. R. Buchanan, T. P. A. Hase, B. K. Tanner, P. J. Chen, L. Gan, C. J. Powell, W. F. Egelhoff, Anomalously large intermixing in aluminum–transition-metal bilayers, Physical Review B **66** (2002) 104427. doi:10.1103/PhysRevB.66.104427.

[202] E. Longo, C. Wiemer, M. Belli, R. Cecchini, M. Longo, M. Cantoni, C. Rinaldi, M. D. Overbeek, C. H. Winter, G. Gubbiotti, G. Tallarida, M. Fanciulli, R. Mantovan, Ferromagnetic resonance of co thin films grown by atomic layer deposition on the sb_2te_3 topological insulator, Journal of Magnetism and Magnetic Materials **509** (2020) 166885. doi:https://doi.org/10.1016/j.jmmm.2020.166885.

[203] H. He, L. Tai, D. Wu, H. Wu, A. Razavi, K. Wong, Y. Liu, K. L. Wang, Enhancement of spin-to-charge conversion efficiency in topological insulators by interface engineering, APL Materials **9** (7) (2021) 071104. doi:10.1063/5.0049044.

[204] M. Caminale, A. Ghosh, S. Auffret, U. Ebels, K. Ollefs, F. Wilhelm, A. Rogalev, W. E. Bailey, Spin pumping damping and magnetic proximity effect in pd and pt spin-sink layers, Physical Review B **94** (1) (2016) 014414. doi:10.1103/PhysRevB.94.014414.

[205] B. B. Singh, S. K. Jena, M. Samanta, K. Biswas, B. Satpati, S. Bedanta, Inverse spin hall effect in electron beam evaporated topological insulator bi_2se_3 thin film, physica status solidi (RRL) – Rapid Research Letters **13** (3) (2019) 1800492. doi:10.1002/pssr.201800492.

[206] R. Sun, S. Yang, X. Yang, E. Vetter, D. Sun, N. Li, L. Su, Y. Li, Y. Li, Z.-z. Gong, Z.-k. Xie, K.-y. Hou, Q. Gul, W. He, X.-q. Zhang, Z.-h. Cheng, Large tunable spin-to-charge conversion induced by hybrid rashba and dirac surface states in topological insulator heterostructures, Nano Letters **19** (7) (2019) 4420–4426. doi:10.1021/acs.nanolett.9b01151.

[207] A. Baker, A. Figueroa, L. Collins-McIntyre, G. Van Der Laan, T. Hesjedal, Spin pumping in ferromagnet-topological insulator-ferromagnet heterostructures, Scientific reports **5** (1) (2015) 1–5. doi:10.1038/srep07907.

[208] J. C. Rojas-Sánchez, A. Fert, Compared efficiencies of conversions between charge and spin current by spin-orbit interactions in two- and three-dimensional systems, Physical Review Applied **11** (5) (2019) 054049. doi:10.1103/PhysRevApplied.11.054049.

[209] K. Ando, E. Saitoh, Inverse spin-hall effect in palladium at room temperature, Journal of Applied Physics **108** (11) (2010) 113925. doi:10.1063/1.3517131.

[210] H. Liu, C. Zhang, H. Malissa, M. Groesbeck, M. Kavand, R. McLaughlin, S. Jamali, J. Hao, D. Sun, R. A. Davidson, L. Wojcik, J. S. Miller, C. Boehme, Z. V. Vardeny, Organic-based magnon spintronics, Nature Materials **17** (4) (2018) 308–312. doi:10.1038/s41563-018-0035-3.

[211] R. Dey, A. Roy, L. F. Register, S. K. Banerjee, Recent progress on measurement of spin–charge interconversion in topological insulators using ferromagnetic resonance, APL Materials **9** (6) (2021) 060702. doi:10.1063/5.0049887.

[212] N. H. D. Khang, Y. Ueda, P. N. Hai, A conductive topological insulator with large spin hall effect for ultralow power spin–orbit torque switching, Nature Materials **17** (9) (2018) 808–813. doi:10.1038/s41563-018-0137-y.

[213] H. Wang, J. Kally, J. S. Lee, T. Liu, H. Chang, D. R. Hickey, K. A. Mkhoyan, M. Wu, A. Richardella, N. Samarth, Surface-state-dominated spin-charge current conversion in topological-insulator–ferromagnetic-insulator heterostructures, Physical Review Letters **117** (7) (2016) 076601. doi:10.1103/PhysRevLett.117.076601.

[214] Z. Luo, A. Hrabec, T. P. Dao, G. Sala, S. Finizio, J. Feng, S. Mayr, J. Raabe, P. Gambardella, L. J. Heyderman, Current-driven magnetic domain-wall logic, Nature **579** (7798) (2020) 214–218. doi:10.1038/s41586-020-2061-y.

[215] S. Manipatruni, D. E. Nikonov, I. A. Young, Beyond cmos computing with spin and polarization, Nature Physics **14** (4) (2018) 338–343. doi:10.1038/s41567-018-0101-4.

[216] E. N. Mitchell, C. V. Briscoe, Uniaxial anisotropy in permalloy films at temperatures below 4.2°k, Journal of Applied Physics **37** (3) (1966) 1489–1490. doi:10.1063/1.1708531.

[217] M. D. De Sihues, P. Silva, J. Fermin, Effect of temperature on the ferromagnetic resonance of $ni_{50}fe_{50}$ thin films, Physica B: Condensed Matter **354** (1-4) (2004) 361–364. doi:j.physb.2004.10.018.

[218] Y. Shiomi, K. Nomura, Y. Kajiwara, K. Eto, M. Novak, K. Segawa, Y. Ando, E. Saitoh, Spin-electricity conversion induced by spin injection into topological insulators, Physical Review Letters **113** (19) (2014) 196601. doi:10.1103/PhysRevLett.113.196601.

[219] C. B. Seung-heon, V. P. Amin, Y.-W. Oh, G. Go, S.-J. Lee, G.-H. Lee, K.-J. Kim, M. D. Stiles, B.-G. Park, K.-J. Lee, Spin currents and spin-orbit torques in ferromagnetic trilayers, Nature Materials **17** (6) (2018) 509–513. doi:10.1038/s41563-018-0041-5.

[220] J. Yu, D. Bang, R. Mishra, R. Ramaswamy, J. H. Oh, H.-J. Park, Y. Jeong, P. Van Thach, D.-K. Lee, G. Go, S.-W. Lee, Y. Wang, S. Shi, X. Qiu, H. Awano, K.-J. Lee, H. Yang, Long spin coherence length and bulk-like spin–orbit torque in ferrimagnetic multilayers, Nature Materials **18** (1) (2019) 29–34. doi:10.1038/s41563-018-0236-9.

[221] S. Shi, S. Liang, Z. Zhu, K. Cai, S. D. Pollard, Y. Wang, J. Wang, Q. Wang, P. He, J. Yu, G. Eda, G. Liang, H. Yang, All-electric magnetization switching and dzyaloshinskii–moriya interaction in wte2/ferromagnet heterostructures, Nature Nanotechnology **14** (10) (2019) 945–949. doi:10.1038/s41565-019-0525-8.

[222] Y. Liu, J. Besbas, Y. Wang, P. He, M. Chen, D. Zhu, Y. Wu, J. M. Lee, L. Wang, J. Moon, N. Koirala, S. Oh, H. Yang, Direct visualization of current-induced spin accumulation in topological insulators, Nature Communications **9** (1) (2018) 2492. doi:10.1038/s41467-018-04939-6.

[223] Q. Shao, C. Tang, G. Yu, A. Navabi, H. Wu, C. He, J. Li, P. Upadhyaya, P. Zhang, S. A. Razavi, Q. L. He, Y. Liu, P. Yang, S. K. Kim, C. Zheng, Y. Liu, L. Pan, R. K. Lake, X. Han, Y. Tserkovnyak, J. Shi, K. L. Wang, Role of dimensional crossover on spin-orbit torque efficiency in magnetic insulator thin films, Nature Communications **9** (1) (2018) 3612. doi:10.1038/s41467-018-06059-7.

[224] P. Song, C.-H. Hsu, G. Vignale, M. Zhao, J. Liu, Y. Deng, W. Fu, Y. Liu, Y. Zhang, H. Lin, V. M. Pereira, K. P. Loh, Coexistence of large conventional and planar spin hall effect with long spin diffusion length in a low-symmetry semimetal at room temperature, Nature Materials **19** (3) (2020) 292–298. doi:10.1038/s41563-019-0600-4.

[225] D. C. Vaz, P. Noël, A. Johansson, B. Göbel, F. Y. Bruno, G. Singh, S. McKeown-Walker, F. Trier, L. M. Vicente-Arche, A. Sander, S. Valencia, P. Bruneel, M. Vivek, M. Gabay, N. Bergeal, F. Baumberger, H. Okuno, A. Barthélémy, A. Fert, L. Vila, I. Mertig, J.-P. Attané, M. Bibes, Mapping spin–charge conversion to the band structure in a topological oxide two-dimensional electron gas, Nature Materials **18** (11) (2019) 1187–1193. doi:10.1038/s41563-019-0467-4.

[226] K. Nomura, H. Ohta, A. Takagi, T. Kamiya, M. Hirano, H. Hosono, Room-temperature fabrication of transparent flexible thin-film transistors using amorphous oxide semiconductors, Nature **432** (7016) (2004) 488–492. doi:10.1038/nature03090.

[227] J. A. Rogers, T. Someya, Y. Huang, Materials and mechanics for stretchable electronics, Science **327** (5973) (2010) 1603. doi:10.1126/science.1182383.

[228] D. Son, J. Kang, O. Vardoulis, Y. Kim, N. Matsuhisa, J. Y. Oh, J. W. F. To, J. Mun, T. Katsumata, Y. Liu, A. F. McGuire, M. Krason, F. Molina-Lopez, J. Ham, U. Kraft, Y. Lee, Y. Yun, J. B. H. Tok, Z. Bao, An integrated self-healable electronic skin system fabricated via dynamic reconstruction of a nanostructured conducting network, Nature Nanotechnology **13** (11) (2018) 1057–1065. doi:10.1038/s41565-018-0244-6.

[229] X. Shi, Y. Zuo, P. Zhai, J. Shen, Y. Yang, Z. Gao, M. Liao, J. Wu, J. Wang, X. Xu, Q. Tong, B. Zhang, B. Wang, X. Sun, L. Zhang, Q. Pei, D. Jin, P. Chen, H. Peng, Large-area display textiles integrated with functional systems, Nature **591** (7849) (2021) 240–245. doi:10.1038/s41586-021-03295-8.

[230] L. Yin, K. N. Kim, J. Lv, F. Tehrani, M. Lin, Z. Lin, J.-M. Moon, J. Ma, J. Yu, S. Xu, J. Wang, A self-sustainable wearable multi-modular e-textile bioenergy microgrid system, Nature Communications **12** (1) (2021) 1542. doi:10.1038/s41467-021-21701-7.

[231] S. Zhao, Z. Zhou, C. Li, B. Peng, Z. Hu, M. Liu, Low-voltage control of (co/pt)x perpendicular magnetic anisotropy heterostructure for flexible spintronics, ACS Nano **12** (7) (2018) 7167–7173. doi:10.1021/acsnano.8b03097.

[232] Z. Zhang, E. Liu, W. Zhang, P. K. J. Wong, Z. Xu, F. Hu, X. Li, J. Tang, A. T. S. Wee, F. Xu, Mechanical strain manipulation of exchange bias field and spin dynamics in feco/irmn multilayers grown on flexible substrates, ACS Applied Materials & Interfaces **11** (8) (2019) 8258–8265. doi:10.1021/acsami.8b21421.

[233] I. Fina, N. Dix, E. Menéndez, A. Crespi, M. Foerster, L. Aballe, F. Sánchez, J. Fontcuberta, Flexible antiferromagnetic ferh tapes as memory elements, ACS Applied Materials & Interfaces **12** (13) (2020) 15389–15395. doi:10.1021/acsami.0c00704.

[234] E. Liu, T. Fache, D. Cespedes-Berrocal, Z. Zhang, S. Petit-Watelot, S. Mangin, F. Xu, J. C. Rojas-Sánchez, Strain-enhanced charge-to-spin conversion in Ta/Fe/Pt multilayers grown on flexible mica substrate, Physical Review Applied **12** (4) (2019) 044074. doi:10.1103/PhysRevApplied.12.044074.

[235] G. D. H. Wong, C. C. I. Ang, W. Gan, W. C. Law, Z. Xu, F. Xu, C. S. Seet, W. S. Lew, Reversible strain-induced spin–orbit torque on flexible substrate, Applied Physics Letters **119** (4) (2021) 042402. doi:10.1063/5.0056995.

[236] S. Zhao, Y. Zhao, B. Tian, J. Liu, S. Jin, Z. Jiang, Z. Zhou, M. Liu, Photovoltaic control of ferromagnetism for flexible spintronics, ACS Applied Materials & Interfaces **12** (37) (2020) 41999–42006. doi:10.1021/acsami.0c11954.

[237] J. P. Heremans, R. J. Cava, N. Samarth, Tetradymites as thermoelectrics and topological insulators, Nature Reviews Materials **2** (10) (2017) 17049. doi:10.1038/natrevmats.2017.49.

[238] L. Müchler, F. Casper, B. Yan, S. Chadov, C. Felser, Topological insulators and thermoelectric materials, physica status solidi (RRL) – Rapid Research Letters **7** (1-2) (2013) 91–100. doi:https://doi.org/10.1002/pssr.201206411.

[239] N. Xu, Y. Xu, J. Zhu, Topological insulators for thermoelectrics, npj Quantum Materials **2** (1) (2017) 51. doi:10.1038/s41535-017-0054-3.

[240] L. Francioso, C. De Pascali, I. Farella, C. Martucci, P. Cretì, P. Siciliano, A. Perrone, Flexible thermoelectric generator for ambient assisted living wearable biometric sensors, Journal of Power Sources **196** (6) (2011) 3239–3243. doi:https://doi.org/10.1016/j.jpowsour.2010.11.081.

[241] Y. Wang, Y. Shi, D. Mei, Z. Chen, Wearable thermoelectric generator to harvest body heat for powering a miniaturized accelerometer, Applied Energy **215** (2018) 690–698. doi:https://doi.org/10.1016/j.apenergy.2018.02.062.

[242] E. M. F. Vieira, A. L. Pires, J. P. B. Silva, V. H. Magalhães, J. Grilo, F. P. Brito, M. F. Silva, A. M. Pereira, L. M. Goncalves, High-performance μ-thermoelectric device based on bi_2te_3/sb_2te_3 p–n junctions, ACS Applied Materials & Interfaces **11** (42) (2019) 38946–38954. doi:10.1021/acsami.9b13254.

[243] J. Andzane, A. Felsharuk, A. Sarakovskis, U. Malinovskis, E. Kauranens, M. Bechelany, K. A. Niherysh, I. V. Komissarov, D. Erts, Thickness-dependent properties of ultrathin bismuth and antimony chalcogenide films formed by physical vapor deposition and their application in thermoelectric generators, Materials Today Energy **19** (2021) 100587. doi:https://doi.org/10.1016/j.mtener.2020.100587.

[244] S. Y. Matsushita, K. Ichimura, K. K. Huynh, K. Tanigaki, Large thermopower in topological surface state of sn-bsts topological insulators: Thermoelectrics and energy-dependent relaxation times, Physical Review Materials **5** (1) (2021) 014205. doi:10.1103/PhysRevMaterials.5.014205.

[245] I. Groen, V. T. Pham, N. Leo, A. Marty, L. E. Hueso, F. Casanova, Disentangling spin, anomalous, and planar hall effects in ferromagnet–heavy-metal nanostructures, Physical Review Applied **15** (4) (2021) 044010. doi:10.1103/PhysRevApplied.15.044010.

[246] W. F. Schlosser, Calculation of the atomic volumes of fe-ni and fe-co alloys, physica status solidi (a) **17** (1) (1973) 199–205. doi:https://doi.org/10.1002/pssa.2210170122.

[247] V. Ozolins, E. Majzoub, T. Udovic, Electronic structure and rietveld refinement parameters of ti-doped sodium alanates, Journal of Alloys and Compounds **375** (1-2) (2004) 1–10. doi:10.1016/j.jallcom.2003.11.154.

[248] R. J. Gripshover, J. B. VanZytveld, J. Bass, Thermopower of pure aluminum, Phys. Rev. **163** (1967) 598–603. doi:10.1103/PhysRev.163.598.

[249] A. Pietrikova, P. Lukacs, D. Jakubeczyova, B. Ballokova, J. Potencki, G. Tomaszewski, J. Pekarek, K. Prikrylova, M. Fides, Surface analysis of polymeric substrates used for inkjet printing technology, Circuit World. doi:10.1108/CW-10-2015-0047.

[250] R. Weber, D.-S. Han, I. Boventer, S. Jaiswal, R. Lebrun, G. Jakob, M. Kläui, Gilbert damping of cofe-alloys, Journal of Physics D: Applied Physics **52** (32) (2019) 325001. doi:10.1088/1361-6463/ab2096.

[251] B. Kardasz, B. Heinrich, Ferromagnetic resonance studies of accumulation and diffusion of spin momentum density in fe/ag/fe/gaas(001) and ag/fe/gaas(001) structures, Physical Review B **81** (2010) 094409. doi:10.1103/PhysRevB.81.094409.

[252] Y. Fanchiang, K. Chen, C. Tseng, C. Chen, C. Cheng, S. Yang, C. Wu, S. Lee, M. Hong, J. Kwo, Strongly exchange-coupled and surface-state-modulated magnetization dynamics in bi_2se_3/yttrium iron garnet heterostructures, Nature Communications **9** (1) (2018) 1–9. doi:10.1038/s41467-017-02743-2.

[253] J. Li, C. B. Wilson, R. Cheng, M. Lohmann, M. Kavand, W. Yuan, M. Aldosary, N. Agladze, P. Wei, M. S. Sherwin, et al., Spin current from sub-terahertz-generated antiferromagnetic magnons, Nature **578** (7793) (2020) 70–74. doi:10.1038/s41586-020-1950-4.

[254] P. Vaidya, S. A. Morley, J. van Tol, Y. Liu, R. Cheng, A. Brataas, D. Lederman, E. del Barco, Subterahertz spin pumping from an insulating antiferromagnet, Science **368** (6487) (2020) 160–165. doi:10.1126/science.aaz4247.

[255] I. Groen, S. Manipatruni, W. Y. Choi, D. E. Nikonov, E. Sagasta, C.-C. Lin, T. A. Gosavi, A. Marty, L. E. Hueso, I. A. Young, et al., Spin-orbit magnetic state readout in scaled ferromagnetic/heavy metal nanostructures, Nature Electronics **3** (6) (2020) 309–315. doi: 10.1038/s41928-020-0395-y.